Jan Dlugosz University

in Częstochowa

Ph.D. Thesis

Discipline: Physics

Photoactive hybrid structures based on TiO_2 for photovoltaic applications – a computational approach

Oleksandr Korolevych

Scientific Supervisor: prof. dr. hab. Małgorzata Makowska-Janusik

Czestochowa 2023

I dedicate the Thesis to my family.

Acknowledgement

First and foremost I want to thank my supervisor **Prof. Małgorzata Makowska-Janusik**, for her continuous support in my PhD study and research, for her patient motivation and enthusiasm during every stage of my research work. Her continuous motivation makes that this work comes to life.

I would like to thank **Prof. Maciej Zalas's** research group at Adam Mickiewicz University, (Poznan), and mainly **Aleksandra Bartkowiak** for the experiments done to confirm results of performed computational simulations presented in this work.

Special thanks go to my friends, for their support.

I would like to thank my family for their patience and support in every situation.

The results presented in this study were partially created thanks to the financial support of the National Science Center granted as part of the grant OPUS No. 2017/25/B/ST8/01864 entitled *Photoactive hybrid structures for photovoltaic applications.*

The computer simulations, the results of which constitute the core of the presented dissertation, were made in the Wroclaw Center for Networking and Supercomputing (http://www.wcss.wroc.pl) thanks to the Grant no. 171.

Contents

I. List of publications……………………………………………………….XIII
II. Prize and Awards...……………………………………………………XIII
III. Grants……………………………………………….………………..XIV
IV. Participation in the conferences ……………………………………...XIV
V. Scientific internships abroad ………………………………………..XV
VI. Abstract……………..…………………………………………………XVII
VII.Streszczenie……….......………………………….……………...XIX
VIII. Abbreviations and symbols.…………………...………………………XXI
IX. List of figures.………………………………..…...………………...XXIII
X. List of tables……………………………………………………XXXIV

Chapter 1 – Introduction ………………………..…………………….……..1
1.1. Solar energy conversion.....……………………………………………..1
1.2. Three generations of solar cells.………………………………………...1
1.3. Dye-sensitized solar cells (DSSC)……………………………………...5
1.4. Literature.……………………………………………………………...10
Chapter 2 – Titanium dioxide as a structure for photovoltaic applications…………………………………………………………...17
2.1. Physico-chemical properties of titanium dioxide structures……………18
2.2. Role of dopants in TiO_2 structure………………………………………21
2.3. Nanostructures based on the TiO_2……………………………………....30
2.4. Literature.………………………………………………………………32
Chapter 3 – Sensitizers for the photovoltaic applications in dssc devices …..39
3.1. Ru-complex sensitizers………………………………………………….40
3.2. Selected metal-free organic dyes………………………………………..50
3.3. Literature………………………………………………………………..53
Chapter 4 – Theoretical backgrounds of quantum chemical calculations…..61
4.1. Ab initio methodology…………………………………………………..61
4.2 Methodology of the density functional theory (DFT)……………………65
4.2.1. The Hohenberg-Kohn theorem...…………………………………..65
4.2.2. The Kohn-Sham equations..……………………………………….66
4.2.3. The LDA and GGA approximation.……………………………….68

4.2.4. Perdew-Burke-Ernzerhof (PBE) functional………………………..70
4.2.5. The B3LYP hybrid functional……………………………………...71
4.2.6. The long-range corrected BLYP functional (LC-BLYP)…………..71
4.2.7. Hubbard correction method………………………………………...73
4.3. Plane-wave method……………………………………………………...74
4.4. Born-von Karman boundary conditions…………………………………76
4.5. Semi-empirical methods in quantum chemistry…………………………78
4.5.1. PMx parameterization methods……………………………………….79
4.6. Literature………………………………………………………………..80
Chapter 5 – Thesis and hypotheses of the work………………………………..85
Chapter 6 – Structural and electronic properties of TiO_2 -based materials…87
6.1. Structural and electron properties of bulk TiO_2 crystal structures……...88
6.1.1. Model of the 2×2×1 supercell……………………………………….90
6.1.2. Defective 2×2×1 TiO_2 structures doped substitutionally…………97
6.1.3. Defective 2×2×1 TiO_2 structure doped interstitially…………….105
6.1.4. The 2×2×1 TiO_2 structure doped by nitrogen…………………...106
6.2. Structural and electron properties of thin films based on TiO_2 structures……………………………………………………………...111
6.3. Structural and electron parameters of clusters based on TiO_2 structures……………………………………………………………...120
6.4. Synthesis and experimental investigations of selected TiO_2-based structures ……………………………………………………………..125
6.5. Conclusions……………………………………………………………131
6.6. Literature……………………………………………………………....132
Chapter 7 – Structural and electron properties of selected dyes for dssc applications………………………………………………………………143
7.1. Dyes based on single tris(bipyridine)ruthenium(II) complexes……….143
7.2. Dyes based on the dinuclear dendritic configuration of tris(bipyridine)ruthenium(II) complexes…………………………………...162
7.3. D102 and D149-based molecules with different anchoring groups……183
7.4. Conclusions……………………………………………………………190
7.5. Literature………………………………………………………………192
Chapter 8 – Structural and electronic properties of selected dyes/TiO_2 hybrids…………………………………………………………………….199

8.1. Structural and electron properties of B_X/TiO_2 hybrids…………………199
8.2. Structural and electron properties of mono ruthenium/TiO_2 hybrids….215
8.3. Conclusions……………………………………………………………220
8.4. Literature………………………………………………………………222
Chapter 9 - Conclusions……………………………………………………….227

List of publications

1. Korolevych, O., Zalas, M., Stampor, W., Kassiba, A. H., & Makowska-Janusik, M. "Impact of dyes isomerization effect on the charge transfer phenomenon occurring on the dye/nanosemiconductor interface." *Solar Energy Materials and Solar Cells*, vol.219, pp.110771, **(2021)**. doi:10.1016/j.solmat.2020.110771

2. Bartkowiak, A., Korolevych, O., Chiarello, G. L., Makowska-Janusik, M., & Zalas, M. "How Can the Introduction of Zr^{4+} Ions into TiO_2 Nanomaterial Impact the DSSC Photoconversion Efficiency? A Comprehensive Theoretical and Experimental Consideration." *Materials*, vol.14, no.11, pp.2955, **(2021)**. doi:10.3390/ma14112955

3. Bartkowiak, A., Korolevych, O., Chiarello, G. L., Makowska-Janusik, M., & Zalas, M.. "Experimental and theoretical insight into DSSCs mechanism influenced by different doping metal ions." *Applied Surface Science*, vol.*597*, pp.153607, **(2022)**. doi:10.1016/j.apsusc.2022.153607

4. Pelczarski D, Korolevych O., Gierczyk B, Zalas M, Makowska-Janusik M, Stampor W. "Electronic States of Tris(bipyridine) Ruthenium(II) Complexes in Neat Solid Films Investigated by Electroabsorption Spectroscopy." *Materials (Basel).* vol.19, no.15, pp.2278, **(2022)**. doi:10.3390/ma15062278

5. Bartkowiak A., Korolevych O., Gierczyk B., Pelczarski D., Bossi A., Klein, M. Popenda Ł., Stampor W., Makowska-Janusik M., and Zalas M. "Anchoring ligands modifications of binuclear ruthenium sensitizers and their influence on an electron transport mechanism in dye-sensitized solar cells" work was sent to be published in *Nature Communications*

Prize and Awards

THE BEST POSTER PRESENTATION OF THE CONFERENCE

Oleksandr Korolevych, at al. Poster “PHOTOSTIMULATED CHARGE TRANSFER IN HYBRID PHOTOVOLTAIC MATERIALS.” National Scientific Conference „Novel Trends of Polish Science 2019” – 5-6.12.2019 r., Zakopane

Grants

1. Investigator in the the OPUS grant No. 2017/25/B/ST8/01864 funded by the National Center of Sciences, Poland, Title of grant: *Photoactive hybrid structures for photovoltaic applications*

2. Program stypendialny SSHN na pobyt badawczy, **BGF SSHN 2022** *Campus France 126699Z* University of Le Mans *01/11/2022 to 31/12/2022*

Participation in the conferences

Oral communications:

1. Oleksandr Korolevych, at al.”Obliczenia pasmowe właściwości strukturalnych i elektronowych a-TiO_2 zdefektowanego i domieszkowanego jonami Zr oraz Ni” XIII INTERDYSCYPLINARNA KONFEREN-CJA NAUKOWA TYGEIL 2021 „Interdyscyplinarność kluczem do rozwoju” 25-28.03.2021r, on-line
2. Oleksandr Korolevych, at al. ”Właściwości elektronowe materiałów hybrydowych na bazie TiO_2 i barwników rutenowych”, Kryształki Molekularne 2021, 9-10.06.2021, Częstochowa, on-line
3. Oleksandr Korolevych, at al. ”Właściwości elektronowe materiałów hybrydowych na bazie TiO_2 i nowych barwników rutenowych”, Kryształy Molekularne 2022, 05-09.09.2022, Częstochowa-Kroszyce

Poster:

1. Oleksandr Korolevych, at al. Poster “PHOTOSTIMULATED CHARGE TRANSFER IN HYBRID PHOTOVOLTAIC MATERIALS.” National Scientific Conference „Novel Trends of Polish Science 2019” – 5-6.12.2019 r., Zakopane

Scientific internships abroad

1. University of Le Mans - PPI/PRO/2018/1/00021/U/001 PROM PROGRAMME - INTERNATIONAL SCHOLARSHIP EXCHANGE OF PHD CANDIDATES AND ACADEMIC STAFF PROM 23/04/2019 to 11/05/2019 “RF-sputtering deposition of mixed binary thin films and investigation of related features”

2. Uniwersytet Le Mans, Francja Wyjazd w ramach program Erasmus+ 2019-1-PL01-KA103-063677, 14/03/2022 do 20/05/2022 ”Physical properties of the TiO_2 structures doped by Zr ions”

3. University of Le Mans - Program stypendialny SSHN na pobyt badawczy **BGF SSHN 2022** *Campus France 126699Z* 01/11/2022 to 31/12/2022

Abstract

Thanks to the pioneering work of Grätzel (*Nature* 353 (1991) 737), dye-sensitized solar cells (DSSC) are becoming more and more popular due to the possibility of cheap conversion of solar radiation into electricity. An oxide semiconductor, such as titanium dioxide (TiO_2), in DSSC cells forms an anode on which dye molecules are adsorbed, absorbing light in the visible range. The ability to convert light into electricity depends on the electron properties of the semiconductor and dye as well as the type of their connection. Component compatibility affects the photovoltaic properties of the hybrid material. The proper selection of dyes for a particular semiconductor can be made by employing computer simulations of their electronic and optical properties. Determining the method of electron transfer between the dye and the semiconductor gives the possibility of a well-thought-out selection of photovoltaic components.

The aim of the work was to create a methodology for computer simulations to predict the electron and optical properties of hybrid materials based on ruthenium dye/TiO_2 nanostructure. This allowed us to determine the mechanism of electron transfer between the dye and the semiconductor.

Quantum-chemical calculations of the electron properties of TiO_2 with oxygen vacancies and doped with zirconium (Zr), copper (Cu), manganese (Mn), nickel (Ni), and nitrogen (N) ions in the form of a bulk crystal, thin films, and nanostructures were performed. The impurity ions were selected based on performed experimental studies. A DFT-based method to calculate the structural and electron properties of semiconductor materials was developed using appropriate Hubbard parameters. It has been proven that the use of Hubbard's corrections gives computational results in agreement with the experimental data of both structural and electron parameters. The influence of individual ions and the role of oxygen vacancies in the TiO_2 structure on the charge transfer process in DSSC cells was determined. It was found that the Zr impurities stabilize the anatase form of the TiO_2 nanostructures and generate oxygen vacancies, which is conducive to photoconductivity. It has been proven that doping of the TiO_2 with other ions lowers the band gap of the semiconductor, but only donor levels with high energy dispersion favor photoconversion processes. The results of the performed research

indicate that the type of admixture and its content has a significant impact on the charge transfer in DSSC cells.

Quantum-chemical calculations of electron and optical properties of two groups of ruthenium dyes were carried out. In the first group there were dyes with one trisbipyridine center in the molecule, and in the second - dendrimer dyes with two trisbipyridine centers each. The dyes differed in the position and number of anchor groups (-COOH) and in the construction of the separator between the trisbipyridine and the anchor. It was shown that the intramolecular electron transfer capability depends on the position of the anchor group. Dyes with an anchor in the meta and para position adsorb on the TiO_2 surface in a similar amount, but the efficiency of cells sensitized with para-substituted dye is higher. It was found that the additional anchor group placed in the para position to the metallic center improves the charge transfer. It was shown that the replacement of the ethynyl π-linker with the phenyl one in the dye weakens the intramolecular electron transmission capacity but increases the lifetime of the free charges, which has a positive effect on the operation of DSSC cells.

An innovative method of modeling the geometry of hybrid systems was developed, consisting in substituting a dye in place of the anchor and separator, which made it possible to preserve the structure of trisbipyridine groups. Three types of possible connections between the dye and the semiconductor have been identified. The stability of the resulting hybrid systems and the quantitative charge transfer between the hybrid components were analyzed. Using the method of computer simulations and the results of experimental studies, the mechanism of electron transfer in the studied systems was explained. It was found that two-step dye/semiconductor transitions make the main contribution to the photoconversion process.

The presented work completes the state of the art regarding charge transfer processes in dye cells. The presented results are important for the search for new sensitizers and may be a starting point for further research beyond the field of photovoltaics.

Streszczenie

Dzięki pionierskiej pracy Grätzela (*Nature* 353 (1991) 737) barwnikowe ogniwa słoneczne (DSSC) stają się coraz bardziej popularne ze względu na możliwość taniej konwersji promieniowania słonecznego na energię elektryczną. Półprzewodnik tlenkowy, jakim jest między innymi dwutlenek tytanu (TiO_2), w ogniwach DSSC tworzy anodę, na której są zaadsorbowane molekuły barwnika, absorbujące światło w zakresie widzialnym. Zdolność konwersji światła na energię elektryczną zależy od właściwości elektronowych półprzewodnika oraz barwnika jak również rodzaju ich połączenia. Kompatybilność komponentów wpływa na właściwości fotowoltaiczne materiału hybrydowego. Właściwego doboru barwników do konkretnego półprzewodnika można dokonać na drodze symulacji komputerowych ich właściwości elektronowych i optycznych. Określenie sposobu transferu elektronów miedzy barwnikiem a półprzewodnikiem daje możliwość przemyślanego doboru komponentów fotowoltaicznych.

Celem pracy było stworzenie metodyki prowadzenia symulacji komputerowych pozwalających przewidywać właściwości elektronowe i optyczne materiałów hybrydowych na bazie barwnik rutenowy/nanostruktura TiO_2. Dało to możliwość określenia mechanizmu przepływu elektronów między barwnikiem a półprzewodnikiem.

Przeprowadzono obliczenia kwantowo-chemiczne właściwości elektronowych TiO_2 zdefektowanego wakansami tlenowymi oraz domieszkowanego jonami cyrkonu (Zr), miedzi (Cu), manganu (Mn), niklu (Ni) i azotu (N) w formie kryształu objętościowego, cienkich warstw oraz nanostruktur. Jony domieszek wybrano na podstawie prowadzonych badań eksperymentalnych. Opracowano metodę obliczeń DFT właściwości strukturalnych i elektronowych materiałów półprzewodnikowych wykorzystując odpowiednie poprawki Hubbarda. Udowodniono, że stosowanie poprawek Hubbarda daje zgodność wyników obliczeniowych z doświadczalnymi zarówno parametrów strukturalnych jak i elektronowych. Ustalono wpływ poszczególnych jonów oraz rolę wakansów tlenowych w strukturze TiO_2 na proces przenoszenia ładunku w ogniwach DSSC. Stwierdzono, że domieszki Zr stabilizują anatazowe nanostruktury TiO_2 oraz generują wakanse tlenowe, co sprzyja fotoprzewodnictwu. Udowodniono, że domieszkowanie TiO_2 pozostałymi jonami obniża przerwę energetyczną

półprzewodnika, ale tylko poziomy donorowe o dużej dyspersji energetycznej sprzyjają procesom fotokonwersji. Rezultaty przeprowadzonych badań wskazują, że rodzaj domieszki oraz jej zawartość ma znaczący wpływ na transfer ładunku w ogniwach DSSC.

Przeprowadzono obliczenia kwantowo-chemiczne właściwości elektronowych i optycznych dwóch grup barwników rutenowych. W pierwszej grupie były barwniki posiadające jedno centrum trisbipirydynowe w molekule, a w drugiej - barwniki dendrymerowe zawierające po dwa centra trisbipirydynowe. Barwniki różniły się od siebie pozycją i ilością grup kotwiczących (-COOH) oraz budową separatora między trisbipirydyną a kotwicą. Pokazano, że zdolności wewnątrzcząsteczkowego przenoszenia elektronów zależą od pozycji grupy kotwiczącej. Barwniki z kotwicą w położeniu *meta* i *para* adsorbują na powierzchni TiO_2 w podobnej ilości, ale wydajność komórek uczulonych *para*-podstawionym barwnikiem jest większa. Stwierdzono, że dodatkowa grupa kotwicząca umieszczona w pozycji *para* do centrum metalicznego usprawnia przepływ ładunku. Pokazano, że wymiana π-łącznika etynylowego na fenylowy w barwniku powoduje osłabienie zdolności wewnątrzcząsteczkowej transmisji elektronów ale zwiększa czas życia ładunków swobodnych, co ma pozytywny wpływ na działanie ogniw DSSC.

Opracowano nowatorską metodę modelowania geometrii układów hybrydowych, polegającą na podstawieniu barwnika w miejsce kotwicy i separatora, co dało możliwość zachowania struktury grup trisbipirydynowych. Stwierdzono trzy typy możliwych połączeń między barwnikiem a półprzewodnikiem. Przeanalizowano stabilność powstałych układów hybrydowych oraz ilościowy transfer ładunku między komponentami hybryd. Wykorzystując metodę symulacji komputerowych oraz wyniki badań eksperymentalnych wyjaśniono mechanizm transferu elektronów w badanych układach. Stwierdzono, że główny wkład do procesu fotokonwersji mają przejścia dwuetapowe barwnik/półprzewodnik.

Przedstawiona praca uzupełnia stan wiedzy dotyczący procesów transferu ładunku w ogniwach barwnikowych. Zaprezentowane wyniki mają znaczenie dla poszukiwania nowych sensybilizatorów oraz mogą stanowić punkt wyjścia do dalszych badań wykraczających poza obszar fotowoltaiki.

Abbreviations and symbols

ACN - Acetonitrile

AM1 - Austin Model 1

APW - augmented plane wave method

ASC - Apparent surface charge

B3LYP - Becke-3–Lee–Yang–Parr functional

B3LYP/B3LYP - geometry optimized by DFT/B3LYP(LANL2DZ) method and oscillators calculated by DFT/B3LYP(LANL2DZ) method

CB - conductional band

CBM – conductional band minimum

CIS - singlet configuration interaction method

C-PCM - conductor-like PCM

CPV- Concentrated Photovoltaics

CVD - chemical vapor deposition

DFT - density functional theory

DFT+U - DFT methodology augmented by Hubbard parameters

DKH2 - Douglas–Kroll–Hess formalism

DKH2/B3LYP - geometry optimized by DFT/B3LYP-DKH2(jorge-TZP-DKH) method and oscillators calculated by DFT/B3LYP(LANL2DZ) method

DKH2/DKH2 - geometry optimized by DFT/B3LYP-DKH2(jorge-TZP-DKH) method and oscillators calculated by DFT/B3LYP-DKH2(jorge-TZP-DKH) method

DKH2/TD/PM6 - geometry optimized by DFT/B3LYP-DKH2(jorge-TZP-DKH) method and oscillators calculated by TD/PM6 method

DMF – Dimethylformamide

DSSC - dye-sensitized solar cells

EA - Electroabsorption spectroscopy

E_g - energy bandgap

$\mathbf{E_{ox}}$ - oxidation potentials

$\mathbf{E_{red}}$ - reduction potentials

FTO - fluorine-doped tin oxide.

GEA - gradient expansion approximation

GGA - generalized gradient approximation

HF - Hartree-Fock

HF/TD/PM6 - geometry optimized by HF method with LANL2DZ basis set for Ru and 6-31G for remaining atoms and oscillators calculated by TD/PM6 method

HOMO - higher occupied molecular orbital

I_D - denotes the indoline part of the D102 and D149 molecules

ILCT - inter ligand charge transfer

IPCE - incident-photon-to-current efficiency
J_{max} - photocurrent for the maximum power output
jorge-TZP-DKH - Triple zeta valence quality plus polarization (DKH) (Data from F. E. Jorge)
J_{sc} - short-circuit current
LANL2DZ - Los Alamos National Laboratory 2 double-zeta basis sets
LAPW - linearized versions of the APW method
LC-BLYP - long-range corrected BLYP functional
LDA - local density approximation
LUMO - lower unoccupied molecular orbital
m_e - electron rest mass
Me - methyl
m_e^* - effective mass of an electron
m_h^* - effective mass of a hole
MLCT - metal to ligand charge transfer
NHE - Normal Hydrogen Electrode
NIR - Near-infrared
OPE - oligophenylene–ethynylene bridges
PAA - poly(acrylic acid)
PAW - projector-augmented wave
PBE - Perdew-Burke-Ernzerhof functional
PCE - power conversion efficiency
PCM - polarizable continuum model
PF_6 - dihexafluorophosphate
PLA - poly(lactic acid)
PM3 - parametric method 3
PM6 - parametrization method 6
PM7 - parametrization method 7
PRA - random phase approximation
LSD - local spin density approximation
PSC - perovskite solar cells
PV - photovoltaic
RHF - Restricted Hartee Fock
$Ru(bpy)_3^{+2}$ - tris-substituted bipyridine ruthenium(II) complex
SCF - Self-consistent field
SHE - Standard Hydrogen Electrode
TBA^+ - tetra-n-butylammonium
t-Bu - tert-butyl
TD/PM6 - time-dependent PM6 parametrized method
TDHF - time-dependent HF
UV-vis - Ultraviolet–visible
VB - valence band
VBM - valence band maximum
V_{max} - photovoltage for the maximum power output
V_{oc} - open-circuit voltage
XRD - X-ray diffraction

List of figures

Figure 1.1. Spectral absorption distribution for three photo-absorption layer system (reprinted from[10]**Błąd! Nie zdefiniowano zakładki.**). The bottom layer is made from InGaAs (E_g = 0.97-0.99 eV), the middle layer – GaAs (E_g = 1.43 eV), and the top layer – InGaP (E_g = 1.88 eV)……………………………….3

Figure 1.2. Schematic structure of perovskite crystal, perovskites acting as sensitizers on TiO_2 and incident-photon-to-current efficiency measures for example of perovskite solar materials[20]……………..5

Figure 1.3. Schematic energy diagram and basic principles for DSSC with liquid electrolyte part: band position of TiO_2 and schematic energy level for $Ru(pby)_3^{+2}$ I^-/I^-_3 electrolyte, counter electrode(Ag -4.3eV or Au-4.9eV or Pt -6.35eV E vs. vacuum): 1) light absorption on dye, 2)electron injection from dye to semiconductor, 3)electron transfer in semiconductor to the working electrode, 4) interception of the oxidized dye by a redox mediator, 5) oxidized defuse toward the counter electrode, 6)redox mediator regeneration and 7)parasitic recombination, blue line(must be avoided)………………………...7

Figure 1.4. Schematic energy diagram for a dye-sensitized solar cell. Ref [37]……………………………………………………………………8

Figure 2.1. Energy position of the band gap of the several metal oxides used in DSSC applications possessing $E_g > 3$ eV………………………….17

Figure 2.2. Schematic energy diagram for oxygen vacancies created in anatase TiO_2 crystals[17]…………………………………………………….21

Figure 2.3. The valence versus radius plot of anatase to rutile transformation, categorizing inhibiting and promoting dopants, based on the published work[24.]…………………………………………………22

Figure 2.4. Experimentally and computationally predicted inhibition of anatase to rutile transformation[24]….……………………………………23

Figure 2.5. Experimentally and computationally predicted the promotion of anatase to rutile transformation[24]……………………………….....23

Figure 2.6. Scanning electron microscopy images of TiO_2: (A, A’) microsphere[42], (B, B’) nanobeads[43], (C, C’) nanowires[44], (D, D’) nanofibers[45], (E, E') nanorods[46], (F, F') nanotubes[48] (G, G') nanobelts[47], and (J, J') nanosheets[49]. A, A'—mesoporous TiO_2 microspheres with tunable sizes. B—the nanobeads sample, B'—samples after a solvothermal process with different amounts of ammonia. C, C'—Cross-sectional of $H_2Ti_2O_5H_2O$ nanowire arrays. D, D'—the nanobeads sample, E—cross-sectional of the TiO_2 nanorod arrays grown on bare and E'—seeded-FTO substrates. F—Cross-sectional of converted TiO_2 nanotube arrays with a closed top-end, F' F" —top view of converted TiO_2 nanotubes with a closed and opened top-end G—the cross-section of the double-layered film (particles+belts), and up layer (G') surfaces of TiO_2 P–B double-layered film. J, J'—TiO_2 nanosheets with Nb-doped (100) and (001)……………………….…………………………………...31

Figure 2.7. Calculated size dependence of the TiO_2 bandgap energy from reference[51]………………………………………………………...31

Figure 2.8. Band gap position in crystal anatase and single nanosheets of $Ti_{0.91}O_{2-0.36}$ 99 (the difference in anatase band position in this figure and figure 2.1 bases on fact that were used nonaqueous electrolyte charge compensating ion NH^{4+} and Li^+) from[50]…………………32

Figure 3.1. Schematic structure of the most know ruthenium dyes and their UV-vis 52 absorption spectra measured in ethanol…………………….40

Figure 3.2. Conduction and valence band position of TiO_2 and schematic representation of the energy levels and structures of the selected Ru-complexes: $Ru(bpy)_3^{+2}$, N3, N719, N749, and Z907……………...42

Figure 3.3. Schematic structure and graphic representation of $[Ru(bpy)_3](PF_6)_2$ structure [CAS Number 60804-74-2]. The $Ru(bpy)_3^{+2}$ molecules are stabilized by the dihexafluorophosphate $(PF_6)_2$…………………...43

Figure 3.4. Schematic structure of $[Ru(bpy)_3](PF_6)_2$ –based complexes[28]……44

Figure 3.5. Schematic structure representation of $[Ru(pby)_3](PF_6)_2$ complexes consisting of poly(lactic acid) (PLA) and poly(acrylic acid) (PAA)[29]……………………………………………………...45

Figure 3.6. Schematic structure representation of $[Ru(bpy)_3](PF_6)_2$ complexes from the manuscript[30] and [31]……………………………………..46

Figure 3.7. The structures of the [Ru(4,4′-X_2-bpy)$_2$(Mebpy-CN)]-$(PF_6)_2$, where X =−CH_3,−OCH_3,−$N(CH_3)_2$ molecules and their UV-vis absorption spectra measured in acetonitrile[31]……………………………...47

Figure 3.8. Structure of isomeric [Ru(bpy)$_3$]$(PF_6)_2$ complexes, RuLm, RuLo, and RuLp [37]……………………………………………………48

Figure 3.9. Structure of B_1 molecule………………………………………50

Figure 3.10. Molecular structures of the indoline dyes D131 (R_1), D102 (R_2), and D149 (R_3)……………………………………………………51

Figure 3.11. Normalized UV-vis absorption spectra measured for indoline dyes D102[39], D131[44], and D149[51] in tert-butyl alcohol/acetylonitryl (1/1) solvent……………………………………………………………52

Figure 6.1. Optimized crystal structures of the 2×2×1 supercells: A) virgin structure, B) TiO_2:Zr, C) TiO_2:Zr_{in} (Blue atoms—Ti, red atoms—O, green atoms—Zr)……………………………………………91

Figure 6.2. Brillouin zone pass for TiO_2 crystals in anatase polymorph. Electron properties of the a-TiO crystal were calculated in the points of the Brillouin zone as follows Γ-X-M-Γ-Z-R-A-Z[X-R]M-A………...93

Figure 6.3. Energy band structure and electron DOS calculated by DFT/PBE+U method for the a-TiO_2 crystal structure (U_{Ti}=9.25 and J_{Ti}=1.00 eV) ……………………………………………………………………94

Figure 6.4. Energy band structure and electron DOS calculated by DFT/PBE+U method for the t-ZrO_2 crystal structure (U_{Zr}=9.25 and J_{Zr}=1.00 eV) ……………………………………………………………………95

Figure 6.5. Energy band structure and electron DOS calculated by DFT/PBE+U method for the 2×2×1 TiO_2 crystal structure (U_{Ti}=9.25 and J_{Ti}=1.00 eV)…………………………………………………………………..97

Figure 6.6. Energy band structure calculated by DFT/PBE+U method for the 2×2×1 TiO_2 crystal structure with v(O) and v(Ti) vacancies (U_{Ti}=9.25 and J_{Ti}=1.00 eV)……………………………………………98

Figure 6.7. Energy band structure calculated by DFT/PBE+U method for the 2×2×1 TiO_2:Zr and TiO_2:Zr:v(O) crystal structure (U_{Ti}= U_{Zr}=9.25 and J_{Ti}= J_{Zr}=1.00 eV)…………………………………………………100

Figure 6.8. Energy band structure calculated by DFT/PBE+U method for the 2×2×1 TiO_2 crystal doped substitutionally by Ni, Mn, and Cu ions

(J_M=1.00 eV, where M=Ti, Cu, Ni, Mn, U_{Ti}=9.25, U_{Ni}= 6.00 eV, U_{Cu}=U_{Mn}=7.00 eV)…………………………………………...102

Figure 6.9. Energy band structure calculated by DFT/PBE+U method for the 2×2×1 TiO_2 crystal doped substitutionally by Ni, Mn, and Cu ions accompanied by oxygen vacancies (J_M=1.00 eV, where M=Ti, Cu, Ni, Mn, U_{Ti}=9.25, U_{Ni}= 6.00 eV, U_{Mn}= U_{Cu}= 7.00 eV)…………..104

Figure 6.10. Optimized unit calls of the 2×2×1 TiO_2 crystal doped by N atoms: a) substitutionally TiO_2:N; b) interstitially TiO_2:N_{in}; c) interstitially with oxygen vacancy TiO_2:N_{in}:v(O); d) interstitially with oxygen vacancy located far from N atom TiO_2:N_{in}:v(O) far; e) N substitute O atom TiO_2:N_o. (Blue atoms - Ti, red atoms - O, and grey atoms – N)…………………………………………………………..107

Figure 6.11. Energy band structure calculated by DFT/PBE+U method for the 2×2×1 TiO_2 crystal doped interstitially by N atom with different Hubbard correction parameters for N atom and U_{Ti}=9.25 eV, J_{Ti}=1.00 eV …………………………………………………...108

Figure 6.12. UV-vis absorption spectra of TiO_2 (P25) and N-TiO_2 calcined at 400°C for 3h measured experimentally[58]………………………..109

Figure 6.13. Energy band structure calculated by DFT/PBE+U method for the 2×2×1 TiO_2 crystal doped interstitially by N accompanied by oxygen vacancies located close and far from N atom (U_{Ti}= U_N =9.25 eV, J_{Ti}=J_N=1.00 eV)……………………………………………..109

Figure 6.14. Energy band structure and electron DOS calculated by DFT/PBE+U method for the 2×2×1 TiO_2 crystal doped substitutionally by N replacing O atom (U_{Ti}= U_N =9.25 eV, J_{Ti}=J_N=1.00 eV)…………110

Figure 6.15. Valence band maximum (VBM) and conduction band minimum (CBM) for structures based on a-TiO_2 crystals structure modified by dopants and vacancies calculated by DFT/PBE+U method normalized by scaling factor concerning pristine anatase crystal……………………………………………………………111

Figure 6.16. Structure of the a-TiO_2 thin films cut with a crystallographic plane: a) (101), b) (010), c) (001), d) (110), and e) (111) based on 2×2×1 super cell and cut with a crystallographic plane: f) (101), and g) (110) based on 1×1×1 unit cell (Ti - blue atoms, O - red atoms)……112

Figure 6.17. Structure of the TiO_2 (4) films defected by dopants: a) TiO_2:Zr (Zr - green atom), b) TiO_2:Zr:v(O), c) TiO_2:v(O), d) TiO_2:N_O (N - light blue atom), e) TiO_2:Ni (Ni - grey atom), and f) TiO_2:+Ni (Ti-blue atoms and O—red atoms)……………………………………..115

Figure 6.18. Structure of the TiO_2 (2) films defected by a) the Zr atom (TiO_2:Zr, Zr - green atom), b) the Ni atoms (TiO_2:Ni, Ni - grey atom), and c) TiO_2:Ni_o films (N - light blue atom), (Ti-blue atoms, O – red atoms) ………………………………………………………………..115

Figure 6.19. Energy band structures calculated by the DFT/PBE+U method for bulk TiO_2 crystal (2×2×1 super cell of TiO_2), for the thick film of TiO_2, described in the text as (4) and for the thin film of TiO_2, described in the text as (2) (Ti - blue atoms, O - red atoms), in all configurations the same Hubbard parameters were used (U_{Ti}=9.25 eV and J_{Ti}=1 eV)………………………………………………...116

Figure 6.20. Energy band structures calculated by DFT/PBE+U method for the thick film of TiO_2 (4) doped by Zr ions (TiO_2:Zr), doped by Zr ions and accompanied by v(O) (TiO_2:Zr:v(O)), and pristine TiO_2 structure defected by v(O) (TiO_2:v(O)). In all configurations were used the same Hubbard parameters (U_{Ti}=U_{Zr}=9.25 eV and J_{Ti}= J_{Zr}=1 eV)………………………………………………………………117

Figure 6.21. Energy band structures calculated by DFT/PBE+U method for the TiO_2:N_O film (4), the TiO_2:Ni film (4), and the TiO_2:+Ni film (4). In all configurations were used the same Hubbard parameters (U_{Ti}= 9.25 eV, U_{Ni}= 6.00 eV, U_N= 9.25 eV, J_{Ti}= J_{Ni}= J_N=1 eV)………..118

Figure 6.22. Energy band structures calculated by the DFT/PBE+U method for thin films (2) of TiO_2:Zr, TiO_2:Ni, and TiO_2:N_O structures. In all configurations were used the same Hubbard parameters (U_{Ti}=U_{Zr}= 9.25 eV, U_{Ni}= 6.00 eV, U_N= 9.25 eV, J_{Ti}= J_{Zr}=J_{Ni}= J_N=1 eV)…...119

Figure 6.23. Top and lateral view of the $(TiO_2)_{28}$, $(TiO_2)_{28}H_9$, and $(TiO_2)_{28}H_{15}$ clusters (from left to right, respectively) (Ti - green atoms, O - red atoms, and H – grey atoms)…………………………………...120

Figure 6.24. The UV-vis absorption spectra calculated by TD/PM6 for $(TiO_2)_{28}$, $(TiO_2)_{28}H_9$, and $(TiO_2)_{28}H_{15}$ clusters presented in Fig. 6.23……..121

Figure 6.25. Top and lateral view of the $(TiO_2)_{28}H_{15}$, $(TiO_2)_{35}H_{13}$, $(TiO_2)_{42}H_{12}$, and $(TiO_2)_{51}H_{26}$ clusters (from left to right, respectively) (Ti - green atoms, O - red atom, and H – grey atoms)………………………..122

Figure 6.26. UV-vis absorption spectra calculated by TD/PM6 for $(TiO_2)_{28}H_{15}$, $(TiO_2)_{35}H_{13}$, and $(TiO_2)_{42}H_{12}$ clusters presented in Fig. 6.25…….123

Figure 6.27. XRD spectra measured for the TiO_2 thin film deposited on the Si plate versus temperatures………………………………………..126

Figure 6.28. XRD spectra measured for the thin film based on TiO_2 deposited on the Si plate: (a) pristine TiO_2, (b) TiO_2:Zr, (c) TiO_2:Mn, and (d) TiO_2:Ni annealed at temperatures 400℃-600℃ with step 50℃………………………………………………………………..127

Figure 6.29. XRD spectra measured for thin films deposited on a Si plate for pure TiO_2 (a) and with TiO_2:N (b) annealed at temperatures 400℃-600℃ with step 50℃………………………………………………………...128

Figure 6.30. Normalized Raman spectra for measured for thin films of the TiO_2 (black line) and the TiO_2:Zr (red line) deposited on silicon plates a) and on Borofloat 33 b)…………………………………………...129

Figure 6.31. a) Transmittance spectra measured for thin films deposited on Borofloat 33 glass. b) Estimated optical band gaps for thin films in the case of indirectly allowed transitions………………………...130

Figure 7.1. Normalized UV–vis absorption spectra for $Ru(bpy)_3^{2+}(PF_6^-)_2$ measured in acetonitrile[10] (experiment) compared to calculated data: geometry optimized by DFT/B3LYP(LANL2DZ) method and oscillators calculated by DFT/B3LYP(LANL2DZ) method (B3LYP/B3LYP), geometry optimized by DFT/B3LYP-DKH2(Jorge-TZP-DKH) method and oscillators calculated by DFT/B3LYP(LANL2DZ) method (DKH2/B3LYP), geometry optimized by DFT/B3LYP-DKH2(jorge-TZP-DKH) method and oscillators calculated by DFT/B3LYP-DKH2(jorge-TZP-DKH) method (DKH2/DKH2)………………………………………146

Figure 7.2. Structure of the Ru-complexes named as RuLp (para-position of anchor group) (a), RuLm (meta-position of anchor group) (b), and RuLo (orto-position of anchor group) (c) with hexafluorophosphate (PF_6^-) stabilizers………………………………………………147

Figure 7.3. Normalized UV–vis absorption spectra calculated by DFT/B3LYP method for the RuLp, RuLm, and RuLo molecules stabilized by the $(PF_6^-)_2$ in vacuum (black) and solvent DMF (red)………………151

Figure 7.4. UV-vis absorption spectra measured experimentally for the RuLm, RuLo, and RuLp molecules in MeOH-EtOH 4-1 mixture at 298 K (b)[11]………………………………………………………...152

Figure 7.5. UV–vis absorption spectra measured experimentally[25] (blue line) and calculated for the RuLp structure optimized by the DFT/B3LYP-DKH2(jorge-TZP-DKH) method using the DFT/B3LYP-DKH2(jorge-TZP-DKH) method (DKH2/DKH2)………………156

Figure 7.6. a) Stick-bar spectrum of the calculated oscillator strengths using the DKH2/DKH2 method for RuLp with stabilizers overlaid on the experimental absorption spectrum of the RuLp film; b) The EA spectrum calculated using the DKH2/DKH2 method for all excited states presented in part a) of the figure compared with the experimental EA spectrum of the film…………………………..157

Figure 7.7. Normalized UV–vis absorption spectra calculated by semiempirical method TD/PM6, CIS/PM6, and CIS/PM7 for the RuLp molecule stabilized by the $(PF_6^-)_2$ in vacuum (black) and measured ones (red). a) The RuLp molecules optimized by the DFT/B3LYP-DKH2(jorge-TZP-DKH) method (DKH2), b) RuLp structure optimized by HF method with LANL2DZ basis set for Ru and 6-31G for remaining atoms (HF)………………………………………………………160

Figure 7.8. Normalized UV-vis absorption spectra for the RuLp molecule measured experimentally, calculated by the DFT/B3LYP-DKH2(jorge-TZP-DKH) for the RuLp molecule optimized by DFT/B3LYP-DKH2(jorge-TZP-DKH) method (DKH2/DKH2), calculated by TD/PM6 method for the molecule optimized by DFT/B3LYP-DKH2(jorge-TZP-DKH) method (DKH2/TD/PM6 and calculated by TD/PM6 method for RuLp molecule optimized by HF method with LANL2DZ basis set for Ru and 6-31G for remaining atoms (HF/TD/PM6). The molecular orbitals accessing the electron excitations corresponding to the MLCT and ILCT peaks calculated at HF/TD/PM6 level…………………………………161

Figure 7.9. Schematic structure of dinuclear dendritic configuration of the tris(bipyridine)ruthenium(II) complexes named B_1, B_2, B_3, and B_4 ……………………………………………………………..163

Figure 7.10. Normalized UV-vis absorption spectra of B_1, B_2, and B_3 molecules measured experimentally in ACN………………………………166

Figure 7.11. Energy diagram for the first MLCT absorption peak of B_1 a) calculated by the TDDFT/B3LYP with $(PF_6^-)_4$ stabilizer in a vacuum and b) calculated by the TDDFT/B3LYP with $(PF_6^-)_4$ stabilizer in DMF. Single excitation transitions creating the first MLCT peak with the atom orbitals analysis are presented………167

Figure 7.12. Energy diagram for the main absorption peak of B_2 a) calculated by the TDDFT/B3LYP with $(PF_6^-)_4$ stabilizer in a vacuum and b) calculated by the TDDFT/B3LYP with $(PF_6^-)_4$ stabilizer in DMF. Single excitation transitions creating the first MLCT peak with the atom orbitals analysis are presented ……………………………168

Figure 7.13. Energy diagram for the main absorption peak of B_3 a) calculated by the TDDFT/B3LYP with $(PF_6^-)_4$ stabilizer in a vacuum and b) calculated by the TDDFT/B3LYP with $(PF_6^-)_4$ stabilizer in DMF. Single excitation transitions creating the first MLCT peak with the atom orbitals analysis are presented ……………………………168

Figure 7.14. Energy diagram for the main absorption peak of B_4 a) calculated by the TDDFT/B3LYP with $(PF_6^-)_4$ stabilizer in a vacuum and b) calculated by the TDDFT/B3LYP with $(PF_6^-)_4$ stabilizer in DMF. Single excitation transitions creating the first MLCT peak with the atom orbitals analysis are presented……………………………..169

Figure 7.15. Normalized UV–vis absorption spectra calculated by TD-DFT/B3LYP for the B_1, B_2, B_3, and B_4 with $(PF_6^-)_4$ stabilizer in a) vacuum and in b) DMF………………………………………….170

Figure 7.16. Normalized UV-vis spectra for a) B_1 and b) B_2 measured experimentally in ACN (blue line) and calculated (green line) in a vacuum using molecular structures optimized by the DFT/B3LYP-DKH2(jorge-TZP-DKH) method and oscillators calculated by DFT/B3LYP-DKH2(jorge-TZP-DKH) method (DKH2/DKH2) ……………………………………………………………..171

Figure 7.17. Normalized UV–vis absorption spectra calculated by DKH2/DKH2 method for the B_1, B_2, and B_3 molecules stabilized by the $(PF_6^-)_4$ in vacuum (black) and solvent ACN (red)……………………………172

Figure 7.18. Energy diagrams calculated for B_1, B_2, and B_3 molecules by DKH2/DKH2 in vacuum (blue line) and ACN (green line), and experimental data measured in ACN (violet line)…………………………………………………………...174

Figure 7.19. Normalized UV–vis absorption spectra calculated by semiempirical methods TD/PM6, CIS/PM6, and CIS/PM7 for the B_1 molecule stabilized by the $(PF_6^-)_2$ in vacuum (black) optimized by the DFT/B3LYP-DKH2(jorge-TZP-DKH) method (DKH2) (a) and optimized by HF method with LANL2DZ basis set for Ru and 6-31G for remaining atoms (HF) (b) compared with experimental data (red line)……………………………………………………………179

Figure 7.20. Normalized UV-vis absorption spectra calculated in vacuum by the DFT/B3LYP-DKH2(jorge-TZP-DKH) method for B_1 molecule optimized by DFT/B3LYP-DKH2(jorge-TZP-DKH) method (DKH2/DKH2), calculated by TD/PM6 method for the molecule optimized by DFT/B3LYP-DKH2(jorge-TZP-DKH) method (DKH2/TD/PM6), and calculated by TD/PM6 method for molecule optimized by HF method with LANL2DZ basis set for Ru and 6-31G for remaining atoms (HF/TD/PM6) compared to the experimental results. The molecular orbitals accessing the electron excitations corresponding to the MLCT and ILCT peaks calculated at HF/TD/PM6 level……………………………………………..181

Figure 7.21. Normalized UV–Vis absorption spectra calculated by semi-empirical method TD/PM6, CIS/PM6, and CIS/PM7 for the B_2 molecule stabilized by the $(PF_6^-)_2$ in vacuum (black) optimized by the DFT/B3LYP-DKH2(jorge-TZP-DKH) method (DKH2) (a) and optimized by HF method with LANL2DZ basis set for Ru and 6-31G for remaining atoms (HF) (b) compared with experimental data (red)..……………………………………………………………182

Figure 7.22. Schematic structures of the four new dyes, based on D102…….184

Figure 7.23. Schematic structures of the four new dyes, based on D149…….184

Figure 7.24. UV–vis absorption spectra calculated by TDDFT/B3LYP for D102-based molecules in vacuum (black) and in DMF (red)…………186

Figure 7.25. UV–vis absorption spectra calculated by TDDFT/B3LYP for D149-based molecules in vacuum (black) and in DMF (red)…………190

Figure 8.1. Structure of the $(TiO_2)_{28}H_{15}$ cluster with benzene attached to the semiconductor by -COOH anchoring groups in various configurations (in two different perspectives) a) single connection (Type 1) b) double connection with one privileged anchor of the -COOH (Type 2) and c) strong double connection (Type 3). (Ti—green, O—red, C—grey, and H—white color)...………………...202

Figure 8.2. The UV-vis absorption spectra calculated by TD/PM6 method for a) $(TiO_2)_{28}H_{15}$ cluster, b) for B_1 dye in a vacuum, and c) for $B_1/(TiO_2)_{28}H_{15}$ hybrid possessing Type 1 connection…..……….204

Figure 8.3. Molecular orbitals contributing to the ground and excited states of excitation at 455 nm and 451 nm calculated by using TD/PM6 method for the $B_1/(TiO_2)_{28}H_{15}$ structure possessing Type 1 bonds between dye and semiconducting nanostructure………………...206

Figure 8.4. The UV-vis absorption spectra calculated by TD/PM6 method for a) $(TiO_2)_{28}H_{15}$ cluster, b) for B_2 dye in a vacuum, c) for B_3 dye in a vacuum, d) for $B_2/(TiO_2)_{28}H_{15}$ hybrid, and e) for $B_3/(TiO_2)_{28}H_{15}$ hybrid possessing bond of Type 1……………………………….207

Figure 8.5. Molecular orbitals contributing to the ground and excited states of excitation at 454 nm for $B_2/(TiO_2)_{28}H_{15}$ (a) and at 462 nm for $B_3/(TiO_2)_{28}H_{15}$ (b) calculated by using the TD/PM6 method. Between the dye and TiO_2 cluster the Type 1 bond is created...208

Figure 8.6. Molecular orbitals contributing to the ground and excited states of excitation at 456 nm for $B_2/(TiO_2)_{28}H_{15}$ (a) and at 463 nm for $B_3/(TiO_2)_{28}H_{15}$ (b) calculated by using the TD/PM6 method. Between the dye and TiO_2 cluster the Type 2 bond is created………………………………………………………...210

Figure 8.7. Molecular orbitals contributing to the ground and excited states of excitation at 468 nm for $B_2/(TiO_2)_{28}H_{15}$ (a) and at 467 nm for $B_3/(TiO_2)_{28}H_{15}$ (b) calculated by using the TD/PM6 method.

Between the dye and TiO_2 cluster the Type 3 bond is created………………………………………………………...211

Figure 8.8. Collection of the UV-vis absorption spectra calculated for $B_2/(TiO_2)_{28}H_{15}$ and $B_3/(TiO_2)_{28}H_{15}$ possessing Type 1, Type 2, and Type 3 bonds. The main important excitations with MLCT nature and electron transfer occurring at mentioned photoexcitations are marked...213

Figure 8.9. Location of frontiers orbitals calculated by parametrized PM6 semiempirical method for $RuLp/(TiO_2)_{49}$, $RuLm/(TiO_2)_{49}$, and $RuLo/(TiO_2)_{49}$ hybrids……………………………………..............217

Figure 8.10. Charge generation in dye/TiO_2 interface in DSSC[20]…………….217

Figure 8.11. The UV-vis absorption spectra calculated by TD/PM6 method a) for the $(TiO_2)_{28}H_{15}$ cluster, b) for the $RuLp/(TiO_2)_{28}H_{15}$ hybrid, and c) for $RuLm/(TiO_2)_{28}H_{15}$ hybrid. The bond of Type 1 between dye and TiO_2 is created…………………………………………………...219

Figure 8.12. Molecular orbitals contributing to the ground and excited states of excitation at 451 nm for $RuLp/(TiO_2)_{28}H_{15}$ (a) and at 447 nm for $RuLm/(TiO_2)_{28}H_{15}$ (b) calculated by using the TD/PM6 method. Between the dye and TiO_2 cluster the Typ 1 bond is created………………………………………………………...220

List of tables

Table 2.1. Structural parameters of the TiO_2 crystal in anatase and rutile polymorph……………………………………………………...19

Table.2.2. Structural properties of pristine and Zr^{4+} doped nano TiO_2 calcined at 500 ◦C [22]……………………………………………………..24

Table 2.3. The J-V characterization of DSSC devices containing pristine and Zr-doped nanostructured TiO_2 [23]…………………………………….25

Table 2.4. Structural and electron properties of Ni^{2+} doped nanostructures of TiO_2 calcined at 450˚C from [29]……………………………………26

Table 2.5. The J-V characterization of the DSSC devices containing pristine and Ni-doped TiO_2 calcined at 450˚C from [29]…………………….27

Table 2.6. The J-V characterization of the DSSC devices containing pristine and Cu-doped TiO_2 calcined at 450˚C from[32]…………………….28

Table 2.7. Structural parameters of the pristine and Mn^{2+}-doped TiO_2 nanostructures calcined at 300˚C from [33]………………………….28

Table 2.8. The J-V characterization of the DSSC devices containing TiO_2 nanoparticles as a mixture of anatase and rutile (P25) and Mn-doped TiO_2 calcined at 500˚C from [35]……………………………………29

Table 2.9. Structural properties and the J-V characterization of the DSSC devices containing pristine TiO_2 nanostructures, mixed anatase and rutile TiO_2 structures (P25), and N-doped TiO_2 calcined at 450 ◦C for 4 h [39]………………………………………………………..30

Table 3.1. UV-vis absorption spectral data of Ru-based complexes (measured in ethanol)……………………………………………………...41

Table 3.2. The first UV-vis absorption peaks of the $[Ru(pby)_3](PF_6)_2$-based complexes presented in Fig. 3.4 [28]………………………………..44

Table 3.3. Spectroscopy data obtained for $Ru(bpy)_3^{+2}$–based complexes consisting of poly(lactic acid) (PLA) and poly(acrylic acid) (PAA)[29]……………………………………………………...46

Table 3.4. UV-vis obtained data and oxidation (E_{ox}) and reduction (E_{red}) potentials of the selected $[Ru(bpy)_3](PF_6)_2$ complexes presented in Fig. 3.6[30,31]……………………………………………………47

Table 6.1. Parameters of the unit cell of the stoichiometric a-TiO_2 relaxed structure by applying DFT/PBE and DFT/PBE+U methods with different Hubbard parameters, compared to experimental data…..90

Table 6.2. Structural parameters of the pristine a-TiO_2 2×2×1 supercell and its nonstoichiometric modification relaxed by applying DFT/PBE+U method (U_{Ti}= U_{Zr}=6 and J_{Ti}= J_{Zr}=1 eV)…………………………...92

Table 6.3. Bandgap energy calculated by DFT/PBE* and DFT/PBE+U method applying Hubbard correction for the unit cell of the a-TiO_2 and t-ZrO_2 and 2×2×1 supercell of the a-TiO_2. In all cases the J_{Ti}=J_{Zr}=1 eV………………………………………………………………93

Table 6.4. Total energy per atom for thin (2) and thick (4) films of TiO_2 obtained by geometry optimization procedure using DFT/PBE method…………………………………………………………..114

Table 6.5. Electron properties of the clusters $(TiO_2)_{28}H_{15}$, $(TiO_2)_{35}H_{13}$, and $(TiO_2)_{42}H_{12}$ calculated by TD/PM6 method (Ti - green atoms, O - red atoms, H - light grey atoms)…………………………………124

Table 7.1. Distances between Ru atoms and neighboring N atoms calculated for $[Ru(bpy)_3]^{2+}$ molecule stabilized by $(PF_6^-)_2$ ions predicted by different computational methods. Presented values are given in Å…………………………………………………………...145

Table 7.2. Distances between Ru and N atoms in the RuLm, RuLo, and RuLp molecules obtained via computer modeling using the DFT/B3LYP-LANL2DZ method…………………………………………...149

Table 7.3. Position of the first absorption peak λ_{max} (nm) calculated by the TDHF, DFT/B3LYP, and DFT/LC-BLYP methods for the RuLm, RuLo, and RuLp molecules and the experimental data [23]………150

Table 7.4. Electron properties of the $Ru(bpy)_3^{+2}$ as well as the RuLp, RuLm, and RuLp dyes with PF_6- stabilizers and location of their frontiers orbitals calculated by DFT/LC-BLYP, DFT/B3LYP, and *ab initio* (TDHF) method…………………………………………………153

Table 7.5. Position of the main absorption peak for MLCT and ILCT states calculated for RuLp by using different methodologies CIS/PM6, CIS/PM7, and TD/PM6 for the geometries optimized applying DFT/B3LYP-DKH2(jorge-TZP-DKH) (DKH2) and HF method with LANL2DZ basis set for Ru and 6-31G for remaining atoms (HF) compared with data obtained at DKH2/DKH2 level of calculations and experimental data…………………………...160

Table 7.6. Electric dipole moments, positions of the absorption peaks λ_{max} belonging to the MLCT transition, and contribution of the molecular orbitals to the selected excitations calculated by the DFT/B3LYP for the B_1, B_2, B_3, and B_4 molecules with $(PF_6^-)_4$ stabilizer, in a vacuum and DMF……………………………………………………...167

Table 7.7. Electric dipole moments, the HOMO, LUMO, and energy gap (E_g) values obtained from the calculations performed at DKH2/DKH2 level in a vacuum and ACN compared with experimental data obtained using cyclic voltammetry (in ACN) for B_1, B_2, and B_3 molecules……………………………………………………..173

Table 7.8. Positions of the absorption peaks λ_{max} belonging to the MLCT transfer, and contribution of the molecular orbitals to the selected excitations calculated by the DKH2/DKH2 method for the B_1, B_2, and B_3 molecules with $(PF_6^-)_4$ stabilizer, in a vacuum and ACN………………………………………………………..175

Table 7.9. Molecular orbitals giving a contribution to the MLCT transfer of electrons calculated by the DKH2/DKH2 method for B_1 molecule with stabilizers $(PF_6^-)_4$ in vacuum and ACN……………………..175

Table 7.10. Molecular orbitals giving a contribution to the MLCT transfer of electrons calculated by the DKH2/DKH2 method for B_2 molecule with stabilizers $(PF_6^-)_4$ in vacuum and ACN……………………..176

Table 7.11. Molecular orbitals giving a contribution to the MLCT transfer of electrons calculated by the DKH2/DKH2 method for B_3 molecule with stabilizers $(PF_6^-)_4$ in vacuum and ACN……………………..177

Table 7.12. Main absorption peaks of MLCT and ILCT transitions calculated for B_1 molecule using semiempirical CIS/PM6, CIS/PM7, and TD/PM6 methods for molecular geometries calculated at DFT/B3LYP-DKH2(jorge-TZP-DKH) (DKH2) and HF method with LANL2DZ basis set for Ru and 6-31G for remaining atoms (HF) compared with experimental data………………………………………………..178

Table 7.13. The molecular orbitals accessing the electron excitations corresponding to the MLCT peaks calculated by the TD/PM6, CIS/PM6, and CIS/PM7 for the B_1 molecule optimized by the DFT/B3LYP-DKH2(jorge-TZP-DKH) (DKH2) and HF method with LANL2DZ basis set for Ru and 6-31G for remaining atoms (HF)…………………………………………………………..180

Table 7.14. Electron properties of the B_2 and B_3 molecules calculated by the semiempirical method TD/PM6 for the structures stabilized by the $(PF_6\text{-})_2$ in a vacuum with geometry optimized by the HF method………………………………………………………..183

Table 7.15. Electron parameters calculated by DFT/B3LYP method for D102-based molecules with different anchoring groups………………186

Table 7.16. Frontiers orbitals calculated by DFT/B3LYP method for D102-based molecule with different anchoring groups………………..187

Table 7.17. Electron parameters calculated by DFT/B3LYP method for D149-based molecules with different anchoring groups………………188

Table 7.18. Frontier orbitals calculated by DFT/B3LYP method for D149-based molecules with different anchoring groups……………………...189

Table 8.1. Structural stability of the selected hybrid structures presented in Fig 8.1 possessing bonds mentioned as Type 1, Type 2, and Type 3.…………………………………………………………...203

Chapter 1

INTRODUCTION

1.1. Solar energy conversion

Civilizational development forces an increasing electricity demand. Resources of fossil energy sources, such as coal or natural gas, are becoming scarcer and less accessible. An alternative is solar radiation being a source of renewable energy. The photovoltaic (PV) effect, discovered in 1839 by French physicist Alexandre Edmond Becquerel, is a property of some materials that use solar light to produce electricity. The main idea of research and development in the field of photovoltaics is generally to ensure better efficiency of photovoltaic devices while reducing the costs of obtaining electricity and, most importantly, to enable their use on a large scale.

The use of solar energy requires the development of methods for its conversion into electricity and the production of appropriate materials for this purpose. Today, the most widespread technology that uses solar energy is silicon photovoltaics. The production of silicon-based photovoltaic cells is relatively expensive. Therefore, new, cheaper, and environmentally friendly materials are being sought that would enable the effective conversion of solar energy into electricity.

1.2. Three generations of solar cells

Currently, commonly used photovoltaic elements are based on a silicon material creating first-generation photovoltaic cells. However, the critical issue for this type of photovoltaic device is the high price of pure silicon, the non-flexibility of the material, and the high weight of the devices. Generally, silicon cell technology is based on a combination of n- and p-type doped silicon wafers, thus creating p-n junctions. Silicon solar cells can be divided into two groups: those using monocrystalline and polycrystalline silicon. The construction of monocrystalline silicon solar cells is based on silicon layers possessing a thickness of 0.1 - 0.3 nm and in consequence, they are called thick-film cells. Moreover, crystalline silicon has an indirect energy gap equal to 1.1 eV[1,2] and a very low absorption coefficient[3,4] which necessitates the construction of silicon cells in the form of thick plates. On the other hand, grain boundaries impede charge flow, making polysilicon cells show lower efficiencies than their monocrystalline counterparts. The advantages of silicon-based solar cells include high efficiency, which has exceeded the threshold of 26% in recent years[5]. Difficulties associated with the synthesis process and the costly production of monocrystalline silicon lead scientists to investigate thin-film cells.

The development of the chemical vapor deposition (CVD) technique initiated the production of thin-film solar cells, called second-generation photovoltaic cells. In this case, structures based on amorphous silicon are used. Compared to solar cells made of monocrystalline silicon, thin films of amorphous silicon provide many times more efficient absorption of solar radiation increasing the efficiency of solar cells. Second-generation thin-film solar cells are also built based on chalcogenides. One of the most successful photovoltaic technology is based on cadmium telluride (CdTe) solar cells developed by American manufacturer First Solar[6]. CdTe belongs to the II-IV semiconductor group with a direct band gap of 1.5 eV and high absorption coefficient[7]. For this moment it is one of the most effective structures taking into account the lifetime of the constructed devices[8]. However, CdTe-based cells contain highly toxic cadmium making difficult their production and causing risky and costly recycling and disposal[9]. After the solar generation boom in the last decades, the problem of recycling old cells became important. Environment-friendly materials became a new trend in photovoltaics.

For economic reasons, thin-film cells based on amorphous silicon or semiconducting materials such as CdTe, GaAs, InGaP, and other semiconductors belonging to the groups III-V of the periodic table are competitive with first-generation cells. Certainly, the consumption of fewer amount of materials for their production and the possibility of depositing layers of semiconductors on flexible substrates are their main advantages. Unfortunately, just like the previous generation, they have many limitations, which mainly include stability, low efficiency, and the use of rare (In, Te) and toxic (Cd, As) elements. However, it should be admitted that the second-generation multi-junction cells, due to their high durability and relatively good photoconversion efficiency, dominate over other PV cells. Unfortunately, this is associated with high production costs, for which, as in the case of thin-film cells, toxic elements are used. Third-generation PV devices use all the achievements of first and second-generation cells: promising technological solutions, flexibility, and non-toxicity. Third-generation cells can be divided into two groups. One of them is based on Concentrated Photovoltaics (CPV) approach focusing the sun's rays on the absorber. The technology uses lenses and mirrors to focus solar radiation on a small area. CPV has its roots in space technology and uses multi-junction cells, consisting of several semiconductor materials with different band gaps, stacked on top of each other. On the other side, the use of multiple layers during one photoactivation process makes it possible to overcome the Shockley-Quesser limit. Sharp Corporation pioneered this technology in 2009, combining three semiconductor layers with different band gaps, absorbing light across the entire solar spectrum (see Fig. 1.1)[10,11,12]. They built CVP solar cells with photoefficiency at the level of 44.4 %.

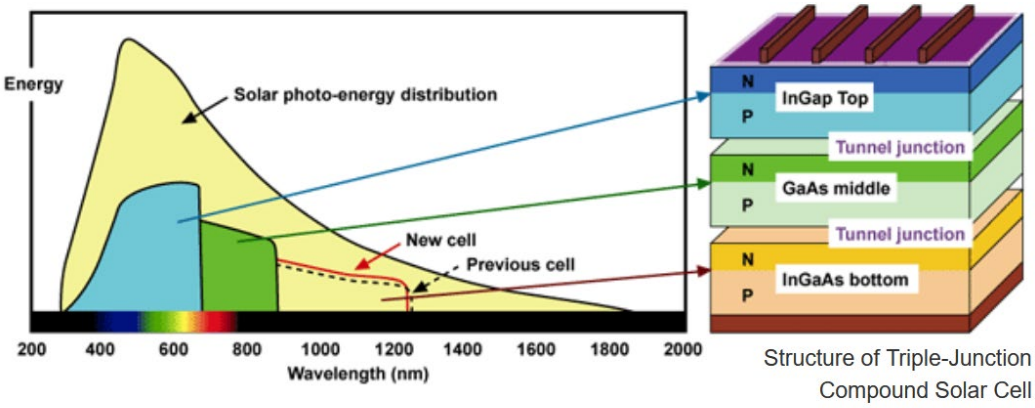
Energy
Solar photo-energy distribution
New cell
Previous cell
200
400
600
800
1000
1200
1400
1600
1800
2000
Wavelength (nm)
N
P
InGap Top
Tunnel junction
N
P
GaAs middle
Tunnel junction
N
P
InGaAs bottom
Structure of Triple-Junction
Compound Solar Cell

Figure 1.1 Spectral absorption distribution for three photo-absorption layer system (reprinted from[10]). The bottom layer is made from InGaAs (E_g = 0.97-0.99 eV), the middle layer – GaAs (E_g = 1.43 eV), and the top layer – InGaP (E_g = 1.88 eV)

Third-generation cells also include organic cells, where photoconversion occurs in organic semiconductors. The main working material in these cells is conjugated polymer, where the π orbitals support the conduction of charge carriers. Organic cells belong to the group of thin-film cells, produced at low temperatures using vacuum evaporation or solution printing techniques. The highest photoconversion efficiency in these cells so far, amounting to 18.07%, was recorded in 2021 by Ming Zhang and coworkers[13].

The other group of third-generation photovoltaic devices is dye solar cells. They are built based on a porous layer of semiconductor nanoparticles sensitized with organic dyes. The light stimulates the dyes in the cell, which are actively involved in the conversion of radiation into energy. One group of these solar cells creates dye-sensitized solar cells (DSSC), which will be described in more detail in the next chapter.

In addition to the above-described third-generation technologies, there are many new concepts for building solar cells. They assume, for example, the use of quantum dots - semiconductor nanocrystals with a size of 1-20 nm[14,15]. By changing the shape and size of quantum dots, it is possible to control the width of their energy gap, which significantly affects the range of absorption of sunlight. In this case, the quantum dots can be used as light-absorbing elements in high-efficiency solar cells. The photoconversion efficiency of Cu–In–Ga–Se quantum dots in the solar cells reached the level of 11.5% [16,17].

Perovskite cells are also representative of the third-generation of solar cells. It is a type of solar cell containing a perovskite structural compound, most commonly hybrid organic-inorganic lead or tin halide-based material, as the active light-collecting layer. The easiest way to characterize perovskite structure is presented in Fig. 1.2. The A-type cation located in the center of the cube is surrounded by B atoms (also positively charged cations) present in the corners of the cube. The faces of the cube are occupied by smaller negatively charged X atoms (anions). Perovskites possess properties such as a wide absorption spectrum, fast and long lifetime of carrier separation, long electron and hole transport distances, and many others that make them very promising materials for semiconductor solar cells. The typical band gap of perovskite material is around 1.5 eV[18]. In South Korea’s Ulsan National Institute of Science and Technology (UNIST) perovskite solar cells were built possessing photoconversion efficiency equal to 25.8% [19]. The principles of perovskite cells were first created by Miyasaka and coworkers[20]. The schematic illustration of the idea of a perovskite solar cell is presented in Fig. 1.2. Also there the incident-photon-to-current efficiency (IPCE) of the $CN_3NH_3PbBr_3$ and $CN_3NH_3PbI_3$ based perovskite solar cells are presented.

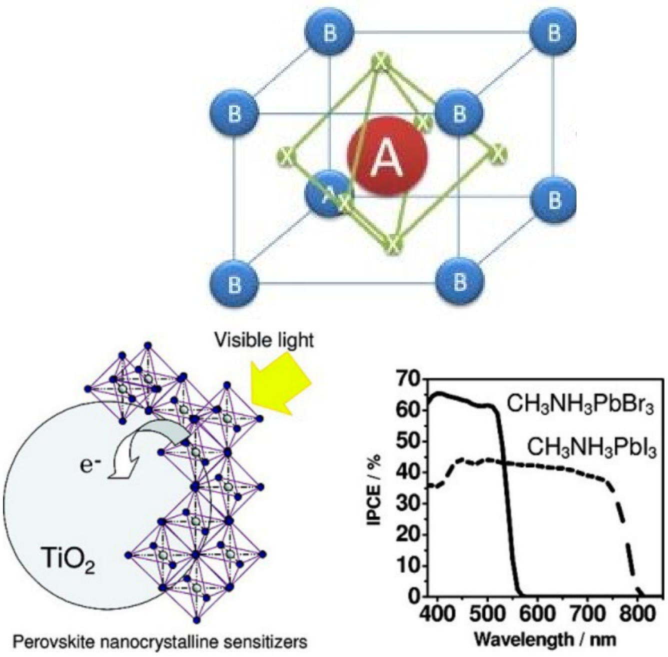

Figure 1.2 Schematic structure of perovskite crystal, perovskites acting as sensitizers on TiO_2 and incident-photon-to-current efficiency measures for example of perovskite solar materials[20]

Comparing the data from market analyses, it can be concluded that traditional photovoltaic technologies based on crystalline silicon maintain their leading position, but in the future, an increasing expansion of 2nd and 3rd generation technologies can be expected. Also, we should not underestimate new concepts in solar cell technologies that are currently in the development stage but may become leading in the future.

1.3. Dye-sensitized solar cells (DSSC)

Grätzel who conducted pioneering research in this field first developed dye-sensitized solar cells (DSSC)[21]. They are becoming more and more popular due to their low-cost conversion of solar radiation into electricity[22]. Compared to silicon cells, dye PV cells are made of cheaper materials safe for the environment. Currently, the maximum efficiency of this type of cell reaches 13%, and the lifetime estimated based on stability tests in operating conditions is up to 10 years[23]. Taking into account the efficiency, the dye cell, unfortunately, cannot be compared to the traditional silicon cell, but its advantages support the spread of this type of device on the market.

The DSSC cell has a layered structure and is a photoelectrochemical system with an electrolyte containing a redox mediator. The diagram of the construction and operation of a DSSC is shown in Fig. 1.3. A particularly important element of the entire system is a porous oxide layer with a thickness of several micrometers, which is deposited on a transparent substrate. Most often it is glass coated with a thin layer of fluorine-doped tin oxide (FTO). The mentioned oxide built a photoanode, a fundamental element of DSSC that can improve the general efficiency of solar cells. Photoanode must be constructed with transparent material allowing the sunlight to reach photoactive elements – dyes deposited on the surface of the oxide. The material creating the photoanode must be highly conductive to transport photoactivated electrons. One of the most selected materials for photo-anode is TiO_2 in anatase form. Much more information concerning the properties of TiO_2 will be presented in Chapter 2. In an effective dye/semiconductor system, the dye absorption on the semiconductor surface must be maximized. This requires a high mesoporosity of the semiconductor structure[24].

The organic dye molecules work as photosensitizers in DSSC. They are the main light harvester making light absorption (1) (see Fig. 1.3), electron injection into photoanode (2), and hole injection into the electrolyte for their recharging. Dyes must follow the selected criteria:

1) Processes (2) and (4) (see Fig. 1.3) require specific distribution of higher occupied molecular orbital (HOMO) and lower unoccupied molecular orbital (LUMO) of dye, comparing the conductional band of the semiconductor. The LUMO (D*) level must have more negative potential than the bottom of the conductional band of the semiconductor (V vs NHE). The HOMO (D/D+) level of dye must be more positive than the potential of electrolyte (V vs NHE) for effective dye recharging process (4), and hole distribution to the counter electrode (5) and electrolyte regeneration (6). The difference between the LUMO (D*) level of dye and the bottom of the conductional band is named electron injection overpotential. The difference between the HOMO (D/D+) level of dye and electrolyte level is named dye regeneration overpotential. All elements of DSCC must be selected in such a way that named overpotential is left on a low level, only slightly higher than zero.

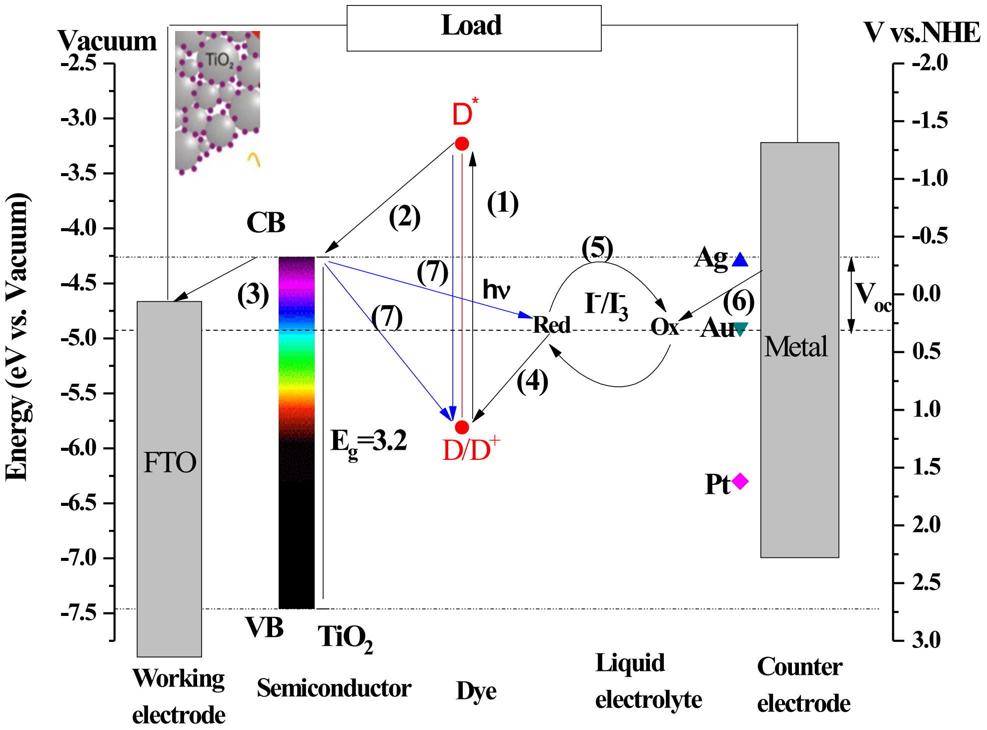
Load
Vacuum
-2.5
-3.0
-3.5
-4.0
-4.5
-5.0
-5.5
-6.0
-6.5
-7.0
-7.5
Energy (eV vs. Vacuum)
TiO$_2$
V vs.NHE
-2.0
-1.5
-1.0
-0.5
0.0
0.5
1.0
1.5
2.0
2.5
3.0
D*
(1)
(2)
CB
(3)
(7)
(7)
hν
(5)
I^-/I_3^-
Ag
(6)
V_{oc}
Red
Ox
Au
Metal
(4)
E_g=3.2
D/D+
FTO
Pt
VB
TiO$_2$
Working electrode
Semiconductor
Dye
Liquid electrolyte
Counter electrode

Figure 1.3. Schematic energy diagram and basic principles for DSSC with liquid electrolyte part: band position of TiO_2 and schematic energy level for $Ru(pby)_3^{+2}$ I^-/I^-_3 electrolyte, counter electrode(Ag -4.3eV or Au-4.9eV or Pt -6.35eV E vs. vacuum): 1) light absorption on dye, 2)electron injection from dye to semiconductor, 3)electron transfer in semiconductor to the working electrode, 4) interception of the oxidized dye by a redox mediator, 5) oxidized defuse toward the counter electrode, 6)redox mediator regeneration and 7)parasitic recombination, blue line(must be avoided)

2) For effective charge injection (2) in a dye/semiconductor system anchoring groups of the dyes take a role. They make the stable connection and charge transfer, moreover, localization of HOMO and LUMO on dyes is critical. The LUMO orbital should be as close to the surface as possible and the HOMO should be as far from the surface as possible. In other cases, the possibility of parasitic recombination (Fig.1.3 blue arrow) will increase but it must be avoided.

Many possible organic structures can be used in DSSC as dye molecules. In the presented work dyes based on ruthenium (II) complexes[25] and modified D102 and D149 were selected. The physicochemical properties of these molecules will be discussed in Chapter 6.

Many different electrolyte structures were developed for DSSCs applications[26]. Here only the most popular, classical redox-mediator will be described. The triiodide/iodide (I_3^-/I^-) is a standard liquid electrolyte for DSSC since it was first time used by M. Grätzel and B. O’Regan[21]. Its oxidation potential

(E^{O}_{Ox}=0.35V vs NHE) is suitable for the HOMO level of the major part of dyes. It has good solubility, and the recombination kinetic between redox couple and TiO_2 is slow[22]. It has been shown that I^- ions are efficiently adsorbed onto the surface of the mesopore TiO_2 making efficient dyes regeneration[27]. The I_3^-/I^- absorbs part of light at 500 nm, and its low redox potential limits the available open-circuit voltage V_{oc} of DSSC systems[28]. Electrolyte I_3^-/I^- as well as Br_3^-/Br^- [29] (up to E^{O}_{Ox}= 1.1 V vs. NHE)/ [30] need two electrons to be reduced at the cathode what's high overpotential corrodes metals. Many electrolytes were presented as the substitution I_3^-/I: Fc/Fc^+ [31] (0.62 V vs NHE), $(SCN)_2/SCN^-$ [32](0.53 V vs SCE)), Ni(III/IV)[33], vanadium V(IV/V)[34] (−0.07 V vs NHE), copper Cu(I/II)[35] (0.65 V vs. NHE) and cobalt Co(II/III) coordination complex (0.51 V vs NHE)[36] .

The cobalt Co(II/III) coordination complex is considered to be a perspective candidate to replace I_3^-/I^- in DSSC. Gribabu and coworkers[37] analyzed the oxidation potential of electrolytes which is presented in Fig. 1.4. The main advantage of Co(II/III) coordination complexes is their weak absorption in visible light. The redox potential is higher than the one of I_3^-/I^- (Fig 1.4). It increases the photovoltage of DSSC from 0.67 V[38] in 2001 to 1 V[39] in 2012. One of the top results for this moment for DSSC based on organic dyes with Co(II/III) redox mediator is 14.3% efficiency[40].

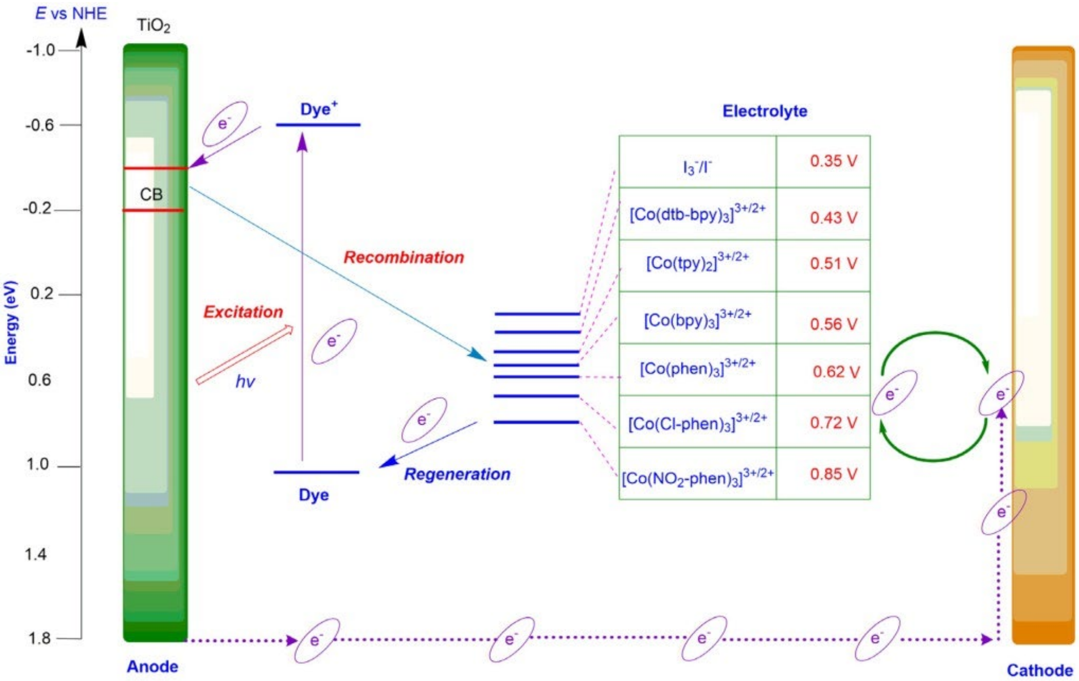
E vs NHE
TiO2
-1.0
-0.6
-0.2
0.2
0.6
1.0
1.4
1.8
Energy (eV)
CB
e⁻
Dye⁺
Dye
Excitation
hv
Recombination
Regeneration
Electrolyte
I3⁻/I⁻ 0.35 V
[Co(dtb-bpy)3]3+/2+ 0.43 V
[Co(tpy)2]3+/2+ 0.51 V
[Co(bpy)3]3+/2+ 0.56 V
[Co(phen)3]3+/2+ 0.62 V
[Co(Cl-phen)3]3+/2+ 0.72 V
[Co(NO2-phen)3]3+/2+ 0.85 V
Anode
Cathode

Figure 1.4. Schematic energy diagram for a dye-sensitized solar cell. Ref . [37]

The counter electrode is the last part that completes the electrical circuit of a DSSC. It must inject electrons into the electrolyte to reduce the redox mediator (6). The long-term stability of the cathode structure is required. Charge transfer resistance for electrodes must be low, with a maximum value near 1 Ω / cm^2 depending on thickness and deposition technique[41]. For this reason, the typical answer for cathode material is platinum (Pt), which was the first used in conventional DSSC. Unfortunately, the price of Pt is a major disadvantage, which shows a critical impact on large-scale applications. Many materials were investigated as cathodes including noble metals such as Au and Ag. Moreover, they do not show work stability. In consequence, different kinds of materials were investigated as cathode: conducting polymers[42], carbon[43, 44], metal sulfide[45], metal oxide,[46] and natural material[47].

Under the above-mentioned conditions, the operation of solar cells can be described in six stages (see Fig. 1.3)[24]:

(1) The incident photon is absorbed from sunlight by a photo-sensitizer, which excites an electron from the higher occupied molecular orbital (HOMO) to the lower unoccupied molecular orbital (LUMO) level of the dye. The ground state is denoted D and the excited state of the dye - D* (see Fig. 1.3). Lifetime of the excited state must be appropriately long for effective charge transfer from the dye to the semiconductor. Typically it is equal to 10^{-9}-10^{-8} s for metal complexes[48] and is shorter for organic dyes <10^{-9} s [49].

(2) Electron injection from the LUMO level of the dye (D^*) to the conduction band of the semiconductor. This process is ultrafast taking pico- or femtosecond time[50]. After injection, a hole is left in the sensitizer (D^+).

(3) Transport of electrons across the photo-anode. The electrons present in the conduction band of the semiconductor flow to The FTO working electrode, and then they are transferred to the external circuit, flowing to the cathode.

(4) Regeneration of the oxidated dye (D^+) by electron injection from redox mediator of liquid electrolyte. This process will recharge the dye and return it to the ground state (D). At the same time, species of electrolyte will oxidate. The time of this process is in the microsecond scale[51].

(5) The oxidized species of liquid electrolyte defuse toward the counter electrode.

(6) Holes reduction on a counter electrode: the oxidated species of liquid electrolyte reduce back.

The cycle is completed.

(7) Parasitic recombination which must be avoided in DSSC:

a. first of the possible scenario: dye does not inject electron to the conductional band of the semiconductor after the light absorption, and after photoexcited lifetime—dye emitted photon, end electron lift from the excited state to ground state.

b. the second scenario is electron back recombination from the conductional band to the oxidated dye (D^+).

c. the third is the electron recombination from the conductional band to the oxide electrolyte, with the electrolyte reducing back.

The above information on dye cells shows new possibilities for their use in photovoltaics. Although DSSC cells still show lower efficiency than competing silicon cells, the huge amount of work carried out in the field of third-generation photovoltaics causes its dynamic development, which translates into a significant increase in cell efficiency observed in recent years. Undisputed the advantage of dye cells is the very process of their production, which, due to the lack of the need to have specialized rooms with high purity, is much cheaper than in the case of cells of the first and second generation.

1.4. Literature

[1] Streetman, B. G. & Sanjay Banerjee., "Solid State electronic Devices (5th ed.)." New Jersey: Prentice Hall. pp. 524, **(2000)**.

[2] Xiang, H., Huang, B., Kan, E., Wei, S.-H. & Gong, X., "Towards Direct-Gap Silicon Phases by the Inverse Band Structure Design Approach." *Physical Review Letters*, vol.110, pp.118702, **(2013)**.

[3] D. K. Schroder, R. N. Thomas & J. C. Swartz., "Free carrier absorption in silicon." *IEEE Transactions on Electron Devices,* vol. 25, no. 2, pp. 254-261, **(1978)**. doi: 10.1109/T-ED.1978.19066.

[4] Guo, Y., Wang, Q., Kawazoe, Y., & Jena, P., "A new silicon phase with direct band gap and novel optoelectronic properties." *Scientific reports*, vol.5 no.1, pp.1-7, **(2015)**.

[5] Yoshikawa, K., Kawasaki, H., Yoshida, W., Irie, & Yamamoto, K., "Silicon heterojunction solar cell with interdigitated back contacts for a

photoconversion efficiency over 26%." *Nature Energy* vol.2, pp.17032 **(2017)**. doi:10.1038/nenergy.2017.32

[6] "First Solar Hits Record 22.1% Conversion Efficiency for CdTe Solar Cell" https://www.greentechmedia.com/articles/read/first-solar-hits-record-22-1-conversion-efficiency-for-cdte-solar-cell

[7] Zheng, X., Kuciauskas, D., Moseley, J., Colegrove, E., Albin, D. S., Moutinho, H., & Metzger, W. K., "Recombination and bandgap engineering in CdSeTe/CdTe solar cells." *APL Materials*, vol.7 no.7, pp.071112, **(2019)**. doi:10.1063/1.5098459

[8] Bhandari, K. P., Collier, J. M., Ellingson, R. J., & Apul, D. S., "Energy payback time (EPBT) and energy return on energy invested (EROI) of solar photovoltaic systems: A systematic review and meta-analysis." *Renewable and Sustainable Energy Reviews*, Elsevier, vol. 47(C), pp. 133-141, **(2015)**.

[9] "Solar Frontier hits 23.35% efficiency with thin-film cell" https://renewablesnow.com/news/solar-frontier-hits-2335-efficiency-with-thin-film-cell-639947/

[10] You, J., Dou, L., Yoshimura, K., Kato, T., Ohya, K., Moriarty, T.,& Yang, Y., "A polymer tandem solar cell with 10.6% power conversion efficiency." *Nature communications*, vol.4, no.1, pp. 1-10, **(2013)**.

[11] Albrecht, S., Saliba, M., Baena, J. P. C., Lang, F., Kegelmann, L., Mews, M., .& Rech, B., "Monolithic perovskite/silicon-heterojunction tandem solar cells processed at low temperature." *Energy & Environmental Science*, vol.9, no.1, pp.81-88, **(2016)**.

[12] Sharp Develops Solar Cell with World's HighestConversion Efficiency of 37.9% Sets New Record with Triple-Junction Compound Solar Cell https://global.sharp/corporate/news/130424.html

[13] Zhu, L., Zhang, M., Zhong, W., Leng, S., Zhou, G., Zou, Y.,& Zhang, Y., "Progress and prospects of the morphology of non-fullerene acceptor based high-efficiency organic solar cells." *Energy & Environmental Science*, vol.14 no.8, pp.4341-4357, **(2021)**.

[14] Santra, P. K., & Kamat, P. V., "Mn-doped quantum dot sensitized solar cells: a strategy to boost efficiency over 5%." *Journal of the American Chemical Society*, vol.134, no.5, pp.2508-2511, **(2012)**.

[15] Yun, H. J., Paik, T., Diroll, B., Edley, M. E., Baxter, J. B., & Murray, C. B., "Nanocrystal size-dependent efficiency of quantum dot sensitized solar cells in the strongly coupled CdSe nanocrystals/TiO_2 system." *ACS Applied Materials & Interfaces*, vol.8, no.23, pp.14692-14700, **(2016)**.

[16] Peng, W., Du, J., Pan, Z., Nakazawa, N., Sun, J., Du, Z., & Zhong, X., "Alloying strategy in Cu–In–Ga–Se quantum dots for high efficiency quantum dot sensitized solar cells." *ACS Applied Materials & Interfaces*, vol.9, no.6, pp.5328-5336, **(2017)**.

[17] Mandal, P., "Application of plasmonics in solar cell efficiency improvement: a brief review on recent progress." *Plasmonics*, pp.1-21, **(2022)**.

[18] Organic-Inorganic Halide Perovskite Photovoltaics - From | Nam-Gyu Park | Springer **(2016).**

[19] Min, H., Lee, D. Y., Kim, J., Kim, G., Lee, K. S., Kim, J., & Il Seok, S., "Perovskite solar cells with atomically coherent interlayers on SnO_2 electrodes." *Nature*, vol.598, no.7881, pp.444-450, **(2021)**.
doi: 10.1038/s41586-021-03964-8

[20] Kojima, A., Teshima, K., Shirai, Y., & Miyasaka, T., "Organometal halide perovskites as visible-light sensitizers for photovoltaic cells." *Journal of the american chemical society*, vol.131, no.17, pp.6050-6051, **(2009)**.

[21] O'regan, B., & Grätzel, M., "A low-cost, high-efficiency solar cell based on dye-sensitized colloidal TiO_2 films." *Nature*, vol.353 no.6346, pp.737-740, **(1991)**.

[22] Boschloo G., & Hagfeldt, A., "Characteristics of the iodide/triiodide redox mediator in dyesensitized solar cells." *Accounts of Chemical Research*, vol. 42, pp.1819-18726, **(2009)**.

[23] Mathew S., Yella A., Gao P., Humphry-Baker R., & Grätzel M., "Dye-sensitized solar cells with 13% efficiency achieved through the molecular engineering of porphyrin sensitizers." *Nature Chemistry*, vol.6, pp.242-247, **(2014)**.

[24] Delices, A., "Organized Organic Dye/Hole Transporting Materials for TiO_2- and ZnO-based Solid-State Dye-Sensitized Solar Cells (s-DSSCs)." Diss. Université Sorbonne Paris Cité, **(2017)**.

[25] Rillema, D. P., Jones, D. S., Woods, C., & Levy, H. A., "Comparison of the crystal structures of tris heterocyclic ligand complexes of ruthenium (II)." *Inorganic Chemistry*, vol.31, no.13, pp.2935-2938, **(1992)**.

[26] Iftikhar, H., Sonai, G. G., Hashmi, S. G., Nogueira, A. F., & Lund, P. D., "Progress on Electrolytes Development in Dye-Sensitized Solar Cells." *Materials*, vol.12, no.12, pp.1998, **(2019)**. doi:10.3390/ma12121998

[27] Pelet, S., Moser, J. E., & Grätzel, M., "Cooperative effect of adsorbed cations and iodide on the interception of back electron transfer in the dye sensitization of nanocrystalline TiO_2." *The Journal of Physical Chemistry B*, vol.104, no.8, pp.1791-1795, **(2000)**.

[28] Nusbaumer, H., Zakeeruddin, S. M., Moser, J. E., & Grätzel, M., "An Alternative Efficient Redox Couple for the Dye-Sensitized Solar Cell System." *Chemistry–A European Journal*, vol.9, no.16, pp.3756-3763, **(2003)**.

[29] Kakiage, K., Osada, H., Aoyama, Y., Yano, T., & Hanaya, M., "Achievement of over 1.4 V photovoltage in a dye-sensitized solar cell by the application of a silyl-anchor coumarin dye." *Scientific reports*, vol.6, no.1, pp.1-6, **(2016)**.

[30] Teng, C., Yang, X., Li, S., Cheng, M., & Sun, L., "Tuning the HOMO Energy Levels of Organic Dyes for Dye-Sensitized Solar Cells Based on Br^-/Br^{3-}Electrolytes." *Chemistry - A European Journal*, vol.16, no.44, pp.13127–13138, **(2010)**. doi:10.1002/chem.201000460

[31] Daeneke, T., Kwon, T.-H., Holmes, A. B., Duffy, N. W., Bach, U., & Spiccia, L., "High-efficiency dye-sensitized solar cells with ferrocene-based electrolytes." *Nature Chemistry*, vol.3, no.3, pp.211–215, **(2011)**. doi:10.1038/nchem.966

[32] Bergeron, B. V., Marton, A., Oskam, G., & Meyer, G. J., "Dye-Sensitized SnO_2 Electrodes with Iodide and Pseudohalide Redox Mediators." *The Journal of Physical Chemistry B*, vol.109, no.2, pp.937–943, **(2005)**. doi:10.1021/jp0461347

[33] Li, T. C., Spokoyny, A. M., She, C., Farha, O. K., & Hupp, J. T., "Ni(III)/(IV) Bis(dicarbollide) as a Fast, Noncorrosive Redox Shuttle for Dye-Sensitized Solar Cells. " *Journal of the American Chemical Society*, vol.132, no.13, pp.4580–4582, **(2010)**. doi:10.1021/ja100396n

[34] Apostolopoulou, A., Vlasiou, M., Tziouris, P. A., Tsiafoulis, C., & Stathatos, E., "Oxidovanadium(IV/V) Complexes as New Redox Mediators in Dye-Sensitized Solar Cells: A Combined Experimental and Theoretical Study." *Inorganic Chemistry*, vol.54, no.8, pp.3979–3988, **(2015)**. doi:10.1021/acs.inorgchem.5b001

[35] Jilakian, M., & Ghaddar, T. H., "Eco-Friendly Aqueous Dye-Sensitized Solar Cell with a Copper (I/II) Electrolyte System: Efficient Performance under Ambient Light Conditions." *ACS Applied Energy Materials*, vol.5, no.1, pp.257-265, **(2022)**.

[36] Hart, K. F., Joe, N. S., Miller, R. M., Nash, H. P., & Morris, A. M., "Synthesis and Characterization of trans-Dichlorotetrakis(imidazole)cobalt(III) Chloride: A New Cobalt(III) Coordination Complex with Potential Prodrug Properties." *Bioinorganic Chemistry and Applications*, pp.1–7, **(2018)**. doi:10.1155/2018/4560757

[37] Giribabu, L., Bolligarla, R., & Panigrahi, M., "Recent Advances of Cobalt (II/III) Redox Couples for Dye-Sensitized Solar Cell Applications." *The Chemical Record*, vol.15, no.4, pp.760-788, **(2015)**.

[38] Nusbaumer, H., Moser, J.-E., Zakeeruddin, S. M., Nazeeruddin, M. K., & Grätzel, M., "CoII(dbbip)$_2^{2+}$Complex Rivals Tri-iodide/Iodide Redox Mediator in Dye-Sensitized Photovoltaic Cells." *The Journal of Physical Chemistry B*, vol.105, no.43, pp.10461–10464, **(2001)**. doi:10.1021/jp012075a

[39] Kashif, M. K., Axelson, J. C., Duffy, N. W., Forsyth, C. M., & Bach, U. A., "New Direction in Dye-Sensitized Solar Cells Redox Mediator Development: In Situ Fine-Tuning of the Cobalt(II)/(III) Redox Potential through Lewis Base Interactions." *Journal of the American Chemical Society*, vol.134, no.40, pp.16646–16653, **(2012)**. doi:10.1021/ja305897k

[40] Kakiage, K., Aoyama, Y., Yano, T., Oya, K., & Hanaya, M., "Highly-efficient dye-sensitized solar cells with collaborative sensitization by silyl-anchor and carboxy-anchor dyes. " *Chemical Communications*, vol.51, no.88, pp.15894–15897, **(2015)**. doi:10.1039/c5cc06759f

[41] Murakami, T.N. & Grätzel, M., "Counter Electrodes for DSC: Application of Functional Materials as Catalysts. " *Inorganica Chimica Acta*, vol.361, pp.572-580, **(2008)**. doi:10.1016/j.ica.2007.09.025

[42] Gunasekera, S. S. B., Perera, I. R., & Gunathilaka, S. S., "Conducting polymers as cost effective counter electrode material in dye-sensitized solar cells." *Solar energy. Springer, Singapore*, pp.345-371, **(2020)**.

[43] Gao, C., Wang, H., Hu, Z., & Wu, M., "A novel carbon bead string cathode for dye-sensitized solar cells." *Electrochimica Acta*, vol.255, pp.9–14, **(2017)**. doi:10.1016/j.electacta.2017.09

[44] Hao, F., Dong, P., Luo, Q., Li, J., & Lin, H., "Recent advances in alternative cathode materials for iodine-free dye-sensitized solar cells." *Energy & Environmental Science*, vol.6, no.7, pp.2003, **(2013)**. doi:10.1039/c3ee40296g

[45] Salleh, S.A., Rahman, M.Y.A. & Aziz, T.H.T., "Effect of annealing temperature on the performance of dye-sensitized solar cell using nickel sulphide–reduced graphene oxide cathode." *Bulletin of Materials Science*, vol.44, pp.224, **(2021)**. doi:10.1007/s12034-021-02514-2

[46] Wang, W., Xu, X., Liu, Y., Zhong, Y., & Shao, Z., "Rational Design of Metal Oxide-Based Cathodes for Efficient Dye-Sensitized Solar Cells." *Advanced Energy Materials*, pp.1800172, **(2018)**. doi:10.1002/aenm.201800172

[47] Maiaugree, W., Lowpa, S., Towannang, M., Rutphonsan, P., & Amornkitbamrung, V., "A dye sensitized solar cell using natural counter electrode and natural dye derived from mangosteen peel waste." *Scientific reports*, vol.5, no.1, pp.1-12, **(2015)**.

[48] Vamvounis, G., Glasson, C. R., Bieske, E. J., & Dryza, V., "Modulating electron injection from an organic dye to a titania nanoparticle with a photochromic energy transfer acceptor." *Journal of Materials Chemistry C*, vol.4, no.26, pp.6215–6219, **(2016)**. doi:10.1039/c6tc01584k

[49] Hara, K., Sato, T., Katoh, R., Furube, A., & Arakawa, H., "Molecular Design of Coumarin Dyes for Efficient Dye-Sensitized Solar Cells." *The Journal of Physical Chemistry B*, vol.107, no.2, pp.597–606, **(2003)**. doi:10.1021/jp026963x

[50] Ghadiri, E., Zakeeruddin, S. M., Hagfeldt, A., Grätzel, M., & Moser, J. E., "Ultrafast charge separation dynamics in opaque, operational dye-sensitized solar cells revealed by femtosecond diffuse reflectance spectroscopy." *Scientific reports*, vol.6, no.1, pp.1-13, **(2016)**.

[51] Ardo, S., & Meyer, G. J., "Photodriven heterogeneous charge transfer with transition-metal compounds anchored to TiO_2 semiconductor surfaces." *Chemical Society Reviews*, vol.38 no.1, pp.115–164, **(2009)**. doi:10.1039/b804321n

Chapter 2

TITANIUM DIOXIDE AS A STRUCTURE FOR PHOTOVOLTAIC APPLICATIONS

Owing to the photoinduced activity and semiconductor properties of oxides they are widely investigated concerning their photovoltaic properties. Especially transition metal oxides are a relevant class of materials for energy-related applications. They are compounds composed of oxygen atoms bound to a metal with partially filled *d* electron orbitals. These materials are generally insulators at room temperature when they are stoichiometric and not doped. Various types of imperfections and impurities occurring in the discussed crystals change their physico-chemical properties.

The metal oxide semiconductors used as effective photo-anodes in DSSCs should fulfill specific criteria[1]. They should be n-type semiconductors characterized by effective charge transfer and possess high efficiency of charge collection. In DSSCs, the TiO_2, ZnO, Nb_2O_5, $SrTiO_3$, and SnO_2 metal oxide as wide-bandgap semiconductors are generally used. The energy positions of the bandgap (E_g) of mentioned materials are presented in Fig. 2.1 [1-3].

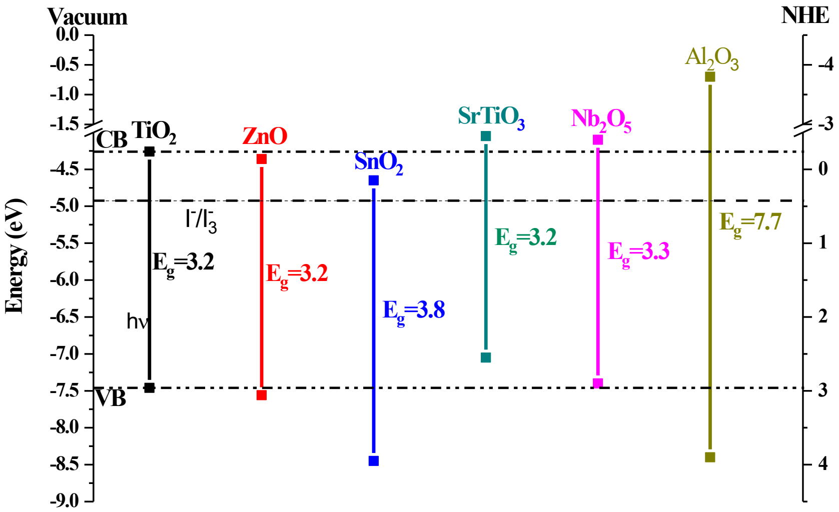

Figure 2.1. Energy position of the bandgap of the several metal oxides used in DSSC applications possessing $E_g > 3$ eV

Unfortunately, all materials presented in Fig. 2.1 have an energy gap $E_g >$ 3.0 eV and they require ultraviolet irradiation for photoactivation. This feature ensures that the mentioned materials are almost completely transparent to visible light. Because UV light accounts for only a small fraction (8%) of the sun's energy compared to visible light (45%), each shift in the optical response of metal oxide wide-bandgap semiconductors from the UV to the visible spectral range will have a positive effect on the photovoltaic efficiency of these materials. An initial approach to shift the optical response of semiconductors from the UV to the visible spectral range has been their doping with transition-metal elements. To increase the effectiveness of the absorption of visible light by the photo-anode, organic molecules (sensitizers) can be also attached to its surface. Sensitizers are an important element of the DSSC structures. In this case, the redox potential of sensitizers must be higher than the bottom of the conductional band of the semiconductor. It is necessary for effective charge transfer from dye molecules to photo-anode ensuring the high electric conductivity of both components. To increase the absorption surface of the semiconductors anchoring a large number of sensitizers the anodic materials usually are performed in nanostructured or mesoporous form.

Among different metal oxides, TiO_2 has been extensively studied for photo-anode applications. Among all the above-mentioned oxides, TiO_2 is cheap in production, non-toxic, and has a good time response and thermal stability[4]. The DSSCs based on TiO_2 nanostructures with an adsorbed large amount of dyes have attracted great interest in the past few decades[5]. Especially interesting are nonstoichiometric TiO_2 anatase crystals possessing structural vacancies and interstitial or substitutional dopants.

2.1. Physico-chemical properties of titanium dioxide structures

Titanium dioxide (TiO_2) has a large number of polymorphs depending on pressure and temperature. Three of them: anatase, rutile, and brookite[6,7] exist at atmospheric pressure. Unfortunately, only the metastable anatase and stable rutile can be used as photovoltaic materials but the best-photoactivated results are obtained for TiO_2 in anatase form. One of the main problems is the metastability of anatase and its irreversible transformation to rutile with critical changing in its electronic properties and photovoltaic performance. The mentioned polymorph transformation can occur at different temperatures and sometimes is unexpected. The methods to prevent or inhibit this transformation will be described in Chapter 2.2.

Pure TiO_2 is a non-toxic colorless oxide with a high reflective index and brightness. Brookite belongs to the orthorhombic crystal structures, and booth anatase and rutile belong to the tetragonal crystal structures. The structural parameters of the TiO_2 in anatase and rutile polymorph are collected in Table 2.1. Rutile is a thermodynamically stable polymorph with a direct band gap equal to 3.0 eV[6]. The anatase polymorph possesses an indirect band gap equal to 3.2 eV[6] and the thermodynamically most stable plane (101). The bottom of conducting band of anatase is localized at a higher potential (~ -4.2 eV)[8] than it is observed for rutile.

Table 2.1. Structural parameters of the TiO_2 crystal in anatase and rutile polymorph.

TiO_2 polymorph	Anatase	Rutile
Crystal structure	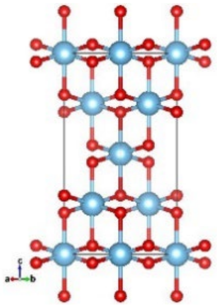	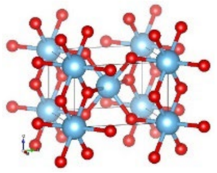
Space group	$I4_1/amd$	$P4_2/mnm$
Structure elements per unit cell	4	2
Lattice parameters (Å)	a=b=3.785 c=9.514[9]	a=b=4.594 c=2.959[9]
Band gap	~3.2[6]	~3.0[6]
Reflective index[10,11]	2.52[10] 2.54[11]	2.70[10] 2.79[11]

The phase mixture of anatase and rutile presents synergistic effects and increases the photovoltaic properties of a material in comparison with separated components[12]. However, the pristine anatase possesses better photovoltaic properties than pure rutile. It is worth noticing that different crystallographic directions in the same material also can change its photovoltaic parameters[13]. In summarising one can conclude that the anatase form of the TiO_2 is better than its rutile form in photovoltaic applications because:

1) The high band gap energy of anatase polymorphs requires to use of dyes. In consequence, molecules with a higher redox potential can be used as sensitizers. This idea is explained in Chapter 3. On the other side, the bottom of the anatase conduction band is located lower than the one of the rutile, which makes some well know sensitizers useful for working correctly with anatase systems.
2) The indirect band gap of the TiO_2 in anatase form is lower than the indirect band gap in rutile. There is a rule saying that the lifetime of electron-hole pairs is longer in indirect materials than in direct ones. It means that the possibility of charge transfer at the surface of anatase is higher than in rutile, where the higher possibility of exciton recombination occurs[14].
3) The effective mass of the electrons is much bigger in rutile compared with anatase. In addition, the dispersion of effective masses of charge carriers in rutile has strong anisotropy along crystallographic directions. It was reported that in the <001> direction $m_e^* \approx 2 - 4\, m_e$ and in <100> $m_e^* \approx 10 - 15\, m_e$[15]. In the case of anatase, the effective mass of electrons has a maximum value $m_e^* \approx 3.7\, m_e$ in direction <001>, and the minimum $m_e^* \approx 0.59\, m_e$ in the <100> and <010> directions. In the case of holes in anatase, mentioned dependence has a different trend. In directions <100> and <010> the $m_h^* \approx 2.33\, m_h$, in direction <001> $m_h^* \approx 0.98\, m_h$. For <101> direction the $m_e^* \approx 0.61\, m_e$ and $m_h^* \approx 2.22\, m_h$[16].

The TiO_2 oxides is a typical AB_2 crystal possessing in its structure different kinds of defects. The most popular are oxygen vacancies. These vacancies change the electron properties of the material. Was shown that an energy level created by oxygen vacancies in anatase TiO_2 has 0.75 - 1.18 eV lower energy than the bottom of conducting band of a pristine TiO_2 single crystal (see Fig. 2.2)[17]. The energy states created by oxygen vacancies in the TiO_2 anatase crystal are located 2.02 - 2.45 eV above the valence band, which corresponds to a wavelength of 506 - 614 nm. It means that the optical absorption edge will shift itself into the red spectrum region. Energy states of the oxygen vacancies serve as electron traps and help suppress their recombination. It increases the lifetime of the separated electrons and holes[18]. The simplified illustration of bulk trapping states of photoinduced electrons is shown in Fig. 2.2. The trapping of electrons generated by picosecond laser in colloidal TiO_2 was observed experimentally[19].

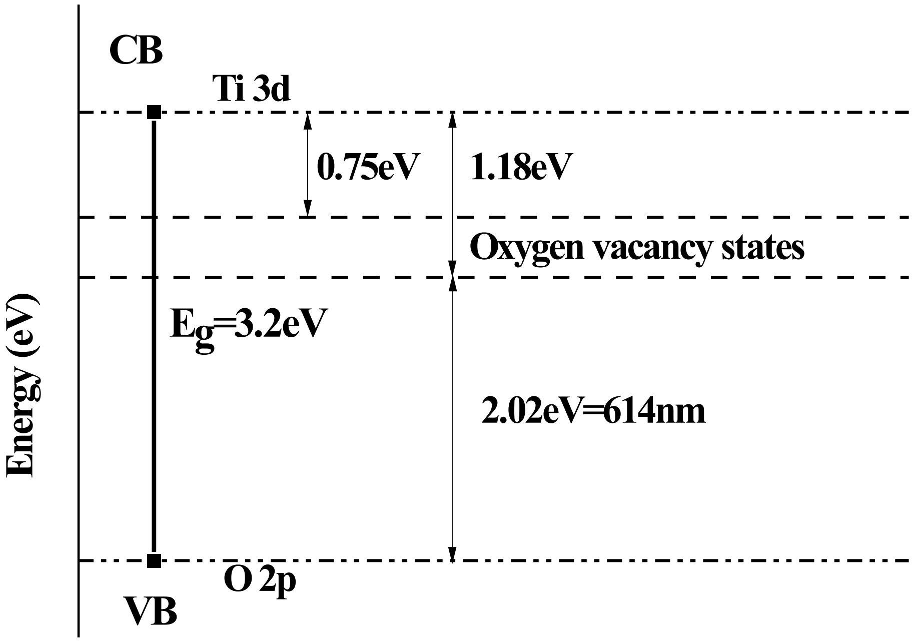

Figure 2.2 Schematic energy diagram for oxygen vacancies created in anatase TiO_2 crystals[17]

2.2. Role of dopants in TiO_2 structure

Many studies have attempted to understand the role of dopants in the TiO_2 structure in the improvement of the photovoltaic properties of these materials [23, 25 27, 29, 34, 35-39]. Dopants in TiO_2 tend to reduce the band gap of undoped material introducing the electron or hole trapping levels[28-39], and improving charge carrier separation[20]. Many of the cation dopants were described in terms of their influence on the kinetic behavior of anatase to rutile transformation. Hanaor and Sorrell suggested that small cations with low valence accelerate the transition from anatase to rutile (see Fig. 2.3)[24]. On the other side, the selected cation substituting the Ti^{4+} ions causes the charge compensation of the structure requiring increasing oxygen vacancies near the dopant. This creates the formation of Ti ions with lower valence near the dopant area, that makes enhances charge carrier transport and accelerates phase transition. Conversely, is complicated to form oxygen vacancies and Ti^{3+} ions by the ion with large valence ≥ 4. The lattice deformation takes the role in the case of cations possessing a large difference in ionic radius compared with Ti^{4+} ion. It means that substituting cations must have an ionic radius not greatly different from the Ti^{4+}. In case of the great difference in ionic radius, cations cannot enter to anatase structure but they can coexist with it. Inhibitors and promotors of TiO_2 anatase to rutile transformation are presented in Fig. 2.3.

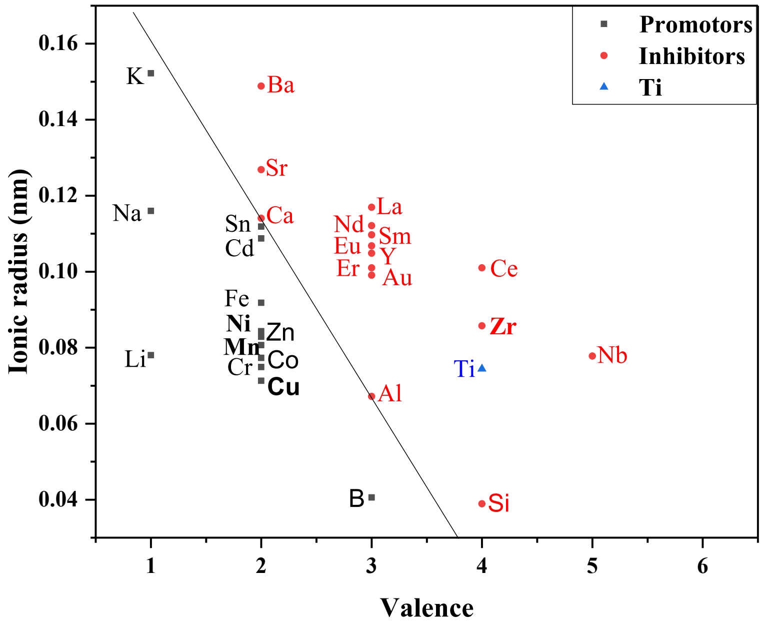

Figure 2.3. The valence versus radius plot of anatase to rutile transformation, categorizing inhibiting and promoting dopants, based on the published work[24].

Anionic dopants are interesting for improving the photocatalytic and photovoltaic properties of TiO_2 [21] . Doping anions can be represented as ions filling oxygen vacancies in the crystalline structure of TiO_2. The stability of these structures strongly depends on the size of the impurity ion. For example, in the case of nitrogen, whose ion is only 6% larger than oxygen, this substitution is typical and described in papers[38].

The dopants influence the stability of the crystal structure of the semiconducting materials. In the case of TiO_2, the phase transformation from anatase to rutile depends on impurities, conditions of material synthesis, and external conditions of its use. In this case, the phase transition should be interpreted in terms of temperature-time condition, particle size and shape, surface area, and atmosphere. Variable dopants can almost prevent the transformation from anatase and rutile (see Fig. 2.4), but the other ones can promote the transformation (see Fig. 2.5)[24]. Ti and Zr atoms are located in the same group of elements that give comparable physicochemical properties. However, Zr^{4+} is bigger and much more electropositive than Ti^{4+}. The strong connection between Zr and the nearest O atoms makes ZrO_2 chemically very stable. In consequence, in the mixed systems with the presence of TiO_2 and ZrO_2 structural units, the Ti-O bonds became more stable and more difficult to break them. This increases lattice stability at elevated temperatures[22,23]. In other words, the Zr dopants provide thermostabilizing effect on TiO_2 which decreases the specific surface area of TiO_2 at the higher temperature (see Table 2.2).

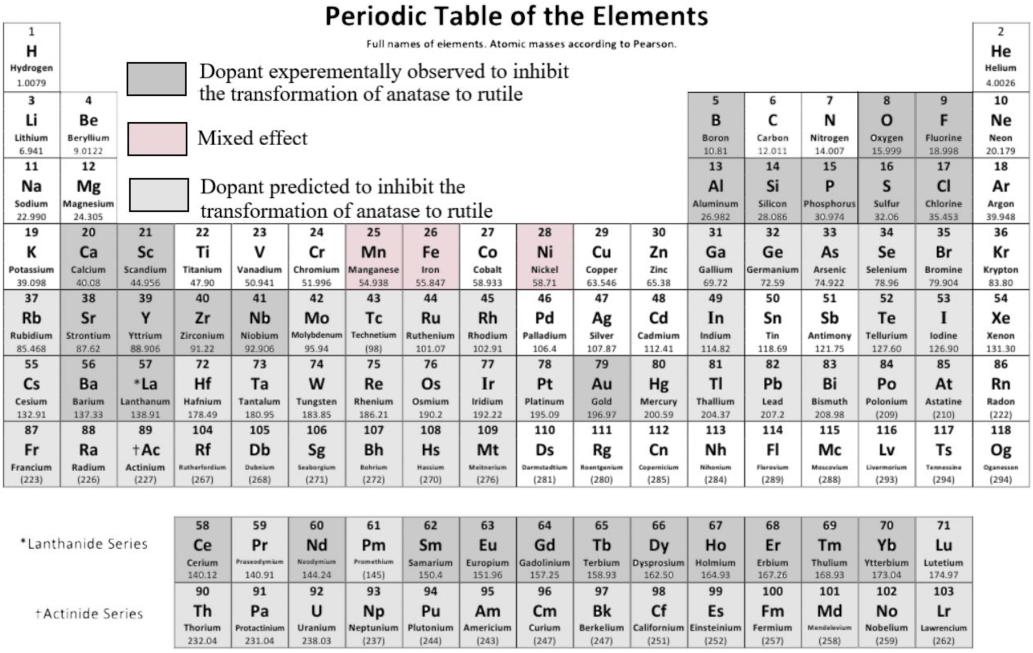
Periodic Table of the Elements
Full names of elements. Atomic masses according to Pearson.
Dopant experementally observed to inhibit the transformation of anatase to rutile
Mixed effect
Dopant predicted to inhibit the transformation of anatase to rutile
*Lanthanide Series
†Actinide Series

Figure 2.4. Experimentally and computationally predicted inhibition of anatase to rutile transformation[24]

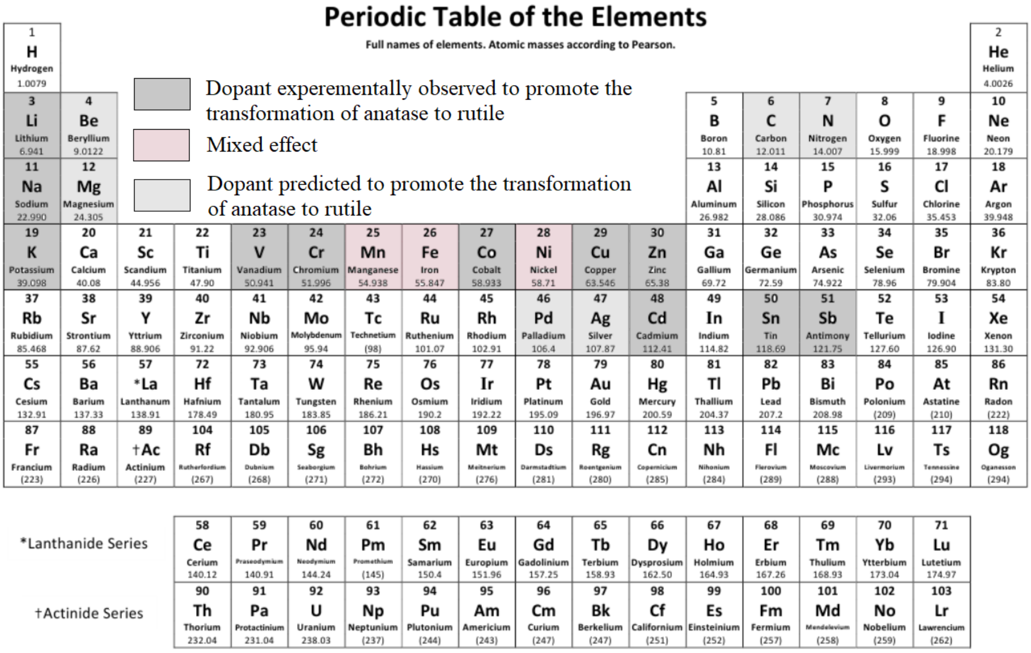
Periodic Table of the Elements
Full names of elements. Atomic masses according to Pearson.
Dopant experementally observed to promote the transformation of anatase to rutile
Mixed effect
Dopant predicted to promote the transformation of anatase to rutile
*Lanthanide Series
†Actinide Series

Figure 2.5. Experimentally and computationally predicted the promotion of anatase to rutile transformation[24]

Table.2.2. Structural properties of pristine and Zr^{4+} doped nano TiO_2 calcined at 500 ˚C [22]

	Specific surface area (m^2/g)	Pore diameter (nm)	Particle size (nm)	Band gap Energy (eV)
Nano TiO_2	66	3.6	18-20	3.21
0.5 mol% Zr^{4+}-TiO^2	80	4.3	12-15	3.23
1.0 mol% Zr^{4+}-TiO^2	95	4.8	8-12	3.27
2.0 mol% Zr^{4+}-TiO^2	125	5.2	6-12	3.29
3.0 mol% Zr^{4+}-TiO^2	133	5.6	4-10	3.31
5.0 mol% Zr^{4+}-TiO^2	139	5.1	4-12	3.31

The increasing value of bandgap energy for Zr^{4+}-doped TiO_2 nanoparticles can be characterized by the quantum confinement size effect. It means that a decrease in particle size increases the band gap energy (Table 2.2). Additionally, the change in the energy gap value is also caused by the increase in the concentration of Zr impurities in the TiO_2 structure. It should be noticed, that the Zr^{4+} ions in the TiO_2 structure do not change the structure of the energy bands compared with pristine TiO_2. The valence band is mainly formed by 2p electrons of oxygen anions, and the conduction band is mainly created by 3d electrons of Ti^{4+}. The Zr^{4+} levels are localized higher in the conduction band and do not take part in fundamental absorption furthermore. The O 2p energy states are stabilized more on Zr^{4+} impurities since they are more electropositive than Ti^{4+}. This is the reason for the band gap increase comparing TiO_2:Zr with pristine TiO_2 [31]. The higher concentration of ZrO_2 units in the TiO_2 structure does not have a positive impact on the general efficiency of DSSC[23]. First of all ZrO_2 crystal structure has higher band gap energy (~5 eV) compared with pristine TiO_2, and the negative shift of the conduction band has a critical impact on the low harvesting of excitation energy.

The XRD diffractograms show that the TiO_2:Zr structure exhibit peaks characterizing the ZrO_2 structures attributed to the monoclinic and tetragonal phase[25]. However, the TiO_2 anatase peaks are left almost without changing, which indicates that the major part of Zr atoms is evenly distributed in the whole anatase crystal. It can be seen that concentrations of Zr impurities greater than 10% form a mixed oxide, i.e. ZrO_2 grains are distributed in the TiO_2 anatase structure. This phenomenon decreases the general efficiency of charge carrier transport by creating charge trapping centers and recombination losses on grain borders[26].

Analyzing the influence of the Zr impurities on the photovoltaic properties of anatase TiO_2 Dürr and coworkers[25] have described that 1% of dopants increases the open-circuit voltage (V_{oc}) from 700 up to 715 mV compared with pristine TiO_2, and although increases of solar cell short-circuit current (*Jsc*) from 15.6 to 16.5 mA/cm^2, which is attributed by an increase of surface area to 97 m^2/g (see Table 2.2). In other work was proved that $Ti_{0.95}Zr_{0.05}O_2$ crystal is very applicable for DSSC devices[27]. The proposed doping of TiO_2 increased the surface area from 80 m^2/g to 109 m^2/g increasing the Jsc by 11 %. Although, the mentioned dopant ratio makes an impact on the shift of the conduction band minimum to be more negative value than it is noticed for pure anatase leading to an increase of the V_{oc} by 4 % compared to the pure anatase. The high concentration of Zr equal to 15 % causes the pure photovoltaic properties at all calcined temperatures (see Table 2.3). The value of J_{sc} becomes significantly higher for 5 % doping of Zr than for pristine TiO_2. Pasche and Grohe[23] also describe anatase thermostabilization by Zr dopants. They get results that 5% of the Zr impurities give the best resistance for the thermal degradation of anatase into rutile TiO_2 structure.

Table 2.3. The J-V characterization of DSSC devices containing pristine and Zr-doped nanostructured TiO_2 [23]

		V_{oc} (V)	J_{sc} (mA/cm^2)	FF[1]	η (%)
400°	0.0 mol% Zr^{4+}	0.69	15.65	0.61	6.54
	5.0 mol% Zr^{4+}	0.63	9.26	0.62	3.65
	10.0 mol% Zr^{4+}	0.68	6.17	0.60	2.53
	15.0 mol% Zr^{4+}	0.65	2.02	0.55	0.74
500°	0.0 mol% Zr^{4+}	0.69	8.01	0.63	3.50
	5.0 mol% Zr^{4+}	0.67	9.34	0.60	3.75
	10.0 mol% Zr^{4+}	0.69	4.99	0.58	1.99
	15.0 mol% Zr^{4+}	0.68	4.16	0.59	1.66
600°	0.0 mol% Zr^{4+}	0.63	6.55	0.60	2.48
	5.0 mol% Zr^{4+}	0.64	10.66	0.61	4.16
	10.0 mol% Zr^{4+}	0.64	5.04	0.60	1.92
	15.0 mol% Zr^{4+}	0.60	4.01	0.59	1.43
700°	0.0 mol% Zr^{4+}	0.63	1.08	0.45	0.31
	5.0 mol% Zr^{4+}	0.65	8.65	0.64	3.60
	10.0 mol% Zr^{4+}	0.66	5.12	0.60	2.03
	15.0 mol% Zr^{4+}	0.62	4.19	0.62	1.59

---

[1] File Factor $FF = \frac{J_{\max} \times V_{\max}}{J_{sc} \times V_{oc}}$, where J_{max} and V_{max} represents photocurrent and photovoltage for the maximum power output, and J_{sc} and V_{oc} represents short-circuit current and open-circuit voltage, respectively.

Concluding, one can say that a few percent of the Zr dopant makes a positive impact on the photovoltaic properties of TiO_2 anatase structures. In this case, the Zr ions are evenly distributed in the whole anatase crystal. Zr dopants increase the phase stability of the anatase giving a higher value of the effective surface at higher temperatures. It can have also a positive effect on the increase of the $V_{oc.}$ However, as shown earlier, the electron properties of TiO_2 depend largely on the method and conditions of synthesis and pretreatment of the material.

Nickel ion has 2+ valence and has two electrons less than Ti atom. Was reported that NiO in amorphous form coexists with TiO_2 without its incorporation into the lattice[28]. Often Ni ions are adsorbed on the surface of Ti octahedra through hydrogen bonds, which does not change anatase properties. Some works also suggest that Ni^{2+} ions can be strongly incorporated into the host anatase lattice[29]. The Ti ions substituted by Ni have a strong impact on the crystal structure. The main issue is the significant lattice contraction in the c crystallographic direction almost without any changes in other lattice edges. It mostly decreases the c/a parameter (see Table 2.4). The significant changes in crystal lattice parameters of the Ni doper TiO_2 compare to the pristine structure made a strong impact on crystal growth and reduce its size. As a result of these changes, the final structure of mixed Ti and Ni oxides shows spherical non-uniform size particles, with high agglomeration.

Table 2.4. Structural and electron properties of Ni^{2+} doped nanostructures of TiO_2 calcined at 450°C from[29]

	Avg. crystalline size (nm)	Lattice constant (Å) (Pure anatase) a=3.785, c=9.514)	Volume	c/a	E_g (eV) [29]
0.025Ni(M)	8.90	a=3.756, c=9.283	131.10	2.47	2.52
0.05Ni(M)	8.75	a=3.767, c=9.222	130.86	2.45	2.50
0.1Ni(M)	7.96	a=3.774, c=9.127	130.00	2.42	2.47
0.2Ni(M)	5.37	a=3.791, c=9.044	129.98	2.39	2.21

M-molar %

Insertion of Ni^{2+} ions into the TiO_2 lattice shows a strong redshift of the UV-vis absorption spectra, which is mainly attributed to the Ni^{2+} *d* electrons and *sp-d* exchange interaction[30]. An increase of the Ni dopants in the TiO_2 structure decreases its band gap energy (see Table 2.4). Additionally, the pore diameters decrease with an increased amount of Ni dopant in TiO_2 mesoporous structure making an impact on the effective surface of the semiconductor and influencing its photovoltaic parameters (see Table 2.5). The Ni dopants make insignificant negative shift for the conduction band compared with pristine TiO_2. It can be the result of the confinement quantum size effect occurring when the size of nanostructures decreases with adding Ni ions into the TiO_2 structure.

Table 2.5. The J-V characterization of the DSSC devices containing pristine and Ni-doped TiO_2 calcined at 450°C from[29]

	V_{oc} (V)	J_{sc} (mA/cm^2)	FF	η (%)
-	0.772	7.18	0.45	2.51
0.025Ni(M)	0.733	8.02	0.47	2.81
0.05Ni(M)	0.752	8.60	0.46	2.98
0.1Ni(M)	0.759	8.49	0.46	2.99
0.2Ni(M)	0.786	10.15	0.45	3.60

M-molar %

The influence of calcination temperature on the stability of the Ni-doped TiO_2 structure was also investigated[29]. The XRD diagram shows significant anatase to rutile phase transformation with increasing temperature and the time of calcination[28]. The mentioned phase transition depends on the number of dopants. XRD spectra although show that possible Ni oxide could be incorporated as an amorphous phase without ion distribution into the lattice[28].

Cu dopants do not significantly change the crystal parameters of TiO_2 in anatase form. The $Ti_{0.925}Cu_{0.075}O_2$ structure poses crystal edge a=3.781 Å and c=9.481 Å[31] that is very compatible with pristine anatase[9]. Was shown that doping of the TiO_2 by 3.72 % of Cu ions results in mixed anatase and rutile structure with CuO picks[32]. Occurring structural changes significantly affect the charge trapping and recombination processes. Even a small concentration of Cu ions (0.77 %) causes a two-fold decrease in J_{sc} compared with the pristine TiO_2 (see Table 2.6). With a higher concentration of dopants, the drop in J_{sc} became very significant. For 6.65 % of Cu dopants, the decrease in J_{sc} is 38 times compared to the pristine TiO_2. This although drops the efficiency of the DSSC cell. A decrease in J_{sc} can be due to a few reasons. The presence of CuO in the TiO_2 structure may imply electron injection and diffusion. Presents of Cu^{2+} ions may provoke redox reaction with electrolyte. Additionally, the Cu ions in the TiO_2 structure lead to a decrease in bandgap energy of about 10 % compared to pristine crystal.

Table 2.6. The J-V characterization of the DSSC devices containing pristine and Cu-doped TiO_2 calcined at 450°C from[32]

	V_{oc} (V)	J_{sc} (mA/cm^2)	FF	η (%)
-	0.700	7.237	0.42	2.49
0.767%Cu	0.730	4.121	0.54	1.63
1.66%Cu	0.745	2.801	0.59	1.24
1.95%Cu	0.755	2.372	0.65	1.17
2.38%Cu	0.750	1.928	0.54	0.78
3.24%Cu	0.780	1.492	0.65	0.76
3.72%Cu	0.785	0.585	0.50	0.23
4.43%Cu	0.780	0.402	0.44	0.14
5.01%Cu	0.725	0.238	0.42	0.07
5.17%Cu	0.735	0.238	0.41	0.06
6.65%Cu	0.695	0.190	0.42	0.06

From the structural point of view, the Mn dopants do not have a thermo-stabilization effect on the TiO_2 anatase structure. The Mn dopants in amounts 3.5 and 10 mol % do not show any structural effect at 300°C leaving TiO_2 in anatase form[33] (see Table 2.7). However, at 800°C the structure is completely transformed into rutile. Highly Mn-doped TiO_2 (22%) becomes rutile subjected to calcination at 500°C for 4 h [28].

Table 2.7. Structural parameters of the pristine and Mn^{2+}-doped TiO_2 nanostructures calcined at 300°C from[33]

	Latisse constant(A)	Volume	c/a
-	a=3.78, c=9.57	136.74	2.53
0.03Mn(M)	a=3.79, c=9.57	137.46	2.53
0.05Mn(M)	a=3.80, c=9.58	138.34	2.52
0.1Mn(M)	a=3.80, c=9.59	138.46	2.52

M-molar %

Doping of the TiO_2 by Mn ions decreases the band gap energy up to 3.00 eV and 2.95 eV, for 0.03Mn and 0.1Mn mol% dopant, respectively. This may be due to the emergence of new *d* electron states of the Mn in the bandgap of TiO_2 located near the conduction band absorbing light in the visible region. Among the reported transition metals, the Mn^{2+} ions cause long electron lifetime in the excited states showing benefit in J_{sc} [34]. The photovoltaic parameters of the Mn-doped TiO_2 are presented in Table 2.8. An increase of the Mn impurities in the TiO_2 structure increases its photovoltaic efficiency[35]. Additionally was shown that the fast calcination at 500°C for 30 min preserves the anatase structure of the sample.

Table 2.8. The J-V characterization of the DSSC devices containing TiO_2 nanoparticles as a mixture of anatase and rutile (P25) and Mn-doped TiO_2 calcined at 500°C from [35]

	V_{oc} (V)	J_{sc} (mA/cm^2)	FF	η (%)
P25	0.50	10.1	0.41	2.2
0.6 %Mn	0.56	7.2	0.37	1.5
0.9 %Mn	0.59	8.1	0.43	2.1
1.2 %Mn	0.63	11.1	0.37	2.6
1.9 %Mn	0.61	11.5	0.42	2.9

Concluding, one can say that the substitution of Ti atoms by Mn is possible and it almost does not change the lattice parameters of the anatase structure[33]. It gives the possibility of strong dopant intercalation to the lattice, without high stress occurring in the crystal structure. However, from the thermostabilization point of view, the Ti and Mn mixed oxides show worse effects than pure anatase. Substitution of Ti ions by Mn^{2+} causes a long electron lifetime in the excited state benefiting J_{sc}[34,35] and V_{oc} [35].

All above-presented TiO_2 dopants possess cation character. The N atoms create an anionic dopant in the anatase TiO_2. The substitution of oxygen vacancies by N with criterion $TiO_{2-x}N_x$ is possible[36]. It was observed that the N dopants decrease the size of TiO_2 nanoparticles from 10.5 nm to 9.6 nm[37] decreasing the efficient surface ratio, (see Table 2.9). An increase in the amount of N dopants increases lattice strain and distortion of the O-Ti-N bonds. Substitution of oxygen vacancies by N, giving Ti-N bounds, slightly decreases TiO_2 lattice edge parameters. The mentioned changes have an impact on the UV-vis absorption spectra and electron properties of the TiO_2:N structure. The N impurities shift the UV-vis absorption spectrum into the visible region[38]. The N dopants create TiO_2 lattice distortion causing a bigger effective surface resulting in higher J_{SC}. N-doped TiO_2 (1.21 at%) shows the photoconversion efficiency possessing V_{oc}=0.73 V, J_{sc}=10.52 mA/cm^2, compared to the V_{oc}=0.75 V, J_{sc}= 7.4 mA/cm^2 of the undoped TiO_2 [37]. Data collected in Table 2.9 [39] show that the best overall photovoltaic performance is obtained for the 2.77 % of N dopants.

More information concerning the influence of the Zr, Ni, Mn, Cu, and N dopants on the stability of the TiO_2 anatase structure and its electron and optical properties will be discussed in Chapter 6.

Table 2.9. Structural properties and the J-V characterization of the DSSC devices containing pristine TiO_2 nanostructures, mixed anatase and rutile TiO_2 structures (P25), and N-doped TiO_2 calcined at 450 ◦C for 4 h [39]

	Specific surface area (m^2/g)	Particle size (nm)	Band gap energy (eV)	V_{oc} (V)	J_{sc} (mA/cm^2)	File factor	η (%)
Nano TiO_2	-	23.13	3.16	0.781	13.85	0.66	7.14
P25	43	35.12	3.07	0.744	11.40	0.68	5.76
2.77 mol% N	60	22.74	3.18	0.784	15.58	0.68	8.32
0.29 mol% N	111	17.85	3.25	0.792	15.25	0.64	7.75
0.47 mol%N	124	11.72	3.05	0.733	14.26	0.64	6.68

2.3. Nanostructures based on the TiO_2

Methods of synthesis play a crucial role in the development of new materials. In the progress of synthesis, new forms of the TiO_2 structures were obtained[40,41]. An especially great impact was put on the development of the synthesis method of TiO_2 from 0 (0D) to 3 dimensions (3D): where 0D means microsphere[42] and nanobeads[43], 1D there are nanowires[44], nanofibers[45], nanorods[46], nanobelts[47] , and nanotubes[48]. 2D means the nanosheets[49], and 3D is reserved for different porous structures and volumetric materials. Different forms of the TiO_2 materials are presented in Fig. 2.6.

An example of the size limitation of material is the layered semiconducting system. Was measured that the band gap energy of the titanium electrode based on single nanosheets of the TiO_2 is equal to 3.84 eV[50]. Compared with the volumetric anatase-type electrode the conduction band of the titanium nanosheet is approximately 0.1 eV higher than that of bulk anatase. Meanwhile, the valence band of the TiO_2 nanosheet is 0.6 eV lower than the anatase electrode (see Fig. 2.8).

Such results are critical for photovoltaic devices because the conduction band level remains almost at the same position as it is for bulk structure. It has a critical impact on charge transfer from the dyes to the semiconductor occurring in DSSC devices.

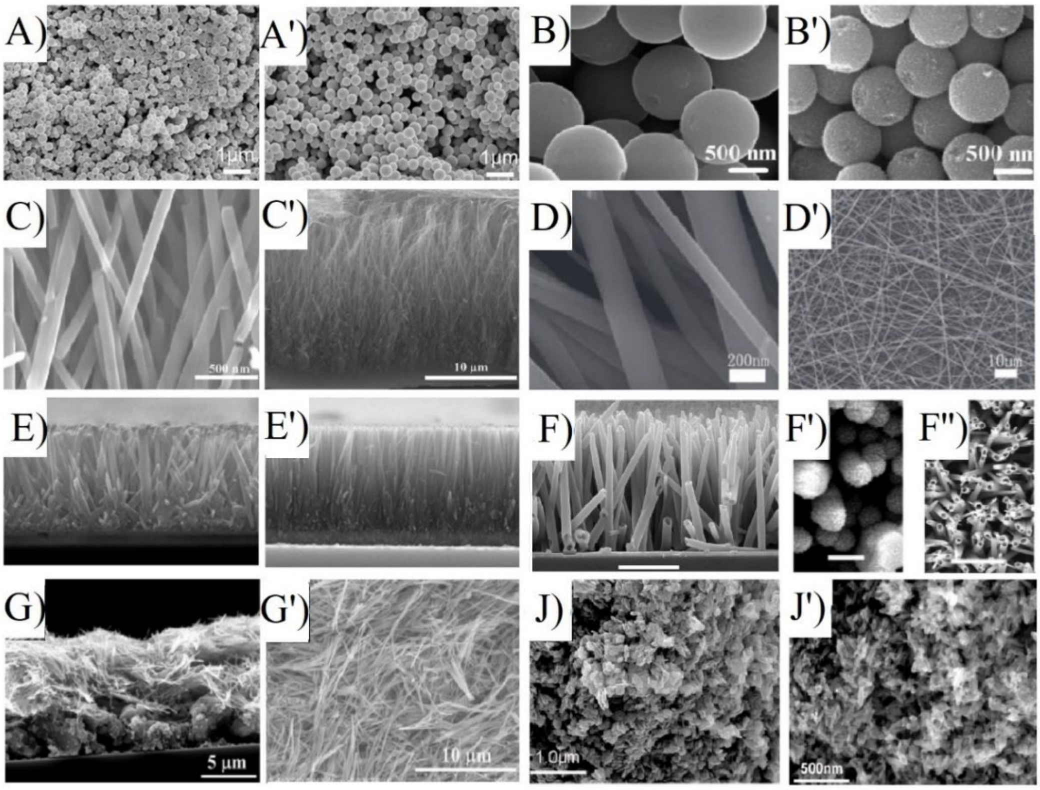

Figure 2.6. Scanning electron microscopy images of TiO_2: (A, A') microsphere[42], (B, B') nanobeads[43], (C, C') nanowires[44], (D, D') nanofibers[45], (E, E') nanorods[46], (F, F') nanotubes[48] (G, G') nanobelts[47], and (J, J') nanosheets[49]. A, A'—mesoporous TiO_2 microspheres with tunable sizes. B—the nanobeads sample, B'—samples after a solvothermal process with different amounts of ammonia. C, C'—Cross-sectional of $H_2Ti_2O_5H_2O$ nanowire arrays. D, D'—the nanobeads sample, E—cross-sectional of the TiO_2 nanorod arrays grown on bare and E'—seeded-FTO substrates. F—Cross-sectional of converted TiO_2 nanotube arrays with a closed top-end, F' F" —top view of converted TiO_2 nanotubes with a closed and opened top-end G—the cross-section of the double-layered film (particles+belts), and up layer (G') surfaces of TiO_2 P–B double-layered film. J, J'—TiO_2 nanosheets with Nb-doped (100) and (001).

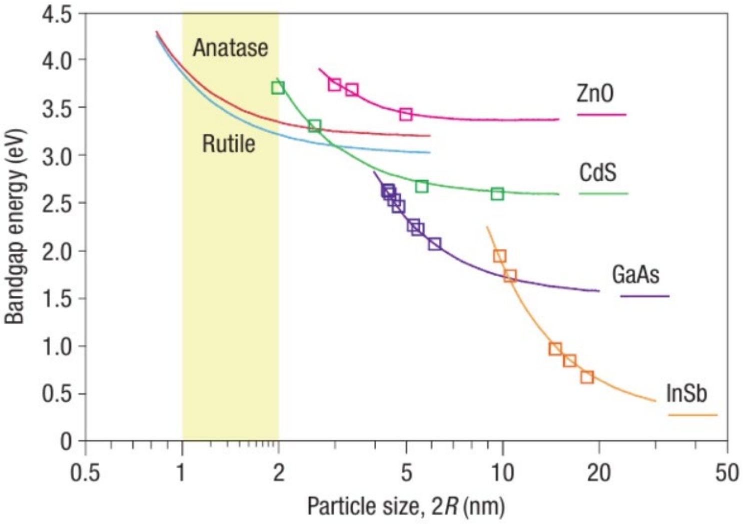

Figure 2.7. Calculated size dependence of the TiO_2 bandgap energy from reference[51]

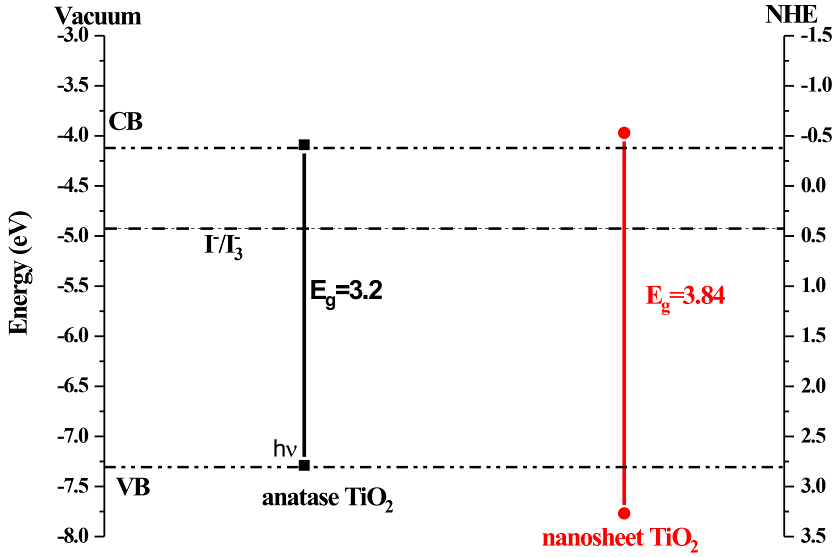

Figure 2.8. Band gap position in crystal anatase and single nanosheets of $Ti_{0.91}O_{2-0.36\ 99}$ (the difference in anatase band position in this figure and figure 2.1 bases on the fact that used nonaqueous electrolyte charge compensating ion NH^{4+} and Li^+) from[50]

2.4. Literature

[1] Delices, A., "Organized Organic Dye/Hole Transporting Materials for TiO_2- and ZnO-based Solid-State Dye-Sensitized Solar Cells (s-DSSCs)." Diss. Université Sorbonne Paris Cité, **(2017)**.

[2] Cavallo, C., Di Pascasio, F., Latini, A., Bonomo, M., & Dini, D., "Nanostructured semiconductor materials for dye-sensitized solar cells." *Journal of Nanomaterials*, vol vol.2017, **(2017)**.

[3] Fan, W., Zhang, Q., & Wang, Y., "Semiconductor-based nanocomposites for photocatalytic H_2 production and CO_2 conversion." *Physical Chemistry Chemical Physics*, vol.15, no.8, pp.2632-2649, **(2013)**.

[4] Hashimoto, K., Irie, H., & Fujishima, A., "TiO_2 photocatalysis: a historical overview and future prospects." *Japanese journal of applied physics*, vol.44, no.12, pp.8269, **(2005)**.

[5] O'Regan, B. & Grätzel, M., "A low-cost, high-efficiency solar cell based on dye-sensitized colloidal TiO_2 films." *Nature*, vol.353, pp.737-740, **(1991)**. doi:10.1038/353737a0

[6] Swamy, V., Gale, J. D., & Dubrovinsky, L. S., "Atomistic simulation of the crystal structures and bulk moduli of TiO_2 polymorphs." *Journal of Physics and Chemistry of Solids*, vol.62, no.5, pp.887-895, **(2001)**.

[7] Reyes-Coronado, D., Rodríguez-Gattorno, G., Espinosa-Pesqueira, M. E., Cab, C., De Coss, R. D., & Oskam, G., "Phase-pure TiO_2 nanoparticles: anatase, brookite and rutile." *Nanotechnology*, vol.19, no.14, pp.145605, **(2008)**.

[8] Gratzel, M., "Photoelectrochemical cells." *Nature*, vol.414, no.6861, pp.338-345 **(2001)**.

[9] Rao, K. K., Naidu, S. N., & Iyengar, L., "Thermal expansion of rutile and anatase." *Journal of the American Ceramic Society*, vol.53, no.3, pp.124-126, **(1970)**.

[10] Thomas, A., "Gemstones: properties, identification and use." New Holland Publishers, **(2008)**.

[11] Fisher, J., & Egerton, T. A., "Titanium compounds, inorganic." Kirk-Othmer Encyclopedia of Chemical Technology **(2000)**.

[12] Scanlon, D. O., Dunnill, C. W., Buckeridge, J., Shevlin, S. A., & Sokol, A. A., "Band alignment of rutile and anatase TiO_2." *Nature materials*, vol.12, no.9, pp.798-801, **(2013)**.

[13] Luttrell, T., Halpegamage, S., Tao, J., Kramer, A., & Batzill, M., "Why is anatase a better photocatalyst than rutile? Model studies on epitaxial TiO_2 films." *Scientific reports*, vol.4, no.1, pp.1-8, **(2014)**.

[14] Yamada, Y., & Kanemitsu, Y., "Determination of electron and hole lifetimes of rutile and anatase TiO_2 single crystals." *Applied Physics Letters*, vol.101, no.13, pp.133907, **(2012)**.

[15] Yagi, E., Hasiguti, R. R., & Aono, M., "Electronic conduction above 4 K of slightly reduced oxygen-deficient rutile TiO_{2-x}." *Physical Review B*, vol.54, no.11, pp.7945, **(1996)**.

[16] Kim, D., Yeo, B. C., Shin, D., Choi, H., & Han, S. S., "Dissimilar anisotropy of electron versus hole bulk transport in anatase TiO_2: Implications for photocatalysis." *Physical Review B*, vol.95, no.4, pp.045209, **(2017)**.
doi: 10.1103/PhysRevB.95.045209

[17] Nakamura, I., Negishi, N., Kutsuna, S., Ihara, T., & Takeuchi, K., "Role of Oxygen Vacancy in the Plasma-Treated TiO_2 Photocatalyst with Visible Light Activity for NO Removal." *Journal of Molecular Catalysis A: Chemical*, vol.161, pp.205-212, **(2000)**. doi:10.1016/s1381-1169(00)0036

[18] Linsebigler, A. L., Lu, G., & Yates, J. T., "Photocatalysis on TiO_2 Surfaces: Principles, Mechanisms, and Selected Results." *Chemical Reviews*, vol.95, no.3, pp.735–758, **(1995)**. doi:10.1021/cr00035a013

[19] Rothenberger, G., Moser, J., Graetzel, M., Serpone, N., & Sharma, D. K., "Charge carrier trapping and recombination dynamics in small semiconductor particles. " *Journal of the American Chemical Society*, vol.107, no.26, pp.8054-8059, **(1985)**.

[20] Sumita, T., Yamaki, T., Yamamoto, S., & Miyashita, A., "Photo-induced surface charge separation of highly oriented TiO_2 anatase and rutile thin films." *Applied Surface Science*, vol. 200 no.(1-4), pp.21–26, **(2002)**. doi:10.1016/s0169-4332(02)00614-1

[21] Serpone, N., "Is the Band Gap of Pristine TiO_2 Narrowed by Anion- and Cation-Doping of Titanium Dioxide in Second-Generation Photocatalysts?" *The Journal of Physical Chemistry B*, vol.110, no.48, pp.24287–24293, **(2006)**. doi:10.1021/jp065659r

[22] Venkatachalam, N., Palanichamy, M., Arabindoo, B., & Murugesan, V., "Enhanced photocatalytic degradation of 4-chlorophenol by Zr^{4+} doped nano TiO_2." *Journal of Molecular Catalysis A: Chemical,* vol.266, no(1-2), pp.158–165, **(2007)**. doi:10.1016/j.molcata.2006.10.

[23] Pasche, A., Grohe, B., Mittler, S., & Charpentier, P. A., "Zr-doped TiO_2 nanoparticles synthesized via a sol–gel route and their application in dye-sensitized solar cells for thermo-stabilization." *Materials Research Express*, vol.4, no.(6), pp.065501, **(2017)**. doi:10.1088/2053-1591/aa742d

[24] Hanaor, D. A., & Sorrell, C. C., "Review of the anatase to rutile phase transformation." *Journal of Materials science*, vol46, no.4, pp.855-874, **(2011)**.

[25] Dürr, M., Rosselli, S., Yasuda, A., & Nelles, G., "Band-Gap Engineering of Metal Oxides for Dye-Sensitized Solar Cells." *The Journal of Physical Chemistry B*, vol.110, no.43, pp.21899–21902, **(2006)**. doi:10.1021/jp063857c

[26] Schattka, J. H., Shchukin, D. G., Jia, J., Antonietti, M., & Caruso, R. A., "Photocatalytic activities of porous titania and titania/zirconia structures formed by using a polymer gel templating technique." *Chemistry of Materials*, vol.14, no.12, pp.5103-5108, **(2002)**.

[27] Kitiyanan, A., Ngamsinlapasathian, S., Pavasupree, S., & Yoshikawa, S., "The preparation and characterization of nanostructured TiO_2–ZrO_2 mixed oxide electrode for efficient dye-sensitized solar cells." *Journal of Solid State Chemistry*, vol.178, no.4, pp.1044–1048, **(2005)**. doi:10.1016/j.jssc.2004.12.043

[28] Ghasemi, S., Rahimnejad, S., Setayesh, S. R., Rohani, S., & Gholami, M. R., "Transition metal ions effect on the properties and photocatalytic activity of nanocrystalline TiO_2 prepared in an ionic liquid." *Journal of Hazardous Materials*, vol.172, no.(2-3), pp.1573–1578, **(2009)**. doi:10.1016/j.jhazmat.2009.08.

[29] Raguram, T., & Rajni, K. S., "Effect of Ni doping on the characterization of TiO_2 nanoparticles for DSSC applications." *Journal of Materials Science: Materials in Electronics*, vol.32, no.13, pp.18264-18281, **(2021)**.

[30] Akshay, V. R., Arun, B., Mandal, G., & Vasundhara, M., "Structural, optical and magnetic behavior of sol–gel derived Ni-doped dilute magnetic semiconductor TiO_2 nanocrystals for advanced functional applications." *Physical Chemistry Chemical Physics*, vol.21, no.5, pp.2519-2532, **(2019)**. doi:10.1039/c8cp06875e

[31] Nagaveni, K., Hegde, M. S., & Madras, G., "Structure and photocatalytic activity of $Ti_{1-x}M_xO_{2\pm\delta}$ (M= W, V, Ce, Zr, Fe, and Cu) synthesized by solution combustion method." *The Journal of Physical Chemistry B*, vol.108, no.52, pp.20204-20212, **(2004)**.

[32] Navas, J., Fernández-Lorenzo, C., Aguilar, T., Alcántara, R., & Martín-Calleja, J., "Improving open-circuit voltage in DSSCs using Cu-doped TiO_2 as a semiconductor." *Physica Status Solidi (a)*, vol.209, no.2, pp.378–385, **(2011)**. doi:10.1002/pssa.201127336

[33] Chauhan, R., Kumar, A., & Chaudhary, R. P., "Structural and photocatalytic studies of Mn doped TiO_2 nanoparticles." *Spectrochimica Acta Part A: Molecular and Biomolecular Spectroscopy*, vol.98, pp.256-264, **(2012)**.

[34] Santra, P. K., & Kamat, P. V., "Mn-doped quantum dot sensitized solar cells: a strategy to boost efficiency over 5%." *Journal of the American Chemical Society*, vol.134, no.5, pp.2508-2511, **(2012)**.

[35] Zhang, C., Zeng, J. H., & Wang, Y. F., "Manganese doped titanium dioxide with a tunable flat-band potential as photoanode in quantum dot sensitized

solar cells for higher open circuit voltage." *Chemical Physics Letters*, vol.761, no.138099, **(2020)**.

[36] Asahi, R., Morikawa, T., Ohwaki, T., Aoki, K. & Taga, Y., "Visible-Light Photocatalysis in Nitrogen-Doped Titanium Oxides." *Science*, vol.293, pp.269-271, **(2001)**. doi:10.1126/science.1061051

[37] Kang, S. H., Kim, H. S., Kim, J. Y., & Sung, Y. E., "Enhanced photocurrent of nitrogen-doped TiO_2 film for dye-sensitized solar cells." *Materials Chemistry and Physics*, vol.124, no.1, pp.422-426, **(2010)**.

[38] Kuriechen, S. K., Murugesan, S., & Paul Raj, S., "Mineralization of azo dye using combined photo-fenton and photocatalytic processes under visible light." *Journal of Catalysts*, vol.2013, **(2013)**.

[39] Guo, W., Shen, Y., Boschloo, G., Hagfeldt, A., & Ma, T., "Influence of nitrogen dopants on N-doped TiO_2 electrodes and their applications in dye-sensitized solar cells." *Electrochimica Acta*, vol.56, no.12, pp.4611–4617, **(2011)**. doi:10.1016/j.electacta.2011.02.09

[40] Fujishima, A., & Honda, K., "Electrochemical photolysis of water at a semiconductor electrode." *Nature*, vol.238, no.5358, pp.37-38, **(1972)**.

[41] Xiaodong. Y. & Chen X.. "Titanium dioxide nanomaterials." Encyclopedia of inorganic and bioinorganic chemistry, pp.1-38, **(2015)**.

[42] Chen, W., Qiu, Y., Yan, K., & Yang, S., "Surfactant directed self-assembly of size-tunable mesoporous titanium dioxide microspheres and their application in quasi-solid state dye-sensitized solar cells." *Journal of power sources*, vol.196, no.24, pp.10806-10816, **(2011)**.

[43] Chen, D., Huang, F., Cheng, Y. B., & Caruso, R. A., "Mesoporous anatase TiO_2 beads with high surface areas and controllable pore sizes: a superior candidate for high-performance dye-sensitized solar cells." *Advanced Materials*, vol.21, no.21, pp.2206-2210, **(2009)**.

[44] Wu, W. Q., Rao, H. S., Xu, Y. F., Wang, Y. F., & Kuang, D. B., "Hierarchical oriented anatase TiO_2 nanostructure arrays on flexible substrate for efficient dye-sensitized solar cells. "*Scientific reports*, vol.3, no.1, pp.1-7, **(2013)**.

[45] Zheng, D., Xiong, J., Guo, P., Li, Y., & Gu, H., "Fabrication of improved dye-sensitized solar cells with anatase/rutile TiO_2 nanofibers." *Journal of nanoscience and nanotechnology*, vol.16, no.1, pp.613-618, **(2016)**.

[46] Wang, J., Zhang, T., Wang, D., Pan, R., & Xia, H., "Improved morphology and photovoltaic performance in TiO_2 nanorod arrays based dye sensitized solar cells by using a seed layer." *Journal of Alloys and Compounds*, vol.551, pp.82-87, **(2013)**.

[47] Fan, J., Li, Z., Zhou, W., Miao, & Shao, G., "Dye-sensitized solar cells based on TiO_2 nanoparticles/nanobelts double-layered film with improved photovoltaic performance." *Applied Surface Science*, vol.319, pp.75-82, **(2014)**.

[48] Xu, C., Shin, P. H., Cao, L., Wu, J., & Gao, D., "Ordered TiO_2 nanotube arrays on transparent conductive oxide for dye-sensitized solar cells." *Chemistry of Materials*, vol.22, no.1, pp.143-148, **(2010)**.

[49] Jiang, L., Sun, L., Yang, D., Zhang, J., & Deng, W. Q., "Niobium-doped (001)-dominated anatase TiO_2 nanosheets as photoelectrode for efficient dye-sensitized solar cells." *ACS applied materials & interfaces*, vol.9, no.11, pp.9576-9583, **(2017)**.

[50] Sakai, N., Ebina, Y., Takada, K., & Sasaki, T., "Electronic band structure of titania semiconductor nanosheets revealed by electrochemical and photoelectrochemical studies." *Journal of the American Chemical Society*, vol.126, no.18, pp.5851-5858, **(2004)**.

[51] Satoh, N., Nakashima, T., Kamikura, K., & Yamamoto, K., "Quantum size effect in TiO_2 nanoparticles prepared by finely controlled metal assembly on dendrimer templates." *Nature Nanotechnology*, vol.3, no.2, pp.106–111, **(2008)**. doi:10.1038/nnano.2008.2

Chapter 3

SENSITIZERS FOR THE PHOTOVOLTAIC APPLICATIONS IN DSSC DEVICES

Dye-sensitized solar cells (DSSC)[1] are a low-cost and efficient alternative to conventional silicon solar cells. The key elements of the DSSC are organic dyes adsorbed on the surface of a mesoporous or nanocrystalline oxide semiconductor working as the photoanode. The main requirements for efficient dye sensitizers are as follows:

1) stability - sensitizers must be structurally stable in the ground, excited, and oxidized states; they should be photo-electrochemically stable giving the number of oxidation and reduction work cycles higher than 10^6;
2) possessing an appropriate anchor group - the sensitizers must have an anchoring moiety to make its efficient chemisorption on the surface of the semiconductor;
3) efficient absorption of the visible light – the high-efficiency absorption of electromagnetic waves in visible as well as in NIR region is needed; high energy of lower unoccupied molecular orbital (LUMO) and appropriately high occupied molecular orbital (HOMO) energy to absorb required light is needed;
4) HOMO and LUMO must be separated in the space through the dye molecule - LUMO should be localized near the anchoring group, as close to the semiconductor surface as possible, and HOMO as far as possible; it means efficient charge injection.

The sensitizers used in DSSC applications can be divided into Ru-complexes, metal-free organic dyes, quantum-dot dyes, mordant dyes, natural dyes, and perovskite-based sensitizers. In the present work, only selected Ru-complexes and metal-free organic dyes will be characterized.

3.1. Ru-complex sensitizers

The dyes satisfying almost all desired properties are Ru-complex sensitizers. The most popular and earliest Ru-based sensitizers are presented in Fig. 3.1. The earlier known sensitizer is cis-bis(isothiocyanato)bis(2,2'-bipyridyl-4,4'-dicarboxylato)-ruthenium(II) molecule (N3)[2] [CAS number: 141460-19-7]. It is a mononuclear ruthenium dye with two thiocyanate (NCS) ligands. Its main peak of light absorption is attributed to the metal-to-ligand charge transfer (MLCT). The molecular orbitals HOMO and LUMO of the N3 are mainly derived from the *d*-orbitals of the ruthenium and π* orbitals of the ligand, respectively. In ethanol, the N3 has three absorption peaks at 534 nm, 396 nm, and 313 nm (Table 3.1). The N3 is used as a reference dye with its synthesis as a starting point to improve the electron and optical properties of new dyes and the overall efficiency of DSSC devices.

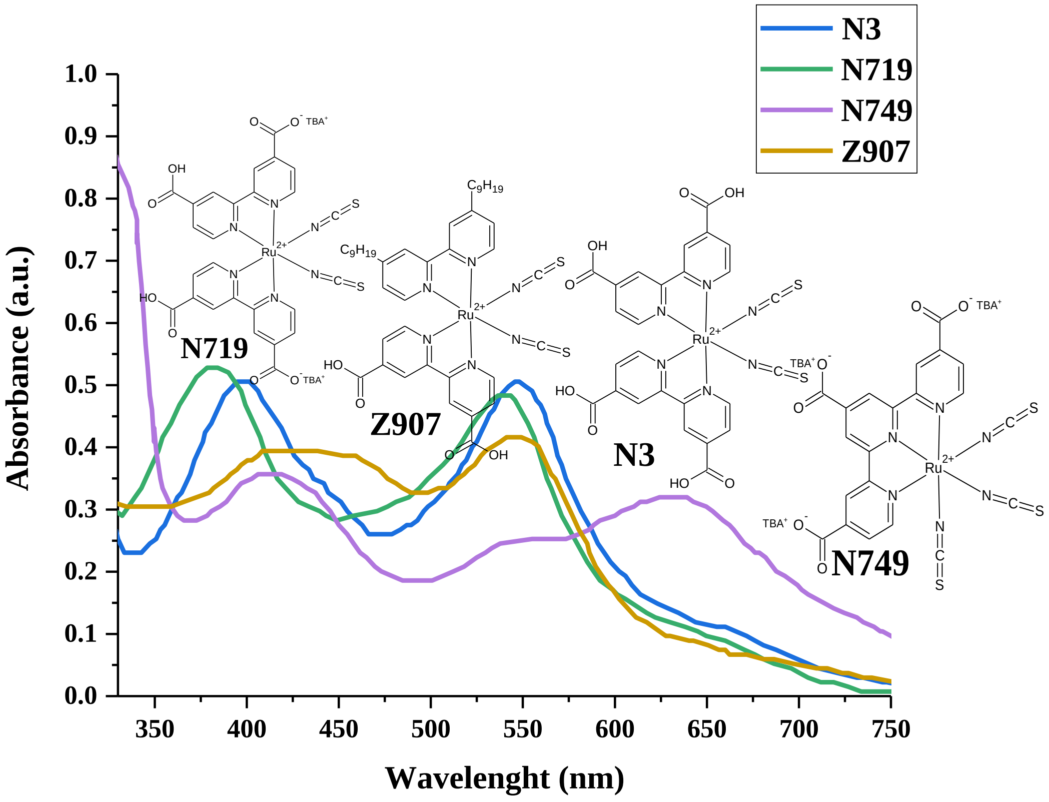

Figure 3.1. Schematic structure of the most know ruthenium dyes and their UV-vis absorption spectra measured in ethanol

Discussing the problem of the dyes working at the TiO_2 surface should be taken into account that the conduction band of the TiO_2 has a Nernstian dependence on pH[3]. The fully protonated sensitizer upon light adsorption transfers most of its protons to the TiO_2 surface charging it positively. The electric field associated with the surface dipole generated in this fashion enhances the adsorption of the ruthenium complexes and assists electron injection from the excited state of the sensitizers to the TiO_2 conduction band, favoring high photocurrents. However, the open-circuit potential (V_{oc}) will be low due to the positive shift of the conduction band edge induced by surface protonation. On the other hand, if the sensitizer carries no protons at all, one expects a high value for V_{oc} while short-circuit photocurrent (J_{sc}) will be low. Thus, there should be an optimal degree of protonation of the sensitizer for which the V_{oc} and J_{sc} determining the power conversion efficiency of the DSSC, reaches a maximum. For that reason, carboxyl acid was substituted by the carboxyl salt tetra-n-butylammonium (TBA^+) (see N719 in Fig. 3.1). The mentioned change increases the V_{oc} of the molecule N719[4] [CAS number: 207347-46-4] compare with N3 dye. Adding the TBA+ to the pyridine ligands decreases also the solubility of the sensitizers.

Table 3.1. UV-vis absorption spectral data of Ru-based complexes (measured in ethanol)

Dye	Absorption λ_{max} (nm)	Emission λ_{max} (nm) (298 K)
N3	534, 396, 313[2]	755[2]
N719	535, 395, 312[4]	830[4]
N749	620, 415, 341, 329[9]	950[9]
Z907	521, 371,295[5,6]	763[5]

The carboxylic acid groups are the most employed to anchor dyes at the TiO_2 surface ensuring a strong bond and good electron communication. The disadvantage of using this linker is its sensitivity to water. The presence of water can hydrolyze the bond between dye and TiO_2 negatively influencing the stability of the dye adsorption. It can happen in a DSSC when a liquid electrolyte is employed for dye regeneration. To minimize the influence of traces of water on the long-term performance of a DSSC, dyes with attached hydrophobic chains have been designed. Among them, the Z907 dye is one of the most stable toward desorption from the TiO_2 surface[7].

The problem in the N3, N719, and Z907 dyes concerns the absence of their absorption in the NIR region. It gives the idea of new dyes moving from two bipyridyl ligands to terpyridyl derivatives with three SCN ligands. In consequence, the N749 molecule called the black dye was synthesized[8] (see N749 in Fig. 3.1) [CAS number: 359415-47-7]. The shift of the LUMO level of N749 moves the MLCT transmission to longer wavelengths up to 920 nm[9] (see Table 3.1).

All molecules presented in Fig. 3.1 are characterized by high stability, high absorption in visible light, efficient charge injection into a semiconductor, and MLCT yielding conversion efficiency higher than 12.5%. All the mentioned advantages show that these molecules have a great potential for DSSC applications, which makes the structures very interesting for research[10,11]. The oxidation and reduction potentials energy diagram measured for the N3[12], N719[13,14], Z907, and N749[15,16] dyes compared with the conduction and valence band of the TiO_2 in anatase form[17] are presented in Fig. 3.2. These data are presented regarding the triiodide/iodide (I_3^-/I^-) redox mediator[1]. One can see that all presented dyes possess LUMO levels above the conduction band of the TiO_2. It means that these dyes can be used in TiO_2-based DSSCs.

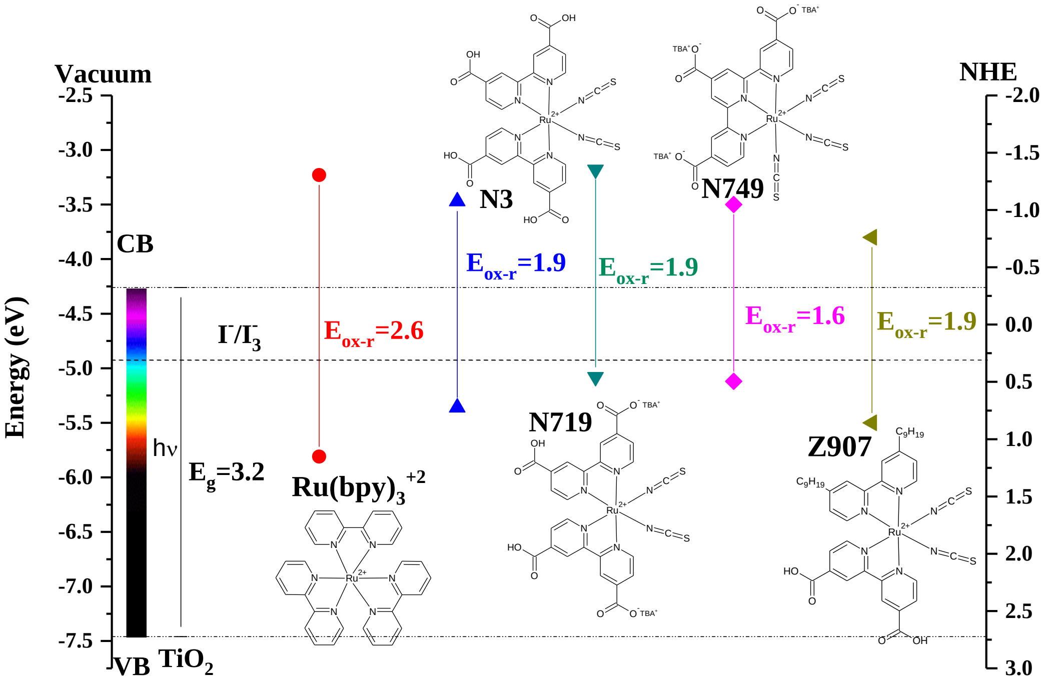

Figure 3.2. Conduction and valence band position of TiO_2 and schematic representation of the energy levels and structures of the selected Ru-complexes: $Ru(bpy)_3^{+2}$, N3, N719, N749, and Z907

The N719 and N749 are examples of efficient sensitizers that absorb a wide range of visible light. Although they are very efficient light-to-electron converters. The problem arises when considering the possibility of decomposition of the −NCS group. This inconvenience resulted in the synthesis of a group of new sensitizers based on tris-substituted bipyridine ruthenium(II) complex ($Ru(bpy)_3^{+2}$)[18,19,20] presented in Fig 3.2. The $Ru(bpy)_3^{+2}$ molecule possesses excellent photochemical and photophysical characteristics, such as light absorption and light emission[21], that can be utilized to improve the energy conversion efficiency of DSSCs[22]. The structure and the properties of $Ru(bpy)_3^{+2}$ have been well studied. The $Ru(bpy)_3^{+2}$ molecule is highly stable and a large variety of chemical transformations in the bipyridine rings can be accomplished. It has a D_3 symmetry and its nitrogen atoms create an octahedral environment around the central Ru atom[23] (see Fig. 3.3). Was found that the Ru-N bond distances are equal to 2.056 Å. In solvent and crystal arrangement, the mentioned bonds can increase[23]. Due to the visible light absorption and the photophysical properties it is selected as a photosensitizer in the light-driven system playing an important role in the development of solar energy devices.

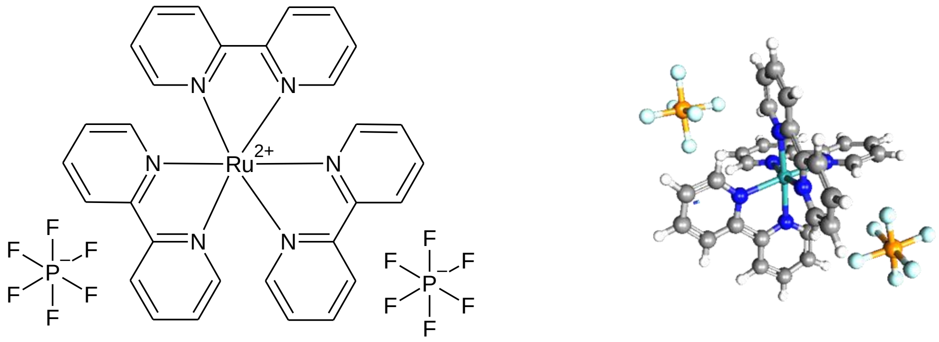

Figure 3.3. Schematic structure and graphic representation of $[Ru(bpy)_3](PF_6)_2$ structure [CAS Number 60804-74-2]. The $Ru(bpy)_3^{+2}$ molecules are stabilized by the dihexafluorophosphate $(PF_6)_2$.

The three bipyridyl ligands contain σ-donor orbitals localized on the nitrogen atoms and π-donor and π*-acceptor orbitals delocalized on the aromatic rings. The ligand-centered π*-orbitals are lower in energy than the metal-centered σ* orbitals. The absorption spectrum of the $Ru(bpy)_3^{+2}$ molecule has two peaks: in the visible region at 450 nm (MLCT π_M- π_L^*) and in the UV region at 291 nm (ligand-centered LC(π_L- π_L^*) absorption)[24]. Important is to notice that the solvent presence does not change significantly the position of the mentioned peaks. For example, in H_2SO_4 the first peak is at 453 nm[24], in CH_2C1_2 it is at 454 nm[24], in acetonitrile - 451 nm[25,26] and in ethanol - 452 nm[27]. The cyclic voltammetry measurements show that the main used solvents do not change the energy levels of oxidation and reduction potentials. It is contrary to the other ruthenium-based dyes shown in Fig. 3.2 where the solvent can critically shift the position of HOMO and LUMO energy levels.

As was reported earlier the $Ru(bpy)_3^{+2}$ molecule has the main absorption peak in visible light (MLCT absorption) including the blue region. Much emphasis was placed on the development of new $Ru(bpy)_3^{+2}$-based dyes with MLCT absorption shifted into a longer wavelength. In consequence, molecules presented in Fig. 3.4 were synthesized[28]. Their spectroscopy parameters are given in Table 3.2. Comparing these data with the first UV-vis absorption peak measured for the $[Ru(bpy)_3](PF_6)_2$ structure one can see that the developed modifications of the $Ru(bpy)_3^{+2}$ structure shift absorption spectrum for 10 nm into the red side.

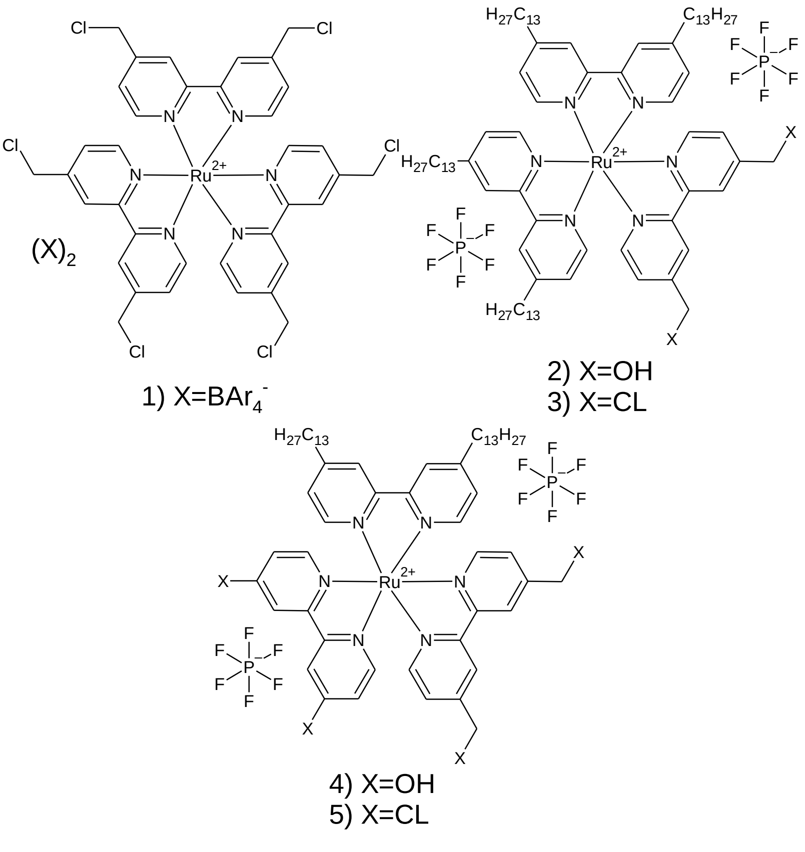

Figure 3.4. Schematic structure of $[Ru(bpy)_3](PF_6)_2$ –based complexes[28]

Table 3.2. The first UV-vis absorption peaks of the $[Ru(pby)_3\,](PF_6)_2$-based complexes presented in Fig. 3.4 [28]

Structure	Solvent	Absorption λ_{max} (nm)
1) $[Ru\{bpy(CH_2Cl)_2\}_3](BAr'_4)_2$	CH_3CN	460
2) $[Ru\{bpy(C_{13}H_{27})_2\}_2\{bpy(CH_2OH)_2\}](PF_6)_2$	$CHCl_3$	463
3) $[Ru\{bpy(C_{13}H_{27})_2\}_2\{bpy(CH_2Cl)_2\}](PF_6)_2$	$CHCl_3$	462
4) $[Ru\{bpy(C_{13}H_{27})_2\}\{bpy(CH_2OH)_2\}_2](PF_6)_2$	$CHCl_3$	460
5) $[Ru\{bpy(C_{13}H_{27})_2\}\{bpy(CH_2Cl)_2\}_2](PF_6)_2$	$CHCl_3$	459

The idea was also to extend the length of the side groups attached to the bipyridine group. Johnson and Fraser[29] used $Ru(bpy)_3^{+2}$ to synthesize the ruthenium tri(bipyridine)-centered star block copolymers consisting of poly(lactic acid) (PLA) as the hydrophobic core and poly(acrylic acid) (PAA) as the hydrophilic corona that can be used as elements of drug delivery systems. Their structures are presented in Fig. 3.5 and they are not used as sensitizers. The attached polymers shift the position of the MLCT peak not more than 15 nm into the red side of the spectrum. The positions of the first absorption peaks of molecules presented in Fig. 3.5 are collected in Table 3.3.

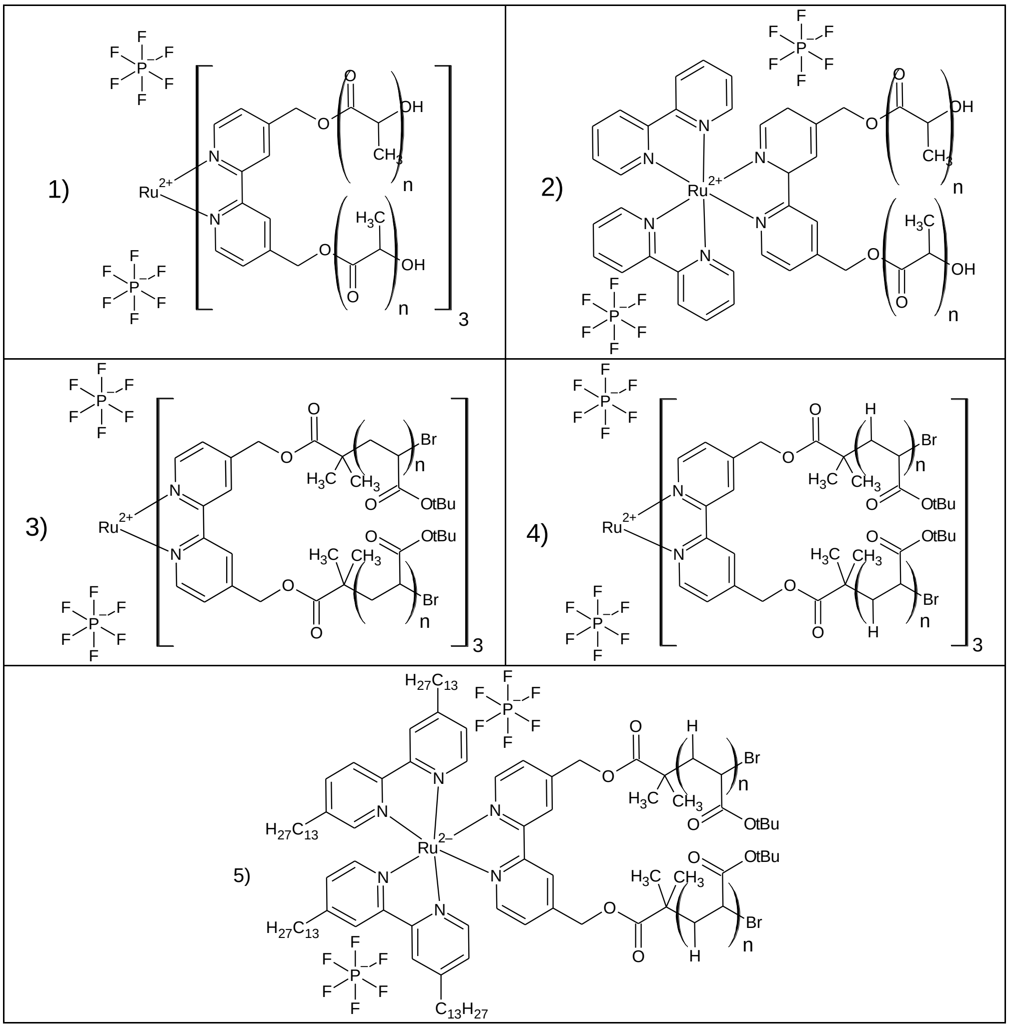

Figure 3.5. Schematic structure representation of $[Ru(pby)_3](PF_6)_2$ complexes consisting of poly(lactic acid) (PLA) and poly(acrylic acid) (PAA)[29]

Contrary to the molecules presented in Fig. 3.4 and 3.5 the $Ru(bpy)_3^{+2}$ structure was modified by adding the side groups to all bipyridines. The methyl

(Me) anchoring groups or ter-butyls (t-Bu) [30] were added to the bipyridine (see Fig. 3.6). Was shown that the anchoring groups change the UV-vis absorption spectra slightly moving the first absorption peak into the red side (up to 7 nm). This substitution also does not change significantly the oxidation and reduction potentials of new molecules (see Table 3.4).

Table 3.3. Spectroscopy data obtained for $Ru(bpy)_3^{+2}$–based complexes consisting of poly(lactic acid) (PLA) and poly(acrylic acid) (PAA)[29]

Structure	Solvent	Absorption λ_{max} (nm)	Emission λ_{max} (nm)
1) $[Ru(bpyPLA_2)_3](PF_6)_2$	CH_2Cl_2	468	622
2) $[Ru(bpy)_2(bpyPLA_2)](PF_6)_2$	CH_2Cl_2	468	622
3) $[Ru(bpyPtBA_2)_3](PF_6)_2$	CH_2Cl_2	468	621
4) $[Ru(bpyPAA_2)_3](PF_6)_2$	H_2O	468	620
5) $[Ru\{bpy(C_{13}H_{27})_2\}(bpyPAA_2)_2](PF_6)_2$	H_2O	467	621

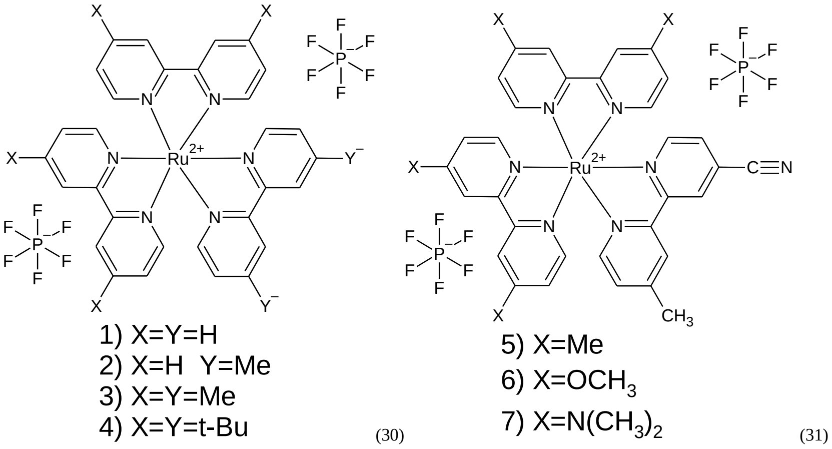

Figure 3.6. Schematic structure representation of $[Ru(bpy)_3](PF_6)_2$ complexes from the manuscript [30] and [31]

The more significant changes are seen in absorption spectra and reduction and oxidation potentials for the dyes presented in Fig. 3.6 and denoted as molecules 5-7. There, one bipyridine is substituted by -Me and -C≡N, and the other two are substituted by X= -Me, $-OCH_3$ or $-N(CH_3)_2$ groups[31]. Comparing the data collected in Table 3.4 for the $Ru(bpy)_3^{+2}$ and dye 7 one can see important changes. The UV-vis absorption spectra of molecules 5-7 (see Fig. 3.7) can be described through two MLCT transfers from d_π(Ru) to π^*(Mebpy-CN) and from d_π(Ru) to π^*(4,4′-X_2-bpy). Coordination of a 4,4′-X2-bpy ligand diminishes the wave number of the lowest-energy MLCT band in the order of increasing donor strength of −X: $-H \leq -CH_3 \leq -OCH_3 \leq -N(CH_3)_2$.

Table 3.4. UV-vis obtained data and oxidation (E_{ox}) and reduction (E_{red}) potentials of the selected $[Ru(bpy)_3](PF_6)_2$ complexes presented in Fig. 3.6[30 ,31]

Structure	Solvent	Absorption λ_{max} (nm)	Emission λ_{max} (nm)	E_{ox} (V vs. SCE) (V)	E_{red} (V vs. SCE) (V)
1) [30]	H_2O/CH_3CN (1:1)	452	612	+1.17	-1.41
2) [30]		455	618	+1.11	-1.44
3) [30]		459	620	+1.00	-1.54
4) [30]		459	618	+1.04	-1.42
5) [31]	CH_3CN	478, 444	666	+1.24	-1.25 -1.61 -1.86
6) [31]		488, 446	709	+1.06	-1.26 -1.61 -1.76
7) [31]		532, 448	798	+0.64	-1.38 -1.62 -1.93

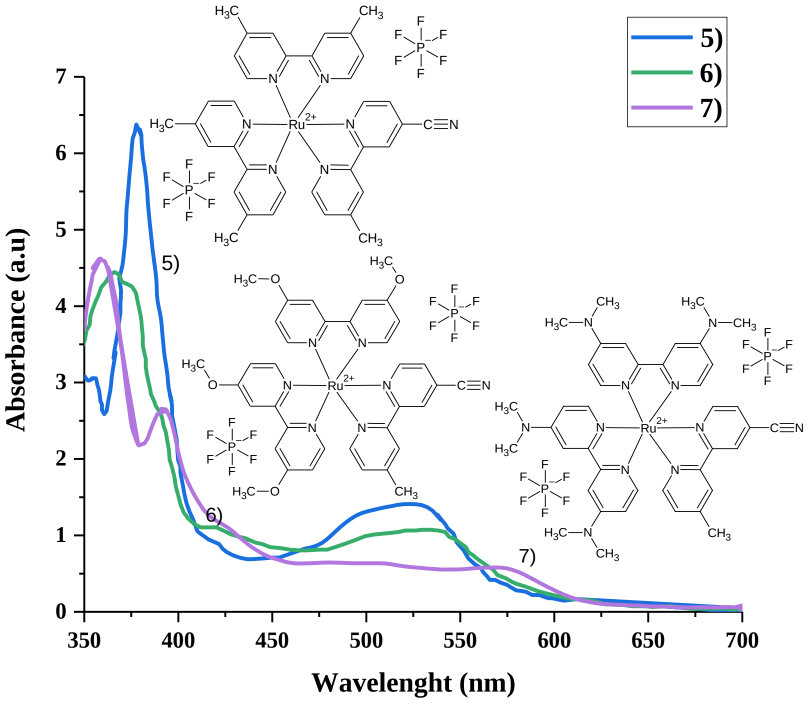

Figure 3.7. The structures of the $[Ru(4,4'\text{-}X_2\text{-}bpy)_2(Mebpy\text{-}CN)]\text{-}(PF_6)_2$, where X =$-CH_3$, $-OCH_3$,$-N(CH_3)_2$ molecules and their UV-vis absorption spectra measured in acetonitrile[31].

It is known that the addition of electron-donor or electron-acceptor groups to the 4- and 4′-positions of bipyridine alters the physicochemical properties of $Ru(bpy)_3^{+2}$ complexes[32]. Bipyridine with electron-donor substituent groups has π orbitals suitable to mix with *d* orbitals of Ru(II). This effect destabilizes the HOMO orbital. On the other hand, the LUMO orbital is a π* orbital centered in the bipyridine and it can be stabilized by introducing electron-acceptor substituents in the bipyridine rings. The usual procedure to obtain red-sensitive Ru(II) complexes is the addition of better π- acceptor ligands than bipyridine to decrease the energy of the LUMO and better σ-donor ligands to increase the energy of the HOMO. The overall result of combining both trends is a decrease in the HOMO−LUMO gap and a shift of light absorption and emission maxima to the NIR spectrum region, among other physicochemical property changes.

Enhancing asymmetry of the bipyridine substitution induces absorption over all visible wavelengths with appreciable quantum yields in the NIR region. The observed changes in redox potentials, MLCT absorption, and excited state dynamics can be rationalized with the important contribution of ligand substitutions in modulating electron densities and orbital energies in these complexes, which can be used as dyes in DSSC. However, Funaki et al.[8] found that the longer the phenylene-ethynylene chain the lower the efficiency of the solar cell, and explained this phenomenon by the aggregation of the dye molecules on the electrode surface. On the other side, in $Ru(bpy)_3^{+2}$ dyes on the TiO_2 surface, electron injection occurs from the ligand attached to TiO_2, whereas recombination occurs between an electron in TiO_2 and the oxidized Ru center[33]. The latter reaction can lower the efficiency of TiO_2 solar cells. A way to minimize this deleterious process would be to increase the distance between TiO_2 and the dye metal center, thereby decreasing the rate of recombination.

Kilsa et al.[34] investigated a series of $Ru(bpy)_3^{+2}$-based dyes in which the distance between the ruthenium center and the anchoring group has been varied. These dyes have a single anchoring carboxyl group attached via a rigid linker to one of the bipyridine ligands (see Fig. 3.8, para-position). The authors do not prove that the efficiency of the DSSC depends on spacer length. They suggest that the Ru-TiO_2 electron tunneling distance is roughly the same for longer and shorter spacers, as the one-carboxyl attachment to the surface is flexible enough for the Ru center to approach the TiO_2 surface in all cases.

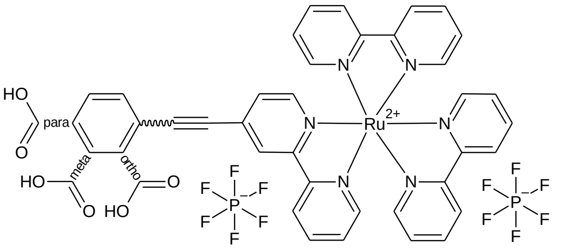

Figure 3.8. Structure of isomeric $[Ru(bpy)_3](PF_6)_2$ complexes, RuLm, RuLo, and RuLp [37]

Therefore, to better understand the electron transfer process between the dye molecule and the TiO_2 electrode three bis(2,2′-bipyridine) (4-(2-(carboksyphenyl)ethynyl)-2,2′-bipyridine)ruthenium(II) hexafluorophosphates (RuLo, RuLm, RuLp) were investigated (see Fig. 3.8). In this case, the anchoring –COOH moieties are in para-, meta-, and orto-position. It was proved that the efficiency of the DSSC can depend on the position of the single anchoring group[35]. An explanation of the mechanism of the mentioned process is the subject of the presented dissertation and will be deeply discussed in Chapters 7 and Chapter 8.

The single ruthenium-centered dyes as N3 or N719 give the photon to current conversion efficiencies in DSSC at the level of 10.0 % and 11.2 %[2,36], respectively. However, these values are still not high enough as expected for commercial DSSC applications. The mainstream research in ruthenium sensitizers is focused on structure modification of the ligands to improve light harvesting and electron injection efficiency and, in consequence, the efficiency of the DSSCs. In consequence, the dinuclear dendritic-like ruthenium dye consisting of two trisbipyridyl ruthenium(II) derivatives clipped with an ethyl 3,5-diethynylbenzoate group was synthesized. This molecule was called B_1 (see Fig. 3.9)[37]. The UV-vis absorption spectrum of B_1 in ethanolic solution shows the absorption bands between 200 and 350 nm, corresponding to the ligands π–π^* electron transfer. Also, an additional strong band is present at 325 nm, assigned to the more extended delocalized bond structure of the B_1 anchoring ligand, playing the role of an antenna. The broad bands with a maximum at 460 nm correspond to the metal-to-ligand charge transfer (MLCT), characteristic of ruthenium polypyridine complexes[38]. Was shown that the adsorption of B_1 on the TiO_2 electrode is less efficient than that of similar mononuclear ruthenium-based dyes. This phenomenon is probably related to the bulky molecule of B_1 and the presence of only one anchoring –COOH group in the molecule, which may decrease the binding abilities of this dye. In consequence, the two other dinuclear dendritic-like ruthenium dyes consisting of two trisbipyridyl ruthenium(II) derivatives possessing two anchoring groups each one were synthesized. These molecules as the subject of this work will be presented and discussed in Chapter 7.

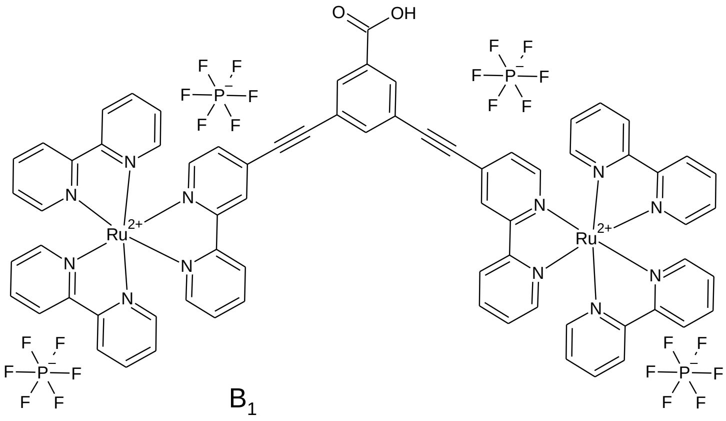

Figure 3.9. Structure of B_1 molecule

3.2. Selected metal-free organic dyes

Ruthenium is a rare and expensive metal, limiting its potential photovoltaic application. In this case, the research interest is to develop metal-free organic dyes. Promising dyes used for photovoltaic applications are chromophores based on indoline structures[39]. These molecules are relatively chip, with a simple preparation procedure, and exhibit high efficiencies and excellent performers in DSSCs. Compared to the Ru-complex dyes, they have a much higher molecular extinction coefficient and thus require a thinner oxide matrix and a smaller amount of immobilized dye. It is also noteworthy that indoline dyes are efficient with a titania semiconductor matrix[40,41]. Introducing the aromatic units into the core of the indoline structure, the absorbance in the infrared (IR) region as well as the absorption coefficient of the dye can be enhanced significantly[42].

The indoline dyes (see Fig. 3.10) contain an arylamine moiety that acts as an electron donor and is joined to a carboxylic moiety that functions as an electron acceptor and also as an anchoring group to attach the dye to the nanostructured TiO_2. When indoline dyes are absorbed on TiO_2 films, their absorption maxima are substantially red-shifted compared with the values in solution, making them favorable for light harvesting[43]. Since these dyes can be synthesized and purified cheaply, an evaluation of their performance is of considerable interest in the context of future commercial exploitation of DSSCs.

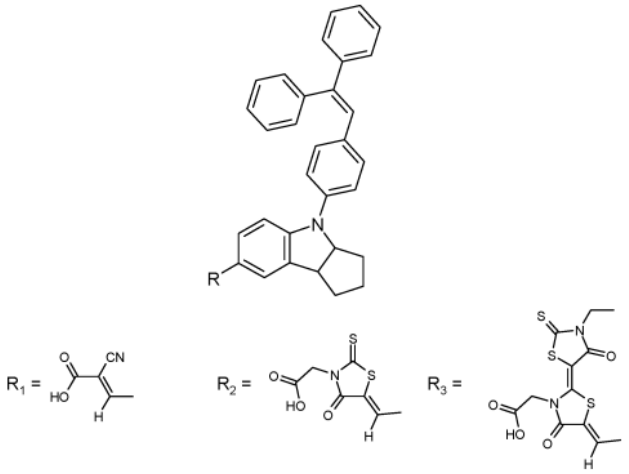

Figure 3.10. Molecular structures of the indoline dyes D131 (R_1), D102 (R_2), and D149 (R_3).

One of the simplest indoline-based dyes is the D131 molecule (CAS Number: 652145-29-4) (see Fig.3.10). It absorbs light in the visible region, however, the main absorption pick is localized in the blue region[44]. The goal was to extend the UV-vis absorption spectra of the D131 dyes to the red side. In consequence, the D102 (CAS number [652145-28-3][47]) and D149 (CAS Number: [786643-20-7]) molecules were synthesized (see Fig. 3.10). The D131, D102, and D149 molecules share the same electron donor unit (i.e. a substituted indoline) while three different acceptors are used: a cyanoacrylic acid group in the case of D131, one rhodanine for D102 and rhodanine dimer for D149. In all cases, the anchoring group is a carboxylate either directly linked (D131) or connected by -CH_2 spacer (D102 and D149) to the acceptor moiety. It is worth noting that in all systems the donor and acceptor properties of the indoline unit are enhanced by the presence of a 4-(2,2 diphenylethenyl)phenyl) substituent acting as a donor π conjugated to the indoline ring.

The UV-vis absorption spectra experimentally measured in tert-butyl alcohol/acetylonitryl (1/1) show that the first absorption peak is located at 451 nm, 503 nm, and 532 nm for D131, D102, and D149, respectively[45] (see Fig. 3.11). The dye D102 has a very strong absorption coefficient (55800 $Lmol^{-1}cm^{-1}$ at 419 nm)[46], which is four times stronger than the one of the ruthenium dye N3 (13900 $Lmol^{-1}cm^{-1}$ at 541 nm)[39]. In 2003 Horiuchi, Uchida, and co-workers showed that the power conversion efficiency of D102-based DSSC is 6.1 %[47] but D149 showed a more prominent efficiency equal to 8.0 %[48]. Gratzël et al. achieved 9.0 % efficiency based on D149 by optimizing the TiO_2 electrode thickness[48]. It was proved that the cyanoacrylic acid is an efficient acceptor group but its dual role as both acceptor and anchor group in D131 could favor fast charge recombination thus explaining the lower efficiency of D131-based DSSC compared with D102 and D149[49]. Was shown that the photoconversion efficiency of these dyes strongly depends also on the semiconductor morphology[49]. Howie et al. showed that indoline dyes D102, D131, and D149 attach to the semiconductor surface via bidentate binding and with different orientations (parallel or vertical) to the substrate surface influence the efficiency of DSSCs[50].

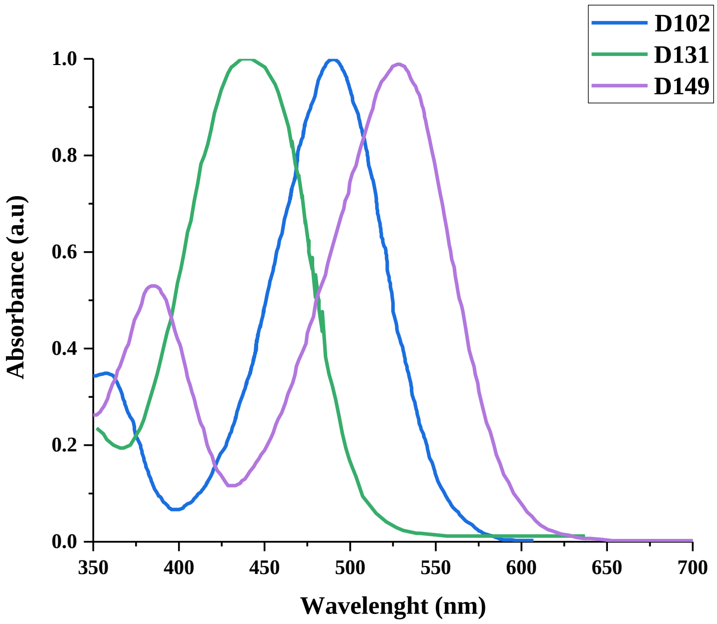

Figure 3.11. Normalized UV-vis absorption spectra measured for indoline dyes D102[39], D131[44], and D149[51] in tert-butyl alcohol/acetylonitryl (1/1) solvent

Unfortunately, was proved that the D102 dye exhibits a strong tendency to form aggregates on the TiO_2 surface[52]. Dye aggregation is generally considered as undesired phenomenon in DSSC, leading to reduced photon-to-current conversion efficiency (IPCE) values under intermolecular excited state quenching[53]. In some limited cases, a controlled aggregation has been proven to enhance the photocurrent generation as a result of the larger spectral window where light is absorbed, possibly combined with an efficient charge transfer from the aggregate excited state to the semiconductor[54]. An appropriate molecular design can prevent in some measure the dye-aggregation on the nanocrystalline-TiO_2 surface, improving the overall photovoltaic performance[55]. Despite the very similar molecular structure of the

D149 and D102, was shown that the D149 exhibits an extremely different response to aggregation on TiO_2 compared with D102[52].

As a general strategy, new efficient dyes should ideally combine sufficiently strong donor and acceptor moieties properly covalently linked to the semiconductor surface via conjugate anchor groups. In this respect, more attention should be paid to the future design of purposely tailored anchoring groups when aiming at rationally increasing the performance of organic dyes for DSC applications. Therefore, in Chapter 7 two different anchoring groups attached to the D102 and D149 molecules will be studied and discussed.

3.3. Literature

[1] O'Regan, B. & Grätzel, M., "A low-cost, high-efficiency solar cell based on dye-sensitized colloidal TiO_2 films." *Nature*, vol.353, pp.737-740, **(1991)**. doi:10.1038/353737a0

[2] Nazeeruddin, M. K., Kay, A., Rodicio, I., Humphry-Baker, R., & Grätzel, M., "Conversion of light to electricity by cis-X2bis (2, 2'-bipyridyl-4, 4'-dicarboxylate) ruthenium (II) charge-transfer sensitizers (X= Cl^-, Br^-, I^-, CN^-, and SCN^-) on nanocrystalline titanium dioxide electrodes." *Journal of the American Chemical Society*, vol.115, no.14, pp.6382-6390, **(1993)**.

[3] Huang, S. Y.; Schlichtho¨rl, G.; Nozik, A. J.; Gra¨tzel, M.; Frank, A., "Charge Nazeeruddin recombination in dye-sensitized nanocrystalline TiO_2 solar cells." *The Journal of Physical Chemistry B*, vol.101, no.14, pp.2576-2582, **(1997)**.

[4] Nazeeruddin, M. K., Zakeeruddin, S. M., Humphry-Baker, R., Jirousek, M., & Grätzel, M., "Acid− Base equilibria of (2, 2 ‘-Bipyridyl-4, 4 ‘-dicarboxylic acid) ruthenium (II) complexes and the effect of protonation on charge-transfer sensitization of nanocrystalline titania." *Inorganic Chemistry*, vol.38, no.26, pp.6298-6305, **(1999)**.

[5] Niedzwiedzki, D. M., "Photophysical properties of N719 and Z907 dyes, benchmark sensitizers for dye-sensitized solar cells, at room and low temperature." *Physical Chemistry Chemical Physics*, vol.23, no.10, pp.6182-6189, **(2021)**.

[6] Joseph, K. V., Anthonysamy, A., Sudhagar, P., Cho, W., & Kim, J. K.. "Ruthenium (II) quasi-solid state dye sensitized solar cells with 8% efficiency using a supramolecular oligomer-based electrolyte." *Journal of Materials Chemistry*, A vol.2, no.33, pp.13338-13344, **(2014)**.

[7] Kroon, J. M., Bakker, N. J., Smit, H. J. P., Liska, P., & Tulloch, G. E., "Nanocrystalline dye-sensitized solar cells having maximum performance." *Progress in Photovoltaics: Research and Applications*, vol.15, no.1, pp.1-18, **(2007)**.

[8] Funaki T, Yanagida M, Onozawa-Komatsuzaki N, Kawanishi Y, & Sugihara H., "Ruthenium (II) complexes with π expanded ligand having phenylene–ethynylene moiety as sensitizers for dye-sensitized solar cells." *Solar Energy Materials and Solar Cells*, vol.93, no.6–7, pp.729–732, **(2009)**.

[9] Nazeeruddin, M. K., Pechy, P., & Grätzel, M., "Efficient panchromatic sensitization of nanocrystalline TiO_2 films by a black dye based on atrithiocyanato–ruthenium complex." *Chemical Communications*, vol.18, pp.1705-1706, **(1997)**.

[10] Wang, P., Zakeeruddin, S. M., Exnar, I., & Grätzel, M., "High efficiency dye-sensitized nanocrystalline solar cells based on ionic liquid polymer gel electrolyte." *Chemical Communications*, vol.24, pp.2972-2973, **(2002)**.

[11] Wang, P., Zakeeruddin, S. M., Moser, J. E., Nazeeruddin, M. K., & Grätzel, M., "A stable quasi-solid-state dye-sensitized solar cell with an amphiphilic ruthenium sensitizer and polymer gel electrolyte." *Nature materials*, vol.2, no.6, pp.402-407, **(2003)**.

[12] Anthonysamy, A., Lee, Y., Karunagaran, B., Ganapathy, V., & Kim, J. K., "Molecular design and synthesis of ruthenium (II) sensitizers for highly efficient dye-sensitized solar cells." *Journal of Materials Chemistry*, vol.21, no.33, pp.12389-12397, **(2011)**.

[13] Arifin, Z., Soeparman, S., Widhiyanuriyawan, D., & Suyitno, S., "Performance Enhancement of Dye-Sensitized Solar Cells Using a Natural Sensitizer." *International Journal of Photoenergy*, vol.2017, pp.1–5, **(2017)**. doi:10.1155/2017/2704864

[14] Boschloo, G., & Hagfeldt, A., "Characteristics of the Iodide/Triiodide Redox Mediator in Dye-Sensitized Solar Cells." *Accounts of Chemical Research*, vol.42, no.11, pp.1819–1826, **(2009)**. doi:10.1021/ar900138m

[15] Latini, A., & Panetta, R., "Test of Different Sensitizing Dyes in Dye-Sensitized Solar Cells Based on Nb_2O_5 Photoanodes." *Energies*, vol.11, no.4, pp.975, **(2018)**.

[16] Islam, A., Sugihara, H., & Arakawa, H., "Molecular design of ruthenium (II) polypyridyl photosensitizers for efficient nanocrystalline TiO_2 solar cells." *Journal of Photochemistry and Photobiology A Chemistry*, vol.158, no.2-3 pp.131-138, **(2003)**.

[17] Gratzel, M., "Photoelectrochemical cells." *Nature*, vol.414, no.6861, pp.338-345, **(2001)**.

[18] Rillema, D. P., Allen, G., Meyer, T. J., & Conrad, D., "Redox properties of ruthenium (II) tris chelate complexes containing the ligands 2, 2'-bipyrazine, 2, 2'-bipyridine, and 2, 2'-bipyrimidine." *Inorganic chemistry*, vol.22, no.11, pp.1617-1622, **(1983)**.

[19] Davison, T. W., "Ruthenium complexes of new heterocyclic ligands." **(2014).**

[20] Teplý, F., "Photoredox catalysis by $[Ru(bpy)_3]^{2+}$ to trigger transformations of organic molecules. Organic synthesis using visible-light photocatalysis and its 20th century roots." *Collection of Czechoslovak Chemical Communications*, vol.76, no.7, pp.859-917, **(2011)**.

[21] Kalyanasundaram, K., "Photophysics, photochemistry and solar energy conversion with tris(bipyridyl)ruthenium(II) and its analogues." *Coordination Chemistry Reviews*, vol.46, pp.159–244, **(1982)**.

[22] Campagna, S.; Puntoriero, F.; Nastasi, F.; Bergamini, G.; & Balzani, V., "Photochemistry and photophysics of coordination compounds: Ruthenium." *Topics in Current Chemistry*, vol.280, pp.117–214, **(2007)**.

[23] Rillema, D. P., Jones, D. S., Woods, C., & Levy, H. A., "Comparison of the crystal structures of tris heterocyclic ligand complexes of ruthenium (II)." *Inorganic Chemistry*, vol.31, no.13, pp.2935-2938, **(1992)**.

[24] Durham, B., Caspar, J. V., Nagle, J. K., & Meyer, T. J., "Photochemistry of tris (2, 2'-bipyridine) ruthenium (2^+) ion." *Journal of the American Chemical Society*, vol.104, no.18, pp.4803-4810, **(1982)**.

[25] Crutchley, R. J., & Lever, A. B. P., "Comparative chemistry of bipyrazyl and bipyridyl metal complexes: spectroscopy, electrochemistry and photoanation." *Inorganic Chemistry*, vol.21, no.6, pp.2276-2282, **(1982)**.

[26] Rillema, D. P., Allen, G., Meyer, T. J., & Conrad, D.,"Redox properties of ruthenium (II) tris chelate complexes containing the ligands 2, 2'-bipyrazine, 2, 2'-bipyridine, and 2, 2'-bipyrimidine." *Inorganic chemistry*, vol.22, no.11, pp.1617-1622, **(1983)**.

[27] Mongey, K., "Photophysics of mixed-ligand polypyridyl ruthenium (II) complexesimmobilised in silica sol–gel monoliths." *Journal of Materials Chemistry*, vol.7, no.8, pp.1473-1479, **(1997)**.

[28] Wu, X., Collins, J. E., McAlvin, J. E., Cutts, R. W., & Fraser, C. L., "Ruthenium tris (bipyridine)-centered linear and star-shaped polystyrenes: Making atom transfer radical polymerization and metal complex initiators compatible." *Macromolecules*, vol.34, no.9, pp.2812-2821, **(2001)**.

[29] Johnson, R. M., & Fraser, C. L., "Metalloinitiation routes to biocompatible poly (lactic acid) and poly (acrylic acid) stars with luminescent ruthenium tris (bipyridine) cores." *Biomacromolecules*, vol.5, no.2, pp.580-588, **(2004)**.

[30] Deponti, E., & Natali, M., "Photocatalytic hydrogen evolution with ruthenium polypyridine sensitizers: unveiling the key factors to improve efficiencies." *Dalton Transactions*, vol.45, no.22, pp.9136-9147, **(2016)**.

[31] Salomón, F. F., Vega, N. C., Parella, T., Moran Vieyra, F. E., & Katz, N. E., "Novel Heteroleptic Ruthenium (II) Complexes with 2, 2′-Bipyridines Containing a Series of Electron-Donor and Electron-Acceptor Substituents in 4, 4′-Positions: Syntheses, Characterization, and Application as Sensitizers for ZnO Nanowire-Based Solar Cells. " *ACS omega*, vol.5, no.14, pp.8097-8107, **(2020)**.

[32] Juris, A., Balzani, V., Barigelletti, F., Campagna, S., & von Zelewsky, A. V., "Ru(II) polypyridine complexes: photophysics, photochemistry, eletrochemistry, and chemiluminescence." *Coordination Chemistry Reviews*, vol.84, pp.85−277, **(1988)**.

[33] Hagfeldt, A., & Graetzel, M., "Light-induced redox reactions in nanocrystalline systems." *Chemical reviews*, vol.95, no.1, pp.49-68, **(1995)**.

[34] Kilså, K., Mayo, E. I., Kuciauskas, D., Villahermosa, R., & Gray, H. B., "Effects of bridging ligands on the Current−Potential behavior and interfacial kinetics of ruthenium-sensitized nanocrystalline TiO_2 photoelectrodes." *The Journal of Physical Chemistry*, vol.107, no.18, pp.3379–3383, **(2003)**.

[35] Zalas, M., Gierczyk, B., Bossi, A., Mussini, P. R., & Stampor, W., "The influence of anchoring group position in ruthenium dye molecule on performance of dye-sensitized solar cells." *Dyes and Pigments*, vol.150, pp.335-346, **(2018)**.

[36] Nazeeruddin, M. K., Pechy, P., & Grätzel, M., " Efficient panchromatic sensitization of nanocrystalline TiO_2 films by a black dye based on a trithiocyanato–ruthenium complex." *Chemical Communications*, vol.18, pp.1705-1706, **(1997)**.

[37] Zalas, M., Gierczyk, B., Klein, M., Siuzdak, K., & Łuczak, T., "Synthesis of a novel dinuclear ruthenium polypyridine dye for dye-sensitized solar cells application." *Polyhedron*, vol.67, pp.381-387, **(2014)**.

[38] Veikko, U., Zhang, X., Peng, T., Cai, P., & Cheng, G., "The synthesis and characterization of dinuclear ruthenium sensitizers and their applications in photocatalytic hydrogen production." *Spectrochimica Acta Part A: Molecular and Biomolecular Spectroscopy*, vol.105, pp.539-544, **(2013)**.

[39] Horiuchi, T., Miura, H., & Uchida, S., "Highly-efficient metal-free organic dyes for dye-sensitized solar cells." *Chemical Communications*, vol.24, pp.3036-3037, **(2003)**.

[40] Kuang, D., Uchida, S., Humphry-Baker, R., Zakeeruddin, S. M., & Grätzel, M., "Organic Dye-Sensitized Ionic Liquid Based Solar Cells: Remarkable Enhancement in Performance through Molecular Design of Indoline Sensitizers. " *Angewandte Chemie International Edition*, vol.47, no.10, pp.1923–1927, **(2008)**. doi:10.1002/anie.200705225

[41] Ogura, R. Y., Nakane, S., Morooka, M., Orihashi, M., & Noda, K., "High-performance dye-sensitized solar cell with a multiple dye system." *Applied Physics Letters*, vol.94, no.7, pp.54, **(2009)**.

[42] Ito S., Miura H., Uchida S.,Takata M., & Grätzel M., "High-conversion-efficiency organic dye-sensitized solar cells with a novel indoline dye." *Chemical Communications*, pp.5194–5196, **(2008)**.

[43] Howie, W. H., Claeyssens, F., Miura, H., & Peter, L. M., "Characterization of solid-state dye-sensitized solar cells utilizing high absorption coefficient metal-free organic dyes." *Journal of the American Chemical Society*, vol.130, no.4, pp.1367-1375, **(2008)**.

[44] Ito, S., Dharmadasa, I. M., Tolan, G. J., Roberts, J. S., & Grätzel, M., "High-voltage (1.8 V) tandem solar cell system using a $GaAs/Al_XGa_{(1-X)}As$ graded solar cell and dye-sensitised solar cells with organic dyes having different absorption spectra." *Solar Energy*, vol.85, no.6, pp.1220-1225, **(2011)**.

[45] Wang, B., Li, N., Yang, L., Dall'Agnese, & Wang, X. F. "Organic dye/$Cs_2AgBiBr_6$ double perovskite heterojunction solar cells." *Journal of the American Chemical Society*, vol.143, no.36, pp.14877-14883, **(2021)**. doi:10.1021/jacs.1c07200

[46] Schmidt-Mende, L., Bach, U., Humphry-Baker, R., Horiuchi, T., & Gratzel, M., "Organic Dye for Highly¨ Efficient Solid-State Dye-Sensitized Solar Cells." *Advanced Materials*, vol.17, pp.813−815, **(2005)**.

[47] Horiuchi, T., Miura, H., & Uchida, S., "Highly efficient metal-free organic dyes for dye-sensitized solar cells." *Journal of Photochemistry and Photobiology A: Chemistry*, vol.164, no.(1-3), pp.29–32, **(2004)**. doi:10.1016/j.jphotochem.2003.

[48] Ito, S., Zakeeruddin, S. M., Humphry-Baker, R., Liska, P., & Grätzel, M., "High-efficiency organic-dye-sensitized solar cells controlled by nanocrystalline-TiO_2 electrode thickness." *Advanced Materials*, vol.18, no.9, pp.1202-1205, **(2006)**.

[49] Le Bahers, T., Pauporté, T., Scalmani, G., Adamo, C., & Ciofini, I., "A TD-DFT investigation of ground and excited state properties in indoline dyes used for dye-sensitized solar cells." *Physical chemistry chemical physics*, vol.11, no.47, pp.11276-11284, **(2009)**.

[50] Howie, W. H., Harris, J. E., Jennings, J. R., & Peter, L. M., "Solid-state dye-sensitized solar cells based on spiro-MeOTAD." *Solar energy materials and solar cells*, vol.91, no.5, pp.424-426, **(2007)**.

[51] Cheng, H. M., & Hsieh, W. F., "High-efficiency metal-free organic-dye-sensitized solar cells with hierarchical ZnO photoelectrode." *Energy & Environmental Science*, vol.3, no.4, pp.442-447, **(2010)**.

[52] Pastore, M., & De Angelis, F., "Aggregation of organic dyes on TiO_2 in dye-sensitized solar cells models: an ab initio investigation. " *ACS nano*, vol.4, no.1, pp.556-562, **(2010)**.

[53] Tatay, S., Haque, S. A., O'Regan, B., Durrant, J. R., & Palomares, E., "Kinetic competition in liquid electrolyte and solid-state cyanine dye sensitized solar cells." *Journal of Materials Chemistry,* vol.17, pp.3037–3044, **(2007)**.

[54] Sayama, K., Tsukagoshi, S., Hara, K., Ohga, Y., & Arakawa, H., "Photoelectrochemical properties of J aggregates of benzothiazole merocyanine dyes on a nanostructured TiO_2 film." *The Journal of Physical Chemistry B*, vol.106, pp.1363–1371, **(2002)**.

[55] Khazraji, A. C., Hotchandani, S., Das, S., & Kamat, P. V., "Controlling dye (merocyanine-540) aggregation on nanostructured TiO_2 films. An organized assembly approach for enhancing the efficiency of photosensitization." *The Journal of Physical Chemistry B,* vol.103, pp.4693–4700, **(1999)**.

Chapter 4

THEORETICAL BACKGROUNDS OF QUANTUM CHEMICAL CALCULATIONS

Quantum chemical calculations are very powerful and efficient instruments in modern physics. Using computer modeling one can predict the physical and chemical properties of many different materials without experimental insight. They can be: 0D molekules and clusters, 1D nonotubes and nanovires, 2D layers and surfaces, and 3D crystals. In the mentioned approach important is that depending on the chosen quantum chemical methods the obtained data should be close to the experimental results.

In the present chapter, various kinds of methods used in quantum chemical calculations will be presented. Mostly I will focus on the methods used in preparing the research reported in this work.

4.1. *Ab initio* methodology

All quantum chemical methods are based on different approaches to solving the Schrödinger equation giving information about the physicochemical properties of the atom system. Some of them use experimental parameters to faster the calculation procedures but others do not. The term *ab initio* means *from first principles* or *from the beginning*. Robert Parr and coworkers used the first time this term 70 years ago[1]. Their method was based on the approach that the Schrödinger equation can have a form as follows:

$$\hat{H}\Psi_s(\vec{r},\vec{R}) = E_s\Psi_s(\vec{r},\vec{R}), \tag{4.1}$$

where $\hat{H}$ is the Hamiltonian operator of the full energy of the system, $\vec{r}$ means electron, and $\vec{R}$ denotes nuclear position. In the case when the Hamiltonian operator is time-dependent the Schrödinger equation has the form:

$$\hat{H}\Psi_s(\vec{r},\vec{R},t) = i\hbar\frac{\partial\Psi_s(\vec{r},\vec{R},t)}{\partial t} \ . \tag{4.2}$$

In equations (4.1) and (4.2) the Ψ_s denotes a function describing stationary states *s* of atomic structure with energy E_s. The Hamiltonian is characterized by the relation:

$$\begin{aligned} H = &-\frac{\hbar^2}{2m_i}\sum_i \nabla_i^2 - \sum_A \frac{\hbar^2}{2M_A}\nabla_A^2 + \sum_{i>j=1}\frac{1}{4\pi\varepsilon_0}\frac{e^2}{\left|\vec{r}_i-\vec{r}_j\right|} - \\ &-\sum_{i,A}\frac{1}{4\pi\varepsilon_0}\frac{Z_A e^2}{\left|\vec{r}_i-\vec{R}_A\right|} + \sum_{A,B}\frac{1}{4\pi\varepsilon_0}\frac{Z_A Z_B}{\left|\vec{R}_A-\vec{R}_B\right|} \end{aligned} \quad . \tag{4.3}$$

In consequence, the Schrödinger equation can be presented in more compact notation:

$$\left[\hat{T}_e(\vec{r}) + \hat{T}_N(\vec{R}) + \hat{V}_{ee}(\vec{r}) + \hat{V}_{eN}(\vec{r},\vec{R}) + \hat{V}_{NN}(\vec{R})\right]\Psi_s(\vec{r},\vec{R}) = E_s\Psi_s(\vec{r},\vec{R}), \tag{4.4}$$

where the operator of the kinetic energy of electrons $\hat{T}_e(\vec{r})$, the kinetic energy of nuclei $\hat{T}_N(\vec{R})$, and three operators of potential energy are used $\hat{V}_{ee}(\vec{r}), \hat{V}_{eN}(\vec{r},\vec{R}), \hat{V}_{NN}(\vec{R})$. These operators describe electron-electron, electron-nucleus, and nucleus-nucleus interactions in the studied atomic system. The M_A means mass of the nucleus *A*, m_i is the mass of electron *i*, $\nabla_i^2 = \frac{\partial^2}{\partial x_i^2} + \frac{\partial^2}{\partial y_i^2} + \frac{\partial^2}{\partial z_i^2}$ and $\nabla_A^2 = \frac{\partial^2}{\partial x_A^2} + \frac{\partial^2}{\partial y_A^2} + \frac{\partial^2}{\partial z_A^2}$.

The equation (4.2) is possible to be solved for very simple models such as particles in a potential well, harmonic oscillator, and hydrogen atom. One of the possible solutions to this problem is to use approximations. One of the critical is the Born-Oppenheimer approximation^2 separating electrons and nuclei into two parts of the system. The Born-Oppenheimer approximation allows us to describe the atom system by multiplication of wave functions devoted to the electron and nuclei systems. The new wave function takes the form:

$$\Psi(\vec{r},\vec{R}) = \psi_p(\vec{r},\vec{R}) f_p(\vec{R}), \tag{4.5}$$

where $\psi_p(\vec{r},\vec{R})$ is the electron wave function depending on the electron position and parametrically depending on nuclei position. The $f_p(\vec{R})$ nuclear wave function depends only on nuclei position.

In consequence, the Schrödinger equation can be separated into an electron and nuclear part, respectively:

$$\hat{H}^e(\vec{r},\vec{R})\phi_p(\vec{r},\vec{R}) = E^e_p(\vec{r},\vec{R})\phi_p(\vec{r},\vec{R})$$

$$\text{where } \hat{H}^e(\vec{r},\vec{R}) = -\frac{1}{2m_i}\sum_i \nabla_i^2 + \sum_{i>j=1}\frac{1}{4\pi\varepsilon_0}\frac{e^2}{\left|\vec{r}_i-\vec{r}_j\right|} - \sum_{i,A}\frac{1}{4\pi\varepsilon_0}\frac{Z_A e^2}{\left|\vec{r}_i-\vec{R}_A\right|} \quad , \qquad (4.6)$$

and

$$\hat{H}^N(\vec{R}) f_p(\vec{R}) = E^{tot}_p f_p(\vec{R})$$

$$\text{where } \hat{H}^N = -\sum_A \frac{\hbar^2}{2M_A}\nabla_A^2 + E^e(\vec{R}) + E_{ad}(\vec{R}) \quad . \qquad (4.7)$$

In equation (4.7) the $E^e(\vec{R})$ is the effective potential energy of nuclei in a specific constrained configuration and $E_{ad}(\vec{R})$ is the average value of kinetic energy of moving nuclei. Because the energy $E_{ad}(\vec{R})$ is very small it can be removed from the equation (4.7). It is the main idea of the Born-Oppenheimer approximation.

The electron part of the Schrödinger equation (4.6) can be solved in the *ab initio* approach only for one electron system. The Hartree-Fock approximation allows describing a multielectron system by one electron structure interacting with surrounding electrons. For that, the electron wave function is transferred into spinorbial:

$$\phi_i = \varphi_o \sigma_{m_s} \ , \qquad (4.8)$$

where φ_o is the orbital function and σ_{m_s} is the spin function (spin up or spin down). Taking into account the Pauli principle the N-electron system can be characterized by the Slater determinant:

$$\Psi = \frac{1}{N}\begin{vmatrix} \phi_1(1) & \phi_1(2) & \dots & \phi_1(N) \\ \phi_2(1) & \phi_2(2) & \dots & \phi_2(N) \\ \dots & \dots & \dots & \dots \\ \phi_N(1) & \phi_N(2) & \dots & \phi_N(N) \end{vmatrix} \qquad (4.9)$$

Representing electron wave functions in the form of the Slater determinant, the electron moves independently in the effective field created by the Coulomb repulsion of all other electrons and nuclei. The Slater determinant describes well the system possessing the same number of electrons with spins up and spins down. In this case, for the closed-shell system, the restricted Hartree-Fock (RHF) method is used. For the system where the number of spin-up electrons is not equal to the spin-down electrons (the open-shell system), the unrestricted Hartree-Fock (UHF) method is used.

In the Hartree-Fock approach, the energy of the electron system can be calculated by form:

$$\langle E\rangle = 2\sum_{\mu=1}^{n/2} I_{\mu\mu} + \sum_{\mu>\nu=1}^{n/2}(2J_{\mu\nu} - K_{\mu\nu}), \tag{4.10}$$

where

$$I_{\mu\mu} = \int \varphi_{\mu}^{*}(i)\hat{h}(i)\varphi_{\mu}(i)dv_i, \tag{4.11}$$

and the $\hat{h}$ is one electron Hamiltonian described by the formula:

$$\hat{h}(i) = -\frac{\hbar^2}{2m_i}\nabla_i^2 - \frac{1}{4\pi\varepsilon_0}\sum^{A}\frac{eZ_A}{r_i - R_A} \quad . \tag{4.12}$$

The second part of the equation (4.10) describes the interelectron interaction in a multi-electron system. The $J_{\mu\nu}$ is called Coulomb integral operating for the *i* and *j* electrons possessing μ and ν quantum states, respectively with form:

$$J_{\mu\nu} = \frac{1}{4\pi\varepsilon_0}\iint \varphi_{\mu}^{*}(i)\varphi_{\nu}^{*}(j)\frac{1}{r_i - r_j}\varphi_{\mu}(i)\varphi_{\nu}(j)dv_i dv_j . \tag{4.13}$$

The second part of the two-electron formula is called the exchange integral possessing the form:

$$K_{\mu\nu} = \frac{1}{4\pi\varepsilon_0}\iint \varphi_{\mu}^{*}(i)\varphi_{\nu}^{*}(j)\frac{1}{r_i - r_j}\varphi_{\mu}(j)\varphi_{\nu}(i)dv_i dv_j . \tag{4.14}$$

The description of electrons in molecules is carried out using the linear combination of atomic orbitals method (LCAO). According to molecular orbital theory, all the atomic orbitals of combining atoms first mix to form a new set of orbitals called molecular orbitals. Once the molecular orbitals are formed, the combing atoms lose their identity as atomic orbitals. According to the Ritz method, each atomic orbital is described by a linear combination of well know atomic orbitals ψ_i with the variation parameters C_i:

$$\psi = C_1\psi_1 + C_2\psi_2 + .. + C_n\psi_n \tag{4.15}$$

For a correct description of the molecular orbitals, the lowest energy of the electron system should be found. It is performed by the variation method, where:

$$\langle E_s\rangle = \frac{\int \psi^{*}\hat{H}_e\psi d\tau}{\int \psi^{*}\psi d\tau} \geq E_0 . \tag{4.16}$$

Important is that the obtained energy is higher than the true energy of the ground state of the investigated system. The variation parameters are changing until to get energy within the given functional space. In consequence, it can be found by reaching the statement that:

$$\left(\frac{\partial \langle E_s \rangle}{\partial C_i} \right) = 0, \qquad i = 1..n \tag{4.17}$$

4.2 Methodology of the density functional theory (DFT)

4.2.1. The Hohenberg-Kohn theorem

The density functional theory (DFT) is based on Hohenberg and Kohn's work presented in Physical Review in 1964[3]. The first Hohenberg-Kohn theorem says that the ground states of each interacting many-particle system with a given fixed inter-particle interaction can be characterized by a unique function of an electron density[4]. It has the form:

Theorem I: *The external potential* $V_{ext}(\vec{r})$ *and the total energy of the system is a unique functional of electron density* $\rho(\vec{r})$.

The assumed proof of this theorem is based on two existing potentials $V_{ext_1}(\vec{r})$ and $V_{ext_2}(\vec{r})$. They should differ one from the other and should give rise to the same ground-state density $\rho(\vec{r})$. Those two external potentials belong to two Hamiltonians: $\hat{H}_1 = \hat{T} + \hat{V}_{ee} + \hat{V}_{ext_1}$ and $\hat{H}_2 = \hat{T} + \hat{V}_{ee} + \hat{V}_{ext_2}$. These Hamiltonians represent two different ground state wave functions Ψ_1 and Ψ_2 with different state energies E_{0_1} and E_{0_2} (where $E_{0_1} \neq E_{0_2}$). It is plausible that two Hamiltonians represent the same electron density. Let's create its schematic representation:

$$V_{ext_1}(\vec{r}) \Rightarrow \hat{H}_1 \Rightarrow \Psi_1 \Rightarrow \rho(\vec{r}) \Leftarrow \Psi_2 \Leftarrow \hat{H}_2 \Leftarrow V_{ext_2}(\vec{r}) \tag{4.18}$$

Let's use bra-ket notation representation of Hamiltonian with variational principles:

$$E_{0_1} < \left\langle \Psi_2 \middle| \hat{H}_1 \middle| \Psi_2 \right\rangle = \left\langle \Psi_2 \middle| \hat{H}_2 \middle| \Psi_2 \right\rangle - \left\langle \Psi_2 \middle| \hat{H}_1 - \hat{H}_2 \middle| \Psi_2 \right\rangle . \tag{4.19}$$

When two Hamiltonians $\hat{H}_1$ and $\hat{H}_2$ have differences only in external potentials one can write equation (4.19) in the form:

$$E_{0_1} < E_{0_2} + \left\langle \Psi_2 \middle| \hat{V}_{ext_1} - \hat{V}_{ext_2} \middle| \Psi_2 \right\rangle , \tag{4.20}$$

or

$$E_{0_1} < E_{0_2} + \int \rho(\vec{r})\left\{\hat{V}_{ext_1} - \hat{V}_{ext_2}\right\} d\vec{r}\ ; \qquad (4.21)$$

where $E_{0_1} < E_{0_2} + E_{0_1} - E_{0_2} \Rightarrow E_{0_1} < E_{0_1}$ or $E_{0_1} + E_{0_2} < E_{0_2} + E_{0_1} \Rightarrow 0 < 0$. (4.22)

It proves that for the one ground-state electron density there is only one external potential ($\rho_1(\vec{r}) \Rightarrow \exists! V_{ext_1}(\vec{r})$). One can summarize that $\rho_0(\vec{r})$ consists of all important information about the state $\rho_0 \Rightarrow \hat{H} \Rightarrow \Psi_0 \Rightarrow E_0$:

$$E_0(\rho_0) = T_e(\rho_0) + E_{ee}(\rho_0) + E_{eN}(\rho_0)\,. \qquad (4.23)$$

The form (4.23) can be separated into two parts dependent on the system nuclear-electron attraction $E_{eN}(\rho_0)$ and the universal part $T_e(\rho_0) + E_{ee}(\rho_0)$

$$E_0(\rho_0) = \underbrace{T_e(\rho_0) + E_{ee}(\rho_0)}_{\text{universal}} + \underbrace{E_{eN}(\rho_0)}_{\text{system dependet}}\ . \qquad (4.24)$$

The independent part of (4.24) can be represented by the new quality Hohenberg-Koch functional $\left(E_{HK}(\rho_0) = T_e(\rho_0) + E_{ee}(\rho_0)\right)$ consists of the electron kinetic energy and electron-electron interaction energy.

One can conclude that the density of the ground state uniquely determines the Hamiltonian operator, which characterizes the ground and excited states of the system. Formally, all properties of all states are based on ground-state density.

Theorem II: *A universal functional of energy $E(\rho)$ can be defined in terms of density, with the global minimum value of ground states for this functional.*

Or:

For any positive defined trial density $\rho_t(\vec{r})$ such as $\int \rho_t(\vec{r}) d\vec{r} = N$ there is dependency $E(\rho_t) \geq \mathrm{E}_0$.

One can summarize that the properties of the system defined from an external potential V_{ext} are determined by ground-state density. The ground state energy associated with a density ρ is available in the functional $\int \rho(\vec{r}) V_{eN} d\vec{r} + F_{HK}(\rho)$. This functional represents the minimum value of energy when in input parameters the true ground state density was used.

4.2.2. The Kohn-Sham equations

To find accurate energy for the system appropriate approximation of functional F_{HK} and approximation of kinetic energy is needed. Calculation of true kinetic energy is a hard and critical process using accurate approximation. This procedure is solved by the Kohn-Sham method which can represent simply a large part of kinetic energies and electron-electron functional.

Let's introduce a fictitious system of non-interacting N electrons with ground-state density $\rho(\vec{r})=\sum_{i}^{N}\left|\varphi_i(\vec{r})\right|^2$ and a single determinant wave function φ described by the equation:

$$\left[-\frac{1}{2}\nabla^2+V_s(\vec{r})\right]\varphi_i(\vec{r})=\varepsilon_i(\vec{r}), \tag{4.25}$$

where $V_s(\vec{r})$ is external potential. According to the Hohenberg-Kohn theorem, this system represents exactly known electron density, kinetic energy, and total energy:

$$T_s=-\frac{1}{2}\sum_{i}^{N}\left\langle\varphi_i\left|\nabla^2\right|\varphi_i\right\rangle, \tag{4.26}$$

$$E_{V_s}(\rho)=T_s(\rho)+\int\rho(\vec{r})V_s(\vec{r})d\vec{r}\ , \tag{4.27}$$

with an unknown part of the exchange-correlation energy defined as $E_{xs}(\rho)$:

$$E_{xc}(\rho)=F_{HK}(\rho)-\frac{1}{2}\int\frac{\rho(\vec{r}_1)\rho(\vec{r}_2)}{\left|\vec{r}_1-\vec{r}_2\right|}d\vec{r}_1d\vec{r}_2-T_s(\rho). \tag{4.28}$$

According to the idea of the Koch-Sham scheme, one can conclude that for the ground state density ρ of an interacting system, the non-interacting system exists possessing the same ground state density. Using that fact, the equation for interacting and non-interacting systems solves for the same density:

$$V_s(\vec{r})=V(\vec{r})+\int\frac{\rho((\vec{r}\,')}{\left|\vec{r}-\vec{r}\,'\right|}d(\vec{r}\,')+V_{xc}\left(\rho\right), \tag{4.29}$$

and

$$\left[-\frac{1}{2}\nabla^2+V(\vec{r})+\int\frac{\rho((\vec{r}\,')}{\left|\vec{r}-\vec{r}\,'\right|}d(\vec{r}\,')+V_{xc}\left(\rho\right)\right]\varphi_i(\vec{r})=\varepsilon_i(\vec{r}). \tag{4.30}$$

Important is that the kinetic energy of the real interacting system $T(\rho)=\left\langle\varphi(\rho)\left|\hat{T}\right|\varphi(\rho)\right\rangle$ is not equal to the kinetic energy of the non-interacting system $T_s(\rho)$ even when both systems have the same ground-state density ρ. It follows the form:

$$\begin{gathered}\left\langle \varphi(\rho)\left|\hat{T}\right|\varphi(\rho)\right\rangle + \int \rho(\vec{r})V_s(\vec{r})d\vec{r} = \left\langle \varphi(\rho)\left|\hat{H}\right|\varphi(\rho)\right\rangle \geq \\ \geq \left\langle \varphi_s(\rho)\left|\hat{H}_s\right|\varphi_s(\rho)\right\rangle = \hat{T}_s + \int \rho(\vec{r})V_s(\vec{r})d\vec{r}\end{gathered} \quad , \qquad (4.31)$$

where φ_s and $\hat{H}_s$ are Kohn-Sham determinant and Hamiltonian, respectively. The $T(\rho) \geq T_s(\rho)$ and exchange-correlation part of kinetic energy is $T_{xs}(\rho) = T(\rho) - T_s(\rho)$.

4.2.3. The LDA and GGA approximation

The simplest and most often used approximation of exchange-correlation energy is local density approximation (LDA). It is based on the idea of the homogeneous electron gas $e_{xc}^{\hom}(\rho_0)$ dependent on homogeneous density ρ_0:

$$E_{xc}^{LDA}(\rho(\vec{r})) = e_{xc}^{\hom}(\rho_0)\Big|_{\rho_0=\rho(\vec{r})} . \qquad (4.32)$$

In the case of the not homogenous system density has linear causing $\rho(\vec{r})$ and exchange-correlation energy functional is characterized as:

$$E_{xc}^{LDA}(\rho) = \int e_{xc}^{\hom}(\rho(\vec{r})d\vec{r} . \qquad (4.33)$$

The mentioned approximation works correctly in the case of computer modeling of the electron densities for 1D structures as atoms and molecules. It works also for systems with low varying densities as it is observed for metals.

The quantity $e_{xc}(\rho(\vec{r}))$ can be split into the exchange and correlation parts:

$$e_{xc}(\rho(\vec{r})) = e_x(\rho(\vec{r})) + e_c(\rho(\vec{r})) . \qquad (4.34)$$

The exchange part e_x represents the exchange energy of the investigated system (electrons). It is an equal form to the Hartree-Fock exchange found in the Slater approximation:

$$e_x = -\frac{3}{4}(\frac{3}{\pi})^{\frac{1}{3}} \int \rho(\vec{r})^{\frac{4}{3}} d(\vec{r}) . \qquad (4.35)$$

Important is that there is no such explicit expression to calculate the correlation part e_c. Various authors have presented an analytic expression of e_c based on a sophisticated interpolation scheme. From a historical point of view, the first widely used representation of e_c was developed by Vosko, Wilk, and Nussair in 1980. Another known representation of e_c was given by Perdew and Wang in 1992. Their approximation uses the homogeneous electron gas obtained in random phase approximation (PRA) to describe the correlation energy density.

In the case of the unrestricted version, two spin densities $\rho_\alpha(\vec{r})$ and $\rho_\beta(\vec{r})$ are used, where $\rho(\vec{r}) = \rho_\alpha(\vec{r}) + \rho_\beta(\vec{r})$. In consequence, the local spin density approximation (LSD) is characterized as:

$$E_{xc}^{LSD}(\rho_\alpha, \rho_\beta) = \int \varepsilon_{xc}(\rho_\alpha(\vec{r}), \rho_\beta(\vec{r}))d\vec{r}\,. \tag{4.36}$$

In the case of spin compensated situation the $\rho_\alpha(\vec{r}) = \rho_\beta(\vec{r}) = \frac{1}{2}\rho(\vec{r})$. However, when $\rho_\alpha(\vec{r}) \neq \rho_\beta(\vec{r})$ the spin-polarized case should be implemented. The degree of spin polarization is often measured through the spin-polarized parameter:

$$\zeta = \frac{\rho_\alpha(\vec{r}) - \rho_\beta(\vec{r})}{\rho(\vec{r})}, \tag{4.37}$$

where the ζ attains values from 0 (spin compensated) to 1 (fully spin-polarized).

The LDA approximation does not work correctly for all atomic systems. The first logical step to obtaining better accuracy of calculation is to use not only information about density $\rho(\vec{r})$ at a particular point $\vec{r}$, but although have information about the gradient of charge density $\nabla\rho(\vec{r})$. This form better represents the properties of true electron charge density (inhomogeneous charge gas). In other words, using the first term of Taylor expansion of uniform density is expected to get a better approximation to the exchange-correlation functional. This form of functional is called gradient expansion approximation(GEA):

$$E_{xc}^{GEA}(\rho_\alpha, \rho_\beta) = \int \rho\varepsilon_{xc}(\rho_\alpha, \rho_\beta)d\vec{r} + \sum_{\alpha,\beta}\int C_{xc}(\rho_\alpha, \rho_\beta)\frac{\nabla\rho_\alpha}{\rho^{2/3}{}_\alpha}\frac{\nabla\rho_\beta}{\rho^{2/3}{}_\beta}d\vec{r} + .., \tag{4.38}$$

where

$$E_{xc}^{GEA}(\rho_\alpha, \rho_\beta) = E_x^{LSD}(\rho_\alpha, \rho_\beta) + b\int \frac{\nabla\rho_\alpha}{\rho^{2/3}{}_\alpha}\frac{\nabla\rho_\beta}{\rho^{2/3}{}_\beta}d\vec{r} + .. \quad , \tag{4.39}$$

or

$$E_{xc}^{GEA}(\rho_\alpha, \rho_\beta) = E_c^{LSD}(\rho_\alpha, \rho_\beta) + \int C(\rho_\alpha, \rho_\beta)\frac{\nabla\rho_\alpha}{\rho^{2/3}{}_\alpha}\frac{\nabla\rho_\beta}{\rho^{2/3}{}_\beta}d\vec{r} + \ldots \tag{4.40}$$

Here b is the constant and $C(\rho_\alpha, \rho_\beta)$ is a function response to the theory. Unfortunately trying to solve real molecular systems the big problems of GEA in many cases are shown. It shows even worse results than a typical simple LDA approximation. One of the reasons for this failure is that analysis of the gradient expansion shows that its short-range part, near the electron, is represented well by the gradient expansion, but the long-range part is considerably worsened.

The mentioned problem was solved by implementing the generalized gradient approximation (GGA):

$$E_{xc}^{GGA}(\rho_\alpha,\rho_\beta)=\int f(\rho_\alpha,\rho_\beta,\nabla\rho_\alpha,\nabla\rho_\beta)d\vec{r}\ . \tag{4.41}$$

In practice the E_{xc}^{GGA} is usually split into the exchange and correlation parts:

$$E_{xc}^{GGA}=E_{x}^{GGA}+E_{c}^{GGA}\ , \tag{4.42}$$

and they are sought individually. The gradient corrected exchange functional is defined as:

$$E_{x}^{GGA}=E_{x}^{LDA}-\sum_{\sigma}\int F_x(s_\sigma)\rho_\sigma^{4/3}(\vec{r})d(\vec{r})\,, \tag{4.43}$$

where s_σ is the reduced density gradient:

$$s_\sigma(\vec{r})=\frac{\left|\nabla\rho_\sigma(\vec{r})\right|}{\rho_\sigma^{4/3}(\vec{r})}\quad . \tag{4.44}$$

$F_x(s_\sigma)$ is the exchange enhancement factor dependent on the reduced density gradient for GGA. It is a measure of the density inhomogeneity. In consequence, the s_σ is a local inhomogeneous parameter, which assumed large values not only for the large gradient but although regions with small densities such as exponential tails far from the nuclei. In the case of homogenous electron gas $s_\sigma = 0$ everywhere.

4.2.4. Perdew-Burke-Ernzerhof (PBE) functional

The GGA functionals can be divided into two groups: the functionals that contain empirical parameters whose values have been fitted to reproduce experiments or more accurate calculations and the functionals with non-empirically determined parameters. An example of a non-empirical GGA functional is the Perdew-Burke-Ernzerhof (PBE) functional. The enhancement factor of the exchange functional mentioned in (4.43.) applied to PBE methodology takes the form[5]:

$$E_x^{PBE}(s)=1+\kappa-\frac{\kappa}{\left(1+\frac{\mu}{\kappa}s^2\right)}\ , \tag{4.45}$$

where $\kappa = 0.804$ and $\mu = 0.21951$.

PBE yields reasonably accurate atomization energies for molecules while providing generally at least comparable predictions of properties for solids in comparison with LSDA. PBE usually generates too-long lattice constants for solids, with about equal but opposite errors compared with the LSDA.

4.2.5. The B3LYP hybrid functional

Some of the interactions, for example, the vdW interactions are non-local and their properties cannot be predicted at the level of LDA approximation. Semilocal GGA, which depends only on the density and its gradient, cannot describe the long-range correlation-induced interactions. In consequence, the semilocal XC approximations cannot describe in detail many nonlocal features. A simple way to develop nonlocal XC functionals is to use physically motivated orbital-free nonlocal ingredients, such as exchange-hole models[6,7] or the reduced Hartree potential[8], and hybridize a semilocal approximation with the exact exchange functional.

The Becke-3–Lee–Yang–Parr (B3LYP) functional, which minimally fits experimental data, is the most popular functional in chemistry. It belongs to the hybrid functionals. It is based on GGA calculating exchange energy according to Beck functional (B3) and correlation energy according to Lee, Yang, and Parra (LYP) functional. The B3LYP functional is presented as:

$$E_{XC}^{B3LYP} = (1 - a_0)E_X^{LSDA} + a_0 E_{HF}^{HF} + a_x E_x^{B88} + \\ + a_c E_C^{LYP\,88} + (1 - a_c)E_C^{VWN\,80}\,. \tag{4.46}$$

The E_x^{B88} is Becke's gradient correction to the exchange functional. The suggested coefficients present in (4.46) are equal to $a_0 = 0.2, a_x = 0.72, a_c = 0.81$. The VWN local correlation expression has been used to provide the different coefficients of local and gradient-corrected correlation functionals. The B3LYP hybrid functional works well calculating vibrational frequencies and UV-vis spectra of the molecules[9]. It is commonly used because it gives a good compromise between computational cost and the accuracy of results.

4.2.6. The long-range corrected BLYP functional (LC-BLYP)

DFT methods have a problem reproducing Rydberg excitation energies, oscillator strengths, and charge-transfer excitation mainly in organic molecules.

The calculations of charge-transfer excitation energies by employing B3LYP functional show that they are significantly underestimated with increasing intermolecular distance[10]. It suggests that in mentioned case the exchange-correlation functional should be created concerning the charge-transfer problem. While charge transfer is based on single excitation that is taken into consideration in the HF wave function, it is assumed that this failure may come from the insufficient long-range exchange effect in the exchange functionals[11]. Especially, for this reason, the functionals named long-correlated (LC) were developed. The LC scheme integrates the long-range orbital-orbital interaction part in the exchange functional combined with the HF exchange integral. Tsuneda and co-workers[12] present this deficiency through the Ewald split of r_{12}^{-1}:

$$\frac{1}{r_{12}} = \frac{1-\mathrm{erf}(\mu r_{12})}{r_{12}} + \frac{\mathrm{erf}(\mu r_{12})}{r_{12}}, \tag{4.47}$$

where the first term presents the short-range interaction and the second accounts for the long-range interaction. The $r_{12} = |r_1 - r_2|$ is a coordinate vector of electron distribution and μ is a parameter that defines the separation of the short and long parts. The short-range part of the exchange interaction is implemented by modification of the usual exchange functional form $E_x = -(1/2)\ \sum_\sigma \int \rho_\sigma^{4/3}\ K_\sigma d^3r$, into:

$$E_x^{sr} = -\frac{1}{2}\sum_\sigma \int \rho_\sigma^{4/3} K_\sigma \left\{ \begin{matrix} 1 - \frac{8}{3} a_\sigma \cdot \\ \cdot \left[\sqrt{\pi}\, erf\left(\frac{1}{2a_\sigma}\right) + 2a_\sigma(b_\sigma - c_\sigma)\right] \end{matrix} \right\} d^3r\,, \tag{4.48}$$

where a_σ, b_σ and c_σ are:

$$a_\sigma = \frac{\mu K_\sigma^{1/2}}{6\sqrt{\pi}\rho_\sigma^{1/3}}, \qquad b_\sigma = \exp\left(-\frac{1}{4a_\sigma^2}\right) - 1\,, \quad c_\sigma = 2a_\sigma^2 b_\sigma + \frac{1}{2}. \tag{4.49}$$

The part *erf*(μr_{12}) has been multiplied by the square of the one-particle density matrix for the uniform electron gas and then integrated. The K_σ allows the incorporation of generalized gradient approximation functionals. The long-range part of the exchange interaction is presented by the HF exchange integral:

$$E_x^{lr} = -\frac{1}{2}\sum_\sigma \sum_i^{occ} \sum_j^{occ} \int\int \psi_{i\sigma}^*(r_1)\psi_{j\sigma}^*(r_1) \cdot$$

$$\cdot \frac{\mathrm{erf}\ (\mu r_{12}}{r_{12}} \psi_{i\sigma}(r_2)\psi_{j\sigma}(r_2) d^3r_1 d^3r_2 \qquad , \tag{4.50}$$

where $\psi_{i\sigma}$ is the *i*th σ-spin molecular orbital.

When μ is equal to zero, the LC-DFT calculation responds to the pure DFT calculation, and when $\mu = \infty$ the calculations correspond to the standard HF calculation. Tsuneda has shown that the LC method with μ = 0.33 provides well results for most of the investigated phenomena[11]. The LC functional gives more accurate excitation energies compared to results obtained by the B3LYP functional. It can be confirmed that the accurate LC results may be due to the long-range correction rather than the hybridization of the HF exchange integral[13]. Another important advantage of the LC-DFT is the accurate description of orbital energies[12].

4.2.7. Hubbard correction method

The DFT methodology augmented by Hubbard parameters (DFT+U) was introduced by Anisimov et al.[14] In the developed model a correction of localized states in LDA approximation is implemented and the DFT energy functional is extended by Hubbard parameters:

$$E_{DFT+U}[\rho(r)] = E_{DFT}[\rho(r)] + E_{HUB}^{I}\left[\left\{n_{mm'}^{I\sigma}\right\}\right] - E_{DC}^{I}\left[\left\{n_{mm'}^{I\sigma}\right\}\right] \tag{4.51}$$

where E_{DFT} represents the DFT total energy of an electron system, E_{HUB}^{I} is the Hubbard interaction energy of the localized correlated orbitals (typically localized d or f orbitals) of an atom I, E_{DC}^{I} is the approximated DFT interaction energy of the orbitals which must be subtracted to avoid double counting of the electron interaction occurring at the corrected orbitals. The σ denotes a spin.

The DFT+U theory is designed to give the self-energy correction to localized states embedded in delocalized states. The localized states are characterized by a large Coulomb correlation that is accounted for using the U-term whereas the delocalized states are well described by the LDA or GGA approximations. It was shown that a band gap value and lattice parameters of semiconductors calculated by the DFT+U method can be comparable to experimentally obtained data contrary to semilocal functionals. Changing the correlation energy U and the energy-level separation, the system undergoes a transition between the ionic and Mott insulating phase[15]. The extended Hubbard correction can significantly improve the description of the oxide semiconductors concerning GGA approximation, providing a more accurate estimation of the structural and electronic properties.

4.3. Plane-wave method

There are many possible ways to solve the Kohn-Shame equations. However, since Slater first proposed in 1937[16] the augmented plane wave method (APW) it has started to be one of the most popular methods to solve the electronic structure of solids using density functional theory. It is worth saying that at present, the APW is not practically used but it is important for the development of the LAPW and APW+mo methods.

In regions far away from the nuclei, electrons are described by plane waves. Electrons near nuclei can be described more efficiently by atomic functional. Therefore, all APW descendent methods divide space into two regions: a sphere with a radius r_{MT} surrounding each atom (Muffin Tin sphere) and an interstitial region (I). For a system with one atom per unit cell, the wave function can be characterized as: [17]

$$\phi_{\vec{G}}^{APW}(\vec{r},\vec{k}) = \begin{cases} e^{ik_G\vec{r}} & \vec{r} \in I \\ \sum_L a_L^{k_{\vec{G}}} u_L(r,E) Y_L(\hat{r}) & \vec{r} \in MT \end{cases}, \tag{4.52}$$

where $\vec{G}$ is the reciprocal lattice vector, $\vec{k}$ is the crystal momentum, and $k_{\vec{G}} = \vec{k} + \vec{G}$. The L is the condensed angular momentum index, and $Y_L(\hat{r})$ are the spherical harmonics. The $a_L^{k_{\vec{G}}}$ coefficients are found by expanding each plane-wave into Bassel functions $j_l(k_{\vec{G}} r_{MT})$ at the MT spheres $r = r_{MT}$, requiring the basis set to be continuous at the sphere boundaries. This yields:

$$a_L^{k_{\vec{G}}} = 4\pi i^l Y_L^*(\hat{k}_{\vec{G}}) \frac{j_l(k_{\vec{G}} r_{MT})}{u_l(r_{MT},E)} . \tag{4.53}$$

While the plane waves are energy independent, the u_l depends on the energy at which the Schrodinger equation is evaluated. For a completely energy-independent basis set, the secular equation should be linear in energy. It is then an easy task to find all the eigenvalues by simply diagonalizing the secular matrix. On the other hand, since the oscillations of the physical wavefunctions can vary strongly with energy, a completely energy-independent basis set must be made very large to describe all eigenstates over a wider energy region. A solution to this problem is a compromise, in which the energy independent within a certain energy region augmented plane waves are made. This will make the secular equation linear within this region. The presented method refers to linearized versions of the APW method

(LAPW). The LAPW basis functions have the same form as the APW basis functions in Eqn. (4.52), but with a different augmentation in the muffin-tin region[18,19]. The main idea of the LPAW is that the basis functions $\dot{u}_L$ in the MT sphere are supplemented by their energy derivatives $\dot{u}_L$ but both u_L and $\dot{u}_L$ are now evaluated at fixed energy.

$$\phi_{\vec{G}}^{LAPW}(\vec{r},\vec{k}) = \begin{cases} e^{ik_G\vec{r}} & \vec{r} \in I \\ \sum_L (a_L^{k_{\vec{G}}} u_L(r,\xi_l) + b_L^{k_{\vec{G}}} \dot{u}_L(r,\xi_l))Y_L(\hat{r}) & \vec{r} \in MT \end{cases} \quad (4.54)$$

where $\dot{u}_L \equiv du_l / dE$. The two coefficients $a_L^{k_{\vec{G}}}$ and $b_L^{k_{\vec{G}}}$ are determined by forcing each basis function across the MT boundary. Hamiltonian became linear to the energy, and all energies of the eigenfunction can be found through one diagonalization of the secular matrix. It means that LAPW increases the number of basis sets compared with the APW, due to the less physical shape of the augmenting functions, and it increases the relatively large secular matrix for comparison with APW. This slower convergence of LAPW, with respect to the number of basis functions, has been well-known since the very first applications of the method[20]. Still, there is no doubt that the LAPW method is a great improvement over the energy-dependent APW method. However, an energy-independent APW basis set alone does not provide enough flexibility to find solutions in the region around the fixed energy parameter. The variational freedom can be improved by using a complimentary basis set consisting of local orbitals for physically important l-quantum numbers i.e. $l \leq 3$. The local orbitals put no extra condition on the APW basis set, and the number of plane waves in the interstitial is therefore unaffected.

Local orbitals were first introduced in the LAPW method to treat semi-core states. They are local in the sense that they are completely confined within the MT spheres[21,22]:

$$\phi_{\vec{G}}^{lo}(\vec{r},\vec{k}) = \begin{cases} 0 & \vec{r} \in I \\ (a_L^{lo} u_L(r,\xi_l) + b_L^{lo} \dot{u}_L(r,\xi_l))Y_L(\hat{r}) & \vec{r} \in MT \end{cases} . \quad (4.55)$$

The linear combination includes radial function: u_L and $\dot{u}_L$. In addition, the linearization of energy ξ_l for all basis functions will not affect the calculation but it make them much simpler. The two coefficients a_L^{lo} and b_L^{lo} are determined by normalization (the local orbitals have zero value at the MT spheres boundary). Both, the APW and local orbits are continuous at the sphere boundary but their derivative is discontinuous. Most accurate LAPW methods deal with the full wave function of all possible elements as -s, -p, -d, and -f electron systems.

The wave function of the real objects has a different signature in different regions of the space. However, the wave function for the bonding region must be smooth. In this case, the effective pseudopotential can be implemented. In the region close to the atom core, the strong attractive potential of the nuclei rapidly owns wave function oscillators.

4.4. Born-von Karman boundary conditions

To predict the electron properties of infinite solid materials the periodic potential should be introduced. The translational periodicity of the lattice can be defined by a primitive lattice translations vector:

$$\vec{T} = n_1\vec{a}_1 + n_2\vec{a}_2 + n_3\vec{a}_3\,, \tag{4.56}$$

where vectors $\vec{a}_1, \vec{a}_2$ and $\vec{a}_3$ are nonplanar. The periodic structure of potential $V(\vec{r})$ can be represented as:

$$V(\vec{r}+\vec{T}) = V(\vec{r}) \qquad \text{or} \qquad V(\vec{r}) = \sum_{\vec{G}} V_{\vec{G}} e^{i\vec{G}\vec{r}}\,, \tag{4.57}$$

where $\vec{G}$ are sets of vectors in reciprocal space and $V_{\vec{G}}$ are Fourier coefficients. The reciprocal lattice can be defined by vectors $\vec{G}$, with primitive translation vectors:

$$\vec{G} = m_1\vec{A}_1 + m_2\vec{A}_2 + m_3\vec{A}_3\,, \tag{4.58}$$

where $\vec{A}_j$ are three non-coplanar vectors $a_i\vec{A}_j = 2\pi\delta_{ij}$ and m_j is an integer. In consequence, one can conclude that the existence of a lattice in the *r*-space automatically implies the existence of a lattice in the *k*-space. Using only a one-electron wave function the electron system can be represented correctly. The infinitive number of equivalent dispersion relationships $E(\vec{k}) = E(\vec{k}+\vec{G})$ for all $\vec{G}$ should be used. Because the k-space periodicity exists it means that all information will be contained in a primitive cell of reciprocal lattice named the first Brillouin zone.

In the crystal structure, the wave functions must describe the motion of the electrons through the periodic potential that reflects the translation properties of the lattice. The mentioned wave function looks as follows:

$$\varphi(\vec{r}) = e^{-i(\vec{k}\vec{r}-\omega t)}\,. \tag{4.59}$$

This plane wave function subjects boundary conditions that include symmetry of the crystal:

$$\varphi(\vec{r}+N_j\vec{a}_j)=\varphi(\vec{r}),_{\,j=1..3}, \tag{4.60}$$

where N_j is the number of primitive unit cells in the crystal, and index *j* represents the number of the unit cell in *the j* direction. The volume of k-space is defined as:

$$\frac{\vec{A}_1}{N_1}\cdot\frac{\vec{A}_2}{N_2}\times\frac{\vec{A}_3}{N_3}=\frac{1}{N}\vec{A}_1\cdot\vec{A}_2\times\vec{A}_3 \text{ where } \vec{A}_1\cdot\vec{A}_2\times\vec{A}_3=V_k\ . \tag{4.61}$$

The V_k is the volume of the first Brillouin zone and this means that it has the same number of *k*-points that the number of primitive cells of the crystal.

The Schrodinger equitation for the periodic potential of some particle with the mass m looks like this:

$$H\psi=\left\{-\frac{\hbar^2\nabla^2}{2m}+V(\vec{r})\right\}\psi=E\psi\ . \tag{4.62}$$

The wave function ψ can be presented as a sum of the plane wave function with Born von Karman boundary conditions:

$$\psi(\vec{r})=\sum_{\vec{k}}C_{\vec{k}}e^{i\vec{k}\vec{r}}\ . \tag{4.63}$$

Using dependence (4.63) one can rewrite equation (4.62) in form:

$$\sum_{\vec{k}}\frac{\hbar^2k^2}{2m}C_{\vec{k}}e^{i\vec{k}\vec{r}}+\sum_{\vec{G}}V_{\vec{G}}e^{i\vec{G}\vec{r}}\sum_{\vec{k}}C_{\vec{k}}e^{i\vec{k}\vec{r}}=\sum_{\vec{k}}C_{\vec{k}}e^{i\vec{k}\vec{r}}\,. \tag{4.64}$$

In addition, the potential energy term can be rewritten as:

$$V(\vec{r})\psi=\sum_{\vec{G},\vec{k}}V_{\vec{G}}C_{\vec{k}}e^{i(\vec{G}+\vec{k})\vec{r}}\rightarrow V(\vec{r})\psi=\sum_{\vec{G},\vec{k}}V_{\vec{G}}C_{\vec{k}-\vec{G}}e^{i\vec{k}\vec{r}}, \tag{4.65}$$

and the Schrodinger equation becomes:

$$\sum_{\vec{k}}e^{i\vec{k}\vec{r}}\left\{(\frac{\hbar^2k^2}{2m}-E)C_{\vec{k}}+\sum_{\vec{G}}V_{\vec{G}}C_{\vec{k}-\vec{G}}\right\}=0\,. \tag{4.66}$$

When $e^{i\vec{k}\vec{r}}=1$, the equation (4.66) can obtain presented form:

$$(\frac{\hbar^2k^2}{2m}-E)C_{\vec{k}}+\sum_{\vec{G}}V_{\vec{G}}C_{\vec{k}-\vec{G}}=0\,. \tag{4.67}$$

Using dependence $\vec{k}=\vec{q}-\vec{G}'$, where $\vec{q}$ is located in the first Brillouin zone and $\vec{G}'$ is reciprocal lattice vectors, one can obtain:

$$(\frac{\hbar^2(\vec{q}-\vec{G}')^2}{2m}-E)C_{\vec{q}-\vec{G}'}+\sum_{\vec{G}}V_{\vec{G}}C_{\vec{q}-\vec{G}'-\vec{G}}=0\,. \qquad (4.68)$$

Let's choose a particular value of $\vec{q}$ and general reciprocal lattice vectors $\vec{G}$ to specify the $C_{\vec{k}}$ ($\vec{k}=\vec{q}-\vec{G}$) that will be used to make the wave function ψ defined in (4.63) as follows:

$$\psi_{\vec{q}}(\vec{r})=\sum_{\vec{G}}C_{\vec{q}-\vec{G}}e^{i(\vec{q}-\vec{G})\vec{r}}\ , \qquad (4.69)$$

that can be rewritten:

$$\psi_{\vec{q}}(\vec{r})=e^{i\vec{q}\vec{r}}\sum_{\vec{G}}C_{\vec{q}-\vec{G}}e^{-i\vec{G}\vec{r}}=e^{i\vec{q}\vec{r}}u_{j\vec{q}}\,. \qquad (4.70)$$

The equation (4.70) can be interpreted as (a plane wave with a wavevector within a first Brillouin zone) × (a function of the periodicity of the lattice $u_{j\vec{q}}$). Bloch's theorem says that "The eigenstates ψ of a one-electron Hamiltonian $H=-\frac{\hbar^2\nabla^2}{2m}+V(\vec{r})$ where $V(\vec{r}+\vec{T})=V(\vec{r})$ for all Bravais lattice translation vectors $\vec{T}$ can be chosen to be a plane wave function with the periodicity of the Bravais lattice". In consequence, the $u_{j\vec{q}}$ represents a particular dispersion relationship of the electron sets. The possible states in the band will be given by the number of Born-von Karman wavevectors $\vec{q}$ in the first Brillouin zone.

4.5. Semi-empirical methods in quantum chemistry

Semi-empirical quantum chemistry methods are based on Hartree-Fock formalism but they make many approximations and use many parameters from empirical data. These methods are important for the computation of large molecular, or cluster systems that, in many cases, would be impossible to be studied with using the full Hartree-Fock methods. It is because the electron correlation effects would be too expensive. The development of semi-empirical methods assumes that the Hartree-Fock formalism can be approximated or completely neglects at the level of the two-electron integrals $J_{\mu\nu}$ and $K_{\mu\nu}$ (see equations (4.13) and (4.14)). Instead to calculate these integrals the parameters best describing experimental data or *ab initio* calculations are introduced. The obtained results may be wrong when the calculated molecule differs from the system for which the parameterization was done. On the other side, only selected properties can be calculated by the semi-empirical methods for which these methods were developed.

The oldest semi-empirical method completely neglecting the two-electron integrals is called the Hückel method and the extended Hückel method. The Hückel method treats quantum mechanically only π electrons and is intended for calculations of aromatic conjugated molecules. The extended Hückel method takes into account all the valence electrons. Among the other semi-empirical methods, two basic groups can be distinguished: methods in which only π electrons are quantum-mechanically treated and methods in which all valence electrons are calculated. The most popular method of the first group is the Pariser-Parr-Pople method, which mainly serves to calculate the excited states of the π-electrons [23,24]. The second group includes CNDO, INDO, and NDDO methods introduced by Pople. Parameters implemented into these methods are based on *ab initio* calculations with a minimal basis set not on experimental results. They are currently rarely used, but they make a significant contribution to the development of semi-empirical methodology[25].

4.5.1. PMx parameterization methods

Over the past 40 years, the NDDO and MNDO-type methods have been refined[26,27]. Numerous changes were made to the NNDO methodology. In 1989 Stewart start to develop a new version of the NNDO methods based on their new parametrization. In consequence, the PM3 method (parametric method 3) was created[28]. The elements from the first and second rows were present[29]. Comparing the obtained results with NNDO and AM1 showed significant improvements. Although technique based on a combination of the localized molecular orbitals whit pseudo-diazotization[30] make the PM3 method suitable for large biomolecules with several thousand atoms. It reduced the time of the self-consistent field (SCF) calculation, which makes almost linear scaling from the size of the system.

Stewart continues to improve the accuracy of PM3, adding several heavy elements[31,32]. The most important change was the addition of *d* orbitals to the main group elements and the introduction of diatomic parameters. In consequence, he developed the PM6 parametrized method. It includes a correction in the core-core interactions defined as follows:

$$E_n(A,B) = Z_A Z_B \langle s_A s_A | s_B s_B \rangle \left(1 + x_{AB} e^{-\alpha_{AB}\left(R_{AB}+0.0003R_{AB}^6\right)}\right) \tag{4.71}$$

and resulting in a convergence increase by the addition of a small perturbation. The PM6 method contains atomic and diatomic parameters for 70 elements, including transition metal groups, not previously introduced in any semi-empirical computational methods[33].

The increased accuracy of PM6 compared to PM3 made it the preferred NDDO method, but its fault was the incorrect modeling of various simple solids, which were very different from the species used in the parameter optimization. In consequence, the PM7[34] method was developed. In PM7, correlation effects used in PM3 and PM6 methods have been replaced by Jurečka's dispersion term. This has allowed all of the atomic core–core Gaussian functions to be deleted with the exceptions of H, C, N, and O, as sufficient high-quality reference data available to allow the Gaussian functions for these elements to be defined.

4.6. Literature

[1] Parr, R. G., Craig, D. P., & Ross, I. G., "Molecular orbital calculations of the lower excited electronic levels of benzene, configuration interaction included." *The Journal of chemical physics,* vol.18, no.12, pp.1561-1563, **(1950)**. doi:10.1063/1.1747540

[2] Born, M., & Oppenheimer, R., "Zur quantentheorie der molekeln." *Annalen der physic,* vol.389 no.20, pp.457-484, **(1927)**. doi:10.1002/andp.19273892002

[3] Hohenberg, P., & Kohn, W., "Inhomogeneous electron gas." *Physical review,* vol.136 no.3B, pp.864, **(1964)**. doi:10.1103/physrev.136.b864

[4] Rindt, C. C. M., & Gaastra-Nedea, S. V., "Modeling thermochemical reactions in thermal energy storage systems. In Advances in Thermal Energy Storage Systems" Woodhead Publishing. pp. 375-415, **(2015)**.

[5] Perdew, J.P., Burke, K., & Ernzerhof, M., "Generalized gradient approximation made simple", *Physical Review Letters*, vol.77 no.18, p.3865-3868, **(1996)**. doi:10.1103/physrevlett.77.3865

[6] Janesko, B. G., "Rung 3.5 density functionals: Another step on Jacob's ladder." *International Journal of Quantum Chemistry*, vol.113 no.2, pp.83–88, **(2012)**. doi:10.1002/qua.24256

[7] Wu, Z., Cohen, R. E., & Singh, D. J., "Comparing the weighted density approximation with the LDA and GGA for ground-state properties of ferroelectric perovskites." *Physical Review B*, vol.70 no.10, pp.104-112, **(2004)**. doi:10.1103/physrevb.70.104112

[8] Constantin, L. A., Fabiano, E., & Della Sala, F., "Modified fourth-order kinetic energy gradient expansion with hartree potential-dependent coefficients." *Journal of chemical theory and computation*, vol.13 no.9, pp.4228-4239, **(2017)**. doi:10.1021/acs.jctc.7b00705

[9] Tirado-Rives, J., & Jorgensen, W. L., "Performance of B3LYP density functional methods for a large set of organic molecules." *Journal of chemical theory and computation*, vol.4 no.2, pp.297-306, **(2008)**. doi:10.1021/ct700248k

[10] Dreuw, A., Weisman, J. L., & Head-Gordon, M., "Long-range charge-transfer excited states in time-dependent density functional theory require non-local exchange." *The Journal of chemical physics*, vol.119, no.6, pp.2943-2946, **(2003)**. doi:10.1063/1.1590951

[11] Iikura, H., Tsuneda, T., Yanai, T., & Hirao, K., "A long-range correction scheme for generalized-gradient-approximation exchange functionals." *The Journal of Chemical Physics*, vol.115 issue 8, pp.3540-3544, **(2001)**.

[12] Tsuneda, T., Song, J.-W., Suzuki, S., & Hirao, K., "On Koopmans' theorem in density functional theory." *The Journal of Chemical Physics*, vol.133, pp.174101-17410, **(2010)**. doi:10.1063/1.3491272

[13] Tawada, Y., Tsuneda, T., Yanagisawa, S., Yanai, T., & Hirao, K., "A long-range-corrected time-dependent density functional theory." *The Journal of Chemical Physics*, vol.120 no.18, pp.8425-8433, (2004). doi:10.1063/1.1688752

[14] Anisimov, V. I., Zaanen, J., & Andersen, O. K., "Band theory and Mott insulators: Hubbard U instead of Stoner," *Physical Review B*, vol. 44, pp. 943, **(1991)**. doi:10.1103/physrevb.44.943

[15] Morales-García, Á., Valero, R., & Illas, F., "An Empirical, yet Practical Way To Predict the Band Gap in Solids by Using Density Functional Band

Structure Calculations." *The Journal of Physical Chemistry C*, vol.121, no.43, pp.18862–18866, **(2017)**. doi:10.1021/acs.jpcc.7b07421

[16] Slater J.C., "Wave Functions in a Periodic Potential." *Physical Review*, vol.51, pp.846-851, **(1937)**. doi:10.1103/physrev.51.846

[17] Sjöstedt, E., Nordström, L., & Singh, D., "An alternative way of linearizing the augmented plane-wave method." *Solid state communications*, vol.114 no.1, pp.15-20, **(2000)**. doi:10.1016/s0038-1098(99)00577-3

[18] Andersen O. K., "Linear methods in band theory." *Physical Review B*, vol.12, pp. 3060–3083, **(1975)**. doi:10.1103/physrevb.12.3060

[19] Koelling, D. D., & Arbman, G. O., "Use of energy derivative of the radial solution in an augmented plane wave method: application to copper." *Journal of Physics F: Metal Physics*, vol.5, no.11, pp.2041–205, (1975). 4. doi:10.1088/0305-4608/5/11/016

[20] Koelling, D. D., & Arbman, G. O., "Use of energy derivative of the radial solution in an augmented plane wave method: application to copper." *Journal of Physics F: Metal Physics*, vol.5, no.11, 2041–2054, **(1975)**. doi:10.1088/0305-4608/5/11/016

[21] Goedecker, S., "Treatment of semicore states in the linearized augmented-plane-wave method and other linearized electronic-structure methods", *Physical Review B*, vol.47, pp.9881–9883, **(1993)**. doi:10.1103/physrevb.47.9881

[22] Singh, D., "Ground-state properties of lanthanum: Treatment of extended-core states" *Physical Review B*, vol.43, pp. 6388–6392, **(1991)**. doi:10.1103/physrevb.43.6388

[23] Linderberg, J., & öhrn, Y., "Derivation and Analysis of the Pariser–Parr–Pople Model", *The Journal of Chemical Physics*, vol.49, pp. 716–727, **(1968)**. doi:10.1063/1.1670129

[24] Pople J. A., "Electron Interaction In Unsaturated Hydrocarbons." *Transactions of the Faraday Society*, vol.49, pp.1375-1385, **(1953)**. doi:10.1039/tf9534901375

[25] Pople J.A., & Beveridge D.L., "Approximate Molecular Orbital Theory", McGRAW-Hill Book Company, **(1970)**.

[26] Pople, J. A., Beveridge, D. L., & Dobosh, P. A., " Approximate Self-Consistent Molecular-Orbital Theory. V. Intermediate Neglect of

Differential Overlap." *The Journal of Chemical Physics*, vol.47, no.6, pp.2026–2033, **(1967)**. doi:10.1063/1.1712233

[27] Dewar, M. J. S., & Thiel, W., "Ground States of Molecules. The MNDO Method. Approximations and Parameters", *Journal of the American Chemical Society*, vol.99, pp.4907–4917, **(1977)**. doi:10.1021/ja00457a004

[28] Stewart J.J.P., "Optimization of Parameters for Semiempirical Methods I. Method", *Journal of Computational Chemistry*, vol.10, pp.209–220, **(1989)**. doi:10.1002/jcc.540100208

[29] Stewart J.J.P., "Optimization of parameters for semiempirical methods II. Applications." *Journal of computational chemistry*, vol.10, no.2, pp.221-264, **(1989)**. doi:10.1002/jcc.540100209

[30] Stewart, J., Császár, P., & Pulay, P. "Fast semi-empirical calculations". *Journal of computational chemistry*, vol.3 no.2, pp.227–228, **(1982)**.

[31] Stewart J.J.P., "Optimization of parameters for semiempirical methods. III Extension of PM3 to Be, Mg, Zn, Ga, Ge, As, Se, Cd, In, Sn, Sb, Te, Hg, Tl, Pb, and Bi." *Journal of computational chemistry*, vol.12 no.3, pp.320-341, **(1991)**. doi:10.1002/jcc.540120306

[32] Stewart J.J.P., "Optimization of parameters for semiempirical methods IV: extension of MNDO, AM1, and PM3 to more main group elements. " *Journal of Molecular Modeling*, vol.10 no.2 pp.155-164, **(2004)**. doi:10.1007/s00894-004-0183-z

[33] Stewart J.J.P., "Optimization of parameters for semiempirical methods V: Modification of NDDO approximations and application to 70 elements", *Journal of Molecular Modeling*, vol.13, pp.1173–1213, **(2007)**. doi:10.1007/s00894-007-0233-4

[34] Stewart J.J.P., "Optimization of parameters for semiempirical methods VI: more modifications to the NDDO approximations and re-optimization of parameters." *Journal of molecular modeling*, vol.19 no.1, pp.1-32, **(2013)**. doi:10.1007/s00894-012-1667-x

Chapter 5

THESIS AND HYPOTHESES OF THE WORK

For many years TiO_2 with an anatase structure has been extensively studied for photovoltaic applications, but its wide energy band gap (3.2 eV) allows to use of only a small fraction of solar radiation. Therefore, the pristine TiO_2 crystal is not appropriate material for the conversion of solar energy into electric current. The quantum confinement size effect changes the electron properties of the crystal, so in recent years, the focus has been made on the investigations of the TiO_2 nanostructures. The TiO_2 nanocrystals do not meet their full expectations, because they have low photoconversion efficiency. The proposed dissertation is devoted to the theoretical study of the physical properties of hybrid materials based on bulk and nanostructured TiO_2 sensitized by organic dyes, that potentially can be used to build dye-sensitized solar cells (DSSC). The results obtained by quantum chemical calculations were compared with experimental data.

Based on the literature analysis concerning the subject of the dissertation, the following thesis was proposed: **TiO_2-based structures modified by impurities and/or vacancies as well as sensitized by the appropriate dyes are applicable for the DSSC devices**. T**o choose the best components for DSSC applications the mechanism of charge transfer between them should be explained.** The sensitizers will be the organic molecules anchored at the surface of the semiconductor and absorbing the light in the visible region.

Therefore, the TiO_2 studies are aimed at modification of their composition to produce a material with a low energy gap and high photon energy to electric current conversion coefficient. A variation of the electron band gap with stoichiometry is a key parameter to fine-tune the photocurrent activation and enhance the photoactive parameters of semiconductors under solar light irradiation. Therefore, it is necessary to adjust the active material band gap able to exploit the large part of the solar light spectrum. The strategies used to modify the optical absorption by band gap narrowing consist of the stoichiometry change of semiconductors with a suitable ratio of the oxygen and the doping ions as N, Ni, Mn, and Cu. This gives the possibility of interference to the width of the energy gap from the bottom of the conduction band as well as from the top of the valence band. This approach will help to clarify the hypothesis that *proper doping of semiconductor nanostructures with ions in the presence of oxygen vacancies reduces the energy gap of the material*.

The electron transfer process from the sensitizer to the semiconductor structure plays the main role in the photoinduced charge separation and it affects the efficiency of the solar cells. This fact leads us to hypothesize that *the dye group anchoring the organic molecule on the semiconductor surface has a decisive influence on the photoconversion mechanism and the transfer of charge carriers in photovoltaic hybrid systems*. In this case, commercial dyes like D102 and D149 as well as the ruthenium polypyridine dyes were selected for the proposed study of the photoconductive mechanism. To verify the hypothesis dyes with carboxyl and/or catechol anchoring groups will be tested. Changes in the anchoring groups will characterize the mechanism of photoelectron charge transport occurring between the dye and the semiconductor. It will give the possibility to explain the mechanism of the indirect-type (I-type) and direct-type (II-type) of photoconductivity. **The explanation of unsolved problems related to the mechanism of electron injection from dye to semiconductor is the main task of this work.**

.

Chapter 6

STRUCTURAL AND ELECTRONIC PROPERTIES OF TiO_2 - BASED MATERIALS

In recent years, the research community has shown keen interest in searching for new renewable energy resources. Therefore, solar cells of various types have attracted much attention in energy production owing to their ability to convert the energy of light into electrical energy. Third-generation solar cells are based on nano-sized transition metal oxides playing a major role in the field of photovoltaics. Especially TiO_2 has been widely used in different kinds of solar cell applications. The use of TiO_2 nanoparticles as a photoanode in DSSC gives a power conversion efficiency (PCE) equal to 12.6%[1]. Moreover, the application of TiO_2 nanostructures as the light-scattering layer of DSSC for efficient utilization of the solar spectrum can upgrade the PCE by a few percent[2]. The TiO_2 used as the hollow sphere of the electron transporting layer in the perovskite solar cells (PSC) enhances the PCE up to 19.6%[3].

TiO_2 plays a dominant role in the field of both DSSC and PSC applications[4]. The typical DSSCs photoanode is created with pure TiO_2 in anatase form {$I4_1$/amd[141]}. The pure rutile phase of the TiO_2 has worse charge transport properties than pure anatase. Unfortunately, a bandgap of the TiO_2 anatase structure is equal to 3.2 eV[5] and the anatase does not absorb visible light. In consequence, is necessary to move its bandgap energy into the visible light region to realize photon into electrical energy conversion. It can be done by dopants or nonstoichiometric arrangement of the TiO_2 structure. Also, the sensitizing organic molecules can be adsorbed at the surface of the semiconductor harvesting the light. To anchor a significant amount of sensitizers on the surface of a semiconductor, the surface of an anode should be increased by its porosity or nanostructuring. A large fraction of surface atoms alters the electron properties and, in consequence, the conductivity of the anode having an impact on the performance of DSSC devices. The surface has a prominent role in nanomaterials and is essential for understanding the material's reactivity in the case of sensitizer anchoring.

Additionally, the problem of nanosized anatase is its instability and degradation to the rutile phase which is not desirable in DSSC applications. This problem can be solved by doping the TiO_2 with zirconium dioxide (ZrO_2) in tetra modification. Experimentally it was proved that the $Ti_{1-x}Zr_xO_2$ in anatase form (where x=0.1) has prevented degradation to rutile[6]. Unfortunately, in the mentioned material its energy gap increases according to the electronic properties of the ZrO_2 because the bandgap energy of the ZrO_2 is equal to 5 eV[7].

The results of experiments measuring structural, elastic, and electron parameters of bulk TiO_2 can be well reproduced by different computer simulation approaches, but the electron structure of TiO_2, especially within size limitation, is still a subject of debate. The response of TiO_2 single-crystal polymorphs, surfaces, and nanostructures to optical excitation is of particular topical interest in solar-energy harvesting. In the present Chapter, the evaluation of electron properties versus size limitation of the pristine and modified TiO_2 in anatase form (a-TiO_2) is discussed.

6.1. Structural and electron properties of bulk TiO_2 crystal structures

The electron properties of the TiO_2 crystals cannot be computed correctly by standard density functional theory (DFT)[8,9]. The overestimation of electron delocalization is a known drawback of DFT methods, particularly for systems with localized *d*- and *f*-electrons [10,11]. The origin of the failure of the DFT in transition metal oxides is known to be associated with an inadequate description of the strong Coulomb repulsion between 3*d* electrons localized on metal ions[12]. In many research works the hybrid DFT functionals or Hubbard corrections (*U*) were implemented to improve the computational results[13]. The DFT+U method combines the high efficiency of DFT with an explicit treatment of electron correlation with a Hubbard model for a subset of electron states in the system. Non-integer or double occupations of these states is described by the introduction of two additional interaction terms, namely, the one-site Coulomb interaction term *U* and the exchange interaction term *J*.

This work aimed to predict electron properties of stoichiometric and nonstoichiometric a-TiO_2 structures in bulk form. Nonstoichiometric a-TiO_2 was built as an anatase structure with oxygen v(O) and titanium v(Ti) reduction. Also, the influence of dopants such as Zr, Ni, Mn, Cu, or N atoms on the electron properties of the a-TiO_2 was investigated.

First off all the structural and electron parameters of the pristine TiO_2 crystal structure were calculated to find the best computational method to reproduce the experimental data. All calculations were performed using the Vienna simulation package (VASP)[14,15]. The Kohn–Sham equations were solved using the projector-augmented wave (PAW) method[16,17]. To investigate the electron properties of the chosen structures spatial arrangement of their atoms should be relaxed. For the structural relaxations the Perdew–Burke–Ernzerhof (PBE) functional was used[18, 19] with the long-range dispersion correction implemented by Grimme[20]. As the best method for structural relaxation, the DFT/PBE functional augmented by Hubbard correction was chosen. Was proven that a method giving appropriate parameters compared with experimental data is based on full structural relaxation (relaxation of cell parameters, volume, and atomic position). The Hubbard correction was implemented into calculations as a rotationally invariant LSDA+U method introduced by Liechtenstein et al.[21]. The Brillouin-zone integrations were performed on a Γ-centered Monkhorst-Pack 8 × 8 × 8 k-point grid[22]. The kinetic energy cutoff for plane waves was set to 520 eV. The convergence criterion for the electronic self-consistent loop (SCF) was set to 10^{-5} eV. Full geometry optimization was performed until the largest component of the ionic forces was less than 10^{-4} Hartree. Wave functions were employed by the projector-augmented wave (PAW) method (X-sv-GW basis set, where X is a symbol of an atom).

Correctness of the Hubbard parameters applying for the Ti 3*d* electrons of the stoichiometric a-TiO_2 structure was tested by changing their values from U_{Ti}=0 and J_{Ti}=0 eV up to U_{Ti}=9 and J_{Ti}=1 eV as presented in Table 6.1. In this case, the unit cell parameters (*a, b,* and *c*) and their ratio were analyzed (*c/a*). The *c/a* ratio is a crucial parameter for the anatase structural type since changes in the *c/a* ratio depend on the formation of metal-metal bonds. As was reported in the work of Mattioli and coworkers[23], Hubbard correction increases lattice parameters and Ti-O distances. Similar results were also reported in the work of Arroyo-de Dompablo[24]. Contrary to this, hybrid functionals underestimate the unit cell parameters of the a-TiO_2[25]. The Hubbard parameters U_{Ti}=6 and J_{Ti}=1 eV give a good ratio of the c/a=2.52 in the stoichiometric a-TiO_2 structure. Deviation of the *a* and *c* lattice parameters exists but it is less than 2 % indicating good agreement with experimental data. The octahedral structure of the a-TiO_2 is created for one Ti atom surrounded by 6 O atoms. The Ti-O bonds along the "*c*" direction are longer than those lying in the "*ab*" plane. Both relaxed Ti-O bonds are longer than the experimental ones, and they are equal to 2.001 Å and 1.967 Å, respectively. Experimental results are 1.966 Å and 1.937 Å, respectively[26]. Experimental angles O-Ti-O are equal to 102'38 and 92'60, and the modeled ones are almost identical, equal to 102'23 and 92'57, respectively. In consequence, one may conclude that the Hubbard parameters U_{Ti}=6 and J_{Ti}=1 eV used in the DFT/PBE+U calculations[24] give good reproduction of the experiment stoichiometric a-TiO_2 structure [27,28]. In this case, was decided to relax all investigated TiO_2-based structures applying U_{Ti}=6 and J_{Ti}=1 eV.

Table 6.1. Parameters of the unit cell of the stoichiometric a-TiO_2 relaxed structure by applying DFT/PBE and DFT/PBE+U methods with different Hubbard parameters, compared to experimental data

Method			a=b (Å)	c (Å)	(c/a)
	U_{Ti} (eV)	J_{Ti} (eV)			
DFT/PBE	0	0	3.80	9.65	2.54
DFT/PBE+U	4	1	3.83	9.68	2.53
	6	1	3.85	9.71	2.52
	9	1	3.87	9.75	2.52
Experiment[27,28]			3.79	9.51	2.51

In the case of t-ZrO_2, each zirconium atom maintains its eight coordinated oxygens: four oxygen atoms at a distance of ~ 2.10 Å, and four at a distance of ~ 2.30 Å[29]. The performed calculations of structural relaxation of t-ZrO_2 give the lengths of bounds ~ 2.18 Å and 2.32 Å. These data were obtained by applying U_{Zr}=6 and J_{Zr}=1 eV Hubbard parameters to the DFT/PBE functional. The mentioned calculations were performed as a test for the computer simulations of the physical properties of the TiO_2 structure with impurities.

6.1.1. Model of the 2×2×1 supercell

Based on the unit cell of the a-TiO_2 the 2×2×1 supercell was built. Its structure was optimized by applying parameters described in Chapter 6.1 and

Hubbard parameters U_{Ti}=6 eV and J_{Ti}=1 eV. The full crystal relaxation (applying ISIF=3) was performed. Geometry relaxation has given almost the same results ($2\times a$=7.69 Å, c=9.70 Å, c/a=2.52) as they were obtained after geometry optimization of the unit cell of the a-TiO2 (a=3.84 Å, c=9.71 Å, c/a=2.52). It means that the created supercell $2\times2\times1$ can be used to model the a-TiO_2 crystal structure with its defects. The main limitation of the $2\times2\times1$ supercell application is the dopant ratio equal to 6.25 % obtained in the case of substitution of Ti by impurities. It is a minimum value that can be obtained using the proposed model. The lower impurities level can be obtained by increasing the size of the supercell but the calculations will be very time-consuming and maybe even impossible. The supercells of the a-TiO_2 were modified by oxygen and titanium vacancies and by impurities such as Zr, Ni, Mn, Cu, and N ions. The examples of these structures are presented in Fig. 6.1.

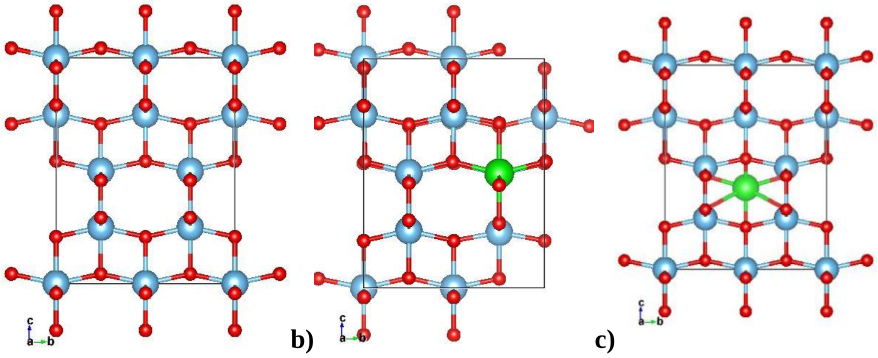

Figure 6.1. Optimized crystal structures of the $2\times2\times1$ supercells: a) virgin structure, b) TiO_2:Zr, c) TiO_2:Zr_{in} (Blue atoms—Ti, red atoms—O, green atoms—Zr)

The structural data of the studied structures after full geometry relaxation are collected in Table 6.2. The a and b supercell edge lengths are multiplied by 2 compared with the primitive unit cell of a-TiO_2. Analyzing the total energy per atom one can see that the value obtained for pristine TiO_2 is equal to -8.73 eV. The oxygen vacancies v(O) shows almost the same total energy and has very similar cell edges (see TiO_2:v(O) in Table 6.2). It can be concluded that v(O) has a very high chance to exist in real a-TiO_2 crystals. The existence of oxygen vacancies is typical for AB_2 crystals from an experimental point of view. Meanwhile, the titanium vacancies v(Ti) show a significant effect on structure stability increasing its total energy and making a strong impact on cell parameters, mostly by decreasing the c edge of the supercell. The presented data allows us to conclude that the probability of existence of the v(Ti) is lower than the existence of v(O). This agrees with the experiment, where oxygen vacancy is one of the most important and prevalent defects of many metal oxides[30]. All the remaining data presented in Table 6.2 will be analyzed in the next paragraph of Chapter 6.1.

Table 6.2. Structural parameters of the pristine a-TiO_2 2×2×1 supercell and its nonstoichiometric modification relaxed by applying DFT/PBE+U method ($U_{Ti}= U_{Zr}=6$ and $J_{Ti}= J_{Zr}=1$ *eV*)

Structure	2a (a=b) (Å)	c (Å)	c/a	Total energy/atom (eV)
TiO_2	7.69	9.70	2.52	-8.73
TiO_2:v(Ti)	7.72	9.62	2.49	-8.43
TiO_2:v(O)	7.68	9.72	2.53	-8.70
TiO_2:Zr*	7.72	9.77	2.53	-8.78
TiO_2:Ni	7.68	9.64	2.51	-8.48
TiO_2:Cu	7.71	9.66	2.51	-8.40
TiO_2:Mn	7.68	9.70	2.53	-8.50
TiO_2:Zr:v(O)	a=7.72/b=7.69	9.78	2.53/2.54	-8.74
TiO_2:Zr:v(O) far**	a=7.72/b=7.70	9.79	2.54/2.54	-8.75
TiO_2:Ni:v(O)	a=7.73/b=7.66	9.68	2.50/2.53	-8.52
TiO_2:Cu:v(O)	a=7.68/b=7.73	9.76	2.54/2.53	-8.46
TiO_2:Mn:v(O)	a=7.69/b=7.73	9.78	2.54/2.53	-8.54
TiO_2:Zr_{in}***	a=7.73/b=7.79	9.70	2.51/2.49	-8.70
TiO_2:Cu_{in}	7.75	9.67	2.50	-8.54
TiO_2:Mn_{in}	a=7.72/b=7.74	9.73	2.52/2.51	-8.60
TiO_2:N	7.69	9.63	2.50	-8.34
TiO_2:N_{in}	7.72	9.75	2.53	-8.56
TiO_2:N_{in}:v(O)	a=7.70	9.77	2.54	-8.56
TiO_2:N_{in}:v(O) far	a= 7.70	9.78	2.54	-8.55
TiO_2:N_O****	a=7.70/b= 7.72	9.69	2.52/2.51	-8.62

* TiO_2:M (where M=Zr, Ni, Cu, Mn, and N) means $Ti_{0,94}M_{0,06}O_2$ (Fig. 6.1B)

** v(O) far—means O vacancy located far from the doped atom (M)

*** TiO_2:M_{in} (where M=Zr, Ni, Cu, Mn, and N) means M atom added into TiO_2 in an interstitial position. (Fig. 6.1C)

**** TiO_2:N_O means that the N atom substitutes the O atom

Electron properties of the a-TiO_2 and t-ZrO_2 crystals were calculated in the points of the Brillouin zone specified in Fig. 6.2 following the path Γ-X-M-Γ-Z-R-A-Z[X-R]M-A, where Γ(0, 0, 0), X(0.5, 0, 0), M(0.5, 0.5, 0), Z(0, 0, 0.5), R(0.5, 0, 0.5) and A(0.5, 0.5, 0.5) by applying sampling with k-point Monckhorst-Pack grids 8×8×8. All other computational parameters were applied as mentioned above. The TiO_2 structures with impurities were built by removing one O atom or one Ti atom from the crystal supercell and substituting it with metal ions or adding an impurity in an interstitial position of the supercell.

To calculate the electron parameters of the a-TiO_2, first of all, the tests were performed using different Hubbard parameters. The calculations were performed for the unit cell of the pristine a-TiO_2 and t-ZrO_2 structures as well as for the 2×2×1 supercell of the a-TiO_2. The obtained results are presented in Table 6.3. The band gap energy of the a-TiO_2 calculated using the GGA/PBE method is underestimated compared with the experimental value. The same results were obtained in the other works[23,24]. It supports the theory that the pure PBE functional cannot be used to calculate electron properties of metal oxides as a-TiO_2 and t-ZrO_2. The DFT/PBE methods underestimate the band gap energy of the t-ZrO_2 giving a value of 3.81 eV but the experimental value is equal to 5.00 eV.

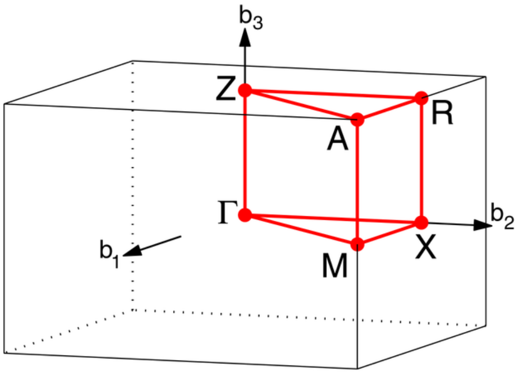

Figure 6.2. Brillouin zone pass for TiO_2 crystals in anatase polymorph. Electron properties of the a-TiO_2 crystal were calculated in the points of the Brillouin zone as follows Γ-X-M-Γ-Z-R-A-Z[X-R]M-A

Table 6.3. Bandgap energy calculated by DFT/PBE* and DFT/PBE+U method applying Hubbard correction for the unit cell of the a-TiO_2 and t-ZrO_2 and 2×2×1 supercell of the a-TiO_2. In all cases the J_{Ti}=J_{Zr}=1 eV

unit cell a-TiO_2		2×2×1 supercell a-TiO_2		unit cell t-ZrO_2	
U_{Ti} (eV)	E_g (eV)	U_{Ti} (eV)	E_g (eV)	U_{Zr} (eV)	E_g (eV)
0.00*	2.02*	0.00*	2.03*	0.00*	3.81*
6.00	2.68	6.00	2.69	6.00	4.70
9.00	3.12	9.00	3.14	9.00	4.83
9.25	3.16	**9.25**	**3.18**	**9.25**	**5.05**
9.50	**3.20**	9.50	3.23	9.50	5.10
9.75	3.24	9.75	3.26	9.75	5.12
10.00	3.28	10.0	3.31	10.0	5.14
E_g(exp) =3.2 eV[26]				E_g(exp) =5.0 eV[5]	

Optimizing geometry of the a-TiO_2 and t-ZrO_2 crystal good structural parameters were obtained applying Hubbard correction as follows U_{Ti}= U_{Zr}=6 eV and J_{Ti}= J_{Zr}=1 eV. Using these parameters for the electron properties calculations the obtained band gap energy is higher than using DFT/PBE method but is still underestimated. Analyzing data presented in Table 6.3, one may decide that the U_{Ti}=9.50 and J_{Ti}=1.00 eV for the Ti atom can be used to calculate the electron properties of the a-TiO_2 unit cell. To calculate electron parameters of the 2×2×1 supercell better results are obtained using parameters U_{Ti}=9.25 eV and J_{Ti}=1.00 eV. Electron parameters of the t-ZrO_2 crystal are well reproduced using U_{Zr}=9.25 eV and J_{Zr}=1.0 eV. The Hubbard parameters of the O atoms were not taken into consideration. In consequence, was proposed to use U_{Ti}=9.25 eV and J_{Ti}=1.00 eV correction to simulate electron properties of pristine and defective TiO_2 structures that will lower possible errors in obtained results and shows the impact of transition between bulk and surface of TiO_2 taking into account the structural changes.

The energy band structure of the a-TiO_2 (Fig. 6.3) and t-ZrO_2 (Fig. 6.4) were calculated by applying U_{Ti}= U_{Zr} =9.25 eV and J_{Ti}= J_{Zr}=1.00 eV. The obtained results show an indirect band gap for the a-TiO_2 structure and a direct band gap for the t-ZrO_2 structure. The valence band of the a-TiO_2 is created by O 2*p* electrons (blue line), and conducting band is predominantly created by Ti 3*d* states (red line). Valence band maximum (VBM) is localized near the M point and conductional band minimum (CBM) is localized at the Γ point. Analogous results were obtained for ZrO_2. Here also the valence band is created by O electrons and the conduction band by the Zr electrons (see Fig. 6.4). The constructed electron density of states (DOS) is presented in Fig. 6.3 and Fig. 6.4 for the a-TiO_2 and t-ZrO_2 structure, respectively. The obtained results follow the data presented by other researchers[31,32], and they are typical for the AB_2 metal oxides.

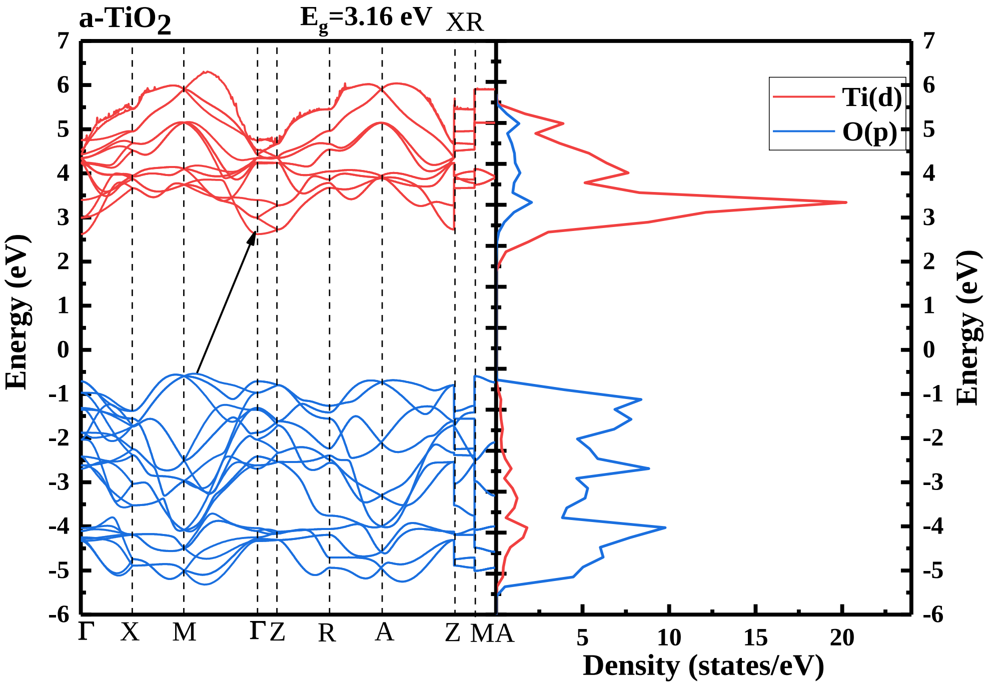

Figure 6.3. Energy band structure and electron DOS calculated by DFT/PBE+U method for the a-TiO_2 crystal structure (U_{Ti}=9.25 and J_{Ti}=1.00 eV)

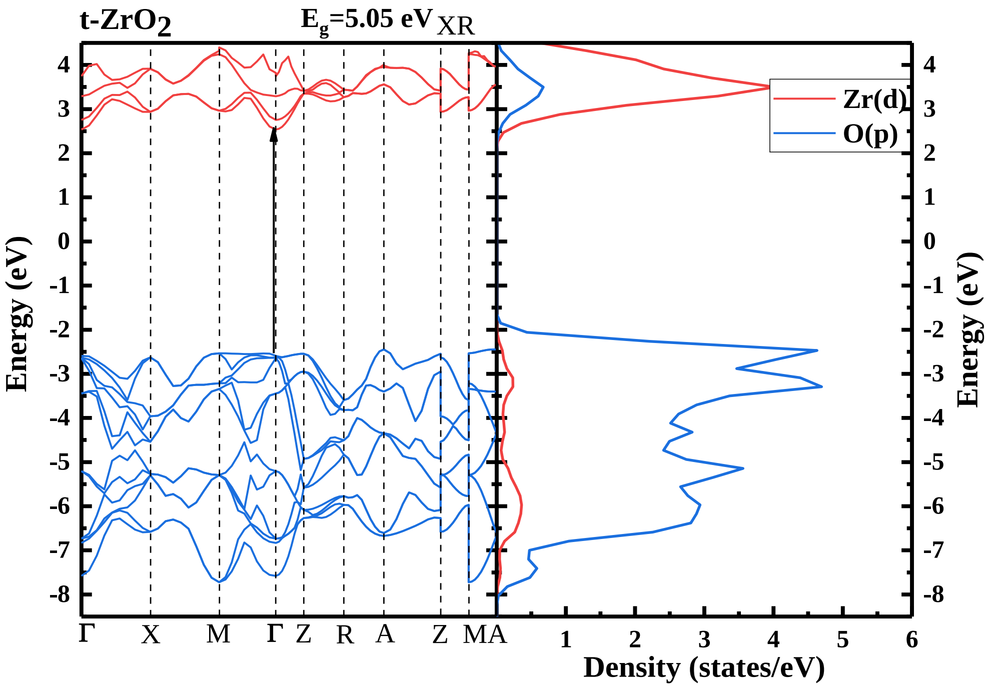

Figure 6.4. Energy band structure and electron DOS calculated by DFT/PBE+U method for the t-ZrO_2 crystal structure (U_{Zr}=9.25 and J_{Zr}=1.00 eV)

From a fundamental solid-state point of view, the calculated dispersion of the energy band structure is principal for the calculation of the carrier's effective masses. The effective mass of electrons (m_e^*) can be evaluated from the curvature (energy derivatives) of the bottom of the conduction band in k-space. The diagonal elements of the effective mass tensor for the electrons and holes of the a-TiO_2 are calculated around the Γ point of the Brillouin zone (BZ) for the conduction band and around the M point of the BZ for the valence band, respectively. Calculations were performed following the equation:

$$\frac{1}{m^*_{e_{ij}}} = \frac{1}{h^2}\frac{\partial^2 E(k)}{\partial k_i k_j} \tag{6.1}$$

where h is the Planck constant and E(k) is the energy of the electron band level. The effective mass of electrons is determined by fitting the conduction band structure to a parabolic function. The effective masses of the holes are calculated analogously.

Analyzing Fig. 6.3 one can say that the curvature of the VBM and CBM possess significant anisotropy comparing Γ – M i Γ – Z directions in the conduction band and M – Γ and M – X in the valence band. In this case, the electron and hole effective masses have also significant anisotropy. The difference in the Ti-O bond lengths in the *c* crystal direction compared with the bonds in the *ab* plane became one of the reasons why effective masses for electrons are so different. In direction Γ – M the effective mass of electrons is equal to $0.54m_e$, in direction Γ – X is equal to $0.58m_e$, meanwhile in direction Γ – Z the electron's effective mass is equal to $3.30m_e$. The opposite trend is noticed for the holes' effective masses. The effective mass of holes in M – Γ is equal to $1.59m_e$, and in the direction of M – X is equal to $1.95m_e$ meanwhile in dimension Γ – Z the effective mass of holes is equal to $1.18m_e$. The obtained results are very similar to data published by Kim and coworkers[31] where electron effective mass possesses a maximum value equal to $3.70m_e$ in the [001] direction and a minimum equal to $0.59m_e$ in the [100] or [010] direction. In the mentioned work was reported that the effective mass of holes has a maximum ($2.33m_e$) in the [100] or [010] direction and a minimum ($0.98m_e$) in the [001] direction. Also, Raghav and coworkers[32], as well as Kus et al.,[33] presented similar results in their works. It will allow us to conclude that the electron conductivity of the a-TiO_2 is better in the *ab* plane than in the *c* direction. The performed calculations also prove the correctness of applied Hubbard parameters to calculate the electron properties of the a-TiO_2-based structures.

The electron parameters were also calculated for the pristine 2×2×1 supercell of the a-TiO_2 to compare these results with data obtained for the primitive unit cell (see Fig. 6.3). Calculations were performed for the high symmetry points located in the Brillouin zone as follows Γ-F-Q-Z-Γ, where Γ(0,0,0), F(0,0.5,0), Q(0,0.5,0.5), Z(0.5,0,0). The energy band structure of the 2×2×1 a-TiO_2 supercell is presented in Fig. 6.5. One can see that the investigated structure remains an indirect semiconductor, with an energy bandgap equal to 3.18 eV. It is slightly higher than the data obtained for the a-TiO_2 (3.16 eV). Electron effective masses calculated in Γ−F and Γ−Z directions are $0.52m_e$ and $3.28m_e$ respectively. The hole's effective mass in Γ direction is equal to $1.72m_e$ and in the F direction is equal to $1.46m_e$. The lowest value effective masses of holes is noticed going from Γ to Z direction and is equal to $1.25m_e$. This is very similar to the data presented earlier for the primitive unit cell of anatase. The DOS presented in Fig. 6.5 shows the same behavior as the one obtained for the unit cell of the a-TiO_2 (see Fig. 6.3). The presented data show that the 2×2×1 supercell can be used to calculate the electron properties of the defected a-TiO_2 structures.

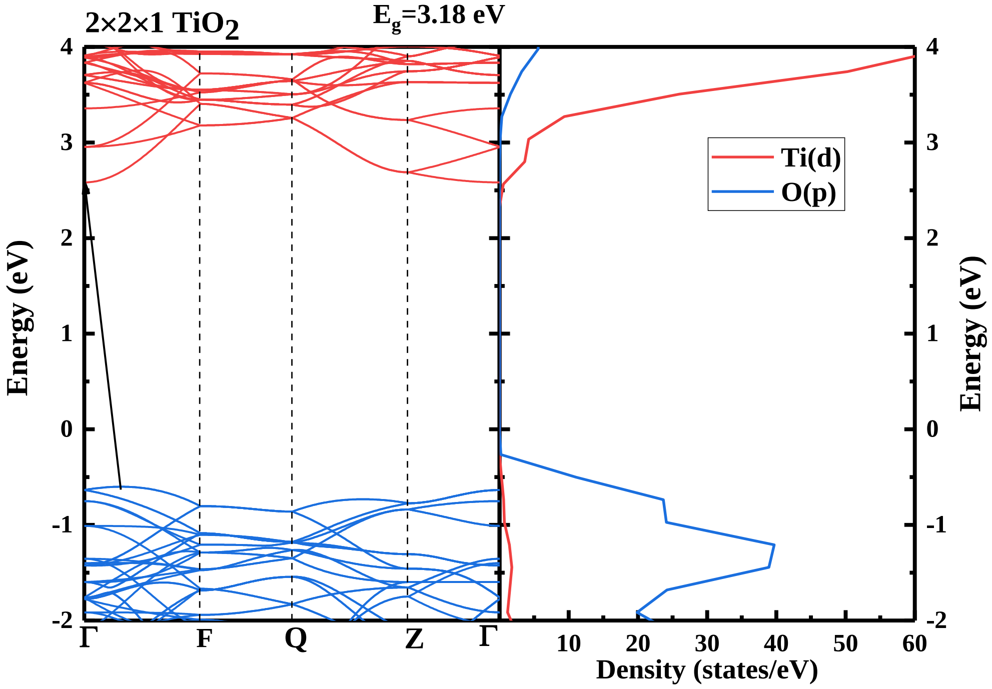

Figure 6.5. Energy band structure and electron DOS calculated by DFT/PBE+U method for the 2×2×1 TiO_2 crystal structure (U_{Ti}=9.25 and J_{Ti}=1.00 eV)

6.1.2. Defective 2×2×1 TiO_2 structures doped substitutionally

The presence of Ti and O vacancies in the a-TiO_2 was investigated using the 2×2×1 supercell approach. Calculations were performed with 6.2 % for cation and with 3.1 % for anion of vacancies present in the crystal structure. Oxygen vacancies v(O) widely exist in metal oxide-based materials as a kind of intrinsic defects[34,35]. They can significantly change the properties of the bulk (e.g., conductivity, band gap energy) and surface (e.g., molecular adsorption, electron properties). Therefore, the description of defects in wide bandgap oxides is an important challenge for modern electronics. Removal of lattice oxygen atoms leads to the creation of the Ti^{3+} ions[36]. From the transport measurements, vacancies appear to be electron donors resulting in metallic-like conductivity at room temperature, because when a vacancy is introduced, two electrons originally trapped by the oxygen are donated to the system. These electrons give rise to an energy state in the bandgap at about 1 eV below the CBM[37]. The presence of the Ti^{3+} ions is also accompanied by the appearance of absorption bands in the visible region due to the occurrence of a new state in the bandgap.

In the work of Finazzi[37] was shown that the computational description of the electron structure of the v(O) in bulk a-TiO_2 is highly method dependent.

Therefore, in the presented work, the GGA/PBE+U method was used with the parameters described for the a-TiO_2 crystal to calculate the electron structure of the v(O) defected TiO_2. The obtained results are shown in Fig. 6.6. There also the influence of the titanium vacancies v(Ti) on the electron structure of the TiO_2 is present. As was mentioned earlier (see Table 6.2) the v(O) in anatase crystal has a high possibility to exist, and meanwhile, the structure with v(Ti) is not stable. The band gap energy of the v(O) defected TiO_2 crystal is equal to 3.28 eV and is a little bit higher than the band gap of the pristine crystal. However, that additional energy band associated with vacancies was created 1 eV lower than CBM[37]. The v(O) defective TiO_2 crystal steel has an indirect band gap. In the case of the v(Ti), any significant changes in bandgap value compared with pristine TiO_2 are not observed. The v(Ti) defective TiO_2 crystal turns into a direct semiconductor. This indicates significant changes in the geometry of the TiO_2:v(Ti) during the relaxation process.

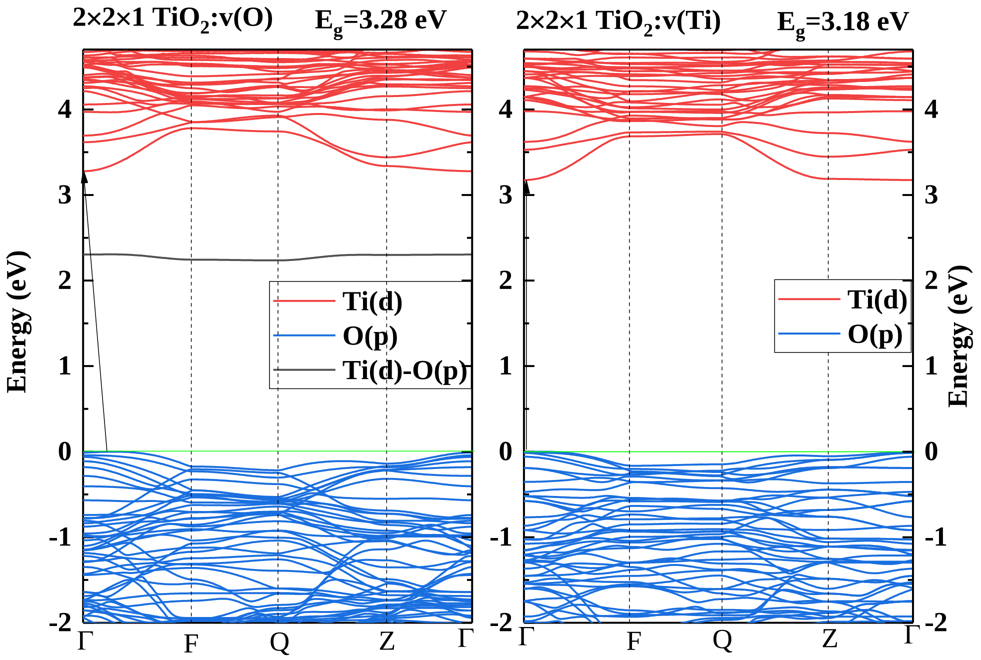

Figure 6.6. Energy band structure calculated by DFT/PBE+U method for the 2×2×1 TiO_2 crystal structure with v(O) and v(Ti) vacancies (U_{Ti}=9.25 and J_{Ti}=1.00 eV)

In the case of TiO_2:v(O), the effective electron masses for Γ−F and Γ−Z directions are $0.59m_e$ and $3.81m_e$, respectively. The hole effective masses for the mentioned structure are equal to $2.88m_e$ and $1.86m_e$, in Γ and F direction respectively. Comparing these data with results obtained for pristine TiO_2 (see Fig. 6.5) one can say that the transport of electrons in the Z direction is going to be more difficult. Also, the transport of holes is worse than is observed for pristine TiO_2. In the case of v(Ti) the effective electron masses for the Γ−F direction do not change compared with the TiO_2 structure, but for the Γ−Z direction, effective electron masses significantly increase. Also, hole electron masses in the Γ−Z direction significantly increase in the TiO_2:v(Ti) structure. It proves the statement that the perturbation of atomic structure in the defective crystal influences the electron properties of the material.

As it was mentioned above, the electron properties of the a-TiO_2 can be improved in the desired direction by adding different dopants. In this case, the Zr, Mn, Cu, Ni, and N atoms were chosen. Analysing the results presented in Table 6.2 one can see that in the case of substitution of the one Ti by Zr, the stability of the new structure became even higher than that of pristine anatase. The TiO_2:Zr structure reaches the highest stability concerning all studied supercells. The *c* edge of the TiO_2:Zr increases compared with the pristine TiO_2 supercell because the Zr ion is bigger than Ti. The mentioned change does not modify the energy bandgap of the TiO_2:Zr structure compared with pristine TiO_2. (see Fig. 6.7 and Fig. 6.5). Effective masses of electrons in the TiO_2:Zr: structure are equal to $0.54m_e$ and $3.84m_e$ for Γ−F and Γ−Z direction, respectively. The effective masses of holes are equal to $1.79m_e$ in the Γ direction and $1.49m_e$ in the F direction. These data are very similar to the ones obtained for the pristine TiO_2 structure. One can conclude that the Zr impurities in the TiO_2 structure stabilize its geometry and do not change its electron properties. The situation is completely different when the Zr impurities are accompanied by oxygen vacancies (TiO_2:Zr:v(O)). In this case, the electron effective masses are equal to $0.58m_e$ and $4.74m_e$ for Γ−F and Γ−Z directions, respectively. The effective masses of holes are equal to $2.91m_e$ in the Γ direction and $2.12m_e$ in the F direction (see Fig. 6.7). One can conclude that the Zr impurities accompanied by v(O) decrease the mobility of electrons in the Z direction preferring the electron transfer in XY direction and also decreases the mobility of holes.

The above-discussed results obtained for the TiO_2:Zr:v(O) structure were studied for the v(O) located close to the Zr ion. The v(O) in the TiO_2:Zr structure were also introduced far from Zr ions (see “TiO_2:Zr:v(O) far” in Table 6.2). This structure does not differ significantly from the TiO_2:Zr:v(O) but the electron properties of both structures are different. The structure with v(O) located far from Zr ions possesses a direct energy gap in contrast to the structure with the v(O) located close to Zr ion, which is indirect. The band gap energy of the "TiO_2:Zr:v(O) far" structure is equal to 3.36 eV, which is not correct compared with experimental data. Results presented in the work of Bartkowiak et al.[38] show that the best agreement is between results obtained for TiO_2:Zr:v(O) and the experiment. The band gap energy measured for TiO_2 doped by Zr^{4+} ions in the content of 0, 1.2 %, 3.7 %, and 5.6 % poses values of 3.22 eV, 3.27 eV, 3.26 eV, and 3.28 eV, respectively keeping the indirect bandgap. It means that the Zr impurities increase the energy gap of the TiO_2 crystal, but it must be remembered that the real crystal structure is always associated with oxygen vacancies. Calculated band gap energy for TiO_2:Zr:v(O) (the v(O) is located close to the Zr^{4+} ions) is equal to the 3.28 eV giving excellent agreement with the experiment.

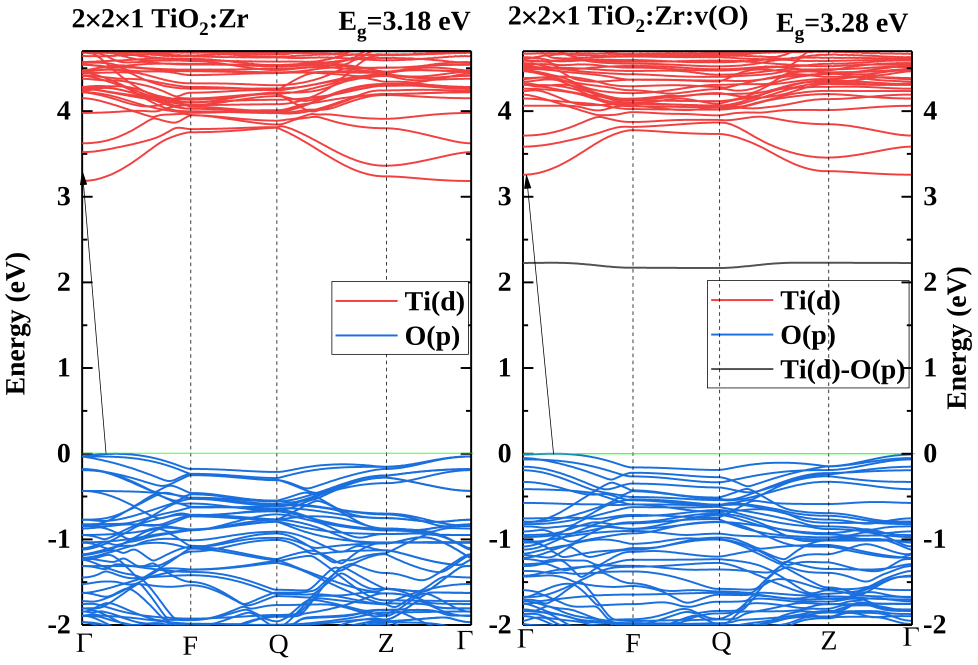

Figure 6.7. Energy band structure calculated by DFT/PBE+U method for the 2×2×1 TiO_2:Zr and TiO_2:Zr:v(O) crystal structure ($U_{Ti}= U_{Zr}$=9.25 and $J_{Ti}= J_{Zr}$=1.00 eV)

Calculating the geometry and electron parameters of the Ni, Mn, and Cu doped TiO_2 crystal the Hubbard correction was also applied. For all impurities, the J_M (where M=Ti, Ni, Mn, and Cu) was chosen to be equal to 1 eV. To optimize the geometry of doped structures the U_{Ti}=6 eV for Ti atoms was chosen according to data presented in Table 6.1 and literature[24,38]. The Hubbard correction selected as U_{Mn}=8 eV is in agreement with the value implemented for MnO antiferromagnetic oxides[39]. The Hubbard parameter U_{Cu}=7 eV was chosen as it was selected for CuO crystal[40]. Was found that the Hubbard correction for the Ni atom varies depending on the publications U_{Ni}=6.3 eV and J_{Ni}=1 eV[41] to U_{Ni}=5.7 eV and J_{Ni}=1 eV[42]. In the presented work calculations with different Hubbard parameters were performed and was found that the best results are obtained using U_{Ni}=6 eV. The chosen parameter is the same as the one proposed for the Ti atom according to the similarity of their ionic radius. Ti has an ionic radius equal to 147 pm and Ni possesses an ionic radius equal to 125 pm.

Analyzing data presented in Table 6.2 one can see that the chosen impurities substitutionally introduced into TiO_2 do not stabilize anatase as it was observed in the case of Zr dopants. A high concentration of impurities equal to 6% makes anatase crystals less stable in the case of all studied dopants. One can conclude that the Ni dopant is too small to correctly substitute titanium in oxygen octahedra. It is manifested in a significant decrease in the *c* cell edge (in TiO_2:Ni_{Zn} c=9.64 Å, in TiO_2 = 9.70 Å). The Ni can be added to the structure only in very low concentration because it makes big stress for the TiO_2 structure. The high concentration of Ni in the anatase structure shows its destruction. It is in agreement with the work of Raguram and Rajni[43] concluding that Ni substituting Ti atom has a strong impact on crystal structure decreasing its *c* edge almost without changing the *c/a* ratio. The Cu and Mn impurities give a crystal unit cell edge equal to 9.66 Å and 9.70 Å, respectively. The obtained data are in agreement with the ones presented by Nagavani and coworkers for the $Ti_{0.925}Cu_{0.075}O_2$ structure[44]. The Mn impurities can be added to the a-TiO_2 structure substitutionally without any significant stress. Also, the stability of the TiO_2:Mn structure is better than the one of the TiO_2:Cu and TiO_2:Ni crystals but it is worst that the stability of the pristine anatase. It is in agreement with the work of Chauchan and Kumar[45]. They show that at 300°C concentrations of 3.5 and 10 mol% of Mn do not show any effect on the host structure. Additionally, they prove that at room temperature the TiO_2 structure is in anatase polymorph but at 800°C became completely rutile. Also, Ghasemi et al. show that higher concentrations of Mn (20 mol%) and calcination temperature of 450°C by 4 hours transfer anatase into rutile almost completely[46].

Analyzing the data presented in Table 6.2, one can see that the TiO_2:Ni:v(O), TiO_2:Cu:v(O), and TiO_2:Mn:v(O) structures are more stable than the native structures without v(O). It allows us to conclude that the Ni, Cu, and Mn-doped TiO_2 structures really can exist only accompanied by v(O). The implemented impurities give 2% changes in the bond length of the investigated crystals compared with the experiment. So it can be concluded that the obtained structures can be used to study electron parameters of the doped TiO_2.

Electron properties of the TiO_2 doped by Cu, Ni, and Mn impurities were calculated using the same method as was presented for the pristine as well as v(O) and v(Ti) defective crystals. They were calculated following a simple path in the Brillouin zone depicted as Γ-F-Q-Z-Γ. Additionally, spin-polarized calculations with Fermi smearing were adopted. In this case, the following Hubbard parameters were used: U_{Ti}=9.25 eV[24,38], U_{Mn}=7 eV[47], U_{Ni}=6 eV[48] , and U_{Cu}=7 eV[49]. For all atoms, the J parameter was equal to 1 eV. The calculated energy band structures are presented in Fig. 6.8.

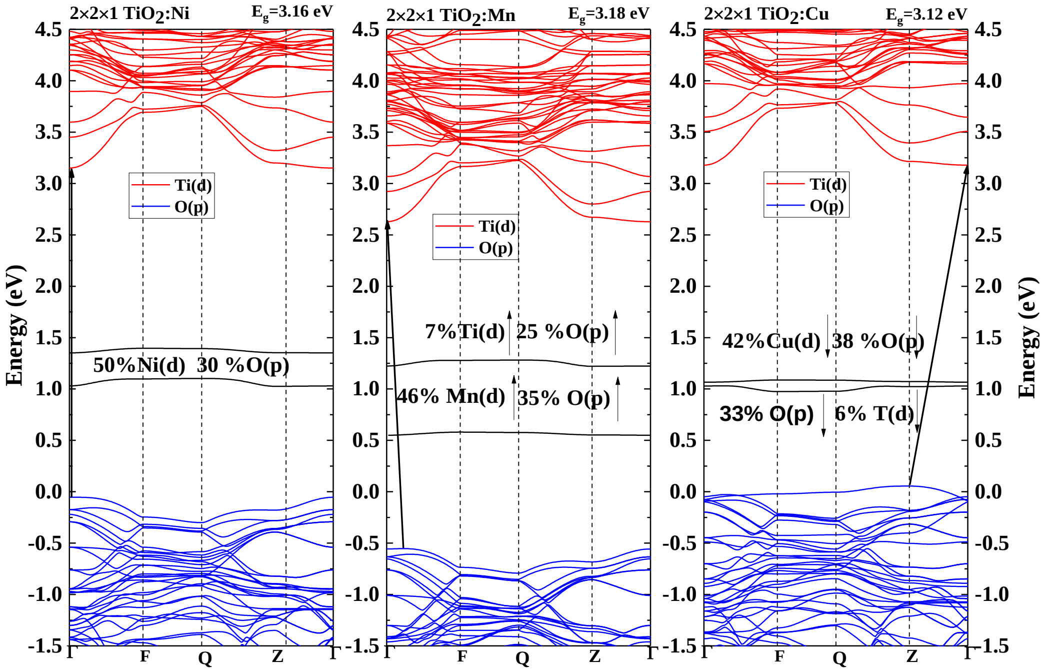

Figure 6.8. Energy band structure calculated by DFT/PBE+U method for the 2×2×1 TiO_2 crystal doped substitutionally by Ni, Mn, and Cu ions (J_M=1.00 eV, where M=Ti, Ni, Mn, Cu, U_{Ti}=9.25, U_{Ni}= 6.00 eV, U_{Cu}=U_{Mn}=7.00 eV)

All studied dopants Ni, Mn, and Cu create two donor states in the bandgap, nearly 1 eV higher than the VBM. Additionally, they do not make any significant effect on the dispersion of Ti(d) states (unoccupied energy levels). Some changes, compared to the pristine TiO_2, in energy dispersion are seen for occupied energy states in the Z point of the Brillouin zone. The Ni impurity changes the character of the semiconductor to be direct. Ni dopants affect the O(p) states giving the effective masses of holes equal to 20.9m_e in the Γ-F direction and 1.41m_e in the Γ-Z direction.

The effective masses of electrons in the Γ-F direction have the same value as it was calculated for pristine TiO_2 but in the Γ-Z direction are equal to $4.10m_e$.

The TiO_2:Mn is an indirect semiconductor as it is noticed for pristine anatase. Effective masses of electrons in Γ−F and Γ−Z directions are equal to $0.58m_e$ and $5.00m_e$, respectively. The effective masses of holes are equal to $3.81m_e$ and $1.82m_e$ in F and Γ direction, respectively. Compared with pristine anatase one can see that effective masses of charge carriers calculated for TiO_2:Mn are bigger.

Cu impurities significantly affect the O(p) states changing the nature of the VBM→CBM transition making it from Z to Γ point of BZ. Electron effective masses of the TiO_2:Cu structure are equal to $0.60m_e$ and $5.62m_e$ in Γ−F and Γ−Z directions, respectively. The hole effective masses from the Z to Q direction are equal to $9.83m_e$ and from Z to Γ direction they are equal to $2.71m_e$. The charge carriers' mobility of the TiO_2:Cu is expected to be the lowest of all investigated doped TiO_2 structures.

The energy band structures calculated for the substitutionally doped TiO_2 by Ni, Mn, and Cu accompanied by v(O) are presented in Fig. 6.9. The TiO_2:Ni:v(O) structure demonstrates the nature of the indirect semiconductor in contrast to the TiO_2:Ni material. The electron effective masses of TiO_2:Ni:v(O) are equal to $0.62m_e$ and $16.33m_e$ in Γ−F and Γ−Z directions, respectively. The effective masses of holes are equal to $1.82m_e$ in the Γ direction and $1.49m_e$ in the F direction. One can see that the v(O) decreases the mobility of the electrons but increases the mobility of holes compared to TiO_2:Ni. The Ni(d) and O(p) states create acceptor energy levels located near the VBM. Additionally, the donor energy level created by the hybridization of the Ni(d), Ti(d), and O(p) is present in the bandgap located close to the CBM (see Fig. 6.9). It explains the strong red shift occurring in TiO_2 crystals doped by Ni^{2+} ions mainly attributed to the Ni^{2+} *d* electrons and *sp-d* exchange interaction[50]. Experimentally, the TiO_2 doped by 5 mol% of Ni exhibits a band gap energy equal to 2.50 eV[43.] It is in agreement with data presented in Fig. 6.9 where the Ni impurities are accompanied by v(O). One can see that the Ni dopants with v(O) decrease the band gap energy of the pristine TiO_2. It allows us to conclude that the TiO_2:Ni:v(O) could be a good candidate for photovoltaic applications. This statement can be given additionally to the fact that Ni impurities increase the porosity of the synthesized mesoporous TiO_2[50] which is useful in photovoltaics.

The Mn impurities accompanied by the v(O) create two acceptor energy levels built by Mn(d) and O(p) states located close to the VBM (see Fig. 6.9). The TiO_2:Mn:v(O) is the indirect semiconductor giving the longest electron excitation lifetime from all doped materials discussed in this work. Santra et al. [51] show that Mn^{2+} gives significant short-circuit current and open-circuit voltage benefiting from a long lifetime of excited electrons[52]. The electron transition can occur from Mn(d)-O(p) states in the Q point of BZ to Ti(d) in Γ point of BZ (black arrow). Here also the fundamental transition from the O(p) state in the F point of BZ to the Ti(d) states in Γ point of BZ is present. Booth transition gives a high electron excitation lifetime beneficial for photoanodes in DSSC.

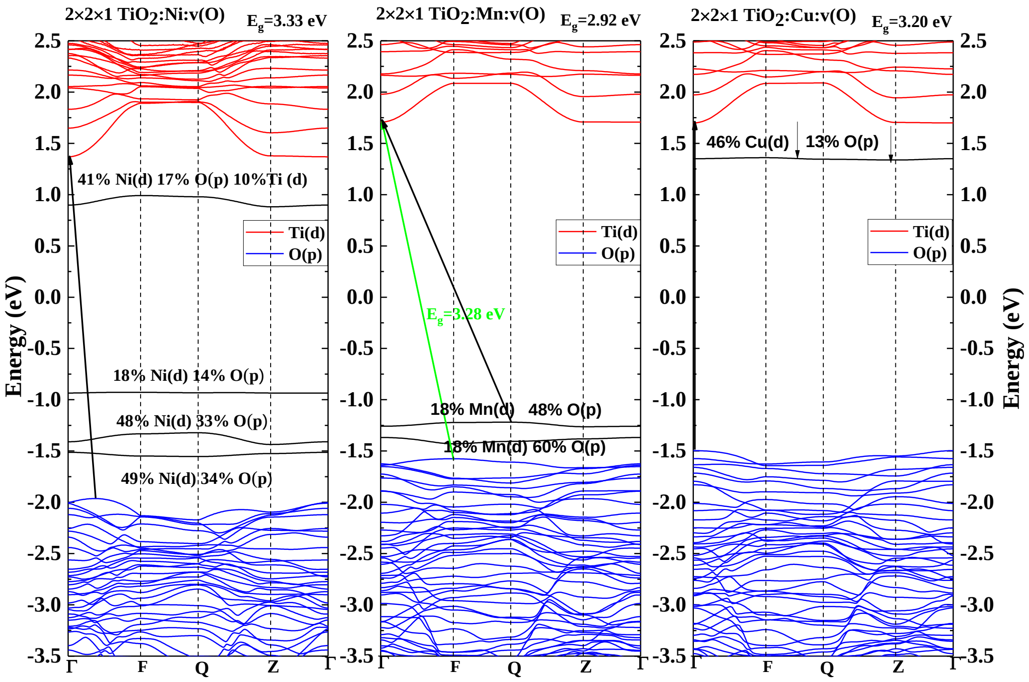

Figure 6.9. Energy band structure calculated by DFT/PBE+U method for the 2×2×1 TiO_2 crystal doped substitutionally by Ni, Mn, and Cu ions accompanied by oxygen vacancies (J_M=1.00 eV, where M=Ti, Ni, Mn, Cu, U_{Ti}=9.25, U_{Ni}= 6.00 eV, U_{Mn}= U_{Cu}= 7.00 eV)

Electron effective masses in the TiO_2:Mn:v(O) material are equal to $0.72m_e$ in the Γ−F direction, however, in the Γ−Z direction the respected value is huge. One can say that it is infinite taking into account the selected model of calculations. The hole effective masses calculated for the TiO_2:Mn:v(O) are higher than the ones calculated for the other studied materials. Chauchan and Kumar[45] detected experimentally a slight redshift in the optical absorption spectrum caused by decreasing energy bandgap of the Mn-doped TiO_2 from 3.00 eV to 2.95 eV compared with pristine TiO_2. They explain this by the appearance of new energy levels created by Mn(d) electrons which is in agreement with the computationally obtained data.

The Cu impurities accompanied by v(O) in TiO_2 structure change the electron structure of the semiconductor to be direct with added very localized Cu(d) donor energy level close to CBM. It is a strong recombination center giving the possibility of a very fast direct transition from the conductional band to donor Cu(d). Electron effective masses calculated for the TiO_2:Cu:v(O) structure are equal to $0.68m_e$ and infinite value in Γ-F and Γ-Z direction, respectively. The effective masses of holes are equal to $5.00m_e$ in the Γ-F direction and $3.16m_e$ in the Γ-Z direction. These values are comparable with the ones obtained for the TiO_2:Mn:v(O) structure. All data mentioned earlier gives the idea that Cu must be avoided as a dopant of TiO_2 crystal for photoactivated devices. Similar results were published by Navas et al.[53] showing that doping of 0.767 % of Cu by mass makes a significant drop in *Jsc* compared with pristine TiO_2. They showed that Cu in TiO_2 structure leads to a decrease in band gap energy exceeding 10%.

6.1.3. Defective 2×2×1 TiO_2 structure doped interstitially

Ions such as Cu, Ni, and Mn were also introduced into the TiO_2 structure interstitially. Unfortunately, the selected method of simulation does not give satisfactory results. Interstitially introduced dopants deform the crystal structure of the TiO_2. They increase the *a* and *b* edges of the unit cells (see Table 6.2). The observed unit cell deformations create stress in the crystal structure causing its instability. One can also conclude that the impurities change drastically the unit cells' parameters making them incompatible with the pristine crystal structure.

Results for the TiO_2 structure doped by Ni in the interstitial position are not presented in Table 6.2, because the geometry optimization procedure performed for this structure did not converge maintaining the required parameters. One can conclude that the $TiO_2:Ni_{in}$ structure is unstable. Structures such as $TiO_2:Zr_{in}$ and $TiO_2:Ti_{in}$ are less stable than TiO_2:Zr and the pristine TiO_2. The $TiO_2:Cu_{in}$ and $TiO_2:Mn_{in}$ structures are more stable but calculated their energy band structures are unrealistic compared with experimental data. Mainly it is argued by the direct band gap observed for all structures.

Computational results obtained for the interstitially doped TiO_2 in anatase form taking into account Cu, Ni, and Mn impurities give the idea to not describe them in detail here. It can be argued by the fact that these structures cannot be used for photovoltaic applications.

The results presented in Chapters 6.1.1 – 6.1.3 are partially reported in the paper titled “Experimental and theoretical insight into DSSCs mechanism influenced by different doping metal ions” and published in *Applied Surface Science*. This work is authored by A. Bartkowiak, O. Korolevych, G. L. Chiarello, M. Makowska-Janusik, and M. Zalas[54]. Also, the results reported here are presented in the work prepared by A. Bartkowiak, O. Korolevych, G. L. Chiarello, M. Makowska-Janusik, and M. Zalas, titled "How Can the Introduction of Zr^{4+} Ions into TiO_2 Nanomaterial Impact the DSSC Photoconversion Efficiency? A Comprehensive Theoretical and Experimental Consideration." published in *Materials*[38]. The experimental part of these works was performed at Adam Mickiewicz University, Poznan mainly by A. Barkowiak. My contribution to the mentioned works was the realization of all quantum chemical calculations.

6.1.4. The 2×2×1 TiO_2 structure doped by nitrogen

In comparison to data presented in Chapters 6.1.2 and 6.1.3, the a-TiO_2 crystal was also doped by N atoms. Contrary to the cation dopants such as Zr, Ni, Mn, and Cu, the N ions are anions. To simulate the geometry of the N-doped TiO_2 the Hubbard correction parameters were applied only for Ti atoms taking into account U_{Ti}=6 eV and J_{Ti}=1 eV. The N and O atoms were taken into consideration without any Hubbard parameters. The created structures for the mentioned calculations are presented in Fig. 6.10.

Analyzing data presented in Table 6.2 one can see that the stability of the newly created N-doped TiO_2 structures is the worst when the N atom is substitutionally introduced into the crystal replacing the Ti atom (see Fig. 6.10.a - TiO_2:N). This structure is mostly unstable from all studied structures in this work. More structurally stable are crystals with N introduced interstitially (see Fig. 6.10.b - TiO_2:N_{in}) and N doped interstitially accompanied by v(O) (see Fig. 6.10.c - TiO_2:N_{in}:v(O) and see Fig. 6.10.d - TiO_2:N_{in}:v(O) far). In the case of the TiO_2:N_{in} structure, it is seen that the N atom moves into a position of oxygen trying to submit it. The same results were described by Harb et al.[55]. One can conclude that better structural stability reflects in unchanged unit cell edges compared with pristine TiO_2 crystal structure. The existence of the TiO_2:N_{in}:v(O) structures was proved by analyzing the rf-sputtering results of TiO_2 film deposition [56,57]. The obtained results show that the N atom completely substitutes near located v(O). Based on all information mentioned earlier, one can make the suggestion, that the TiO_2:N_O configuration shows the highest possibility to exist in real structures[58].

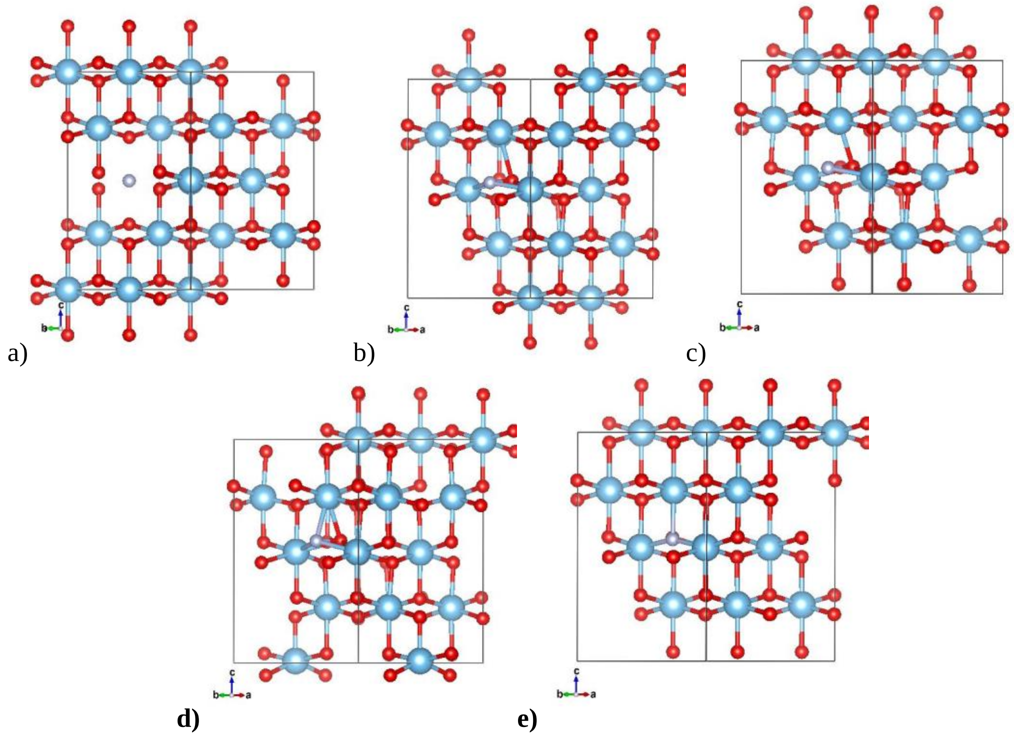

a) b) c)

d) **e)**

Figure 6.10. Optimized unit calls of the 2×2×1 TiO_2 crystal doped by N atoms: a) substitutionally TiO_2:N; b) interstitially TiO_2:N_{in}; c) interstitially with oxygen vacancy TiO_2:N_{in}:v(O); d) interstitially with oxygen vacancy located far from N atom TiO_2:N_{in}:v(O) far; e) N substitute O atom TiO_2:N_o. Blue atoms - Ti, red atoms - O, and grey atoms - N

Calculating electron parameters of the structures presented in Fig. 6.10 the Hubbard correction parameters were used as follows: U_{Ti}=9.25 eV and J_{Ti}=1 eV. The N(p) electrons were considered without Hubbard corrections as well as with U_N=6 eV and J_N=1 eV and also U_N=9.25 eV and J_N=1 eV parameters. Calculated energy band structures using various Hubbard parameters are presented in Fig. 6.11. The TiO_2:N_{in} structure is an indirect semiconductor. Changing the Hubbard parameters the two acceptor energy levels are added close to the VBM. These energy levels are mostly created by the O(p)-N(p) state with small hybridization of the Ti(d). The higher laying acceptor state is significantly localized. The lower acceptor energy level is going to be closer to the VBM increasing the Hubbard parameter from U_N=0 eV up to U_N=9.25 eV.

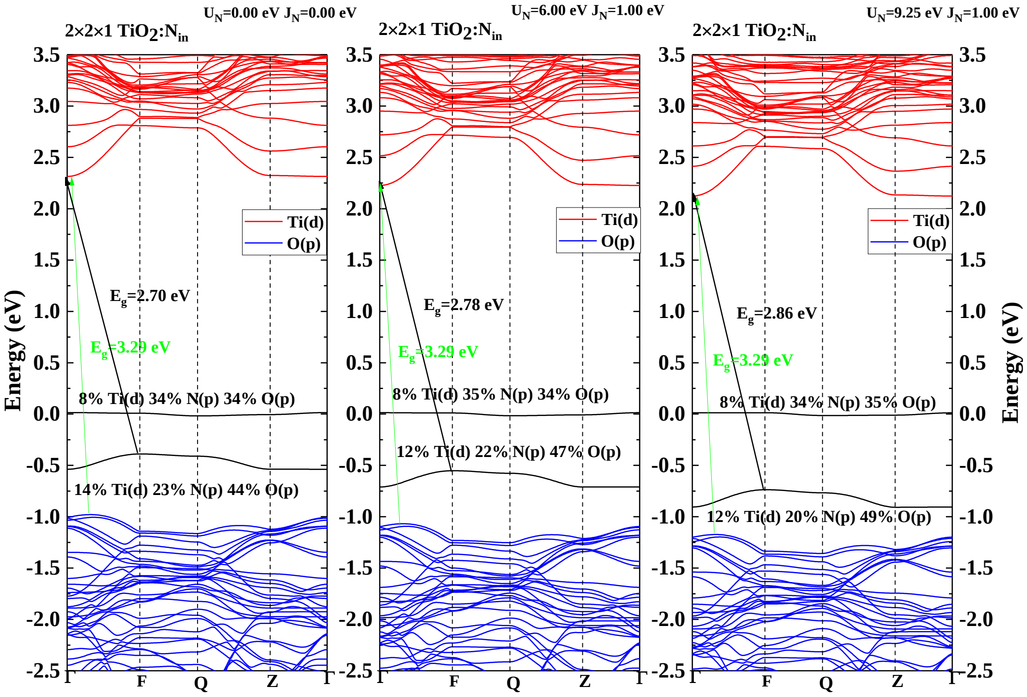

Figure 6.11. Energy band structure calculated by DFT/PBE+U method for the 2×2×1 TiO_2 crystal doped interstitially by N atom with different Hubbard correction parameters for N atom and U_{Ti}=9.25 eV, J_{Ti}=1.00 eV

It is controversial, which of the proposed Hubbard parameters is the best for an appropriate description of the electron properties of the $TiO_2:N_{in}$ structure. Based on experiment data, one can observe that nitrogen in a-TiO_2 made a small shift in UV-vis absorption spectra (see Fg. 6.12). It should be the consequence of the narrowing of the energy bandgap by adding the additional dopant energy states. It allows us to conclude that the appropriate will be to use U_N=9.25 eV and J_N=1.00 eV because these parameters give a hybrid O(p)-N(p) state located close to the valence band (see Fig. 6.11). In consequence was decided to calculate the electron properties of the other N-doped TiO_2 structures applying for N(p) electrons the Hubbard correction parameters equal to U_N=9.25 eV, J_N=1.00 eV.

In Fig. 6.13 the energy band structures for $TiO_2:N_{in}$:v(O) and $TiO_2:N_{in}$:v(O) far are presented. In both cases, the strongly localized energy trap levels created by oxygen vacancies located close to CBM are seen. These donor energy levels can cause the recombination of charge carriers. In these structures, the N impurities create two acceptor states located close to VBM as is seen for the $TiO_2:N_{in}$

structures (see Fig. 6.11). One can conclude that the donor states created by v(O) in the TiO_2:N_{in}:v(O) or in TiO_2:N_{in}:v(O) far can create the shoulder observed in the UV-vis spectrum located at a longer wavelength side. Additionally, should be mentioned that the conductivity of the TiO_2:N_{in}:v(O) and TiO_2:N_{in}:v(O) far structures will be very limited due to low energy dispersion of the donor and acceptor states.

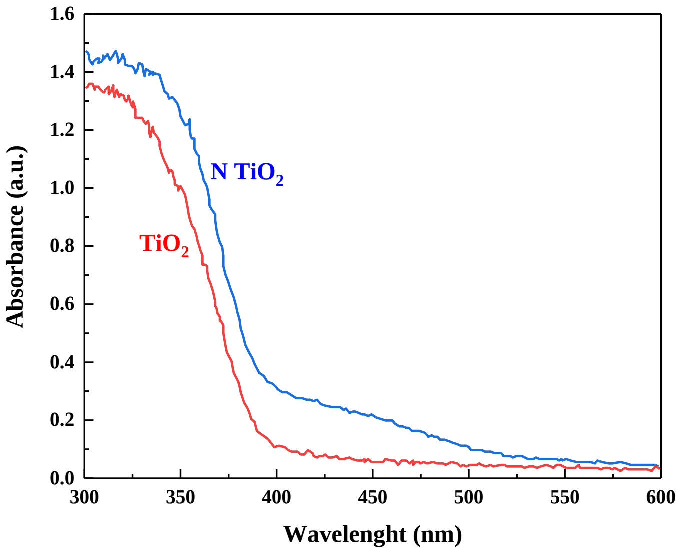

Figure 6.12. UV-vis absorption spectra of TiO_2 (P25) and N-TiO_2 calcined at 400°C for 3h measured experimentally[58]

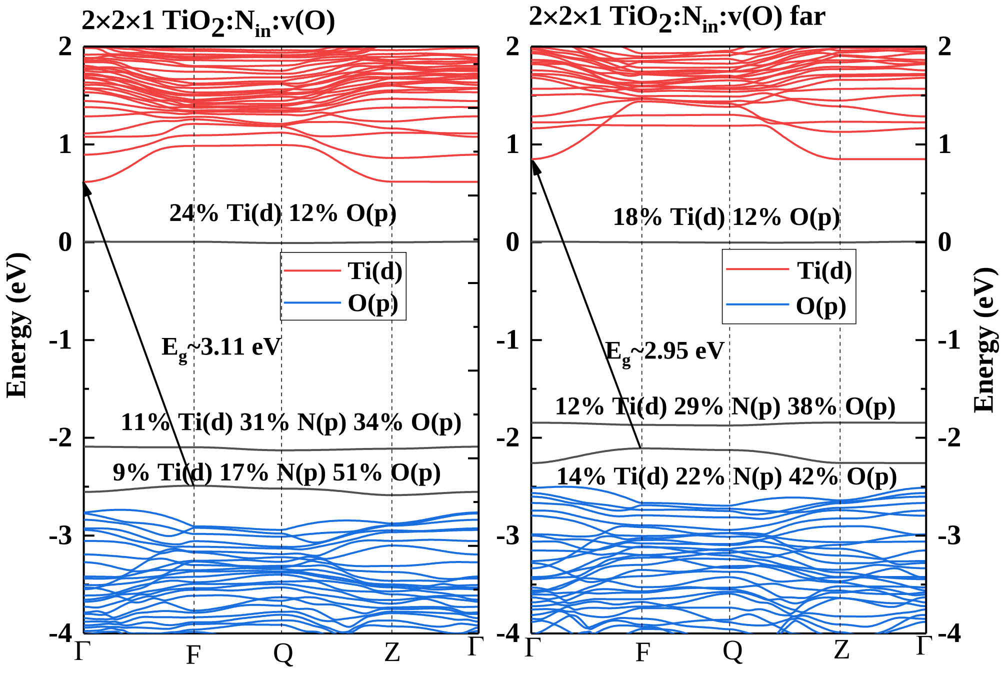

Figure 6.13. Energy band structure calculated by DFT/PBE+U method for the 2×2×1 TiO_2 crystal doped interstitially by N accompanied by oxygen vacancies located close and far from N atom (U_{Ti}= U_N =9.25 eV, J_{Ti}=J_N=1.00 eV)

In Fig. 6.14 the energy band structure and electron density of states calculated for TiO_2:N_O is presented. In this case, an additional dopant energy level is created. This acceptor hybrid N(p)-O(p) energy state is located at a distance of 0.80 eV from the VBM. The obtained results can explain the redshift of the electron absorption spectra of N-doped TiO_2 compared with the pristine anatase observed in the experimental UV-vis spectrum (see Fig. 6.12)^{58}. It can also prove the above-discussed statement that the N atom implemented into the TiO_2 structure interstitially tends to be located in the place of oxygen. Effective masses of electrons calculated for TiO_2:N_O are equal to 0.50m_e and 3.48m_e in Γ−F and Γ−Z direction, respectively. The effective masses of holes are 2.64m_e and 1.84m_e in the Γ and the F direction, respectively. It is worth noticing that the effective electron mass in the Γ−F is the lowest one of all calculated structures. It means that the mobility of electrons in the TiO_2:N_O across the mentioned direction will be the highest.

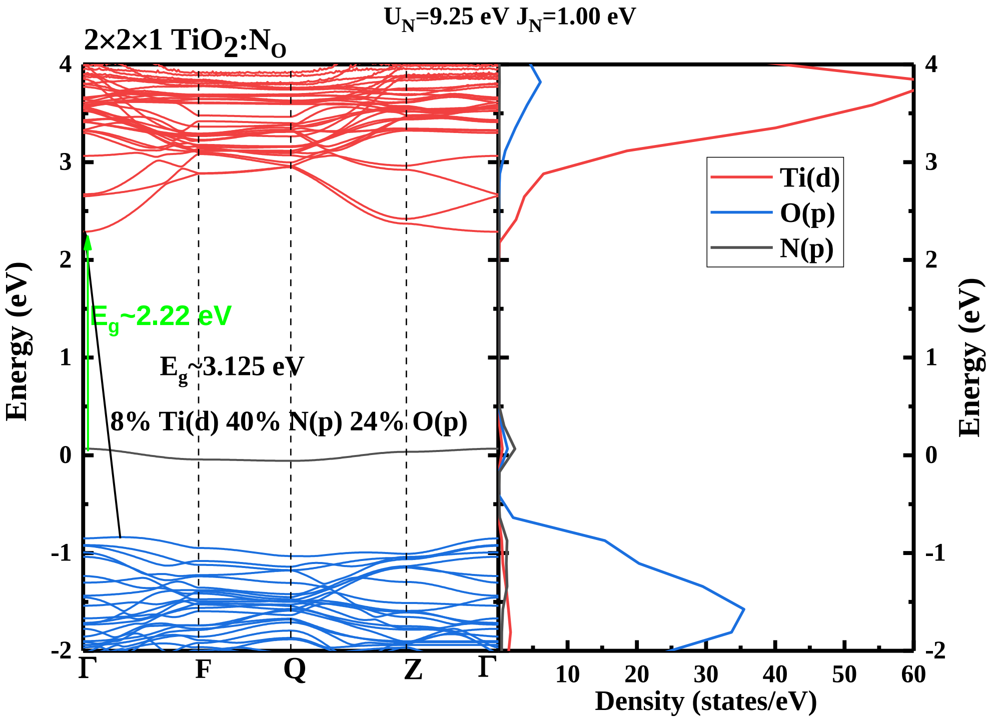

Figure 6.14. Energy band structure and electron DOS calculated by DFT/PBE+U method for the 2×2×1 TiO_2 crystal doped substitutionally by N replacing O atom (U_{Ti}= U_N =9.25 eV, J_{Ti}=J_N=1.00 eV)

Although were made attempts to calculate the position of the VBM and CBM of the calculated a-TiO_2-based structures concerning the vacuum and normal electrode (NSE). First of all the calculated data obtained for a-TiO_2 crystal were rescaled to experimental results^{59}. Then the data obtained for all studied structures were rescaled using the same factor. The final results are presented in Fig. 6.15. One can see that the TiO_2:Ni:v(O), TiO_2:Mn:v(O), and TiO_2:Cu:v(O) show a shift of CBM lowering it at ~0.25 eV compared with the pristine TiO_2. Additionally, for the TiO_2:Mn:v(O) narrowing of the energy bandgap is seen. These materials can be good candidates for DSSC applications. As was mentioned above the TiO_2:Ni_O has a high mobility of electrons and a reduction of energy bandgap is seen but the CBM and VBM shift insignificantly compare with pristine TiO_2.

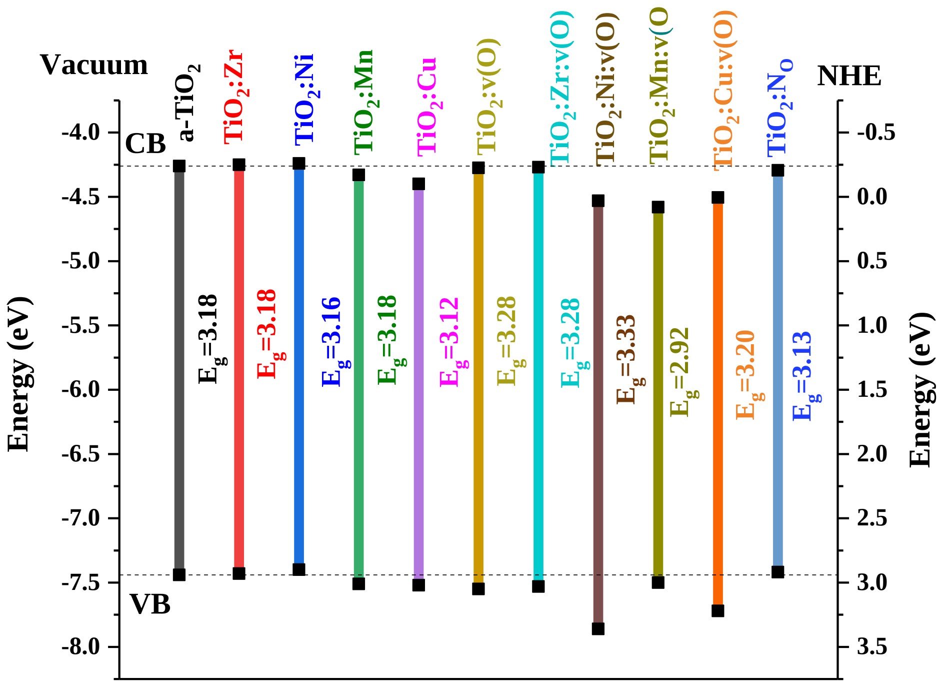

Figure 6.15. Valence band maximum (VBM) and conduction band minimum (CBM) for structures based on a-TiO_2 crystals structure modified by dopants and vacancies calculated by DFT/PBE+U method normalized by scaling factor concerning pristine anatase crystal

6.2. Structural and electron properties of thin films based on TiO_2 structures

In DSSC devices the surface of the semiconductor plays a very important role. In this case, the surface of the modified a-TiO_2 will be investigated according to its structural stability and electron properties. All simulations were performed using the VASP program package. In all calculations, the Hubbard correction parameters were taken into consideration keeping their values as it was specified for bulk structures.

The energetically most stable surface of the a-TiO_2 crystal with energy 0.43 J m^{-2} is the one with indexes (101)[60]. The other crystallographic surfaces have the energies as follows: (010) 0.53 J m^{-2}, (001) 0.90 J m^{-2}, (110) 1.09 J m^{-2}, and (111) 1.61 J m^{-2}[61]. In the presented work thin films of a-TiO_2 were built cutting the crystal by mentioned above crystallographic planes. These structures were based on the 2×2×1 supercell of a-TiO_2 bulk material. In consequence, the super cells were built by adding two times the c-unit cell edge of a-TiO_2 bulk material as a vacuum space (see Fig. 6.16). In the presented thin films 16 units of the TiO_2 were taken into consideration.

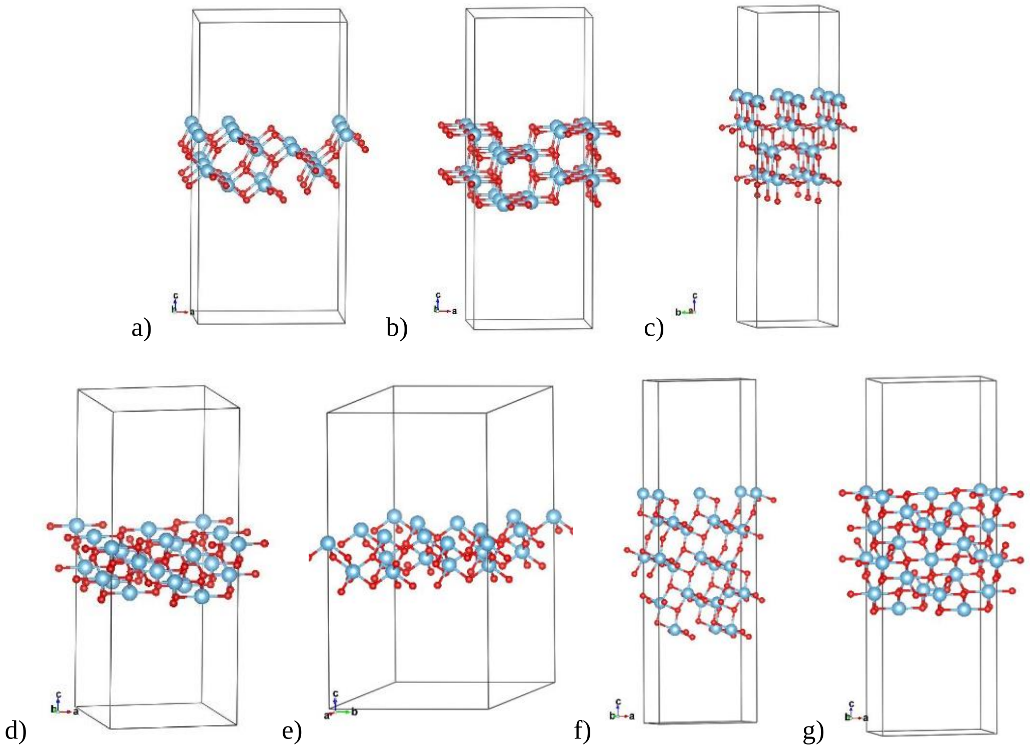

Figure 6.16. Structure of the a-TiO_2 thin films cut with a crystallographic plane: a) (101), b) (010), c) (001), d) (110), and e) (111) based on 2×2×1 super cell and cut with a crystallographic plane: f) (101), and g) (110) based on 1×1×1 unit cell (Ti - blue atoms, O - red atoms)

In our simulation were made attempts to create this film based on the (101) anatase surface (see Fig. 6.16a) but created atomic structure was straggling in the relaxation procedure according to the significant number of dangling bonds. In consequence, its geometry optimization procedure was not finished successfully giving the stable atom configuration. The same situation was noticed for the (001) surface (see Fig. 6.16b). Also, the structure based on (001) crystallographic surface is not a good example for quantum chemical calculations (see Fig. 6.16c) according to the homo-atom arrangement on the surface. In consequence, the top surface of the thin layer is made of Ti atoms and the bottom surface of O atoms, which gives a large dipole moment of the structure and drastically affects its electron properties.

The same problem with an unrealistic dipole moment was noticed for the (111) surface (see Fig 6.16e). The appropriate structural model of the a-TiO_2 thin film was obtained taking into consideration the (110) surface (see Fig. 6.16d). In consequence, was decided that all simulations described in the next stages of the presented work will be carried out for thin-layer structures cut with the crystallographic plane (110). These structures will be called in the text “thin films (2)”. Additionally should be noticed that the experimental existence of this kind of surface of the TiO_2 thin layers was reported in the literature[62,63].

Simulation trials of thin films show other critical issues compared with calculations done for bulk materials. Full structural relaxation performed for thin films shows a strong tendency to decrease vacuum space in the created super cell. To prevent this situation one can proceed in two different ways. First of all the unit cell edges can be frozen (a,b,c=const). The other possibility is to freeze the volume of the super (V_{cell}=const) but super cell edges can change. In both cases, ions in super cell can move. The electron parameters of both structures were calculated. In both cases, the increase of the band gap energy compared with bulk TiO_2 is observed proving the quantum size confinement effect occurring with size limitation. For the structure relaxed with frozen cell edges the calculated band gap energy is equal to 3.62 eV. When the V_{cell} is constant the band gap energy is equal to 3.57 eV. One can conclude that both methods give very similar results. According to the time of simulations was decided to focus on cell edges frozen simulations (a,b,c=const).

To increase the thickness of the simulated thin films their super cells were created based on the unit cell of a-TiO_2 multiplying the thickness of the film by 4 compared with previously described layered structures. In this case, as previously, 16 units of the TiO_2 were used. These films named “thick” (see Fig. 6.16f and 6.16g) were used to study the electron properties of layered TiO_2 materials. These structures will be called in the text “thick films (4)”.

The geometry optimization procedures for thin (2) and thick (4) a-TiO_2 films with frozen super cell edges were performed. The stoichiometric TiO_2 structures as well as structures with defects and impurities were considered. Their total energies per atom are collected in Table 6.4. One can see that thin layers (2) are less stable than thick films (4). The structural stability of pristine anatase significantly decreases after transformation between bulk and films changing the total energy from -8.73 eV (see Table 6.2) to -8.56 eV in the case of TiO_2 thick film (4) and to -8.41 eV in the case of the TiO_2 thin film (2) (see Table 6.4).

Table 6.4. Total energy per atom for thin (2) and thick (4) films of TiO_2 obtained by geometry optimization procedure using DFT/PBE method

Films with (110) surface	Total energy/atom (eV)
TiO_2 (4)	-8.56
TiO_2:v(O) (4)	-8.52
TiO_2:Zr (4)	-8.60
TiO_2:Zr:v(O) (4)	-8.56
TiO_2:N_O (4)	-8.51
TiO_2:Ni (4)	-8.31
TiO_2:+Ni (4)	-8.37
TiO_2 (2)	-8.41
TiO_2:Zr (2)	-8.47
TiO_2:Ni (2)	-8.16
TiO_2:N_O (2)	-8.32

Although were made attempts to calculate dopants' influence on structural and electron properties of TiO_2 films. The constructed structures are presented in Fig. 6.17. The Zr shows a significant stabilization of the TiO_2 structure. Also, the Zr impurities accompanied by v(O) stabilize the anatase films. These structures are more stable than the TiO_2:v(O) films. The stability of the anatase film with oxygen substituted by nitrogen (TiO_2:N_O) is lower than the stability of the Zr-doped structures but the difference is not significant. It means that the TiO_2:N_O structure can exist. The Ni doper film of a-TiO_2 shows the same character as it was observed for bulk materials. The TiO_2:Ni film shows strong structural degradation. The obtained results are similar to the ones obtained by Yuan et al.[64]. Calculations to optimize the geometry of the TiO_2:Ni (4) structure with the Ni ion implemented into anatase structure substitutionally (see Fig.6.17e) and adsorbed at the surface of the TiO_2 (see TiO_2:+Ni structure in Fig. 6.17f) were performed. A similar structure was calculated by Billo et al.[65] for titanium nanoclusters. The constructed TiO_2:Ni and TiO_2:+Ni structures have worst stability than other investigated TiO_2 films (4). One can see that adsorption of the Ni at the surface of the TiO_2 is more probable than the interstitial substitution presented in the TiO_2:Ni.

Analyzing data obtained for the TiO_2 (2) films one can conclude that they are too thin. As was mentioned above they are less stable than the films (4). Adding the dopants into these structures deforms them so much that they are going to be unstable and the calculations cannot be performed. The obtained structures are presented in Fig. 6.18.

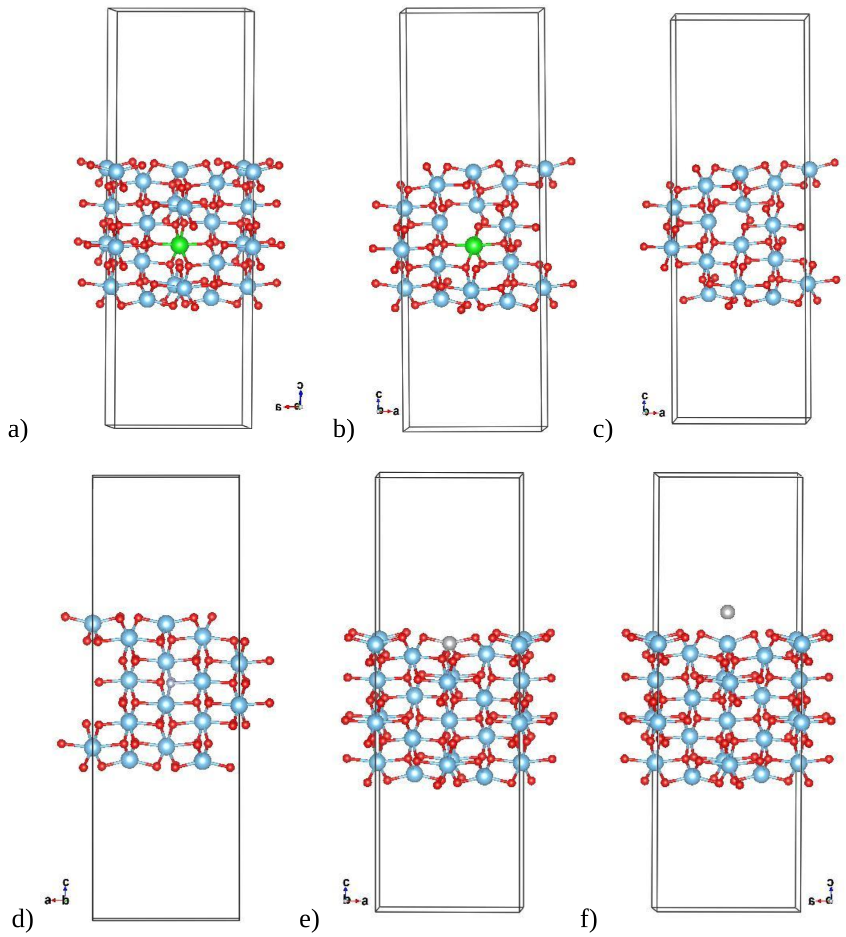

Figure 6.17 Structure of the TiO_2 (4) films defected by dopants: a) TiO_2:Zr (Zr - green atom), b) TiO_2:Zr:v(O), c) TiO_2:v(O), d) TiO_2:N_O (N - light blue atom), e) TiO_2:Ni (Ni - grey atom), and f) TiO_2:+Ni (Ti-blue atoms and O—red atoms)

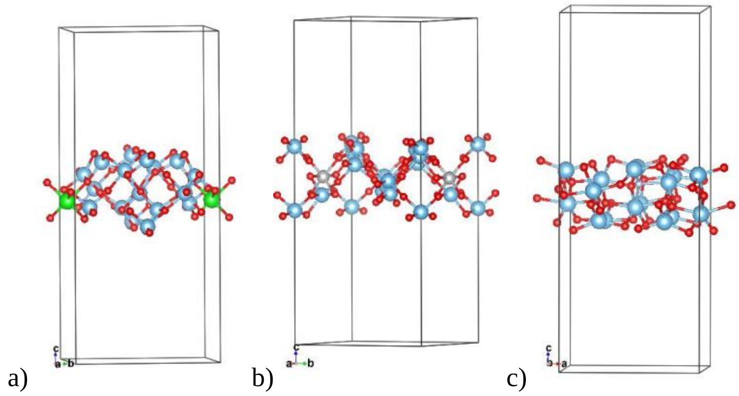

Figure 6.18. Structure of the TiO_2 (2) films defected by a) the Zr atom (TiO_2:Zr, Zr - green atom), b) the Ni atoms (TiO_2:Ni, Ni - grey atom), and c) TiO_2:Ni_o films (N - light blue atom), (Ti-blue atoms, O – red atoms)

Electron properties of the selected films of TiO_2 were calculated by following a simple path in the Brillouin zone depicted as Γ-F-Q-Z-Γ. It is the same path as was used for the 2×2×1 super cell of bulk material. The calculations were performed applying the DFT/PBE method augmented by Hubbard corrections using the same parameters as were applied for bulk TiO_2. The energy band structures calculated for the TiO_2 (2) and TiO_2 (4) thin films compared with the energy band structure calculated for 2×2×1 super cell are presented in Fig. 6.19. One can see that going from bulk to thin film the size quantum confinement effect is observed. The band gap energy calculated for bulk TiO_2 is equal to 3.18 eV. For the thick TiO_2 (4) film, the energy bandgap is equal to 3.24 eV, but for the thin TiO_2 (2) film the energy bandgap is equal to 3.62 eV. The VBM-CBM transition for both films is direct contrary to bulk TiO_2 for which the transition is indirect.

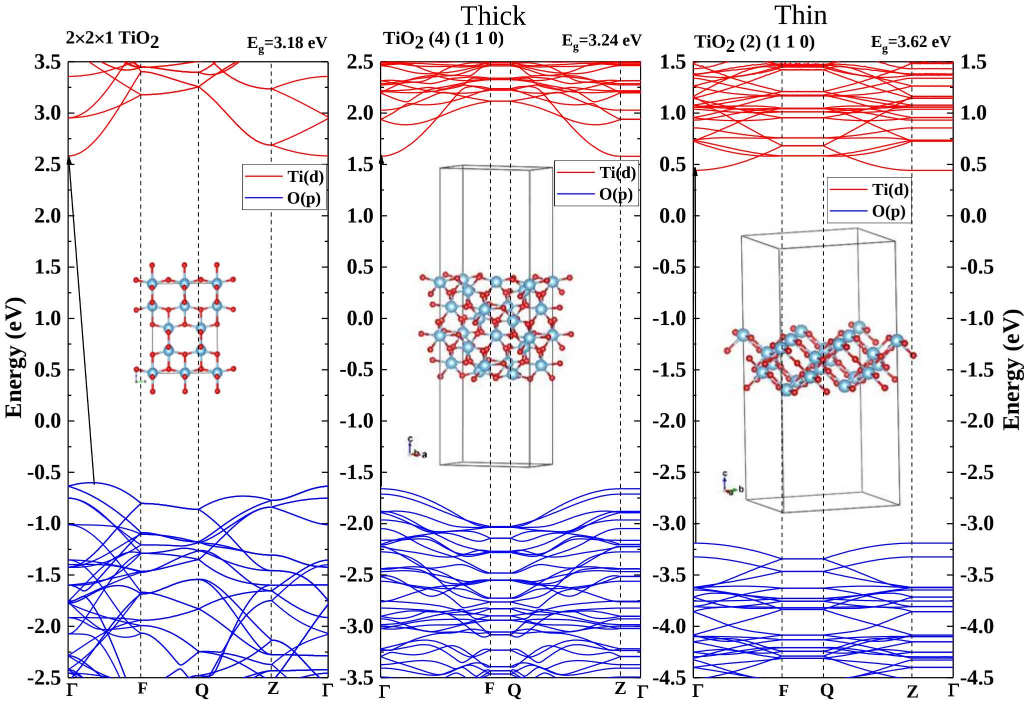

Figure 6.19. Energy band structures calculated by the DFT/PBE+U method for bulk TiO_2 crystal (2×2×1 super cell of TiO_2), for the thick film of TiO_2, described in the text as (4) and for the thin film of TiO_2, described in the text as (2) (Ti - blue atoms, O - red atoms), in all configurations the same Hubbard parameters were used (U_{Ti}=9.25 eV and J_{Ti}=1 eV)

Analyzing Fig. 6.19 one can see that the effective mass for holes and electrons in Γ−Z direction increase to infinity value. Above was mentioned that the effective mass of electrons of the bulk pristine TiO_2 in the Γ−F direction is equal to $0.52m_e$ and the effective mass of holes in the direction of Γ is equal to $1.72m_e$.

Meanwhile for the thick film (4) the effective masses of electrons along the Γ−F direction slightly increase to 0.76m$_e$, and also the effective masses of holes increase to 2.04m$_e$. In the case of thin film (2) the effective mass of electrons increases to 1.08m$_e$, but the effective mass of holes decreases up to the value of 1.83m$_e$.

As was described by Zhang et al.,[8] the introduction of v(O) into the surface of TiO$_2$ results in the shift of the Fermi level toward the conduction-band minimum and generates a defect state within the bandgap of the perfect (110) surface. This state is located at ~2.3 eV higher than the valence band. Exact the same results are given in our simulation performed for the TiO$_2$:Zr:v(O) and TiO$_2$:v(O) layered structures (see Fig. 6.20).

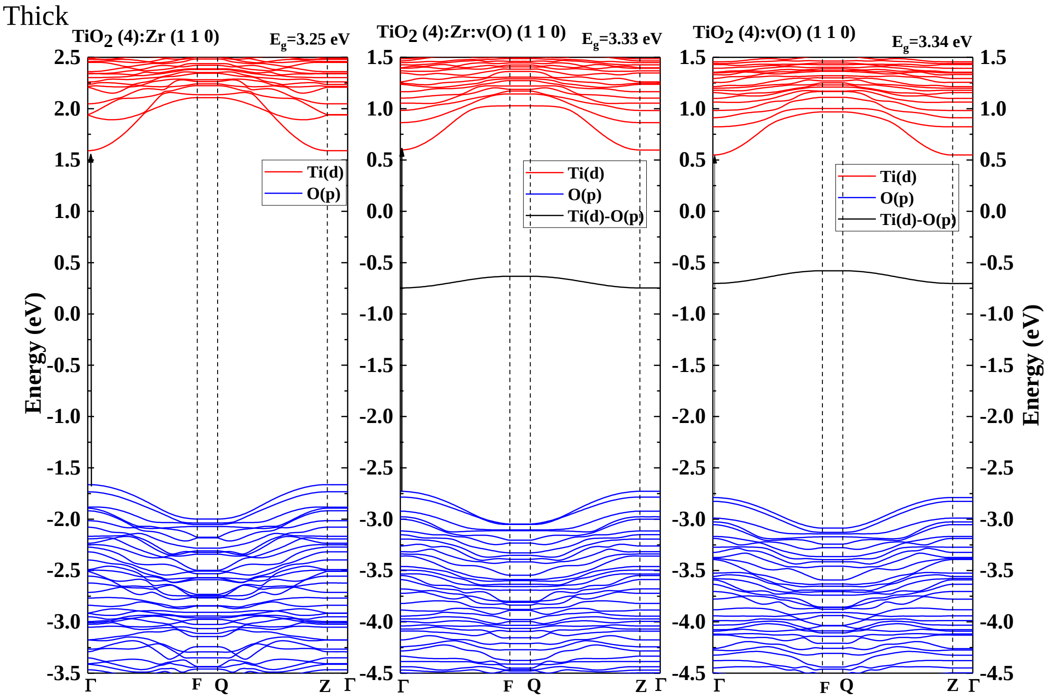

Figure 6.20. Energy band structures calculated by DFT/PBE+U method for the thick film of TiO$_2$ (4) doped by Zr ions (TiO$_2$:Zr), doped by Zr ions and accompanied by v(O) (TiO$_2$:Zr:v(O)), and pristine TiO$_2$ structure defected by v(O) (TiO$_2$:v(O)). In all configurations were used the same Hubbard parameters (U_{Ti}=U_{Zr}=9.25 eV and J_{Ti}= J_{Zr}=1 eV)

In Fig. 6.20 the energy band structures calculated for the TiO$_2$:Zr, TiO$_2$:Zr:v(O), and TiO$_2$:v(O) thick (4) layers are presented. As was shown for the bulk TiO$_2$:Zr structure also for films the Zr ions do not change their electron structure. The calculated effective mass of charge carriers although shows only slight changing between the pristine TiO$_2$ film and defective layers. The effective masses of electrons in the Γ−F direction are equal to 0.77m$_e$ for the TiO$_2$:Zr film, 0.87m$_e$ for the TiO$_2$:Zr:v(O) film, and 0.86 m$_e$ for the TiO$_2$:v(O) film. These values are higher than those values obtained for the TiO_2 (4) film. The effective masses of holes are equal to 1.88m_e, 1.99m_e, and 2.22m_e for TiO_2:Zr, TiO_2:Zr:v(O), and TiO_2:v(O), respectively. The Zr impurities decrease the effective masses of holes and v(O) increases them compared with pristine TiO_2 film structure.

Nitrogen substituting oxygen in $TiO_2:N_O$ decreases the energy band gap creating a dopant energy state near the valence band (see Fig. 6.21). Nitrogen in thin films made the same effect as it was noticed in bulk material. In the Γ−F direction electron's effective mass has the lowest value from all calculated films (0.73m_e). Also, the effective masses of holes are the lowest (1.20m_e). The TiO_2:Ni film structure has an indirect semiconducting character giving a fundamental transition from Ni(d) to O(p) states. These states are strongly localized making it impossible to calculate the effective mass for the hole. Meanwhile, Ti(d) states do not take any significant changes in the direction Γ−F, with electron effective mass equal to 0.78m_e. The film with adsorbed Ni at the TiO_2 surface (TiO_2:+Ni) gives few acceptor energy levels in the forbidden bandgap region. The effective masses of holes are going to be similar to the pristine anatase (2.05 m_e) in the Γ−F direction, and the effective mass of electrons is equal to 0.84m_e.

Thick

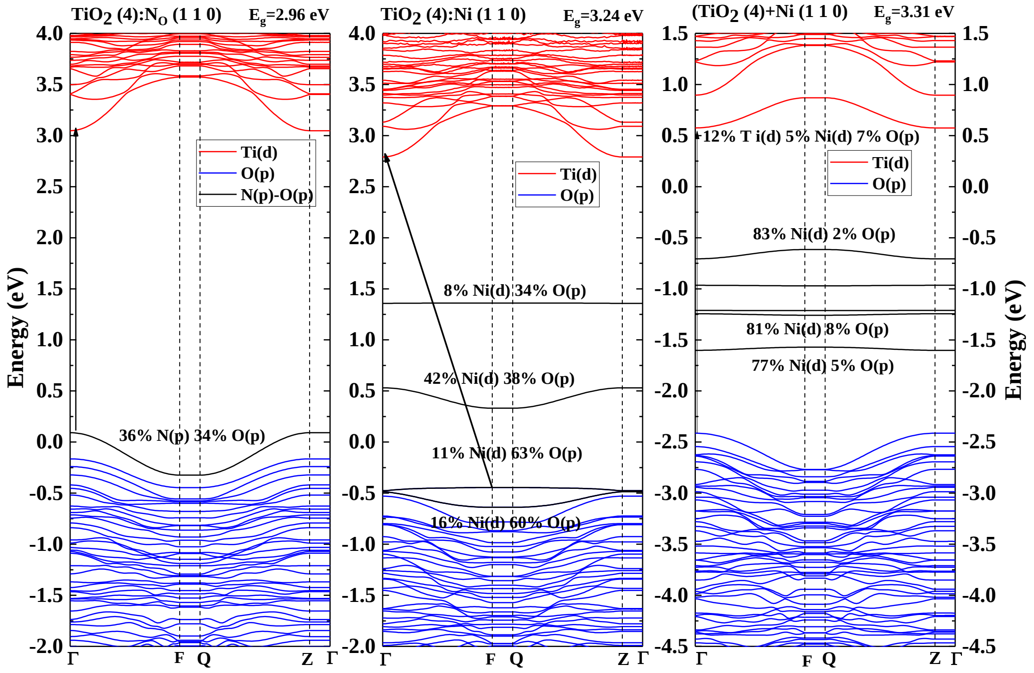

Figure 6.21. Energy band structures calculated by DFT/PBE+U method for the $TiO_2:N_O$ film (4), the TiO_2:Ni film (4), and the TiO_2:+Ni film (4). In all configurations were used the same Hubbard parameters (U_{Ti}= 9.25 eV, U_{Ni}= 6.00 eV, U_N= 9.25 eV, J_{Ti}= J_{Ni}= J_N=1 eV)

Although were simulated electron properties of thin films of TiO_2 (2) (see Fig. 6.22). As was suggested from geometry optimization procedure performance the TiO_2 (2) are too thin to reasonably calculate their electron parameters following the addition of impurities. The dopants make a significant effect on the electron parameters of the host structure. The Zr dopant stabilizes the structure but it makes a significant increase in the band gap energy of the TiO_2:Zr (2) up to 4.24 eV. Simultaneously an effective mass of electrons in the Γ−F direction increases significantly up to $1.69m_e$, and the effective mass of holes in the same direction has infinite value. Also in the case of TiO_2:Ni (2) and TiO_2:N_O (2) their energy states are going to be completely flat. It meant that the charge carriers' mobility in these structures is very low.

Thin

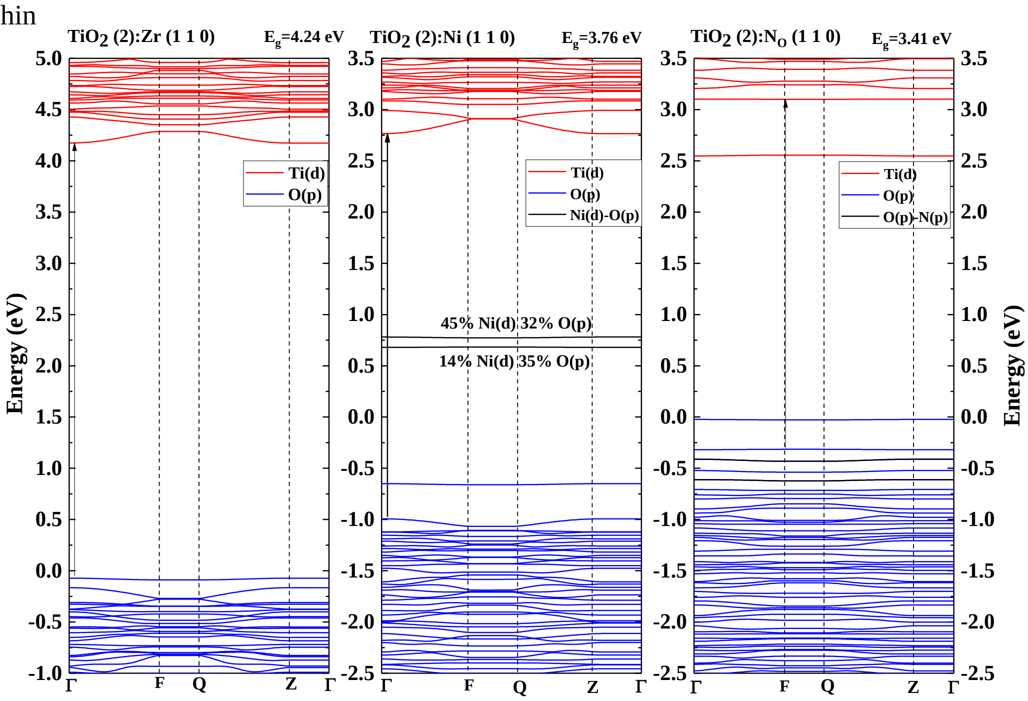

Figure 6.22. Energy band structures calculated by the DFT/PBE+U method for thin films (2) of TiO_2:Zr, TiO_2:Ni, and TiO_2:N_O structures. In all configurations were used the same Hubbard parameters (U_{Ti}=U_{Zr}= 9.25 eV, U_{Ni}= 6.00 eV, U_N= 9.25 eV, J_{Ti}= J_{Zr}=J_{Ni}= J_N=1 eV).

Calculation of the electron properties of other impurities in TiO_2 (2) film was impossible according to the instability of the built atom system. The observed instability is probably because of the small thickness of the layers. Each change in their structure makes a strong effect on obtained electron properties.

6.3. Structural and electron parameters of clusters based on TiO_2 structures

The mesoporous structures of the TiO_2 used for the DSSC application can be modeled as the 0D nanostructural clusters. Compared to the thin films (2D materials) described in Chapter 6.2 clusters are all-dimensional size limited materials. In this Chapter, the nanostructures based on the pristine and modified a-TiO_2 will be investigated and their electron properties will be compared to the experimentally investigated TiO_2-based anodes. The electron properties of nanoparticles are dominated by their high surface-to-volume ratio. Since most photoelectrochemical reactions mediated by TiO_2 are initiated by the surface adsorption of a chemical species. The high surface exposure ensures an overall high density of reactive centers. This feature is specifically exploited in DSSCs.

The clusters constructed for the purposes of this work are based on the a-TiO_2 structure and they are created by the spatial limitation of the thick TiO_2 (4) layer described in Chapter 6.2. Sakai and coworkers show that the TiO_2 clusters with defined (110) and (101) surfaces exist and their energy bandgaps are higher that these values measured for the bulk materials[66]. In the work of Makowska-Janusik et al.[67] is reported that the TiO_2 cluster in diameter less than 1 nm should be saturated at the surface to reduce the number of its dangling bonds. In the mentioned work saturation by different combinations of atoms was proposed and explained. According to the fact that the clusters modeled in the presented work are close to 1 nm, hydrogen saturation was chosen.

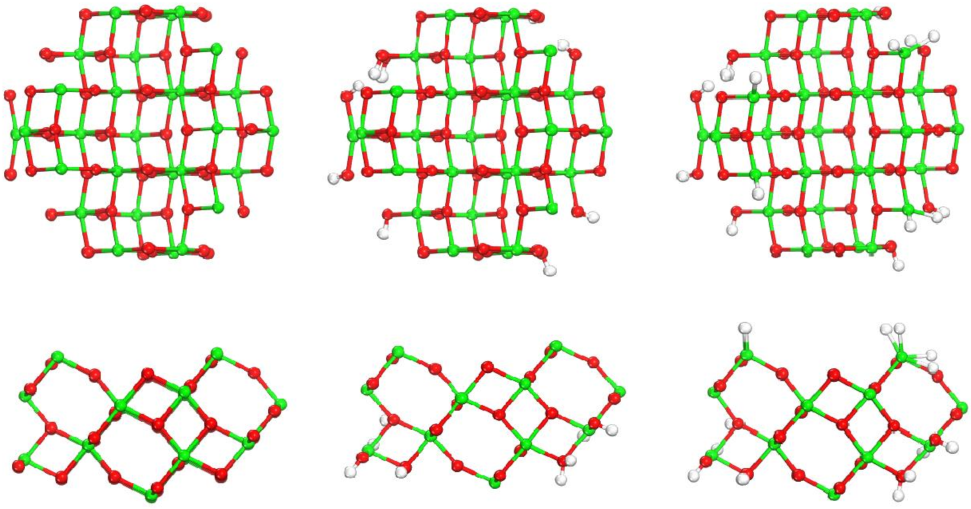

Figure 6.23. Top and lateral view of the $(TiO_2)_{28}$, $(TiO_2)_{28}H_9$, and $(TiO_2)_{28}H_{15}$ clusters (from left to right, respectively) (Ti - green atoms, O - red atoms, and H – grey atoms)

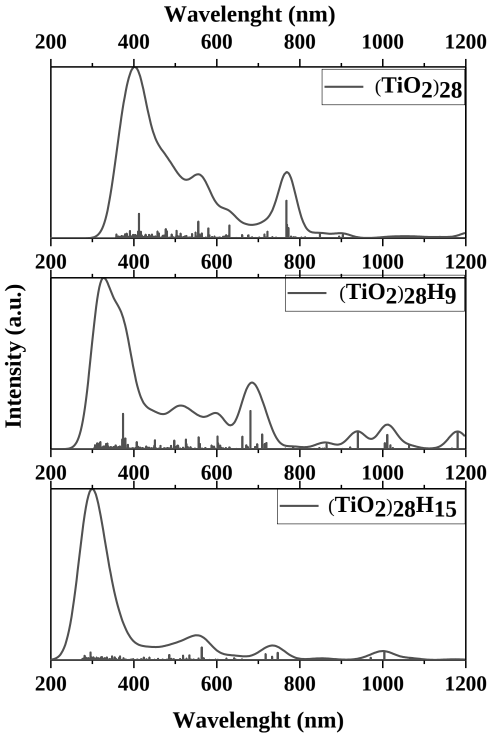

Figure 6.24. The UV-vis absorption spectra calculated by TD/PM6 for $(TiO_2)_{28}$, $(TiO_2)_{28}H_9$, and $(TiO_2)_{28}H_{15}$ clusters presented in Fig. 6.23

First of all, three clusters based on $(TiO_2)_{28}$ anatase units were built. These clusters are presented in Fig. 6.23. They differ one from the other by a different number of saturating atoms. The electron properties of these clusters were calculated without their geometry relaxation. In this case, the TD/PM6[68] semiempirical method implemented in Gaussian 16 package was used[69,70]. The selection of the semi-empirical calculation method is aimed at shortening the calculation time as well as facilitating the calculation of electron properties of hybrid materials based on TiO_2 clusters described in Chapter 8. In this case, also the TD/PM7 method[71] was tested. Unfortunately, the PM7 method does not give good results for TiO_2 structures according to the incorrect parametrization of heavy atoms. The calculations were performed in the restricted Hartree-Fock method (RHF). The SCF convergence criterion was equal to 10^{-12} Hartree. The UV-vis absorption spectra constructed for these clusters are presented in Fig. 6.24. Without saturating hydrogens the obtained spectra do not agree with experimental results. Electron properties are significantly affected by the presence of dangling bonds on the cluster surface. In this case, a significant peak at 775 nm is seen. This peak is not observed in the experiment. When 9 hydrogens are added to the $(TiO_2)_{28}H_9$ surface the mentioned peak moves into the blue region of the spectrum but it is still visible. It means that the used amount of hydrogen is not enough. When the 15 hydrogen atoms were added to the surface of the $(TiO_2)_{28}H_{15}$ cluster the UV-vis spectra are going to be similar to the ones measured experimentally. In the case of the $(TiO_2)_{28}H_9$ cluster, the hydrogens were bonded only to oxygen atoms but in the case of the $(TiO_2)_{28}H_{15}$ cluster, the hydrogens are also bonded to the titanium atoms.

Also, the TiO_2 clusters with different sizes were constructed to investigate the size influence on the optical properties of clusters. These clusters were saturated by hydrogen to eliminate all dangling bonds present at the surface. The idea of these cluster construction was the same as presented earlier. The created clusters $(TiO_2)_{28}H_{15}$, $(TiO_2)_{35}H_{13}$, $(TiO_2)_{42}H_{12}$, and $(TiO_2)_{51}H_{26}$ are presented in Fig. 6.25. These clusters have the radius equal to 7, 8, 9, and 10 Å, respectively.

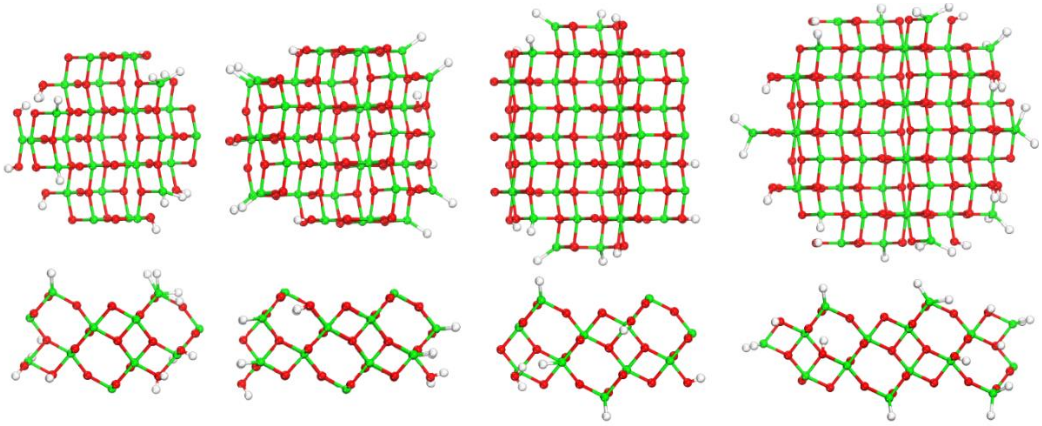

Figure 6.25. Top and lateral view of the $(TiO_2)_{28}H_{15}$, $(TiO_2)_{35}H_{13}$, $(TiO_2)_{42}H_{12}$, and $(TiO_2)_{51}H_{26}$ clusters (from left to right, respectively) (Ti - green atoms, O - red atom, and H – grey atoms)

According to the long time of calculations and memory space consumption, the cluster $(TiO_2)_{51}H_{26}$ was too big to calculate its property by the TD/PM6 method and it was impossible to get the correct data. For the smaller clusters, the UV-vis absorption spectra were calculated (see Fig. 6.26). These spectra are constructed via 450 – 850 calculated excited states. One can see that bigger clusters better reproduce the optical properties of the TiO_2 nanostructures. The long wavelength located peaks observed in the UV-vis spectra are unrealistic for the TiO_2 structures according to their band gap energy value that should be higher than 3 eV. The nature of the UV-vis absorption peaks was studied by focusing on the electron ground-to-excited state transition and the obtained data are collected in Table 6.5.

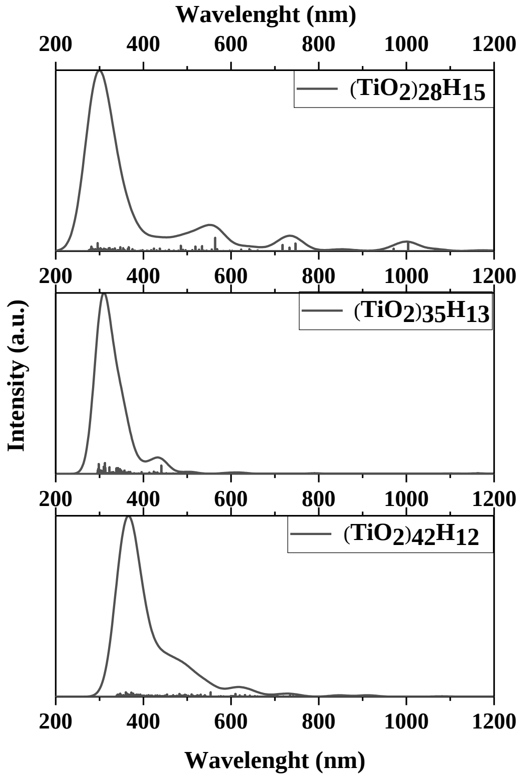

Figure 6.26. UV-vis absorption spectra calculated by TD/PM6 for $(TiO_2)_{28}H_{15}$, $(TiO_2)_{35}H_{13}$, and $(TiO_2)_{42}H_{12}$ clusters presented in Fig. 6.25

For the cluster $(TiO_2)_{28}H_{15}$ the ground-to-excited state transition with the highest oscillator strength (0.026) is observed at 563 nm. This transition is caused by the electrons located at the surface of the cluster (see Table 6.5 focusing on the ground and excited state orbital representation). The molecular orbitals taking part in electron transition at 563 nm are mainly located at the oxygen and titanium atoms possessing dangling bonds and they have hybrid O-Ti nature. The transition present at 296 nm is caused by electron transition from O(p) states to Ti(d) states. This is typical electron excitation from VBM to CBM observed for semiconducting oxides. The same character possesses peaks located at 312 nm for $(TiO_2)_{35}H_{13}$ and 360 nm for $(TiO_2)_{42}H_{12}$. They reproduce the nature of the bulk a-TiO_2. The peaks located at 441 nm for $(TiO_2)_{35}H_{13}$ and 553 nm for $(TiO_2)_{42}H_{12}$ are the consequence of the presence of surface dangling bonds. Analyzing data presented in Fig. 6.26 and Table 6.5 one may see that the $(TiO_2)_{35}H_{13}$ cluster reproduces best the UV-vis absorption spectra obtained experimentally. Unfortunately, this cluster with adsorbed dyes can be too big to calculate the optical properties of hybrids. This problem will be discussed in Chapter 8.

Table 6.5. Electron properties of the clusters $(TiO_2)_{28}H_{15}$, $(TiO_2)_{35}H_{13}$, and $(TiO_2)_{42}H_{12}$ calculated by TD/PM6 method (Ti - green atoms, O - red atoms, H - light grey atoms)

TD/PM6	**λ_{max} (nm), (oscillator strength)**	**Ground state**	**Excited state**
$(TiO_2)_{28}H_{15}$	**563 (0.026)**	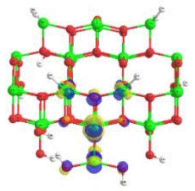	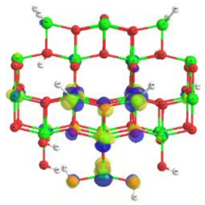
	296 (0.016)	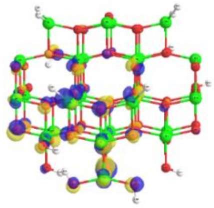	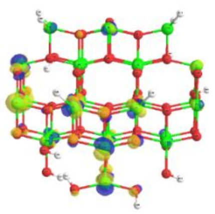
$(TiO_2)_{35}H_{13}$	**441 (0.015)**	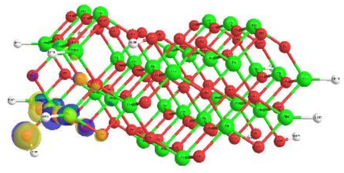	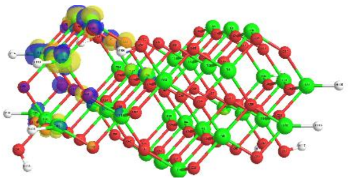
	312 (0.019)	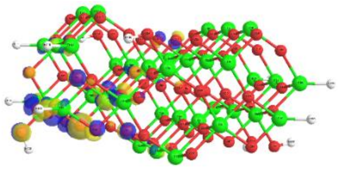	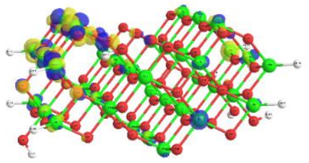
$(TiO_2)_{42}H_{12}$	**553 (0.005)**	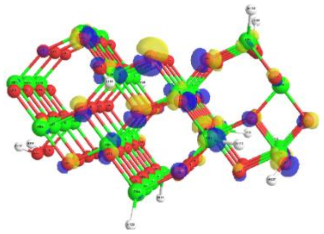	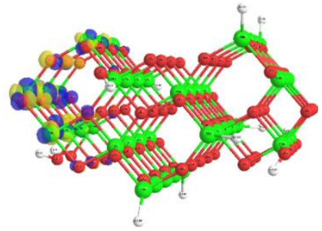
	360(0.005)	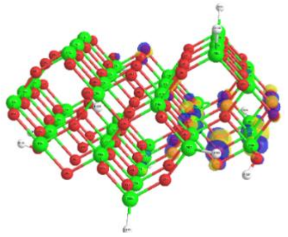	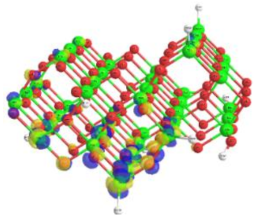

One can conclude that the clusters $(TiO_2)_{28}H_{15}$ and $(TiO_2)_{35}H_{13}$ can be treated as the model to study the electron and optical properties of nanostructured TiO_2. The small intensity peaks located at a wavelength longer than 400 nm are coming from surface atoms whose influence in real nanostructures will be not so important due to the ratio of the number of surface to volume atoms, which is experimentally not so significant compared to the introduced model. In the implemented model these peaks can be omitted discussing the optical properties of nanostructures.

6.4. Synthesis and experimental investigations of selected TiO_2-based structures

As part of my stage at the Department of Physics, Faculty of Science and Technology at Le Mans University (France) I have synthesized and investigated structural and optical properties of selected TiO_2-based nanostructures to compare the obtained results with computationally obtained data discussed previously. The selected materials were synthesized with the same amount of impurities as it was studied computationally. The experimental results serve as a correctness test of implemented computational methods. All experimental investigations were performed by me in the Institute of Molecules and Materials headed by Professor Kassiba.

The TiO_2 films were prepared by rf-sputtering using a titanium dioxide target. In consequence, 4 different samples were prepared: pristine TiO_2 and TiO_2 doped by 6.25 mol% of Zr, Mn, and Ni using the ZrO_2 MnO_2 and NiO oxides. The [Rhodoviol CAS. 9002-89-5] was used as a blender with an amount of 7-10 drops per gram. Targets were pressed by 8 tones and then were annealed in two steps process. Firstly, they were heated up to 400°C for 4 hours for blender burning, and then they were annealed at 1000°C for 10 hours. The obtained targets have a diameter of 3.5 cm and a thickness of 5 mm. Then they were used as sputtering targets. Pure argon flow 96 sccm was used as sputtering and reactive gas. In the case of the N-doped sample argon and nitrogen gas mixture 82.6 and 8.2 sccm, respectively, was used. Depositions were carried out at room temperature with a time equal to 150 min. The pressure in the deposition chamber was 5×10^{-6} mbar. The Si plates and Borofloat 33 glass with a surface size of 20×20 mm were used as substrates for deposition. Before deposition, the substrates were had ultrasonic bath for 15 min in ethanol and then cleaned with compressed air. The thickness of films deposited on Si was equal to 360 nm in the case of pristine TiO_2, 250 nm in the case of TiO_2:Zr, 430 nm - TiO_2:Ni, 384 nm - TiO_2:Mn, and 180 nm for TiO_2:N. All XRD scans were recorded in the conventional 2θ° configurations between 20° and 65° with the step of 0.01°. Crystallization of the films with pure TiO_2 deposited on Si was investigated versus temperatures (Fig. 6.27). Was found that up to 300°C the TiO_2 films left amorphous. At 400°C the TiO_2 structure crystallizes in anatase polymorph. The peaks typical for the anatase form of TiO_2 became visual: 25.23° (101), 37° (004), and 52° (JCPDS card no. 21-1272)[72]. The strong peak at 29° belongs to the (111) of Si substrate material [73,74,75]. In the spectra presented in Fig. 6.27, an undefined peak at 33° is observed. According to the analyses performed for rutile (JCPDS card no. 21-1276) and brookite (JCPDS card no. 29-1360) one can conclude that the TiO_2 polymorph does not show the mentioned XRD peak.

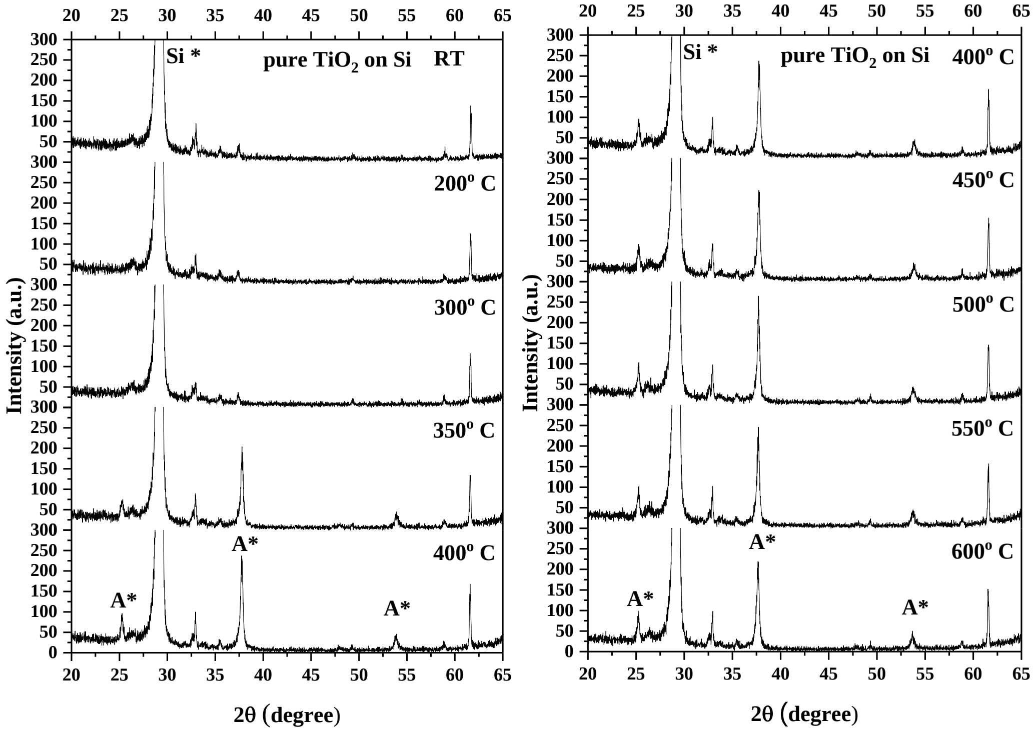

Figure 6.27. XRD spectra measured for the TiO_2 thin film deposited on the Si plate versus temperatures

The XRD spectra measured for TiO_2 doped by cations as Zr, Ni, and Mn are presented in Fig. 6.28. The films with Zr show a few times higher anatase peaks (101) 25.16° than is observed for pure TiO_2. Comparing spectra presented in Fig. 6.28b with the ones collected for t-ZrO_2 (JCPDS card no. 17-0923) any peaks significant for t-ZrO_2 structure are not seen while leaving all the peaks characteristic of TiO_2 anatase polymorph. Based on the obtained results one can suggest that Zr in the anatase structure prevents the titanium dioxide phase transformation, and make the anatase polymorph more privileged.

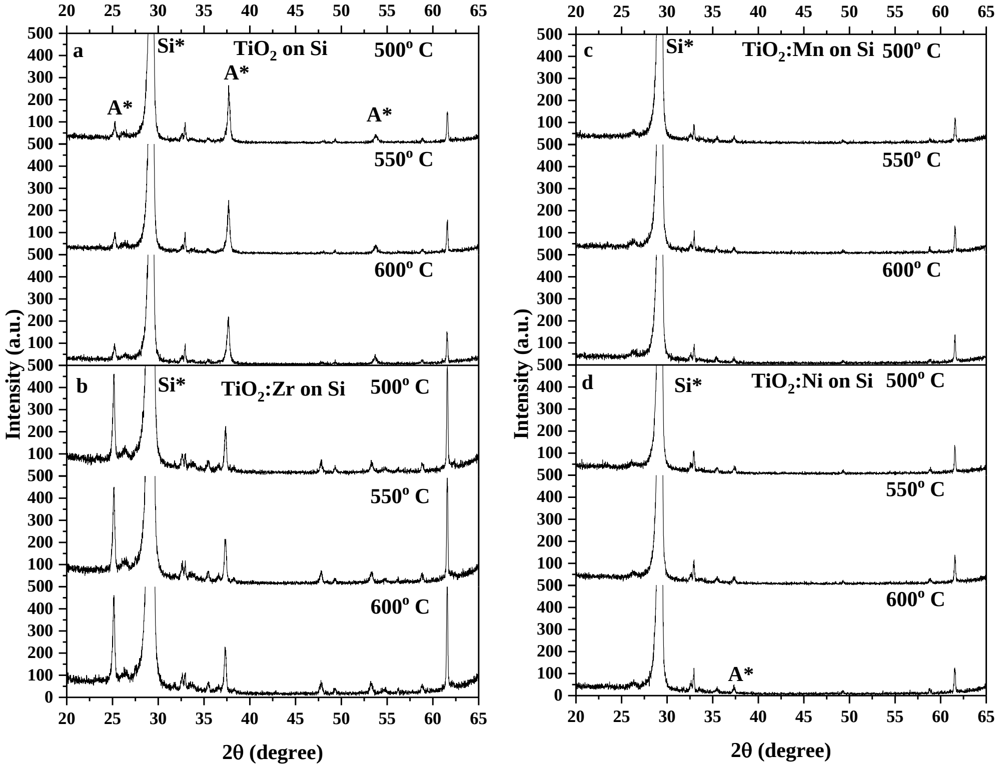

Figure 6.28. XRD spectra measured for the thin film based on TiO_2 deposited on the Si plate: (a) pristine TiO_2, (b) TiO_2:Zr, (c) TiO_2:Mn, and (d) TiO_2:Ni annealed at temperatures 400°C-600°C with step 50°C

The Mn and Ni dopants do not increase the stability of the TiO_2 (see Fig. 6.28c, 6.28d). The XRD spectra, up to 600°C, do not show any significant signs of TiO_2 crystallization. One can conclude that these dopants left the films amorphous. Although the deposition of TiO_2Ni on Borofloat 33 glass shows not good structural stability. Comparing results obtained for the samples on Si and Borofloat 33 glass, one can observe that the pure TiO_2 and TiO_2:Zr crystalize in anatase form although on glass.

The presence of the v(O) is typical for the AB_2 crystals. Adding the nitrogen into the chamber during synthesis become possible to substitute v(O) by impurity[56,57]. The addition of N_2 in such a ratio of 1:10 in Argon flow decries the final thickness of the TiO_2 almost twice compared with pure Argon flow. The XRD profile shows a very high amorphism of the TiO_2:N films (see Fig. 6.29). Only at 500°C the synthesized structures crystalizes but with a high level of distortion from the anatase elementary unit cell. One can conclude that the N impurities introduced substitutionally destroyed the TiO_2 lattice structure of the films. Comparing Fig.6.29.b with TiO_2 anatase (JCPDS card no. 21-1272), and TiO_2 brookite (JCPDS card no. 29-1360) shows us that's the structure of the film probably closer to the deformed anatase, based on the general structure and position of peaks (101) 25.03° and (004) near 37°.

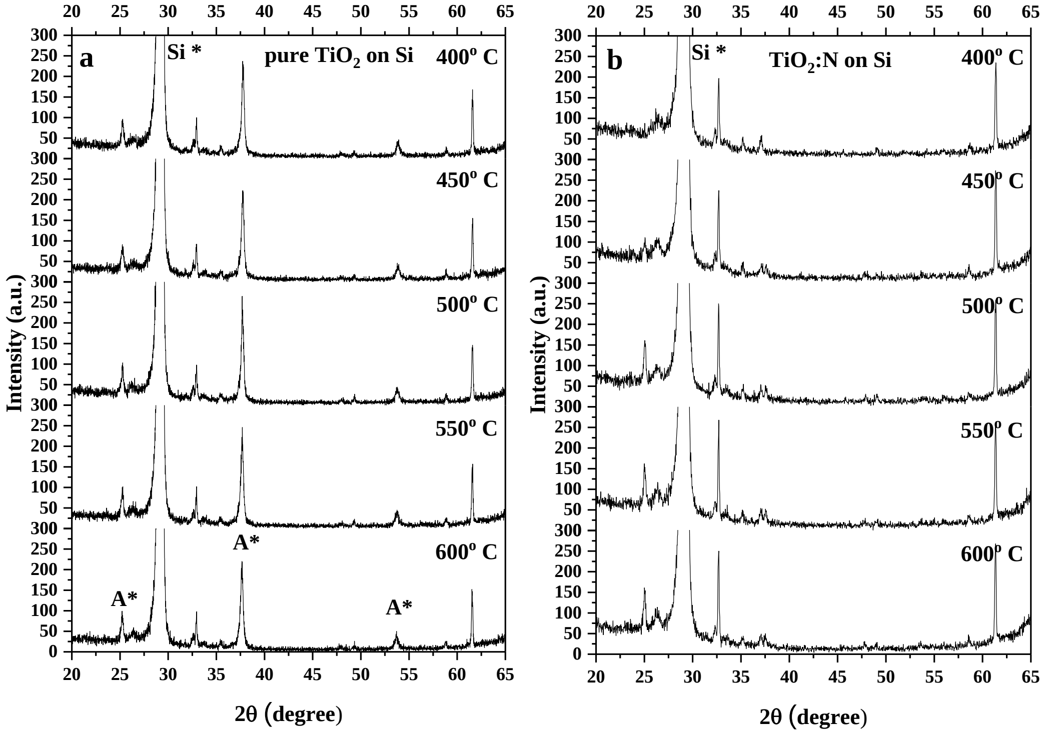

Figure 6.29. XRD spectra measured for thin films deposited on a Si plate for pure TiO_2 (a) and with TiO_2:N (b) annealed at temperatures 400°C-600°C with step 50°C

The Raman spectra were measured for TiO_2 and TiO_2:Zr films deposited on the Si plate and Borofloat glass (see Fig. 6.30). The Raman spectra measured on the Si plate show a main strong band at 520 cm^{-1} and less intensive peaks at 301 cm^{-1} belonging to the Si substrate [76,77,78,]. In literature, the anatase films are characterized by 6 well know active mods: a strong signal peak at 144 cm^{-1} followed by low-intensity peaks located at 197, 399, 513, 519, and 641 cm^{-1} [79]. The main peak observed for TiO_2 film deposited on Si substrate (see Fig. 6.30a), located at 143 cm^{-1} is referenced to anatase structure. The peak at 197 cm^{-1} is not seen. The peaks at 513 and 519 cm^{-1} cannot be analyzed because of overlapping with Si's corresponding peak at 520 cm^{-1}. The TiO_2 deposited on Borofloat 33 (see Fig.

6.30b) shows the main peak at 146 cm^{-1} and the others located at 400, 518, and 639 cm^{-1}.

Analyzing the Raman spectra obtained for TiO_2:Zr structures one can conclude that the Zr atoms are dispersed in the crystal structure. Any evidence mark of the t-ZrO_2 presence is not seen[80]. The TiO_2:Zr increases the stability of the anatase form (see Fig. 6.30b). In this case, of films deposited on glass, a strong positive impact is seen. The peak located at 139 cm^{-1} is significantly higher compared to pristine TiO_2.

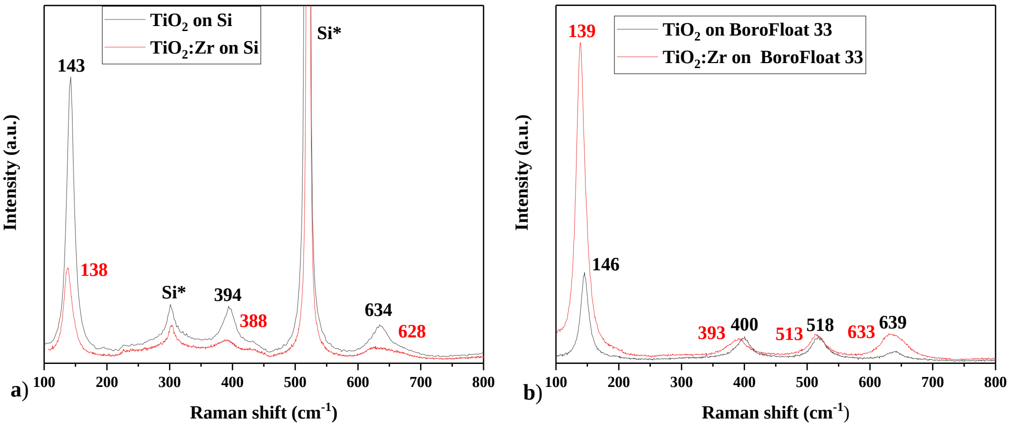

Figure 6.30. Normalized Raman spectra for measured for thin films of the TiO_2 (black line) and the TiO_2:Zr (red line) deposited on silicon plates a) and on Borofloat 33 b)

The Mn and Ni-doped TiO_2 structure shows low structural stability. The Raman spectra measured for TiO_2:Mn and TiO_2:Ni films show mostly their amorphous structure with clear substrate peaks belonging to the Si plate. These spectra as uninteresting were not selected for graphical representation. The N-doped films were annealed at a temperature of 450°C before Raman measurements, but it turned out that this process did not crystallize the sample. In consequence, the obtained Raman spectra do not show any crystallinity of the TiO_2:N films.

The transmission spectra in the optical wave range were measured for films deposited on Borofloat 33 glass (Fig. 6.31a). These spectra were transformed into the UV-vis absorption spectra (Fig. 6.31b) in the case to calculate the optical energy bandgap. The optical band gap was calculated by Tauc's extrapolation method for the indirect electron transitions.

The optical gap and the general structure of absorption spectra in the case of pristine TiO_2 and TiO_2:Zr are very similar to each other with the E_g=3.26 eV and E_g=3.27 eV, respectively. The optical energy band gap measured for TiO_2:Mn is equal to 3.30 eV. The UV-vis absorption spectrum measured for TiO_2:Mn exhibits a small shoulder giving the optical energy gap associated with energy states of dopants equal to 3.06 eV. The sample with deposited TiO_2:Ni was inhomogeneous and very thin. In this case, the obtained optical gap can be the value measured for a glass substrate equal to 3.42 eV. The most controversial results were obtained for the TiO_2:N structures. In this case, the optical energy gap equal to 3.33 eV was measured. The obtained value is higher than the one measured for pristine TiO_2. The results of our computer simulations presented earlier as well as the work of other research groups[56,57] show that N dopants decrease the optical energy gap. The possible reason for the obtained discrepancies can be caused by inhomogeneous film structure or not appropriate crystallization of the deposited TiO_2. These two features greatly affect the electronic properties of the material. Comparing the experimentally obtained data presented in Fig. 6.31b and the calculated result presented in Fig. 6.15 one can conclude that the synthesized films can be compared with the structure doped by metal ions accompanied by v(O). In real structures of oxide semiconductors always the v(O) are present.

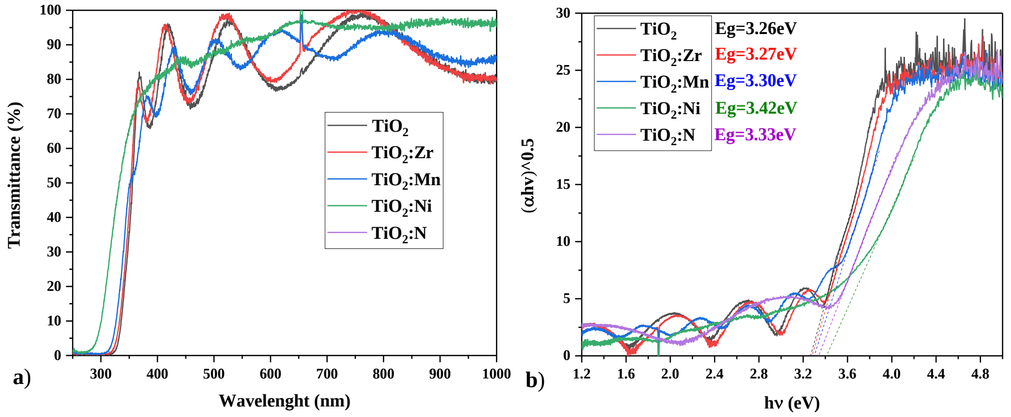

Figure 6.31. a) Transmittance spectra measured for thin films deposited on Borofloat 33 glass. b) Estimated optical band gaps for thin films in the case of indirectly allowed transitions

One should also notice that the synthesized films are relatively thick and they can be compared with bulk-modelled materials. The simulations clearly show a positive stabilizing effect of the Zr atoms in the anatase structure. The same was proved experimentally by XRD measurements. Although Raman spectra show the advantage of Zr-doped anatase in structural stability. Data collected in Table 6.2 clearly show that Ni and Mn in all calculated configurations make the host crystal less stable. Also increasing the number of dopants the crystal stability decreases.

This can be proved by the fact that the synthesis of the TiO_2:Ni and TiO_2:Mn films was impossible to obtain stable materials with impurity content equal to 6.25 mol%.

The data presented in Fig. 6.9 are in agreement with the results presented in Fig. 6.31b. Computationally proved the existence of the impurities energy level in TiO_2:Mn:v(O) structure are manifested by the shoulder present in experimental UV-vis absorption spectrum.

Table 6.2 presents the statement that the 2×2×1 $TiO_2:N_O$ structure has better stability than structures with Ni and Mn impurities. The same is presented by analyzing the XRD spectra. Concluding, one can say that the computational methodology implemented in the presented work to predict the structural and electron properties of the TiO_2-based materials is correct. It can reproduce and explain the nature of properties of defected and doped a-TiO_2 bulk materials and also the ones limited with size going from thin films up to nanostructure.

6.5. Conclusions

As a result of the performed quantum-chemical calculations to predict structural and electron properties of stoichiometric and non-stoichiometric TiO_2 crystals, was shown that using the DFT method augmented by Hubbard correction with appropriate parameters is possible to map the physicochemical properties of semiconductor oxide materials. It so far was unattainable in many literature reports. The appropriate Hubbard parameters were found to characterize the structural and electron parameters of anatase TiO_2 crystals, doped with M=Zr^{4+}, Ni^{2+}, $Mn^{2+,}$ or Cu^{2+} ions and accompanied by oxygen vacancies. The role of vacancies in TiO_2:M materials was determined. Was proved that the v(O) are the main reason for the additional energy level appearance in the TiO_2 bandgap.

As a result of experimental studies and quantum-chemical calculations, it was shown that doping of TiO_2 with Zr^{4+} ions stabilizes its structure in the form of anatase and generates oxygen vacancies. This situation is observed for bulk and thin films of TiO_2. Zr impurities do not change the electron parameters of the native TiO_2 structure. It has been proven that the modification of TiO_2 with M ions (except Zr) creates additional energy states in the bandgap region. The created donor states can be helpful in the enhancement of charge transfer occurring between organic dye and semiconductors in DSSC devices. The crated TiO_2-based structures were also investigated from the charge mobility point of view. The increase in energy dispersion of CBM caused by Ni dopants supports the electron mobility in TiO_2:Ni-based systems. The flattened structure of the donor level of the TiO_2:Cu^{2+} decreases the charge mobility. It will probably support unwanted recombination processes by reducing the lifetime of the electrons injected from the dyes to the semiconductor. It was also shown that Mn dopants create the acceptor level in the TiO_2 bandgap. The creation of additional energy levels close to the edge of the valence band probably will not enhance the charge transfer process in DSSC systems based on TiO_2:Mn.

Going from bulk material to thin films and nanostructures the size quantum confinement effect was observed. Was shown that the band gap energy is higher for the nanostructures than it is observed for the bulk materials. Performing quantum chemical calculations for layered TiO_2 was shown that the mobility of the electrons decreases at the surface of semiconductors. Additionally was found that the mobility of electrons and holes in a direction perpendicular to the surface is very low.

The model of the TiO_2 cluster was implemented. Was proved that for the clusters with a radius close to 1 nm, the saturation of surface dangling bonds should be taken into consideration. The created clusters can be used to model the electron properties of hybrids used in DSSC devices.

Performed computer modeling of newly-designed TiO_2-based materials indicates the most desirable properties of semiconductors working in DSSC applications. It allowed us to obtain materials with a diverse structure of electron bands leading to the development of a charge transfer mechanism and factors influencing its course in a hybrid sensitizer/semiconductor systems. Was proved that the computational methodology implemented in the presented work to predict the structural and electron properties of the TiO_2-based materials is correct.

6.6. Literature

[1] Mathew S., Yella A., Gao P., Humphry-Baker R., & Grätzel M., "Dye-sensitized solar cells with 13% efficiency achieved through the molecular engineering of porphyrin sensitizers." *Nature Chemistry*, vol.6, pp.242-247, **(2014)**.

[2] Yu I. G., Kim Y. J., Kim H. Lee J., C., & Lee W. I., "Size-dependent light-scattering effects of nanoporous TiO_2 spheres in dye-sensitized solar cells." *Journal of Materials Chemistry*. vol.21, pp.532-538, **(2011)**.

[3] Seyed-Talebi, S. M., & Kazeminezhad, I., "Performance improvement of fully ambient air fabricated perovskite solar cells in an anti-solvent process using TiO_2 hollow spheres." *Journal of Colloid and Interface Science*, vol.562 pp.125-132, **(2020)**.

[4] Acchutharaman, K. R., Santhosh, N., Daniel, R. I., Pandian, M. S., & Ramasamy, P. "Enhanced electron harvesting in next generation solar cells by employing TiO_2 nanoparticles prepared through hydrolysis catalytic proces" *Ceramics International*, vol.47, no.15, pp.21263-21270, **(2021)**.

[5] Swamy, V., Gale, J. D., & Dubrovinsky, L. S. "Atomistic simulation of the crystal structures and bulk moduli of TiO_2 polymorphs." *Journal of Physics and Chemistry of Solids*, vol.62, no.5, pp.887-895, **(2001)**.

[6] Pasche, A., Grohe, B., Mittler, S., & Charpentier, P. A., "Zr-doped TiO_2 nanoparticles synthesized via a sol–gel route and their application in dye-sensitized solar cells for thermo-stabilization." *Materials Research Express*, vol.4, no.(6), pp.065501, **(2017)**. doi:10.1088/2053-1591/aa742d

[7] Southon, P. D., Bartlett, J. R., Woolfrey, J. L., & Stevens, M. G., "Evolution of the structure of aqueous zirconia gels during preparation and heating." *Ceramic Transactions*, vol.81, pp.75-80, **(1997)**.

[8] Zhang Y.-F., Lin W., Li Y., Ding K.-N., & Li J.-Q., "A Theoretical Study on the Electronic Structures of TiO_2: Effect of Hartree−Fock Exchange." *The Journal of Physical Chemistry B*, vol.109, pp.19270-19277, **(2005)**.

[9] T. Zhu, & Gao S.-P., "The Stability, Electronic Structure, and Optical Property of TiO_2 Polymorphs." *The Journal of Physical Chemistry C*, vol.118, pp.11385-11396, **(2014)**.

[10] Watson, G. "Atomistic and electronic structure calculation of defects at the surfaces of oxides". *Radiation Effects and Defects in Solids*, vol.157, no6-12, pp.773–781, **(2002)**. doi:10.1080/10420150215767

[11] Nolan, M., Grigoleit, S., Sayle, D. C., Parker, S. C., & Watson, G. W.. "Density functional theory studies of the structure and electronic structure of pure and defective low index surfaces of ceria." *Surface Science*, vol.576, no.1-3, pp.217–229, **(2005)**. doi:10.1016/j.susc.2004.12.016

[12] Hüfner, S.. "Electronic structure of NiO and related 3d-transition-metal compounds." *Advances in Physics*, vol.43, no.2, pp.183–356. **(1994)**. doi:10.1080/00018739400101495

[13] Holbig, E. S. "The Effect of Zr-Doping and Crystallite Size on the Mechanical Properties of TiO_2 Rutile and Anatase." Diss. **(2008)**.

[14] Kresse, G., & Furthmüller, J. "Efficient iterative schemes for ab initio total-energy calculations using a plane-wave basis set." *Physical Review B*, vol.54, no.16, pp.11169–11186, **(1996)**. doi:10.1103/physrevb.54.11169

[15] Shishkin, M., & Kresse, G. "Implementation and performance of the frequency-dependent GW method within the PAW framework." *Physical Review B*, vol.74, no.3, pp.035101, **(2006)**. doi:10.1103/physrevb.74.035101

[16] Blöchl, P. E.. "Projector augmented-wave method." *Physical Review B*, vol.50, no.24, pp.17953–17979, **(1994)**. doi:10.1103/physrevb.50.17953

[17] Kresse, G., & Joubert, D. "From ultrasoft pseudopotentials to the projector augmented-wave method." *Physical Review B*, vol.59, no.3, pp.1758–1775, **(1999)**. doi:10.1103/physrevb.59.1758

[18] Perdew, J. P., Burke, K., & Ernzerhof, M.. "Generalized Gradient Approximation Made Simple." *Physical Review Letters*, vol.77, no.18, pp.3865–3868, **(1996)**. doi:10.1103/physrevlett.77.3865

[19] Perdew, J. P., Burke, K., & Ernzerhof, M. "Generalized Gradient Approximation Made Simple [Phys. Rev. Lett. 77, 3865 (1996)]." *Physical Review Letters*, vol.78, no.7, pp.1396, **(1997)**. doi:10.1103/physrevlett.78.1396

[20] Grimme, S. "Semiempirical GGA-type density functional constructed with a long-range dispersion correction." *Journal of Computational Chemistry*, vol.27, no.15, pp.1787–1799, **(2006)**. doi:10.1002/jcc.20495

[21] Liechtenstein, A. I., Anisimov, V. I., & Zaanen, J.. "Density-functional theory and strong interactions: Orbital ordering in Mott-Hubbard insulators." *Physical Review B*, vol.52, no.8, pp.R5467–R5470, **(1995)**. doi:10.1103/physrevb.52.r5467

[22] Monkhorst, H. J., & Pack, J. D.. "Special points for Brillouin-zone integrations." *Physical Review B*, vol.13, no.12, pp.5188–5192, **(1976)**. doi:10.1103/physrevb.13.5188

[23] Mattioli, G., Alippi, P., Filippone, F., Caminiti, R., & Bonapasta, A.A. "Deep versus Shallow Behavior of Intrinsic Defects in Rutile and Anatase TiO_2 Polymorphs." *The Journal of Physical Chemistry C,* vol.114, no.49, pp.21694–21704, **(2010)**. doi:10.1021/jp1041316

[24] Arroyo-de Dompablo, M. E., Morales-García, A., & Taravillo, M. "DFT+U calculations of crystal lattice, electronic structure, and phase stability under pressure of TiO_2 polymorphs." *The Journal of Chemical Physics,* vol.135, no.5, pp.054503, **(2011)**. doi:10.1063/1.3617244

[25] Deák, P., Aradi, B., & Frauenheim, T. "Polaronic effects in TiO_2 calculated by the HSE06 hybrid functional: Dopant passivation by carrier self-trapping." *Physical Review B*, vol.83, no.15, pp.155207, **(2011)**. doi:10.1103/physrevb.83.155207

[26] Diebold, U. "The surface science of titanium dioxide." *Surface Science Reports*, vol.48 no.(5-8), pp.53–229, **(2003)**. doi:10.1016/s0167-5729(02)00100-0

[27] Burdett, J. K., Hughbanks, T., Miller, G. J., Richardson Jr, J. W., & Smith, J. V. "Structural-electronic relationships in inorganic solids: powder neutron diffraction studies of the rutile and anatase polymorphs of titanium dioxide at 15 and 295 K." *Journal of the American Chemical Society,* vol.109, no.12, pp.3639-3646, **(1987)**.

[28] Rao, K. K., Naidu, S. N., & Iyengar, L. "Thermal expansion of rutile and anatase. " *Journal of the American Ceramic Society*, vol.53, no.3, pp.124-126, **(1970)**.

[29] Kisi, E. H., & Howard, C. J. "Crystal Structures of Zirconia Phases and their Inter-Relation." *Key Engineering Materials*, vol.153-154, pp.1–36, **(1998)**. doi:10.4028/www.scientific.net/kem.153-154.1 .

[30] Pan, X., Yang, M.-Q., Fu, X., Zhang, N., & Xu, Y.-J. " Defective TiO_2 with oxygen vacancies: synthesis, properties and photocatalytic applications." *Nanoscale*, vol.5, no.9, pp.3601, **(2013)**. doi:10.1039/c3nr00476g

[31] Kim, D., Yeo, B. C., Shin, D., Choi, H., & Han, S. S., "Dissimilar anisotropy of electron versus hole bulk transport in anatase TiO_2: Implications for photocatalysis." *Physical Review B*, vol.95, no.4, pp.045209, **(2017)**.
doi: 10.1103/PhysRevB.95.045209

[32] Raghav, A., Hongo, K., Maezono, R., & Panda, E. "Electronic structure and effective mass analysis of doped TiO_2 (anatase) systems using DFT+U." *Computational Materials Science*, vol.214, pp.111714, **(2022)**.

[33] Kus, M., Altantzis, T., Vercauteren, S., Caretti, I., & Cool, P. "Mechanistic insight into the photocatalytic working of fluorinated anatase {001} nanosheets." *The Journal of Physical Chemistry C*, vol.121, no.47, pp.26275-26286, **(2017)**.

[34] Wang, Z., Lin, R., Huo, Y., Li, H., & Wang, L., "Formation, Detection, and Function of Oxygen Vacancy in Metal Oxides for Solar Energy Conversion." *Advanced Functional Materials*, vol.32, no.7, pp.2109503 **(2021).** doi:10.1002/adfm.202109503

[35] Wang, Z., Mao, X., Chen, P., Xiao, M., & Wang, L., "Understanding the Roles of Oxygen Vacancies in Hematite-Based Photoelectrochemical Processes." *Angewandte Chemie - International Edition*, vol.58, pp.1030-1034, **(2019)**.

[36] Mohajernia, S., Andryskova, P., Zoppellaro, G., Hejazi, S., & Schmuki, P., "*Influence of Ti^{3+} Defect-type on Heterogeneous Photocatalytic H2 Evolution Activity of TiO_2.*" *Journal of Materials Chemistry A*, vol.8, no.3, **(2020)**. doi:10.1039/c9ta10855f

[37] Finazzi, E., Di Valentin, C., Pacchioni, G., & Selloni, A., "Excess electron states in reduced bulk anatase TiO_2: Comparison of standard GGA, GGA+U, and hybrid DFT calculations." *The Journal of Chemical Physics*, vol.129, pp.154113, **(2008)**.

[38] Bartkowiak, A., Korolevych, O., Chiarello, G. L., Makowska-Janusik, M., & Zalas, M. "How Can the Introduction of Zr^{4+} Ions into TiO_2 Nanomaterial Impact the DSSC Photoconversion Efficiency? A Comprehensive Theoretical and Experimental Consideration." *Materials*, vol.14, no.11, pp.2955, **(2021)**. doi:10.3390/ma14112955

[39] Zhang, W. B., Deng, Y. H., Hu, Y. L., Han, K. L., & Tang, B. Y. "Structural distortion of B1-structured MnO and FeO. " *Solid state communications*, vol.142, no.(1-2), pp.6-9, **(2007)**.

[40] Ouali, H., Oison, V., Lambert-Mauriat, C., Labidi, A., & Ali, M. "LSDA+ U study of the electronic structure of cupric oxide: comparison between bulk and surfaces."

[41] Nolan, M., Long, R., English, N. J., & Mooney, D. A.. "Hybrid density functional theory description of N- and C-doping of NiO." *The Journal of Chemical Physics*, vol.134, no.22, pp.224703, **(2011)**. doi:10.1063/1.3596949

[42] Shin, H., Luo, Y., Ganesh, P., Balachandran, J., & Heinonen, O. "Electronic properties of doped and defective NiO: A quantum Monte Carlo study. " *Physical Review Materials*, vol.1, no.7, pp.073603, **(2017)**.

[43] Raguram, T., & Rajni, K. S., "Effect of Ni doping on the characterization of TiO_2 nanoparticles for DSSC applications." *Journal of Materials Science: Materials in Electronics*, vol.32, no.13, pp.18264-18281, **(2021)**.

[44] Nagaveni, K., Hegde, M. S., & Madras, G., "Structure and photocatalytic activity of $Ti_{1-x}M_xO_{2\pm\delta}$ (M= W, V, Ce, Zr, Fe, and Cu) synthesized by solution combustion method." *The Journal of Physical Chemistry B*, vol.108, no.52, pp.20204-20212, **(2004)**.

[45] Chauhan, R., Kumar, A., & Chaudhary, R. P., "Structural and photocatalytic studies of Mn doped TiO_2 nanoparticles." *Spectrochimica Acta Part A: Molecular and Biomolecular Spectroscopy*, vol.98, pp.256-264, **(2012)**.

[46] Ghasemi, S., Rahimnejad, S., Setayesh, S. R., Rohani, S., & Gholami, M. R., "Transition metal ions effect on the properties and photocatalytic activity of nanocrystalline TiO_2 prepared in an ionic liquid." *Journal of Hazardous Materials*, vol.172, no.(2-3), pp.1573–1578, **(2009)**. doi:10.1016/j.jhazmat.2009.08.029

[47] Rödl, C., Fuchs, F., Furthmüller, J., & Bechstedt, F., "Quasiparticle band structures of the antiferromagnetic transition-metal oxides MnO, FeO, CoO, and NiO." *Physical Review B*, vol.79, no.23, pp.235114, **(2009)**.

[48] Zhang, W. B., Yu, N., Yu, W. Y., & Tang, B. Y. "Stability and magnetism of vacancy in NiO: A GGA+ U study." *The European Physical Journal B*, vol.64, no.2, pp.153-158, **(2008)**.

[49] Nolan, M., & Elliott, S. D. "The p-type conduction mechanism in Cu_2O: a first principles study." *Physical Chemistry Chemical Physics*, vol.8, no.45 pp.5350-5358, **(2006)**.

[50] Akshay, V. R., Arun, B., Mandal, G., & Vasundhara, M. "Structural, optical and magnetic behavior of sol–gel derived Ni-doped dilute magnetic

semiconductor TiO_2 nanocrystals for advanced functional applications." *Physical Chemistry Chemical Physics*, **(2019)**. doi:10.1039/c8cp06875e

[51] Santra, P. K., & Kamat, P. V., "Mn-doped quantum dot sensitized solar cells: a strategy to boost efficiency over 5%." *Journal of the American Chemical Society*, vol.134, no.5, pp.2508-2511, **(2012)**.

[52] Zhang, C., Zeng, J. H., & Wang, Y. F., "Manganese doped titanium dioxide with a tunable flat-band potential as photoanode in quantum dot sensitized solar cells for higher open circuit voltage." *Chemical Physics Letters*, vol.761, no.138099, **(2020)**.

[53] Navas, J., Fernández-Lorenzo, C., Aguilar, T., Alcántara, R., & Martín-Calleja, J. "Improving open-circuit voltage in DSSCs using Cu-doped TiO_2 as a semiconductor." Physica Status Solidi (a), vol.209, no.2, pp.378–385, **(2011)**. doi:10.1002/pssa.201127336

[54] Bartkowiak, A., Korolevych, O., Chiarello, G. L., Makowska-Janusik, M., & Zalas, M.. "Experimental and theoretical insight into DSSCs mechanism influenced by different doping metal ions." *Applied Surface Science*, vol.*597*, pp.153607, **(2022)**. https://doi.org/10.1016/j.apsusc.2022.153607

[55] Harb, M., Sautet, P., & Raybaud, P.. "Origin of the Enhanced Visible-Light Absorption in N-Doped Bulk Anatase TiO_2 from First-Principles Calculations." *The Journal of Physical Chemistry C*, vol.115, no.39, pp.19394–19404, **(2011)**. doi:10.1021/jp204059q

[56] Peng, S., Yang, Y., Li, G., Jiang, J., & Xu, G., "Effect of N_2 flow rate on the properties of N doped TiO_2 films deposited by DC coupled RF magnetron sputtering." *Journal of Alloys and Compounds*, vol.678, pp.355-359, **(2016)**.

[57] Dobromir, M., Manole, A. V., Nica, V., Apetrei, R., & Luca, D. "Analyzing the Development of N-Doped TiO_2 Thin Films Deposited by RF Magnetron Sputtering." *Sensor Letters*, vol.11, no.4, pp.675-678, **(2013)**. doi:10.1166/sl.2013.2936

[58] Kuriechen, S. K., Murugesan, S., & Paul Raj, S., "Mineralization of azo dye using combined photo-fenton and photocatalytic processes under visible light." *Journal of Catalysts*, vol.2013, **(2013)**.

[59] Cavallo, C., Di Pascasio, F., Latini, A., Bonomo, M., & Dini, D., "Nanostructured semiconductor materials for dye-sensitized solar cells." *Journal of Nanomaterials*, vol vol.2017, **(2017)**.

[60] Liu, G., Yang, H. G., Pan, J., Yang, Y. Q., & Cheng, H. M. "Titanium dioxide crystals with tailored facets." *Chemical reviews*, vol.114, no.19, pp.9559-9612, **(2014)**.

[61] Chen, W., Kuang, Q., Wang, Q., & Xie, Z. "Engineering a high energy surface of anatase TiO_2 crystals towards enhanced performance for energy conversion and environmental applications." *Rsc Advances*, vol.5, no.26, pp.20396-20409, **(2015)**.

[62] Liu, M., Piao, L., Zhao, L., Ju, S., & Wang, W., "Anatase TiO_2 single crystals with exposed {001} and {110} facets: facile synthesis and enhanced photocatalysis." *Chemical Communications,* vol.46, no.10, pp.1664, **(2010)**. doi:10.1039/b924172h

[63] Wu, Q., Wu, Z., Li, Y., Gao, H., & Du, L., "Controllable Synthesis and Photocatalytic Activity of Anatase TiO_2 Single Crystals with Exposed {110} Facets." *Chinese Journal of Catalysis,* vol.33, no.(11-12), pp.1743–1753, **(2012)**. doi:10.1016/s1872-2067(11)6044

[64] Yuan, J., Liu, Y., Bo, T., & Zhou, W.. "Activated HER performance of defected single layered TiO_2 nanosheet via transition metal doping." *International Journal of Hydrogen Energy*, vol.45, no.4, pp.2681–2688, **(2020).** doi:10.1016/j.ijhydene.2019.11.19

[65] Billo, T., Fu, F.-Y., Raghunath, P., Shown, I., Chen, K.-H. "Ni-Nanocluster Modified Black TiO_2 with Dual Active Sites for Selective Photocatalytic CO_2 Reduction." *Small,* vol.14, no.2, pp.1702928, **(2017)**. doi:10.1002/smll.201702928

[66] Sakai, N., Ebina, Y., Takada, K., & Sasaki, T., "Electronic band structure of titania semiconductor nanosheets revealed by electrochemical and photoelectrochemical studies." *Journal of the American Chemical Society,* vol.126, no.18, pp.5851-5858, **(2004)**.

[67] Makowska-Janusik, M., Gladii, O., Kassiba, A., Boucle, J., & Herlin-Boime, N. "Cluster approach to model titanium dioxide as isolated or organic dye sensitized nanoobjects." *The Journal of Physical Chemistry C*, vol.118, no.12, pp.6009-6018, **(2014)**.

[68] Stewart J.J.P., "Optimization of parameters for semiempirical methods V: Modification of NDDO approximations and application to 70 elements", *Journal of Molecular Modeling*, vol.13, p.1173–1213, **(2007)**. doi:10.1007/s00894-007-0233-43

[69] Foresman, J. B., & Frisch, A., "Exploring Chemistry with Electronic Structure Methods, methods second edition." *U.S.A.: Gaussian, Inc.*, **(1993)**.

[70] M.J. Frisch, G.W. Trucks, H.B. Schlegel, G.E. Scuseria, M.A. Robb, J.R. Cheeseman, G. Scalmani, V. Barone, B. Mennucci, G.A. Petersson, H. Nakatsuji, M. Caricato, X. Li, H.P. Hratchian, A.F. Izmaylov, J. Bloino, G. Zheng, J.L. Sonnenberg, M. Hada, M. Ehara, K. Toyota, R. Fukuda, J. Hasegawa, M. Ishida, T. Nakajima, Y. Honda, O. Kitao, H. Nakai, T. Vreven, J.A. Montgomery, J.E. Peralta Jr., F. Ogliaro, M. Bearpark, J.J. Heyd, E. Brothers, K.N. Kudin, V.N. Staroverov, R. Kobayashi, J. Normand, K. Raghavachari, A. Rendell, J.C. Burant, S.S. Iyengar, J. Tomasi, M. Cossi, N. Rega, J.M. Millam, M. Klene, J.E. Knox, J.B. Cross, V. Bakken, C. Adamo, J. Jaramillo, R. Gomperts, R.E. Stratmann, O. Yazyev, A.J. Austin, R. Cammi, C. Pomelli, J.W. Ochterski, R.L. Martin, K. Morokuma, V.G. Zakrzewski, G.A. Voth, P. Salvador, J.J. Dannenberg, S. Dapprich, A.D. Daniels, O¨. Farkas, J. B. Foresman, J.V. Ortiz, J. Cioslowski, D.J. Fox, *Gaussian 09, Gaussian, Inc., Wallingford CT,* **(2009)**.

[71] Stewart J.J.P., "Optimization of parameters for semiempirical methods VI: more modifications to the NDDO approximations and re-optimization of parameters." *Journal of molecular modeling*, vol.19 no.1, p.1-32, **(2013)**. doi:10.1007/s00894-012-1667-x

[72] Scarpelli, F., Mastropietro, T. F., Poerio, T., & Godbert, N.. "Mesoporous TiO_2 Thin Films: State of the Art. Titanium Dioxide - Material for a Sustainable Environment" **(2018)**. doi:10.5772/intechopen.742449

[73] Knipping, J., Wiggers, H., Rellinghaus, B., Roth, P., Konjhodzic, D., & Meier, C. "Synthesis of High Purity Silicon Nanoparticles in a Low Pressure Microwave Reactor." *Journal of Nanoscience and Nanotechnology*, vol.4, no.8, pp.1039–1044, **(2004)**. doi:10.1166/jnn.2004.149

[74] Chen Y, Liu Y, Wang X, Li K, Chen P. Preparation of high purity crystalline silicon by electro-catalytic reduction of sodium hexafluorosilicate with

sodium below 180 °C. *PLoS One*. vol.9, no.8, pp.e105537, **(2014)**. doi: 10.1371/journal.pone.010553

[75] Hossain, S. T., Johra, F. T., & Jung, W.-G.. "Fabrication of Silicon Carbide from Recycled Silicon Wafer Cutting Sludge and Its Purification." *Applied Sciences*, vol.8, no.10, pp.1841, **(2018)**. doi:10.3390/app8101841

[76] Spizzirri, P. G., Fang, J. H., Rubanov, S., Gauja, E., & Prawer, S. "Nano-Raman spectroscopy of silicon surfaces." *arXiv preprint arXiv:1002.2692*. **(2010)**.

[77] Borowicz, P., Latek, M., Rzodkiewicz, W., Łaszcz, A., & Ratajczak, J. "Deep-ultraviolet Raman investigation of silicon oxide: thin film on silicon substrate versus bulk material." *Advances in Natural Sciences: Nanoscience and Nanotechnology*, vol.3, no.4, pp.045003, **(2012)**.

[78] Hrubý, J., Vavrečková, Š., Masaryk, L., Sojka, A., & Neugebauer, P. "Deposition of tetracoordinate Co(II) complex with chalcone ligands on graphene." *Molecules*, vol.25, no.21, pp.5021, **(2020)**.

[79] Castrejón-Sánchez, V. H., Camps, E., & Camacho-López, M. "Quantification of phase content in TiO_2 thin films by Raman spectroscopy." *Superficies y vacío*, vol.27, no.3, pp.88-92, **(2014)**.

[80] Naumenko, A. P., Berezovska, N. I., Biliy, M. M., & Shevchenko, O. V. "Vibrational analysis and Raman spectra of tetragonal zirconia." *Physics and Chemistry of Solid State*, vol.9, no.1, pp.121-125, **(2008)**.

Chapter 7

STRUCTURAL AND ELECTRON PROPERTIES OF SELECTED DYES FOR DSSC APPLICATIONS

One of the main goals of this work was to find appropriate dye molecules that can be used in TiO_2-based DSSC devices. In this case, the Ru-based dyes were selected as the most promising ones. The interest was attended to dyes with donor part based on tris(bipyridine)ruthenium(II) ($Ru(pby)_3^{+2}$) complex in mono- and dinuclear dendritic configuration. These molecules possess the carboxyl functional groups (-COOH), popular in organic sensitizers, as the moieties anchoring dyes to the surface of the semiconducting anode. The idea of the presented work was also to investigate the influence of the anchoring groups on the photovoltaic properties of TiO_2-based DSSC changing their number, position, and type. Additionally, to Ru-based dyes, the two commercial dye molecules possessing the -COOH group were chosen as potential test structures where the anchoring groups can be modified. These molecules, based on indoline derivatives, are named D102 [CAS number: 652145-28-3] and D149 [CAS number: 786643-20-7].

In the present Chapter, the structural, electron, and optical properties of the above-mentioned dyes are presented. The greatest emphasis will be placed on computer modeling of the physicochemical properties of the selected dyes and the analysis of the obtained results regarding the corresponding experimental data.

7.1. Dyes based on single tris(bipyridine)ruthenium(II) complexes

The tris(bipyridine)ruthenium(II) cation ($Ru(pby)_3^{+2}$) is a prototypical metalloorganic complex belonging to the important class of pyridine-based transition metal complexes with numerous applications in functional materials. The molecules based on $Ru(pby)_3^{+2}$ are suitable model systems for the investigation of the optical properties of ruthenium complexes for DSSC applications. Grafting metal complexes onto the surface of a semiconductor can be achieved by modification of their ligands with suitable anchoring groups depending on the nature of the semiconductor surface[1]. Usually, the $Ru(bpy)_3^{+2}$-based molecules are anchored on the surface of the semiconducting material by the carboxyl (-COOH) functional groups introduced into the ruthenium complex. The -COOH groups can be incorporated directly onto the pyridine rings or can be added at the end of a molecular bridge acting as a spacer between the ruthenium complex and the metal oxide surface, as it was described in Chapter 3. The role of the spacer is to define the electron coupling between the sensitizer and the semiconductor and to control the charge injection and recombination. Systematic studies of such materials may provide fundamental insights into the factors controlling excited state relaxation and interfacial electron transfer.

To model properly the $Ru(pby)_3^{+2}$-based molecules first of all the $Ru(pby)_3^{+2}$ stabilized by the two molecules of the hexafluorophosphate ($(PF_6^-)_2$) was modeled to find the best methodology predicting its structure and then to calculate their electron and optical properties. The structure of the $[Ru(bpy)_3]^{2+}(PF_6^-)_2$ complex is presented in Fig. 3.3 (Chapter 3.1). Starting an analysis of the electron properties of the $[Ru(bpy)_3]^{2+}$ molecule first its geometry was optimized by applying the *ab initio* and density functional theory (DFT) formalism implemented in the Gaussian 16 program package[2,3]. The procedure was performed for $[Ru(bpy)_3]^{2+}$ molecule and $[Ru(bpy)_3]^{2+}(PF_6^-)_2$ system placed in a vacuum. The minimum of the potential energy surface was calculated at the restricted Hartree−Fock (RHF) level in D_3 symmetry. The gradient convergence tolerance was equal to 10^{-6} Hartree/Bohr. At the end of the geometry search, the Hessian evaluation was performed to exclude the structures giving negative modes and ensure the thermodynamic equilibrium of the molecule. In the performed calculations the 3-21G or LANL2DZ (Los Alamos National Laboratory 2 double-zeta) basis sets were used for the Ru atom and 6-311++G** or LANL2DZ basis sets for all remaining atoms. The better geometry of the $[Ru(bpy)_3]^{2+}$ was achieved when the molecule is in the neighborhood of the $(PF_6^-)_2$. The geometry of the $[Ru(bpy)_3]^{2+}(PF_6^-)_2$ was also optimized by applying DFT/B3LYP functional augmented by the 2nd order scalar relativistic effects within the Douglas–Kroll–Hess (DKH2) formalism[4,5,6] using the jorge-TZP-DKH basis set[7]. The correctness of the selected optimization method was verified by the comparison of the obtained distance between the Ru atom and the neighboring N atoms and their symmetry to the experimental data. The obtained results are collected in Table 7.1.

Table 7.1. Distances between Ru atoms and neighboring N atoms calculated for $[Ru(bpy)_3]^{2+}$ molecule stabilized by $(PF_6^-)_2$ ions predicted by different computational methods. Presented values are given in Å

Methodology		*Ab initio*/ HF	DFT/B3LYP	DFT/B3LYP	DFT/B3LYP	DFT/B3LYP-DKH2
Basis set	Ru	LANL2D	3-21G	LANL2DZ	LANL2DZ	jorge-TZP-DKH
	Other atoms	LANL2D	6-11++G**	6-11++G**	LANL2DZ	jorge-TZP-DKH
Ru-N		~2.128	2.112	2.100	2.096	2.079
Experiment		2.056 [8]				

The *ab initio* method overestimates the Ru-N bonds and does not give the correct symmetry of the Ru(pby)$_3^{+2}$ molecule why this geometry will be not discussed elsewhere. The DFT method with B3LYP functional yields symmetrical Ru-N bonds, all of which possess the same length. The DFT/B3LYP-DKH2 formalism with the jorge-TZP-DKH basis set gives the Ru-N bonds equal to 2.079 Å. It is the closest value compared with the Ru-N bonds in the Ru(pby)$_3^{+2}$ crystal arrangement (2.056 Å)[8]. Optimization of the Ru(pby)$_3^{+2}$$(PF_6^-)_2$ system keeps the Ru-N bonds and N-Ru-N angles characteristic for D_3 symmetry of the Ru(pby)$_3^{+2}$ ion in the crystal structure, with the phosphorus anions arranged symmetrically on the C_3 axis. Because calculations performed at the DFT/B3LYP-DKH2 level are very time-consuming the geometries obtained at the DFT/B3LYP(LANL2DZ) level of calculations were also considered for future analysis.

The vertical transition energies and oscillator strengths for the first 100 singlet excited states were calculated for structures of Ru(pby)$_3^{+2}$$(PF_6^-)_2$ optimized in their singlet ground states using DFT/B3LYP-DKH2 and DFT/B3LYP(LANL2DZ) method. For the structure with geometry optimized at DFT/B3LYP-DKH2 level, the UV-vis spectra were calculated by the time-dependent DFT (TDDFT) method at the DFT/B3LYP-DKH2(jorge-TZP-DKH) and DFT/B3LYP(LANL2DZ) level. The excitation energy positions and oscillator strengths were calculated using the iterative Davidson method[9] with an accuracy of 10^{-12} Hartree. Due to the dominant role of singlet excited states in absorption, only singlet-singlet transitions were considered. In Fig. 7.1 experimental and calculated UV-vis absorption spectra of the Ru(pby)$_3^{+2}$(PF$_6^-$)$_2$ are presented. The samples are depicted as follows: geometry optimized by DFT/B3LYP(LANL2DZ) method and oscillators calculated by DFT/B3LYP(LANL2DZ) method – B3LYP/B3LYP, geometry optimized by DFT/B3LYP-DKH2(jorge-TZP-DKH) method and oscillators calculated by DFT/B3LYP(LANL2DZ) method – DKH2/B3LYP, geometry optimized by DFT/B3LYP-DKH2(jorge-TZP-DKH) method and oscillators calculated by DFT/B3LYP-DKH2(jorge-TZP-DKH) method – DKH2/DKH2. Analyzing data presented in Fig. 7.1 one can see that all three implemented approaches give reasonable results. The first absorption peak corresponding to metal-to-ligand charge transfer (MLCT) calculated by DKH2/DKH2 method is placed in the center of the experimental peak. The other used two methods shift the spectrum insignificantly into the left and right sides.

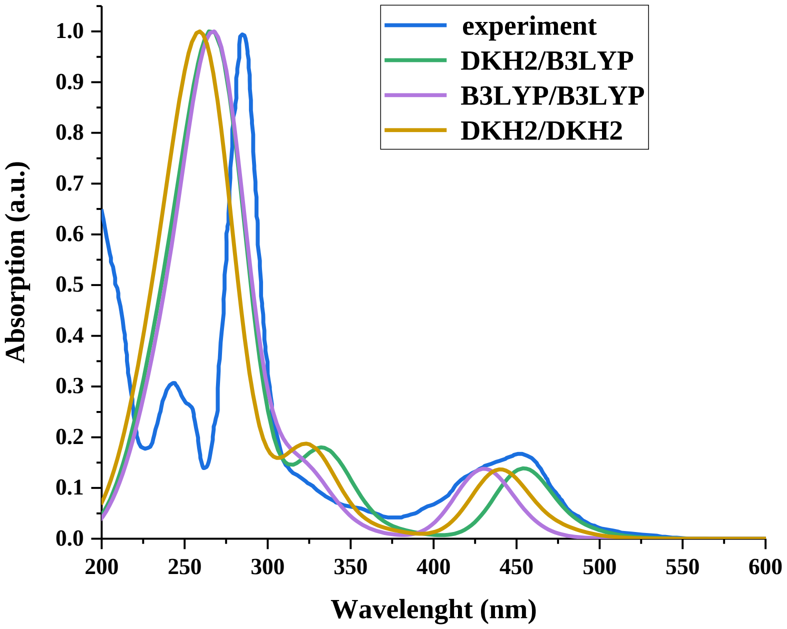

Figure 7.1. Normalized UV–vis absorption spectra for Ru(bpy)$_3^{2+}$(PF$_6^-$)$_2$ measured in acetonitrile[10] (experiment) compared to calculated data: geometry optimized by DFT/B3LYP(LANL2DZ) method and oscillators calculated by DFT/B3LYP(LANL2DZ) method (B3LYP/B3LYP), geometry optimized by DFT/B3LYP-DKH2(Jorge-TZP-DKH) method and oscillators calculated by DFT/B3LYP(LANL2DZ) method (DKH2/B3LYP), geometry optimized by DFT/B3LYP-DKH2(jorge-TZP-DKH) method and oscillators calculated by DFT/B3LYP-DKH2(jorge-TZP-DKH) method (DKH2/DKH2)

Following the conclusions made in Chapter 3, the Ru(pby)$_3^{+2}$-based molecules extended by the spacers and anchoring groups can be used in DSSC applications. In the presented work three Ru(pby)$_3^{+2}$-based molecules with –COOH anchoring groups located in different positions will be discussed (see Fig. 3.8 of Chapter 3.1. and Fig. 7.2). Three investigated molecules employed the carboxyl group as an anchor located in para- (RuLp), meta- (RuLm), or ortho-position (RuLo) to the benzene ring. The synthesis of these molecules was described in the work of Zalas and co-workers[11]. All of the investigated sensitizers possess rod-like spacers between photoactive and anchoring parts of dyes. They are formed by oligophenylene–ethynylene (OPE) bridges terminated by the –COOH groups. The mentioned dyes are proposed to be anchored to a surface of the TiO_2 semiconducting nanosized material which will be described in Chapter 8.

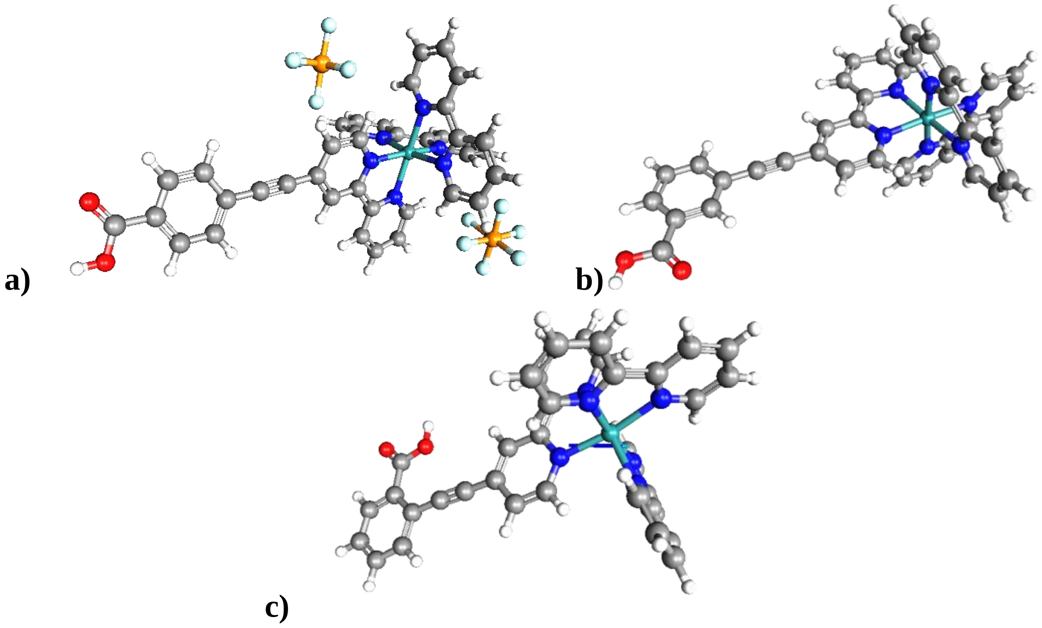

Figure 7.2. Structure of the Ru-complexes named as RuLp (para-position of anchor group) (a), RuLm (meta-position of anchor group) (b), and RuLo (orto-position of anchor group) (c) with hexafluorophosphate (PF_6^-) stabilizers

The point of interest in performing the proposed investigations was to understand the effects of the position of the anchoring group on the overall efficiency of the DSSC cell. The present work aims to explain the photon-to-current efficiency conversion and explain the charge transfer phenomena occurring between the RuLo, RuLm, and RuLp sensitizers and the TiO_2 semiconductor depending on the position of the -COOH anchoring group. The selected molecules serve as a model for the dye/metal oxide interface in DSSCs. In this case, the computer modeling of the structural and electron properties of the investigated molecules was performed. The GAMESS program package[12,13] was used to perform computer simulations. The lowest total energies of the molecules were searched with C1-defined symmetry in a vacuum using the DFT/B3LYP formalism. The calculations were made by applying LANL2DZ basis sets as it was proposed for the $Ru(pby)_3^{+2}(PF_6^-)_2$ complex. The minimum of the potential energy surface was calculated at a restricted Hartree-Fock (RHF) level[14]. Optimal geometries of the molecules were found by applying the quadratic approximation (QA) optimization algorithm based on the augmented Hessian technique[15]. The gradient convergence tolerance was equal to 10^{-5} Hartree/Bohr. At the end of the geometry optimization, the Hessian evaluation was performed to exclude structures giving the negative modes and ensure a thermodynamic equilibrium of the molecules.

The electron properties of the studied molecules were calculated for optimized structures applying the *ab initio* and the DFT methodology with B3LYP and LC-BLYP functionals. In this case, the mixed basis set was used applying the LANL2DZ basis set for Ru and the 6-31++G** basis set for all other atoms. The RHF SCF energy convergence criterion was chosen to be 10^{-12} Hartree. The optical properties of the studied molecules were calculated using the same basis set as it was used for electron properties calculations, applying the time-dependent HF (TDHF) and TDDFT methods. The UV−vis absorption spectra were calculated using the iterative Davidson algorithm[9] with an accuracy of 10^{-12} Hartree. All the mentioned calculations were performed in the GAMESS program package.

To investigate the solvent effect on the electron properties of RuLo, RuLm, and RuLp molecules, the polarizable continuum model (PCM)[16] was used, applying the conductor-like PCM (C-PCM)[17,18] implementation. It is one of the most frequently used apparent surface charge (ASC) models[19,20]. The solvent radius and the dielectric constants were assumed to be the same as the parameters collected in the GAMESS code.

Geometries of the RuLm, RuLo, and RuLp molecules were optimized in a vacuum as well as in the hexafluorophosphate $(PF_6^-)_2$ environment. Two PF_6^- molecules were added to each dye to stabilize the $Ru(bpy)_3^{2+}$ based structures. In Fig. 7.2 examples of the optimized structure of the RuLm, RuLo, and RuLp molecules with and without PF_6^- stabilizers are presented. The RuLp molecule possessing the -COOH group in para- position could not be optimized using the

DFT/B3LYP method without stabilized molecules surrounding the dye, because the assumed convergence criterion equal to 10^{-5} Hartree/Bohr was not achieved during geometry optimization. The structure of the molecule RuLp obtained in this manner does not have any symmetry in the donor part. Also, the electron parameters calculated for the obtained structure of the RuLp molecule without stabilizers are unreal. Structures of the RuLm and the RuLo molecules without stabilizers were successfully optimized reaching the convergence criterion, but geometries of the Ru(bpy)$_3^{2+}$ moieties were deformed. This data ensures us in requirements using two molecules of the PF$_6^-$ as a stabilizer in all cases of the Ru(bpy)$_3^{2+}$-based molecules. In consequence, geometries of the RuLm, RuLp, and RuLo molecules were optimized with added PF$_6^-$ stabilizers. It is known that the relaxed Ru(bpy)$_3^{2+}$ complex should have D3 symmetry and it was ensured by implementing the (PF$_6^-$)$_2$ as a stabilizer. One can conclude that the stabilizer prevents the distortion of the Ru(bpy)$_3^{2+}$ moiety. Distances between Ru and N atoms of the relaxed dye structures are presented in Table 7.2. It is seen that modification of the Ru(bpy)$_3^{2+}$ structure by the spacer and –COOH anchoring group does not change the geometry of the Ru environment.

Table 7.2. Distances between Ru and N atoms in the RuLm, RuLo, and RuLp molecules obtained via computer modeling using the DFT/B3LYP-LANL2DZ method

	RuLm without PF$_6^-$	RuLo without PF$_6^-$	RuLp with PF$_6^-$	RuLm with PF$_6^-$	RuLo with PF$_6^-$
Ru-N (Å)	2.10	2.10	2.17	2.17	2.18
	2.12	2.12	2.17	2.17	2.17
	2.17	2.16	2.17	2.17	2.18
	2.21	2.19	2.17	2.17	2.17
	2.22	2.11	2.17	2.17	2.17
	2.16	2.17	2.17	2.17	2.17

Optical properties of isolated RuLm, RuLo, and RuLp molecules were calculated in a vacuum using the TDHF and TDDFT methods applying the B3LYP (DFT/B3LYP) and LC-BLYP (DFT/LC-BLYP) functionals. The positions of the first UV-vis absorption peaks measured experimentally[11] and predicted computationally are collected in Table 7.3. The dyes were studied as isolated molecules in a vacuum (denoted as “vacuum”), with stabilizers (PF$_6^-$) noticed as "PF$_6$", as well as in DMF solvent (PF$_6^-$/DMF). The effect of the intermolecular interactions occurring between the considered dyes and stabilizers shifts the first absorption peak to shorter wavelengths compared with the data obtained for the isolated dyes. Additionally, the spectra calculated without stabilizers are shifted too much to long wavelengths concerning experimental data. This discrepancy may be caused by an incorrect optimization of the molecular structures and instability of the Ru $(bpy)_3^{2+}$ moiety without $(PF_6^-)_2$.

Table 7.3. Position of the first absorption peak λ_{max} (nm) calculated by the TDHF, DFT/B3LYP, and DFT/LC-BLYP methods for the RuLm, RuLo, and RuLp molecules and the experimental data[25]

Molecule	Environment	TDHF (nm)	DFT/B3LYP (nm)	DFT/LC-BLYP (nm)	Exp (nm)
RuLm	vacuum	693	779	1309	459
	PF_6	263	429	330	
	PF_6/DMF	---	437	---	
RuLo	vacuum	700	796	1219	475
	PF_6	264	419	328	
	PF_6/DMF	---	436	---	
RuLp	vacuum	---	---	---	460
	PF_6	269	433	321	
	PF_6/DMF	---	447	---	

Calculations performed by using the DFT/B3LYP method for the RuLo, RuLm, and RuLp molecules with PF_6^- stabilizers lead to a good agreement with the experimental results. The TDHF and DFT/LC-BLYP calculations shift the UV-vis absorption spectra into short wavelength compared with experimental data. As a consequence of these results, the calculations in a solvent were performed using only DFT/B3LYP method. The first absorption peak calculated in the DMF solvent for molecules surrounded by stabilizers (PF_6/DMF) shows a red shift compared with the calculations performed for dyes and stabilizers in a vacuum (noticed as "PF_6"). The first UV-vis absorption peak measured for the $Ru(bpy)_3^{2+}$ derivatives is dominated by the MLCT and depends on the structural modification of ligands. However, it is located close to 450 nm as it is observed for the $Ru(bpy)_3^{2+}(PF_6^-)_2$ (see Fig. 7.1). The $Ru(bpy)_3^{2+}$ group possesses the D_3 symmetry with free electron pairs on the nitrogen atoms[8]. Therefore, the UV-vis absorption spectrum of the tris(bipyridine)ruthenium(II) molecule measured experimentally exhibits one peak in the visible region at 456 nm (MLCT π_M- π_L^*) and the second one coming from the inter ligand charge transfer (ILCT) absorption located in a UV region (at 291 nm)[8,21].

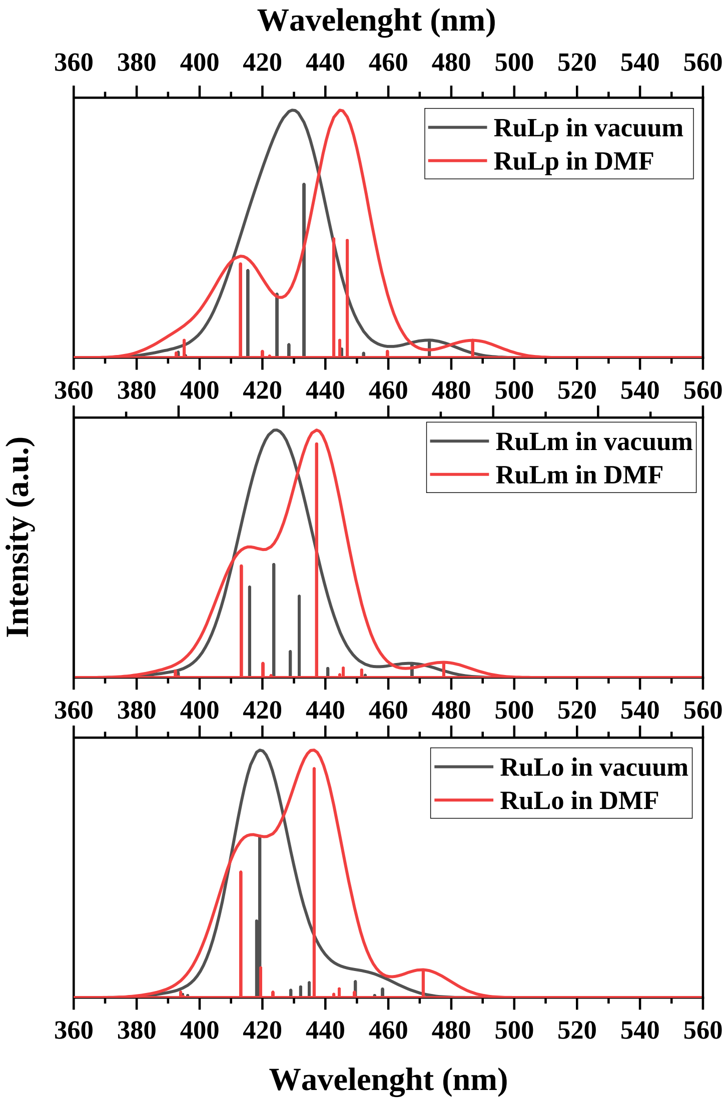

Figure 7.3. Normalized UV–vis absorption spectra calculated by DFT/B3LYP method for the RuLp, RuLm, and RuLo molecules stabilized by the $(PF_6^-)_2$ in vacuum (black) and solvent DMF (red)

The UV-vis absorption spectrum calculated by DFT/B3LYP method for the $Ru(bpy)_3^{2+}$ molecule with the PF_6^- stabilizers has a first absorption peak located at 425 nm – 455 nm depending on the methods of calculations (see Fig. 7.1). All investigated molecules RuLo, RuLp, and RuLm have first MLCT absorption peak in the region corresponding to the $Ru(pby)_3^{+2}(PF_6^-)_2$ complex (see Fig. 7.3 and Table 7.3). The UV-vis absorption spectrum calculated for the RuLo molecule shows the first absorption peak the most shifted into short wavelength. It is seen in the case of vacuum and DMF. It can be caused by the noncentrosymmetric environment of the Ru atom, probably not accurately optimized for the RuLo molecule. Regarding the –COOH anchoring group position, the more pronounced symmetry of the RuLm and RuLp molecules than the one of the RuLo leads to their red-shift of the absorption spectra[22]. The obtained tendency does not reproduce exactly the experimental data (see Fig. 7.4). The influence of the position of the anchoring group is not well reproduced, but the general location of the MLCT peak is in agreement with experimental data, including the computational error.

The experimentally measured UV-vis absorption spectra for RuLp, RuLo, and RuLm dyes are quite similar to one another with only a few differences (see Fig. 7.4). The three complexes display 3 major absorption bands at 245, 290, and 330 nm, and a broader one, in the visible region, between 400 and 520 nm. According to the work of Balzani et al.,[23] the absorption bands below 220 nm and at 290 nm can be ascribed to π-π* electron transition in the ligands, while the 245 nm band and the one in the visible range are assigned to MLCT transitions. The absorption spectra in the visible range have a quite long tail spreading up to 600 nm.

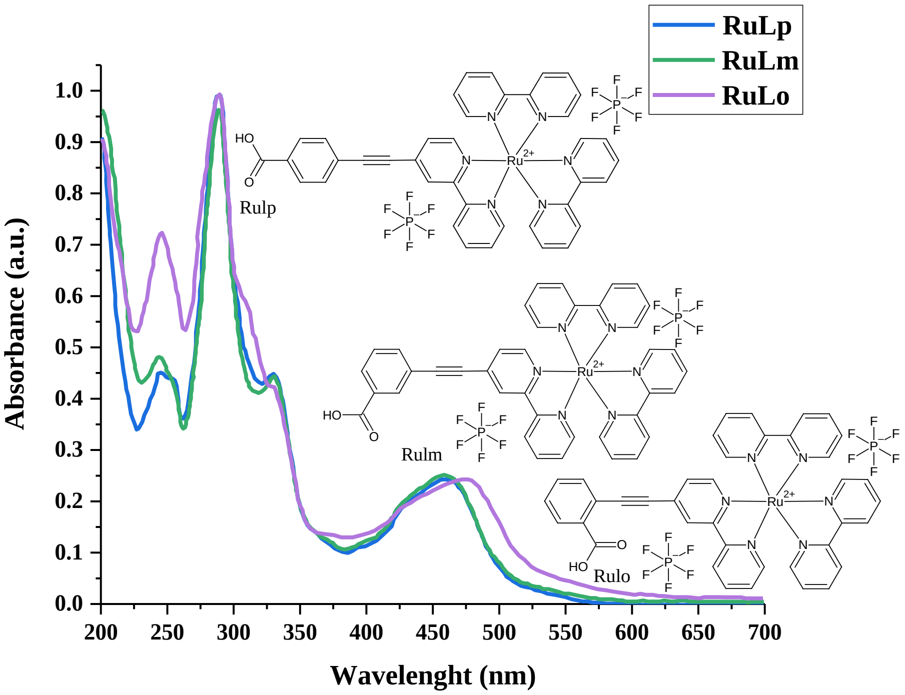

Figure 7.4. UV-vis absorption spectra measured experimentally for the RuLm, RuLo, and RuLp molecules in MeOH-EtOH 4-1 mixture at 298 K (b)[11]

Table 7.4. Electron properties of the Ru(bpy)$_3^{+2}$ as well as the RuLp, RuLm, and RuLp dyes with PF$_6$- stabilizers and location of their frontiers orbitals calculated by DFT/LC-BLYP, DFT/B3LYP, and *ab initio* (TDHF) method.

	Method	HOMO (eV)	LUMO (eV)	ΔE$_{\text{HOMO-LUMO}}$ (eV)	μ (D)	HOMO	LUMO
RuLp	DFT/ LC BLYP	-8.85	-1.19	7.66	1.36	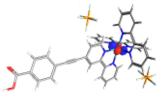	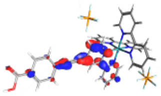
	DFT/ B3LYP	-6.38	-2.99	3.39	1.35	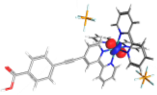	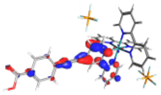
	TDHF	-9.24	0.28	9.52	1.64	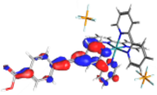	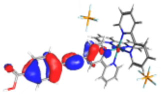
RuLm	DFT/ LC BLYP	-8.83	-1.10	7.70	0.67	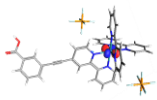	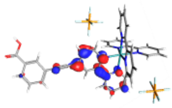
	DFT/ B3LYP	-6.37	-2.91	3.45	0.54	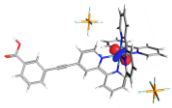	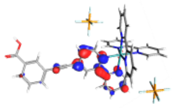
	TDHF	-9.12	0.40	9.52	0.96	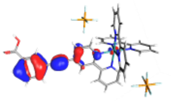	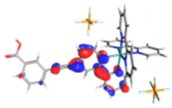
RuLo	DFT/ LC BLYP	-8.85	-1.07	7.77	1.46	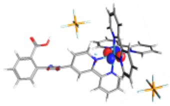	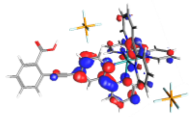
	DFT/ B3LYP	-6.41	-2.91	3.49	1.23	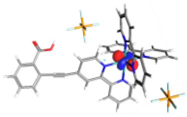	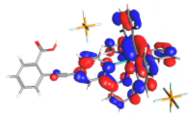
	TDHF	-9.00	0.45	9.45	1.55	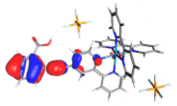	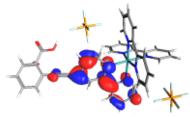
Ru(bpy)$_3^{+2}$	DFT/ LC BLYP	-8.62	-0.82	7.80	0.00	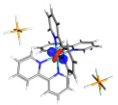	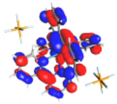
	DFT/ B3LYP	-6.37	-2.82	3.56	0.01	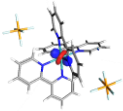	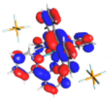
	TDHF	-9.51	0.60	10.11	0.00	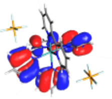	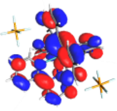

The frontier orbitals of the RuLo, RuLm, and RuLp molecules were calculated by the HF, DFT/B3LYP, and DFT/LC-BLYP methods taking into consideration $(PF_6^-)_2$ stabilizers. Analyzing the data presented in Table 7.4 one can conclude that the HF method does not work correctly with the studied molecules. The *ab initio* method gives bad results not only in the position of the absorption peaks but although in the localization of higher occupied molecular orbitals (HOMO) and lower unoccupied molecular orbitals (LUMO). The HOMO orbital in Ru-based complexes should be located at the Ru atom. The $Ru(pby)_3^{+2}(PF_6^-)_2$ structure can serve here as the test molecule. One can see that the DFT-based methods give good results concerning HOMO localization at $Ru(pby)_3^{+2}$ structure. The HOMO orbitals calculated for the RuLo, RuLm, and RuLp molecules by the TDHF method are spread through ligands, which is incorrect according to the Ru-based systems (see Table 7.4). According to data presented in Table 7.3, one can see that the HF method shifts UV-vis absorption spectra into shorter wavelengths which is caused by occurring of the ILCT transition. In this case, one can conclude that TDHF cannot be used to calculate the electron properties of investigated Ru-based dyes. On the other hand, TDDFT with both functionals: B3LYP and LC-BLYP, shows correct redistribution of HOMO and LUMO orbitals on the RuLp, RuLm, and RuLo dyes (see Table 7.4).

The position of the –COOH moiety does not have any significant effect on the location of the HOMO orbital placed on the Ru atom (Table 7.4). In addition, the HOMO orbital of each molecule is characterized by nearly the same energy. However, significant differences are observed in the LUMO orbitals distribution. In the case of the RuLo molecule, the LUMO orbital is widespread on the whole $Ru(bpy)_3^{2+}$ moiety. During the excitation process of the RuLo dye, the electrons are transferred from the Ru atom to its octahedral environment. The same is observed for the $Ru(bpy)_3^{2+}$ molecule. The LUMO orbital of the RuLm is mostly located on the bipyridine group. The LUMO orbital of the RuLp spreads along the molecule and is located at the OPE spacer, benzene, and –COOH group. The position of the LUMO orbital at the –COOH group favors the charge transfer from the dye molecule into the semiconducting material through the anchoring moiety. The calculations point out that the RuLp molecules should be potentially the most suitable structure for sensitizing semiconductors in DSSCs devices.

Alteration of the -COOH group connection from the *meta*- or *ortho*-isomer into *para*-position improves charge separation occurring between HOMO and LUMO orbitals of the studied dye (see Table 7.4). In consequence, it allows forming of the intramolecular charge transfer (ICT) occurring in the *para*-series of dyes and facilitates higher electron injection from the photoexcited dye into the conduction band of the TiO_2. The overall superior performance of the *para*- compared to the *meta*- and the *ortho*-series of dyes can also be explained based on the observed dipole moments (μ) estimated by DFT/B3LYP calculations (see Table 7.4). One can see that the RuLo and RuLp molecules have similar dipole moments almost three times larger than the one of the RuLm dye. However, the dipole moment of the RuLp molecule is slightly larger than the dipole moment of the RuLo dye. Additionally, it is directed along the molecule's long axis towards the –COOH group. The work of Cahen et al.[24] shows that the open-circuit voltage (V_{oc}) of DSSCs varies linearly with dipole moments of adsorbed dyes increasing when the sensitizers have a dipole moment directed toward the TiO_2 surface. This situation is observed for the RuLp-based systems. It was shown that the highest V_{oc} was measured for the RuLp-based DSSC[11]. It means that the photoefficiency of the hybrid system depends significantly on the direction of the dipole moment. However, the dipole moment value is less critical in the photovoltaic processes. The obtained results are in agreement with the results measured by cyclic voltammetry in the laboratory of the Zalas group[11].

Because the RuLp dye seems to be the most appropriate for the DSSC application its UV-vis absorption spectra were also calculated for the structure optimized by the DFT/B3LYP-DKH2(jorge-TZP-DKH) method using the DFT/B3LYP-DKH2(jorge-TZP-DKH) method, depicted as DKH2/DKH2. The same method was used previously to calculate electron and optical properties of the $Ru(pby)_3^{+2}(PF_6^-)_2$ complex (see Fig. 7.1). One can see that the proposed method reproduces well absorption spectra measured for the RuLp molecule (see Fig. 7.5). The only discrepancy between the experimental and calculated spectra is the peak at 400 nm, which is not seen experimentally. The mentioned peak is attributed to the metal-to-far laying ligand area (spacer) transition. It will be called “external MLCT”. Probably this electron transfer is extinguished by the interaction between the molecule and the environment. The calculated spectra reproduce well the first

MLCT transition at 450 nm, the second MLCT transition at 325 nm, and the ILCT transition at 290 nm with energy positions and intensities roughly consistent with an experiment. The HOMO-LUMO transition at about 528 nm contains Ru-centered HOMO and LUMO almost completely localized at a single bipyridine ligand and its attached carboxyphenyl functional group (external MLCT).

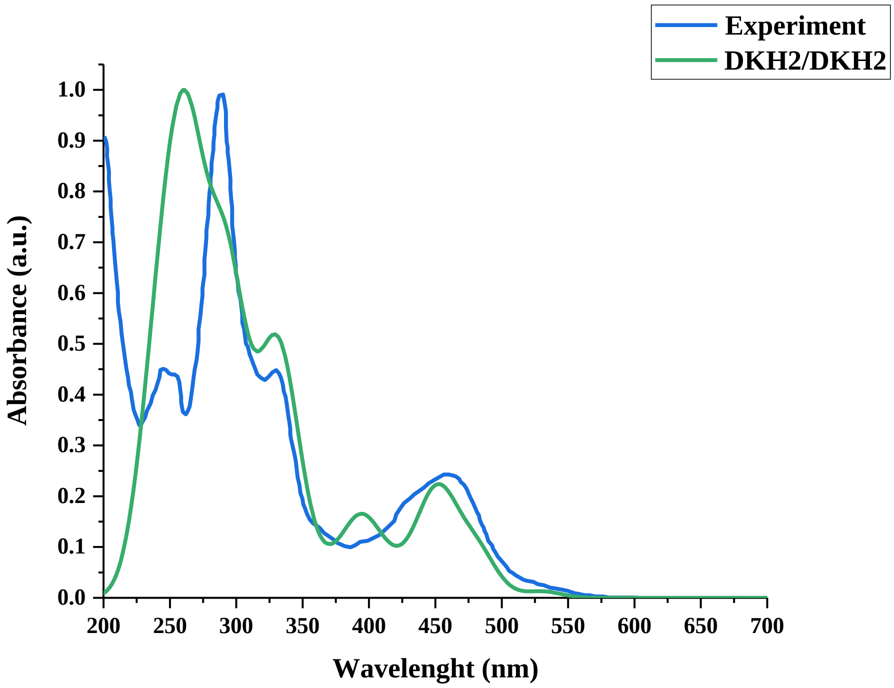

Figure 7.5. UV–vis absorption spectra measured experimentally[25] (blue line) and calculated for the RuLp structure optimized by the DFT/B3LYP-DKH2(jorge-TZP-DKH) method using the DFT/B3LYP-DKH2(jorge-TZP-DKH) method (DKH2/DKH2)

The DKH2/DKH2 obtained data presented in Fig. 7.5 were considered to calculate the electroabsorption spectra for the RuLp molecule. Electroabsorption (EA) spectroscopy, also known as Stark effect spectroscopy, is the most suitable method, specifically dedicated to tracking charge redistribution immediately after photoexcitation[26,27]. When an external electric field is applied to the molecular system, the absorption bands can be broadened, shifted, or changed in intensity. Using the standard EA spectral analysis, based on Liptay theory[28] for well-separated and non-degenerate electronic states, the total electrooptic effect can be quantified in terms of molecular parameters. Thus, changes in the permanent dipole moment ($\Delta\mu$), electron polarizability (Δp), and oscillator strength can be deduced by comparing the observed EA spectra with the derivatives of the absorption spectrum of the molecule. In electron-delocalized molecular systems, the EA spectrum should reproduce the first derivative of the absorption spectrum. In more localized systems with an asymmetric charge distribution and a non-zero permanent dipole moment, the EA signal should mimic the second derivative of the absorption spectrum[28].

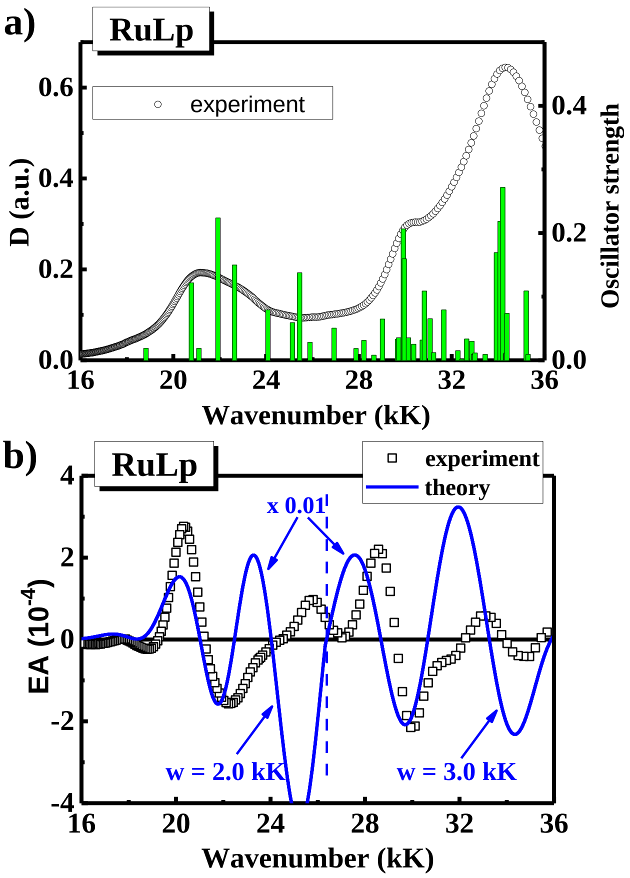

Figure 7.6. a) Stick-bar spectrum of the calculated oscillator strengths using the DKH2/DKH2 method for RuLp with stabilizers overlaid on the experimental absorption spectrum of the RuLp film; b) The EA spectrum calculated using the DKH2/DKH2 method for all excited states presented in part a) of the figure compared with the experimental EA spectrum of the film

In the system created by RuLp molecules accompanied by $(PF_6^-)_2$ stabilizers, characterized by an asymmetric molecular structure, there are no strictly degenerate states, but many electronic states closely lying on the energy scale interact with each other (Fig. 7.6a). The cumulative EA response from all of these states determined computationally (solid line) is compared with the experimental results (squares) in Fig. 7.6b. The computational curve assumes the average bandwidths $\omega = 2$ kK and $\omega = 3$ kK, for the lower and higher energy ranges, respectively, as indicated in the figure by a dashed vertical line. The EA spectrum was calculated for an electric field strength equal to 10^6 V/cm, one order of magnitude higher than the applied experimental electric field.

Analyzing data presented in Fig. 7.6b one can say that apart from the intense negative lobe associated with extended MLCT states at about 25 kK (400 nm), which is not seen in the experiment, the theoretical curve reproduces the main features of the experimental EA spectrum. The obtained EA signal is close to the absorption second derivative taking into account the MLCT peak (low energy leaks). The part of the spectrum with the minimum at about 22.0 kK, is mainly formed by the splitting of the 3E state of $Ru(pby)_3^{+2}$. These observations have key implications for the EA mechanism in $Ru(pby)_3^{+2}$-based systems that exhibit similar EA spectra, due to the robust nature of first MLCT states in such systems. The obtained results prove the resistance of the electron MLCT system to environmental disturbances. Was shown that the obtained changes in dipole moment can be attributed to the transfer of an electron from the Ru to a ligand.

The EA measurements were performed at Technical University in Gadnsk in a laboratory headed by Professor Stampor. The discussed results are reported in the work "Electronic States of Tris(bipyridine) Ruthenium(II) Complexes in Neat Solid Films Investigated by Electroabsorption Spectroscopy" published in *Materials*[29]. The mentioned work is authored by D. Pelczarski, O. Korolevych, B. Gierczyk, M. Zalas, M. Makowska-Janusik, and W. Stampor W. My contribution to the mentioned work is the quantum chemical calculations of electron and optical properties of the studied molecules.

Electron properties of the RuLp molecule were also calculated using the semiempirical parametrized methods, and the obtained results were compared with the data achieved by experiments and the DFT calculations. As was mentioned above the DKH2/DKH2 method gives the best results concerning the electron and optical properties of the RuLp. Unfortunately for the bigger systems such as hybrids or many-atom dyes the DKH2/DKH2 procedure became complicated and time-consuming to be used. In this case, the PM6[30] and PM7[31] parametrized methods can be used.

Two different geometries of RuLp molecule were adapted to calculate their electron parameters semiempirically. The RuLp structure was optimized by the HF method with LANL2DZ basis set for Ru and 6-31G for remaining atoms (maned

HF) and by the DFT/B3LYP-DKH2(jorge-TZP-DKH) method (named DKH2). The semiempirical method cannot be used for geometry optimization of studied molecules because they give noncentrossymetry in Ru-complex. Electron properties of the RuLp molecule were calculated using Gaussian 16[2,3] program package. The SCF convergence criterion was implemented to be not less than 10^{-12} Hartree. The excited states were calculated using the CIS/PM6 (singlet configuration interaction method), TD/PM6 (time-dependent PM6 parametrized method)[32], and CIS/PM7[33]. The PM7 semiempirical method has higher diffuse parameters for heavy atoms than the PM6.

The UV-vis absorption spectra calculated for RuLp by using different methods CIS/PM6, CIS/PM7, and TD/PM6 for the geometries optimized applying DKH2 or HF method compared with experimental data are presented in Fig. 7.7. One can see that the geometry of the RuLp molecule optimized by HF method gives UV-vis spectra overlapped better with experimental data than the geometry obtained at DKH2 level. In Table 7.5 position of the main absorption peak for MLCT and ILCT states calculated for RuLp by using different methodologies CIS/PM6, CIS/PM7, and TD/PM6 for the geometries optimized applying DKH2 and HF method compared with data obtained at DKH2/DKH2 level of calculations and experimentally are presented. One can see that the CIS/PM7 method gives not appropriate results for both geometries optimized at HF as well as at DKH2 level. Generally, better results are given by the PM6 calculations. The DKH2/CIS/PM6 gives an excellent MLCT position, but it has a problem reproducing the ILCT peak, and the obtained spectrum is too diffused.

Analyzing these data one can conclude that obtained position of the MLCT and ILCT peaks goes better with the experiment for the geometry of the RuLp obtained at the HF level and the excited states calculated by the TD/PM6 method. The TD/PM6 method can be used to calculate the electron and optical properties of the Ru complexes with geometries optimized at the HF level. Even the geometry of the complex is not perfect as it is seen after DKH2 optimization the HF geometries will be used to predict the optical spectra of hybrid materials described in Chapter 8.

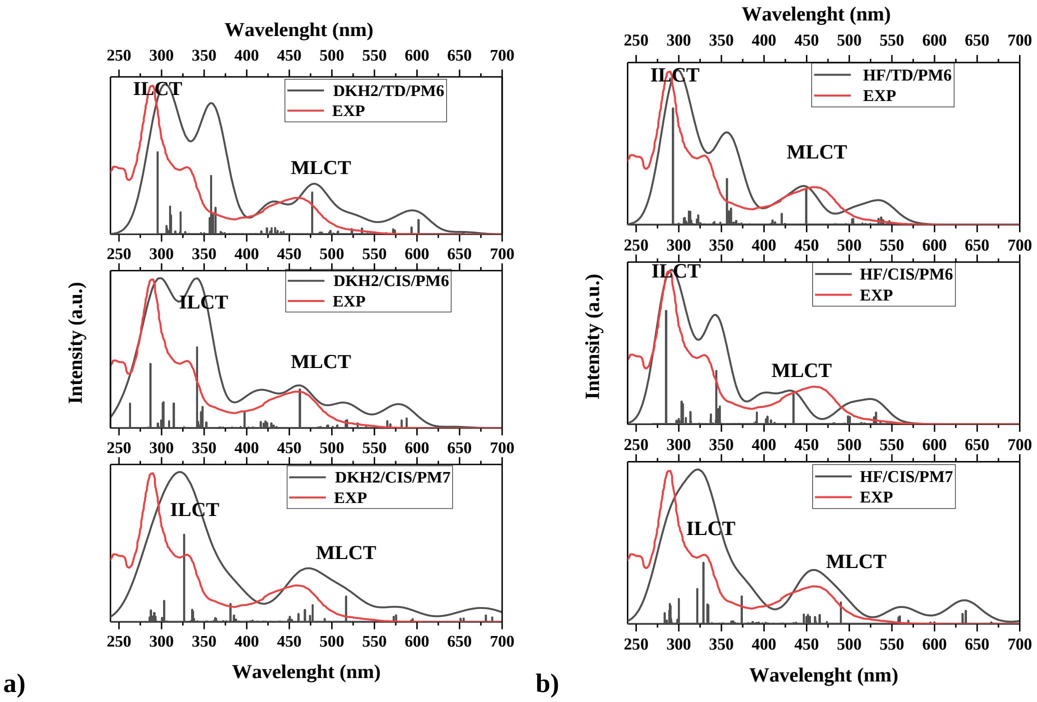

Figure 7.7. Normalized UV–vis absorption spectra calculated by semiempirical method TD/PM6, CIS/PM6, and CIS/PM7 for the RuLp molecule stabilized by the $(PF_6^-)_2$ in vacuum (black) and measured ones (red). a) The RuLp molecules optimized by the DFT/B3LYP-DKH2(jorge-TZP-DKH) method (DKH2), b) RuLp structure optimized by HF method with LANL2DZ basis set for Ru and 6-31G for remaining atoms (HF)

Table 7.5. Position of the main absorption peak for MLCT and ILCT states calculated for RuLp by using different methodologies CIS/PM6, CIS/PM7, and TD/PM6 for the geometries optimized applying DFT/B3LYP-DKH2(jorge-TZP-DKH) (DKH2) and HF method with LANL2DZ basis set for Ru and 6-31G for remaining atoms (HF) compared with data obtained at DKH2/DKH2 level of calculations and experimental data

Level of geometry optimization	Absorption peak	CIS/PM6 (nm)	CIS/PM7 (nm)	TD/PM6 (nm)	DKH2 (nm)	Exp (nm)
DKH2	MLCT	462	517	477	456	459
	ILCT	342	327	295	292	290
HF	MLCT	435	490	450		
	ILCT	285	330	293		

Summary of the results presenting the UV-vis spectra calculated for the RuLp molecules optimized by DKH2 and HF method using DKH2 and TD/PM6 formalism is presented in Fig. 7.8. Analyzing these data one can see that the best results compared with the experiment gives the DKH2/DKH2 method but unfortunately this formalism cannot be applied to calculate optical properties of hybrid systems based on RuLp dye (the subject of Chapter 8). Looking at the semiempirical results, the DKH2/TD/PM6 method gives strong absorption near 600 nm causing discrepancies between experimental and computational data. This method also shifts significantly the MLCT peak into the red side of the spectrum (from 459 nm in the experimental spectrum to 477 nm in the calculated one). Data obtained using HF/TD/PM6 formalism are much more comparable to the experiment. One can see that the first MLCT peak is located at 450 nm. Unfortunately, the TD/PM6 method has a problem reproducing the second MLCT peak regardless of the calculated geometry. It shifts the second MLCT peak of 30 nm into a higher wavelength compared with the experiment. The results presented here are in agreement with the data reported by Juris and co-workers[23]. The authors argue that the MLCT absorption bands observed for the $Ru(bpy)_3^{2+}$ based derivatives in the visible region have a maximum intensity close to 465 nm and they are red-shifted compared to the $Ru(bpy)_3^{2+}$ molecules in a solvent.

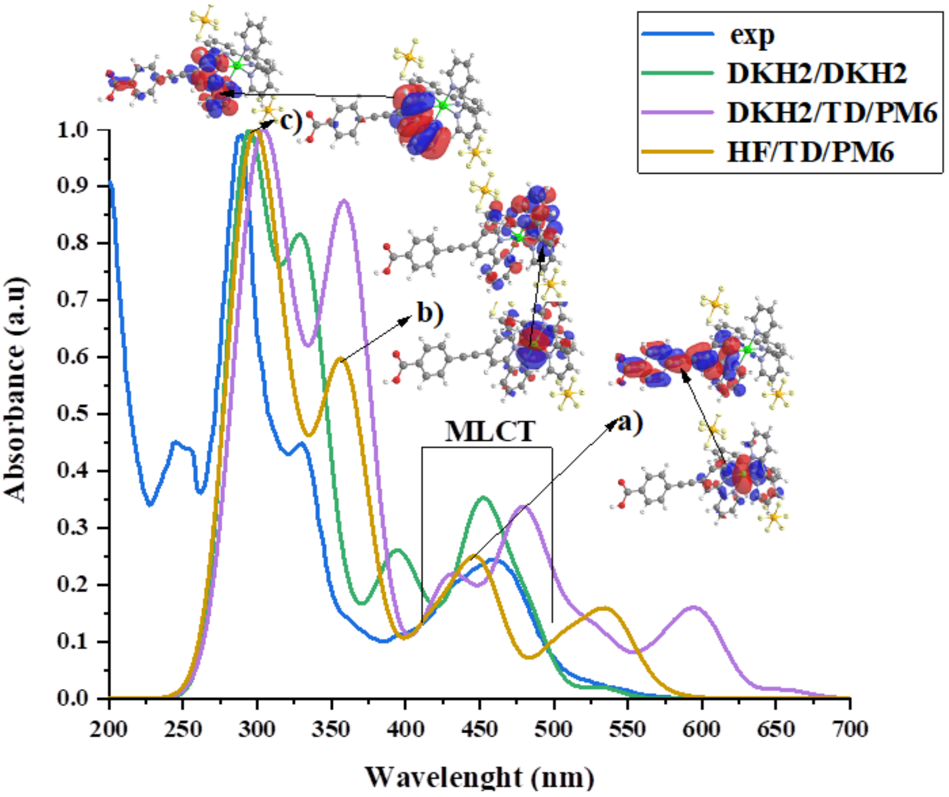

Figure 7.8. Normalized UV-vis absorption spectra for the RuLp molecule measured experimentally, calculated by the DFT/B3LYP-DKH2(jorge-TZP-DKH) for the RuLp molecule optimized by DFT/B3LYP-DKH2(jorge-TZP-DKH) method (DKH2/DKH2), calculated by TD/PM6 method for the molecule optimized by DFT/B3LYP-DKH2(jorge-TZP-DKH) method (DKH2/TD/PM6 and calculated by TD/PM6 method for RuLp molecule optimized by HF method with LANL2DZ basis set for Ru and 6-31G for remaining atoms (HF/TD/PM6). The molecular orbitals accessing the electron excitations corresponding to the MLCT and ILCT peaks calculated at HF/TD/PM6 level

The molecular orbitals accessing the electron excitations corresponding to the MLCT and ILCT peaks calculated at HF/TD/PM6 level are presented in Fig.

7.8. These orbitals correspond to the ones obtained at DKH2/DKH2 level. It means that the critical excitations engaged the appropriate orbitals. Concluding, one can suggest that the TD/PM6 method, a fast method without any critical errors, can be used to calculate the electron properties of hybrid (semiconducting cluster/dye) materials. In this case, better results are obtained for the geometries optimized at the HF level.

The studied dyes with the anchoring group in para-, meta- or ortho-position did not show significant optical differences. Their similar features can be justified by the distribution of their frontier orbitals. Indeed, the anchoring group located in the meta- or ortho-position breaks the conjugation bonds of the systems and affects the electron transfer properties. The enhanced extinction coefficient is attributed to the excited electron being delocalized over a larger π−system in the para-complex, while the meta- or ortho-connection induces a break in the conjugation and thus a smaller extinction coefficient[34]. Studies on rigid rods with pyrene as the chromophore unit also display enhanced extinction coefficients for compounds with the bridge anchored to the chromophore in the para-position. It can be suggested that the charge injection yields in the hybrid systems based on the investigated dyes should depend on the spacer location.

7.2. Dyes based on the dinuclear dendritic configuration of tris(bipyridine)ruthenium(II) complexes

The mainstream research in ruthenium sensitizers is focused on ligands' structure modification to improve their light harvesting and electron injection efficiency. Zalas and coworkers[35] proposed to synthesize the dinuclear tris(bipyridine)ruthenium(II) complexes B_1 (see Fig. 7.9). They propose that the tris(bipyridine)ruthenium(II) moieties will be anchored to the semiconducting material through the π expanded ligand having a phenylene-ethynylene moiety based on the idea that the performed modifications led to an increase in the molar extinction coefficient[36]. The initial investigations show a high extinction coefficient of the B_1 indicating that it can be used as a sensitizing dye in DSSC. Unfortunately, the photovoltaic measurements show a low photon-to-current conversion ability of B_1. Additionally, the measured dye loading parameter shows that the adsorption of B_1 on the TiO_2 electrode is not efficient. This phenomenon may be related to the bulky molecule of B_1 and/or the presence of only one anchoring -COOH group in the structure, which may decrease the binding abilities of this dye.

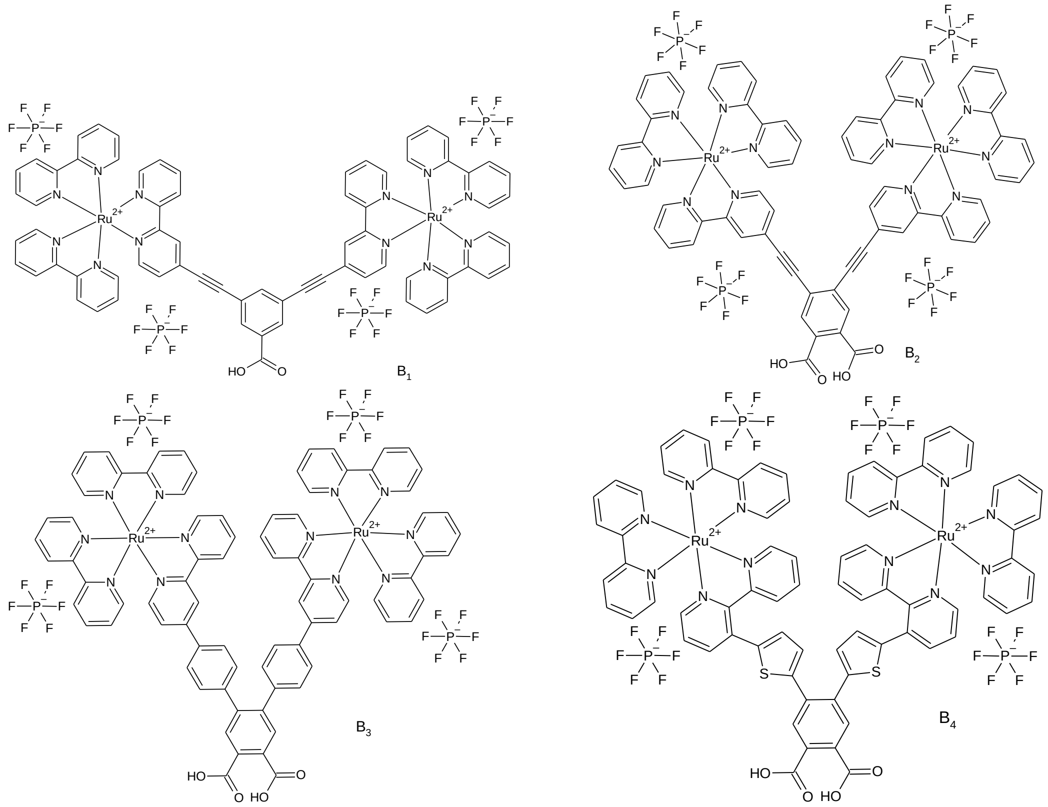

Figure 7.9. Schematic structure of dinuclear dendritic configuration of the tris(bipyridine)ruthenium(II) complexes named B_1, B_2, B_3, and B_4

Based on the information and results obtained for the mononuclear tris(bipyridine)ruthenium(II) complexes as RuLp, RuLp, and RuLm discussed in Chapter 7.1 Zalas with his group decided to synthesize B_2 and B_3, and B_4 molecules (see Fig 7.9). In consequence, the new molecules with additional -COOH anchor groups were designed. In molecules B_3 and B_4, the π-conjugated ethynyl ligands were replaced with phenyl (B_3) or thiophene groups (B_4).

In the present subchapter electron and optical properties of the B_1, B_2, B_3, and B_4 molecules will be discussed. The computationally obtained data will be compared with the experimental results. The methodology of the performed calculations is the same as it was implemented for RuLm, RuLo, and RuLp molecules in Chapter 7.1. The geometries of the molecules were found by applying the total energy minimization procedure in a vacuum using the *ab initio* methodology based on the Hartree-Fock (HF) formalism available in the GAMESS program package. The mentioned procedure was performed for molecules in the hexafluorophosphate $(PF_6^-)_4$ environment. Four PF_6^- molecules were added to each of the simulated B_1, B_2, B_3, and B_4 stabilizers. Quantum chemical calculations were carried out applying the mix basis set. The LanL2DZ basis set was used for the Ru atom and the 6-31G basis set for the remaining atoms of each molecule. The molecular structures were optimized with the gradient convergence tolerance of less than 10^{-5} Hartree/Bohr at a restricted Hartree-Fock (RHF) level[14]. Equilibrated geometries of the molecules were found by applying the quadratic approximation (QA) optimization algorithm based on the augmented Hessian technique. At the end of the geometry search, the Hessian evaluation was performed to exclude structures giving the negative modes and ensure a thermodynamic equilibrium of the molecules. The geometries of the B_1, B_2, and B_3 molecules were also optimized by applying DFT/B3LYP method augmented by the 2nd order scalar relativistic effects within the Douglas–Kroll–Hess (DKH2) formalism[4,6,37] using the jorge-TZP-DKH basis set[7].

The electron and optical properties of the studied molecules were calculated in GAMESS for optimized structures applying the DFT/B3LYP functional. The mixed basis sets as the LanL2DZ for Ru and the (6-31++G**) for other atoms were used. The calculations were performed for molecules in the $(PF_6^-)_4$ environment. The RHF SCF energy convergence criterion was chosen to be 10^{-12} Hartree. The UV−vis absorption spectra were calculated using the iterative Davidson algorithm with an accuracy of 10^{-12} Hartree.

The acetonitrile and DMF solvent effects were taken into consideration using the conductor-like polarizable continuum model (C-PCM)[17,18]. The solvent radii and the dielectric constants were assumed to be the same as the parameters collected in the GAMESS code. The UV-vis absorption spectra were also calculated for the structure optimized by the DFT/B3LYP-DKH2(jorge-TZP-DKH) method using the DFT/B3LYP-DKH2(jorge-TZP-DKH) method (named as DKH2/DKH2) in the Gaussian 16 package.

As was mentioned above the studied B_1, B_2, B_3, and B_4 molecules have the same tris(bipyridine)ruthenium(II) donor groups in the dinuclear dendrimeric arrangement (see Fig. 7.9). They differ in the spacer nature and configuration of the anchoring carboxyl groups (-COOH). The B_1 molecule possesses one anchoring -

COOH group and the remaining molecules possess two anchoring groups attached to the phenyl moiety. All of the investigated sensitizers possess rod-like spacers. The B_1 and B_2 molecules are comprised of oligophenylene–ethynylene (OPE) bridges but the B_3 molecule possesses phenyl as the π–π spacer and B_4 has thiophene.

It was proved that the dendritic B_1 dye is less active in the DSSCs devices than commercially available mononuclear analogs[35,38]. One can conclude that a possible reason for the relatively poor performance of the B_1 dye is the *meta*-position of the -COOH anchoring group to the $Ru(bpy)_3^{2+}$ moiety. A position of the -COOH group probably leads to poor electronic communication with the TiO_2 orbitals, as was noticed for the RuLm dye discussed in Chapter 7.1. In consequence, an interesting scientific goal of the study seems to be an examination of the impact of the -COOH group attachment position on the DSSC performance.

The experimental UV-vis absorption spectra measured for the B_1, B_2, and B_3 molecules in acetonitrile (ACN) are presented in Fig. 7.10. The spectrum of the B_4 dye is not presented because this molecule was unsuccessfully synthesized. The broad bands observed for all molecules with maxima at 460 nm correspond to the MLCT transition, characteristic for ruthenium polypyridine complexes[39,40]. Also, the absorption bands at 250 nm belong to the MLCT transition. The absorption bands located at 280 correspond to the central ligands π–$\pi*$ electron transfer. In the work of Zalas and coworkers[35] was specified that an additional strong band present at 325 nm in the B_1 molecule is assigned to the extended delocalized structure of ligand with the anchoring group, playing the role of an antenna. In the next part of the work, I will try to explain the nature of this peak which is significant for the B_1 molecule and almost disappear for the B_2 molecule. The first MLCT peak of the B_1 and B_2 molecules located at 460 nm is shifted into the red side of the spectrum compared with the B_3 molecule. It is probably caused by adding the phenyl group into the B_3 molecule. The phenyl group increases the value of the molar absorption coefficient of B_3.

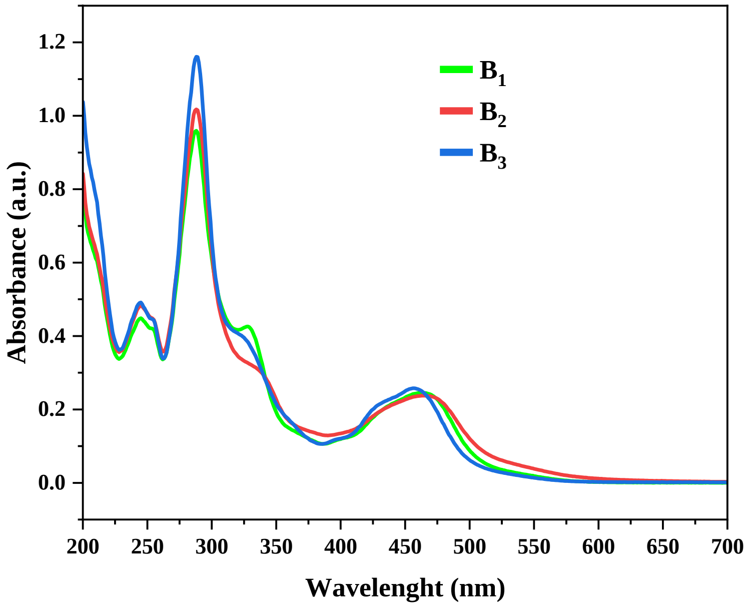

Figure 7.10. Normalized UV-vis absorption spectra of B_1, B_2, and B_3 molecules measured experimentally in ACN

The calculated electron properties of the dinuclear dendritic tris(bipyridine)ruthenium(II) derivatives B_1, B_2, B_3, and B_4 are presented in Table 7.6. These data are obtained for molecules optimized by the *ab initio* method with electron properties calculated at DFT/B3LYP level in a vacuum. One can see that the most polar are molecules B_3 and B_1, but the polarity of the molecules B_2 and especially B_4 is significantly lower. The first absorption peak λ_{max} of the molecules B_1 and B_2 calculated in vacuum are mostly shifted into the red side region compared with B_3 and B_4. The solvent changes the position of the λ_{max} shifting it into the red side of the spectrum for the B_2 molecule. For the remaining molecules, the DMF causes a hypsochromic shift of the spectrum. The solvent chosen as DMF drastically increases the dipole moment of all molecules.

Analyzing the contribution of the molecular orbitals to the first MLCT transition one can see that the main influence comes from HOMO-3 or HOMO-2 to the LUMO transition. This occurs in a vacuum and DMF. The distribution of the few highest ground (HOMO-x) and lowest excited (LUMO+x) states are presented in Fig. 7.11 – 7.14. In these figures also the single excitation transitions creating the first MLCT peak are presented with the atomic orbital analysis. One can see that the MLCT absorption peak of the B_1 in a vacuum is based on HOMO-3 to LUMO and HOMO-3 to LUMO+1 transitions (see Fig. 7.11a). The mentioned transitions are without any contribution from the anchoring group. In the DMF solvent, the spacer atom orbitals are more involved in the lowest excited molecular orbitals (see Fig. 7.11b). It can explain the low response of the B_1 molecule in DSSC devices.

Table 7.6. Electric dipole moments, positions of the absorption peaks λ_{max} belonging to the MLCT transition, and contribution of the molecular orbitals to the selected excitations calculated by the DFT/B3LYP for the B_1, B_2, B_3, and B_4 molecules with $(PF_6^-)_4$ stabilizer, in a vacuum and DMF

	environment	μ (D)	λ_{max} (nm)	Orbital contribution
B_1	in vacuum	5.23	455	HOMO-3→LUMO (53%) HOMO-3→LUMO+1 (33%)
	in DMF	5.47	440	HOMO-2→LUMO (43%) HOMO-2→LUMO+1 (14%)
B_2	in vacuum	4.08	454	HOMO-3→LUMO (62%)
	in DMF	6.26	468	HOMO-3→LUMO (80%)
B_3	in vacuum	6.29	442	HOMO-2→LUMO (65%) HOMO-3→LUMO (10%)
	in DMF	8.40	430	HOMO-3→LUMO (28%) HOMO-4→LUMO (17%) HOMO-3→LUMO+1 (11%)
B_4	in vacuum	2.66	443	HOMO-2→LUMO (63%)
	in DMF	5.75	438	HOMO-2→LUMO (48%) HOMO-4→LUMO (20%) HOMO-4→ LUMO+2 (15%)

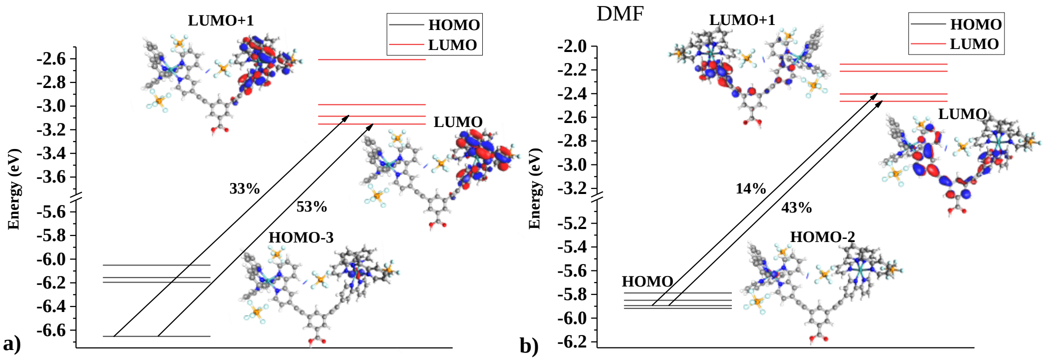

Figure 7.11. Energy diagram for the first MLCT absorption peak of B_1 a) calculated by the TDDFT/B3LYP with $(PF_6-)_4$ stabilizer in a vacuum and b) calculated by the TDDFT/B3LYP with $(PF_6-)_4$ stabilizer in DMF. Single excitation transitions creating the first MLCT peak with the atom orbitals analysis are presented

The two anchoring -COOH groups in the case of the B_2 make a significant impact on its excited states (see Fig. 7.12). The LUMO molecular orbital is strongly separated from the other excited states. It makes electron transition to the LUMO orbital more privileged than it is observed for energetically higher excitations. Transition noticed as HOMO-3 → LUMO observed for the B_2 molecule corresponds to the first MLCT and possesses the highest oscillator strength of all simulated structures. Solvent makes the separation of LUMO from other excited orbitals even more significant than it was observed for vacuum. The LUMO localized on the anchoring group makes the B_2 molecule a good candidate for DSSC application.

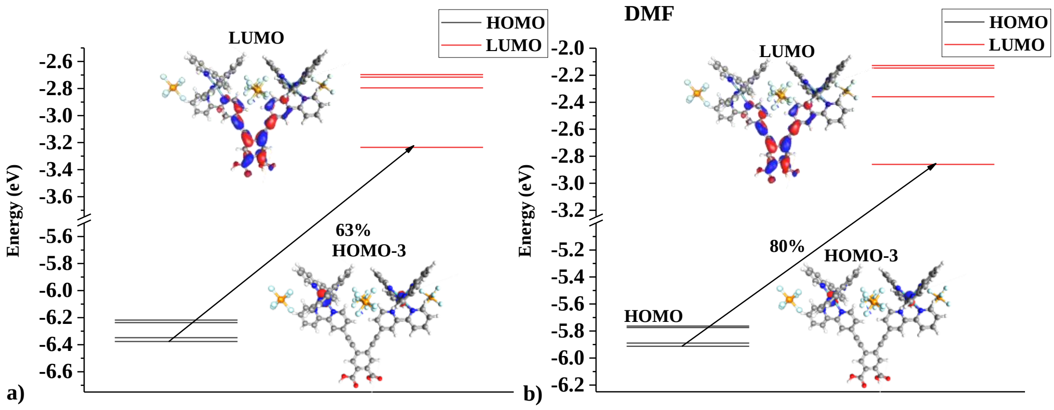
LUMO
HOMO
LUMO
-2.6
-2.8
-3.0
-3.2
-3.4
-3.6
-5.6
-5.8
-6.0
-6.2
-6.4
-6.6
Energy (eV)
63%
HOMO-3
a)
DMF
HOMO
LUMO
LUMO
-2.0
-2.2
-2.4
-2.6
-2.8
-3.0
-3.2
-5.2
-5.4
-5.6
-5.8
-6.0
-6.2
Energy (eV)
80%
HOMO-3
HOMO
b)

Figure 7.12. Energy diagram for the main absorption peak of B_2 a) calculated by the TDDFT/B3LYP with $(PF_6^-)_4$ stabilizer in a vacuum and b) calculated by the TDDFT/B3LYP with $(PF_6^-)_4$ stabilizer in DMF. Single excitation transitions creating the first MLCT peak with the atom orbitals analysis are presented

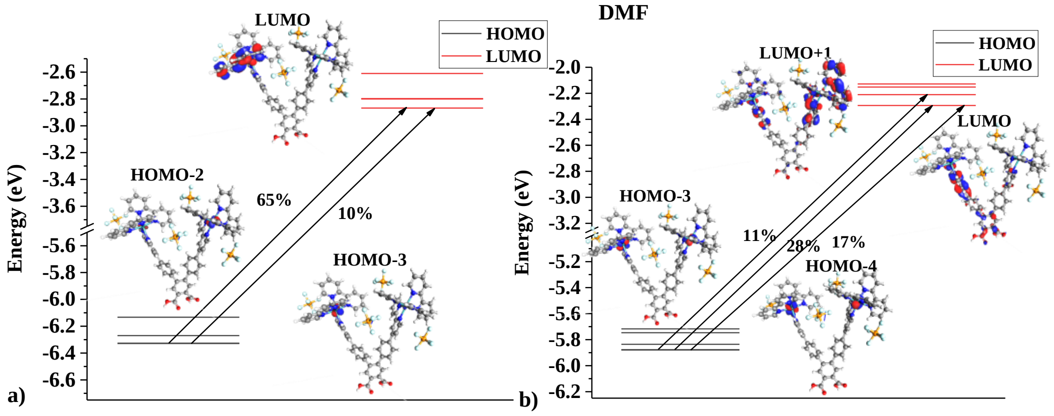
LUMO
HOMO
LUMO
-2.6
-2.8
-3.0
-3.2
-3.4
-3.6
-5.6
-5.8
-6.0
-6.2
-6.4
-6.6
Energy (eV)
HOMO-2
65%
10%
HOMO-3
a)
DMF
LUMO+1
HOMO
LUMO
LUMO
-2.0
-2.2
-2.4
-2.6
-2.8
-3.0
-3.2
-5.2
-5.4
-5.6
-5.8
-6.0
-6.2
Energy (eV)
HOMO-3
11%
28%
17%
HOMO-4
b)

Figure 7.13. Energy diagram for the main absorption peak of B_3 a) calculated by the TDDFT/B3LYP with $(PF_6^-)_4$ stabilizer in a vacuum and b) calculated by the TDDFT/B3LYP with $(PF_6^-)_4$ stabilizer in DMF. Single excitation transitions creating the first MLCT peak with the atom orbitals analysis are presented

In the case of B_3 and B_4 molecules the LUMO orbital is not separated from other excited molecular energy states as it is seen for B_2 (see Fig. 7.13 and 7.14). All electron transitions observed for the B_3 molecule creating MLCT peak are inner $Ru(bpy)_3{}^{2+}$ moiety transitions. In the case of B_4 (Fig 7.14), the inner $Ru(bpy)_3{}^{2+}$ MLCT transition also takes place. The thiophene moiety makes an impact on electron separation during the excitation process. Excited electrons of the first transition are located on the thiophene ring. The solvent effect in molecules B_3 and B_4 causes the higher contribution of spacer molecular orbitals to the first, energetically low-lying excitations. All made observations allow us to conclude that the molecules B_3 and B_4 are rather good candidates for photovoltaic applications, but their suspense should be worst than for the B_2 molecule.

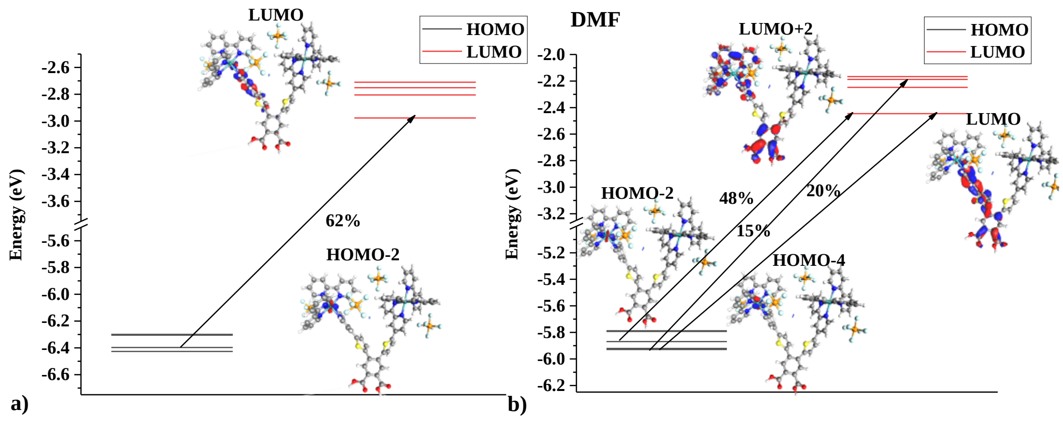

Figure 7.14. Energy diagram for the main absorption peak of B_4 a) calculated by the TDDFT/B3LYP with $(PF_6^-)_4$ stabilizer in a vacuum and b) calculated by the TDDFT/B3LYP with $(PF_6^-)_4$ stabilizer in DMF. Single excitation transitions creating the first MLCT peak with the atom orbitals analysis are presented

In Fig. 7.15 the first MLCT peaks of the UV-vis absorption spectra calculated by the TDDFT/B3LYP method for B_1, B_2, B_3, and B_4 molecules in a vacuum and DMF solvent are presented. One can see that the spectrum of the B_1 and B_2 molecules are similar and then the one for the B_3 and B_4 are also similar. The B_1 and B_2 molecules give an absorption peak at 455nm, but B_3 and B_4 absorb near 442 nm. It is in agreement with the experimental data presented in Fig. 7.10. One can see that the solvent shifts the absorption peak of the B_2 molecule into the red side (bathochromic shift). All the remaining molecules exhibit a hypsochromic shift. The bathochromic shift observed for the B_2 molecule can be caused by charge transfer occurring between donor $Ru(bpy)_3^{2+}$ moiety and the anchoring group. In addition, it can be concluded that phenyl and thiophene reduce the electron-withdrawing properties of the donor, which causes the hypsochromic shift observed for B_3 and B_4.

Comparing the above-discussed data one can say that B_2 has the best properties to be used in photovoltaic applications compare with other calculated molecules. B_1, B_3, and B_4 molecules have typical problem defined by charge transfer from donor to acceptor characterized by inner MLCT transition, with additional charge accumulation on phenyl or thiophene for B_3 and B_4, respectively.

Additionally, the molecule B_4 is not stable structurally which was observed via the energy relaxation process performed during geometry optimization. Probably this is the reason why the problem in the synthesis of the B_4 molecule appears. However, the shift of the photoexcited states to the spacer in the B_3 molecule due to the interaction of the solvent may be a factor terminating the use of this dye in DSSC.

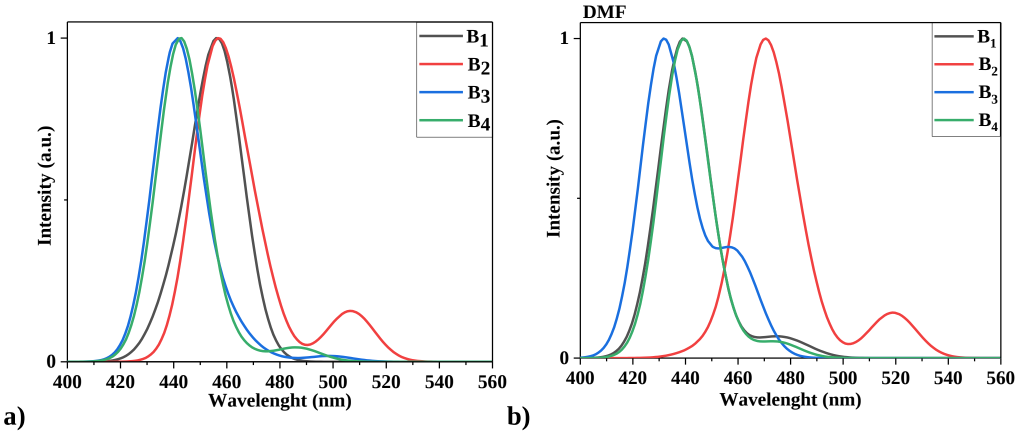

Figure 7.15. Normalized UV–vis absorption spectra calculated by TD-DFT/B3LYP for the B_1, B_2, B_3, and B_4 with $(PF_6\text{-})_4$ stabilizer in a) vacuum and in b) DMF

Optical properties of the B_1, B_2, and B_3 molecules were also calculated using the Douglas–Kroll–Hess (DKH2) formalism with the jorge-TZP-DKH basis set. These molecules were structurally relaxed by applying the DKH2 formalism. This methodology will be called DKH2/DKH2. Due to the complexity of these calculations and no experimental data, molecule B_4 was not studied. These calculations were performed for molecules embedded in a vacuum and ACN solvent, according to experimental conditions.

The spectra calculated in vacuum for the B_1 and B_2 molecules using the DKH2/DKH2 method are shown in Fig. 7.16. The spectrum calculated for molecule B_3 has a shape very similar to the one calculated for B_1. They are normalized to the intensity of the ILCT peak. One can see that the performed calculations well reproduce the experimental data. The computer simulations can well reproduce the position of the first MLCT peak and the ILCT peak for the B_1 molecule. The MLCT peak calculated for the B_2 molecule is spread into two peaks. To explain the nature and shape of the MLCT pekas for B_1, B_2, and B_3 molecules the calculations in a vacuum and an ACN were performed for the narrow range of spectrum and the obtained data are presented in Fig. 7.17.

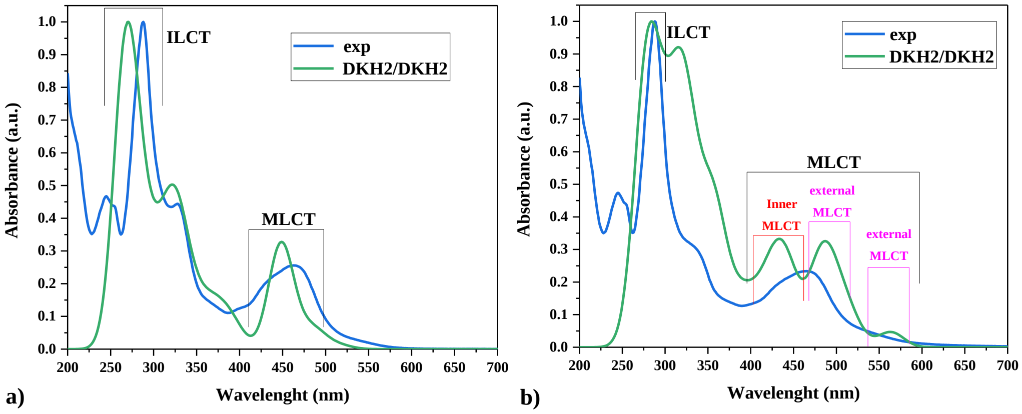

Figure 7.16. Normalized UV-vis spectra for a) B_1 and b) B_2 measured experimentally in ACN (blue line) and calculated (green line) in a vacuum using molecular structures optimized by the DFT/B3LYP-DKH2(jorge-TZP-DKH) method and oscillators calculated by DFT/B3LYP-DKH2(jorge-TZP-DKH) method (DKH2/DKH2)

The UV-vis absorption spectra calculated for the B_1, B_2, and B_3 molecules in vacuum using the DKH2/DKH2 method possess one peak centered at 450 nm (see Fig. 7.17). This peak is attributed to the MLCT present for all molecules based on $Ru(bpy)_3^{2+}$ moiety[41]. It is assigned to the metal-to-bipyridine ligand transition. In Fig. 7.16 it is marked as “inner MLCT”. For the B_1 and B_3 molecules, a small shoulder from the side of long waves in the absorption UV-vis spectrum is seen. This peak is more significant for the B_2 molecule. Analyzing the electron transitions responsible for the peaks laying around 480-490 nm, one can see that they are associated with the metal-to-ligand transition. However, the excited electrons are transferred to the orbitals located at the spacer. Also the peak near 560 nm, significantly observed for the B_2 molecule (see Fig. 7.16b and Fig. 7.17), is created by MLCT transfer from Ru orbitals to the spacer-based orbitals. In the present work, we call this transfer “external MLCT”. The peak at 480-490 nm is created by the transfer of electrons from HOMO-3 to LUMO and the peak at 560 nm is associated with the HOMO to LUMO electron transfer, but its oscillator strength is very low. These states are also present in B_1 and B_3 molecules, but their oscillator strengths are very low (see Fig. 7.17). One can see that solvent enhances the peaks responsible for the external MLCT (480-490 nm) for the B_1 molecule. Under the influence of the solvent, the transfer of electrons from the metal to the spacer is still marked by very low oscillator strength for the B_3 molecule. It can be explained by the fact that the phenyl group added to the spacer of the B_3 molecules affects charge transport from the donor to the acceptor moiety. The mentioned charge transfer is well seen for the B_2 molecule. The peak responsible for the metal-to-bipyridine transition (inner MLCT) is not affected by the solvent for all molecules. It was also proved by the EA studies performed for the B_1 molecules[29].

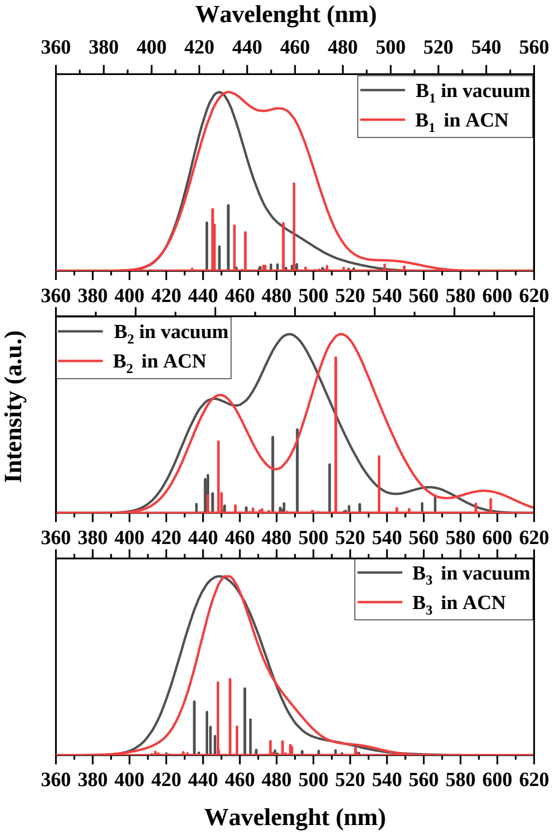

Figure 7.17. Normalized UV–vis absorption spectra calculated by DKH2/DKH2 method for the B_1, B_2, and B_3 molecules stabilized by the $(PF_6\text{-})_4$ in vacuum (black) and solvent ACN (red)

The electron properties of the investigated molecules calculated by the DKH2/DKH2 method in a vacuum and ACN are presented in Table 7.7. Analyzing the electron properties, especially dipole moments of the tested molecules, it can be argued that they will affect the semiconductor conducting band changing the V_{OC} of the photovoltaic cell differently, as was proved for the mono-ruthenium complexes[11]. The B_1 and B_3 molecules have very similar electric dipole moments, but molecule B_2 possesses much lower electric dipole moments. The dipole moment of all molecules increases in the ACN solvent as it was observed for the DMF solvent (see Table 7.6). Most significantly, it is seen for the B_2 molecule. In Table 7.7, HOMO and LUMO energy values and the E_g between them are calculated for B_1, B_2, and B_3 molecules, and the data are compared to experimental results.

Experimentally measured E_g has the lowest value for the B_2. In allows us to conclude that the B_2 will be characterized by the highest reactivity, which may result in the most effective adsorption of these molecules on the surface of the semiconductor compared with B_1 and B_3 molecules[42]. The HOMO energy of the investigated molecules is upshifted going through $B_1 \rightarrow B_2 \rightarrow B_3$. The higher the energy of the HOMO, the greater the capacity to donate electrons will be. It will have consequences in the electron injection in DSSC devices. The additional anchoring group downshifts the LUMO level of the B_2 compared to the B_1. The phenyl group in the spacer moiety of the B_3 upshifts the LUMO giving the highest value of all B_X molecules. This is an important feature favoring the B_3 molecule in photovoltaic applications even if the electron transfer is blocked by its spacer nature.

Table 7.7. Electric dipole moments, the HOMO, LUMO, and energy gap (E_g) values obtained from the calculations performed at DKH2/DKH2 level in a vacuum and ACN compared with experimental data obtained using cyclic voltammetry (in ACN) for B_1, B_2, and B_3 molecules

	environment	μ (D)	calculated		experimental	
			HOMO (eV)	LUMO (eV)	HOMO (eV)	LUMO (eV)
B_1	vacuum	5.66	-6.00	-3.39	-	-
			E_g = 2.61 eV			
	ACN	6.23	-5.54	-3.41	-5.71	-3.19
			E_g = 3.01 eV		E_g = 2.52 eV	
B_2	vacuum	3.46	-6.17	-3.41	-	-
			E_g = 2.76 eV			
	ACN	5.60	-5.52	-2.91	-5.62	-3.21
			E_g = 2.61 eV		E_g = 2.41 eV	
B_3	vacuum	5.29	-6.13	-3.05	-	-
			E_g =3.08 eV			
	ACN	7.43	-5.48	-2.38	-5.57	-3.04
			E_g =3.10 eV		E_g =2.53 eV	

The discussed data are presented graphically in Fig 7.18. Comparing the HOMO and LUMO positions calculated for the B_X molecules in a vacuum and ACN one can see that the solvent shifts HOMO and LUMO into the higher energies for all molecules (see. Table 7.7 and Fig. 7.18). The tendencies of the HOMO and LUMO energy changes for the B_X molecules are well reproduced by the calculations performed in ACN. However, discussing the values of the HOMO and LUMO energies one can see that experimental HOMO energy is better reproduced by calculations performed taking solvent into account, but the LUMO energies are in better agreement with the ones calculated in a vacuum. It means that the HOMO energy is not affected by solvent as it was proved previously. Because LUMO is associated with orbitals located far from the Ru atom it is sensitive to the nature of the environment. The solvent does not change the E_g of the B_X molecule significantly compared with vacuum-calculated data. It is also seen by analyzing the UV-vis spectra presented in Fig. 7.17. It can be concluded that the significant increase in the energy of the LUMO level of the B_3 dye visible in the diagram compared to the B_1 and B_2 dyes is responsible for the hypsochromic shift of the MLCT band on the absorption spectrum. This observation supports the above conclusion about the introduction of phenyl linkers into the B_3 dye structure, which causes the π-π* and dπ-π* transitions to occur at higher energies. In addition, the HOMO levels are also shifted with each modification made, but not as significant as the LUMO levels.

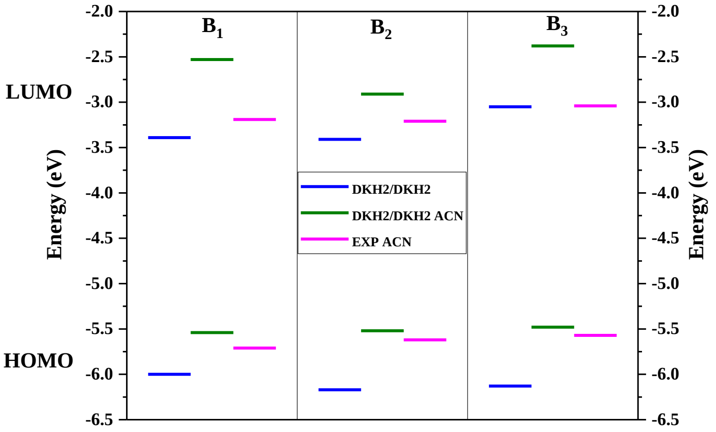

Figure 7.18. Energy diagrams calculated for B_1, B_2, and B_3 molecules by DKH2/DKH2 in vacuum (blue line) and ACN (green line), and experimental data measured in ACN (violet line)

Analyzing data presented in Table 7.8 one may see that the MLCT transfer occurring in the B_1 molecule in vacuum is caused by HOMO-2 →LUMO+6 and HOMO-1 → LUMO+3 transition. The DKH2/DKH2 method creates an MLCT transfer involving deeper molecular orbitals than is seen in the case of DFT/B3LYP calculations (see Table 7.6). The DKH2/DKH2 have a problem with electron distribution at the ground state contrary to the DFT/B3LYP method. In the case of MLCT transfer, the ground state requires the electron location at Ru, but DKH2/DKH2 method spread them to ligands. The DHK2/DHK2 method used to calculate optical properties of B_1 in ACN solvent reproduces the same character of MLCT transfer as it is obtained by DFT/B3LYP method (HOMO-2 → LUMO and

HOMO-2 → LUMO+1). Although the molecular orbitals taking part in the electron excitation are very similar to the ones calculated by DFT/B3LYP method (see Table 7.9). One can conclude that the ACN solvent stabilizes the electrons on the Ru atom.

Table 7.8. Positions of the absorption peaks λ_{max} belonging to the MLCT transfer, and contribution of the molecular orbitals to the selected excitations calculated by the DKH2/DKH2 method for the B_1, B_2, and B_3 molecules with $(PF_6^-)_4$ stabilizer, in a vacuum and ACN

	environment	λ_{max} (nm)	
B_1	in vacuum	454	HOMO-2→LUMO+6 HOMO-1→LUMO+3
	in ACN	489	HOMO-2→LUMO HOMO-2→LUMO+1
B_2	in vacuum	491	HOMO-3→LUMO HOMO-2→LUMO+3
		478	HOMO-3→LUMO HOMO-3→LUMO+2
	in ACN	512	HOMO-3→LUMO
B_3	in vacuum	462	HOMO-3→LUMO+1 HOMO-3→LUMO+5
		435	HOMO-3→LUMO+5 HOMO-1→LUMO+3
	in ACN	455	HOMO-4→LUMO+5 HOMO-3→LUMO
		448	HOMO-4→LUMO+3 HOMO-3→LUMO+5

Table 7.9. Molecular orbitals giving a contribution to the MLCT transfer of electrons calculated by the DKH2/DKH2 method for B_1 molecule with stabilizers $(PF_6^-)_4$ in vacuum and ACN

Method	HOMO-n (eV)	LUMO+n (eV)	λ_{max} (nm)	HOMO-n	LUMO+n
DKH2/DKH2	HOMO-2	LUMO+6	454	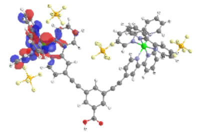	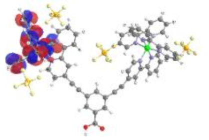
	-6.131	-2.622			
	HOMO-1	LUMO+3		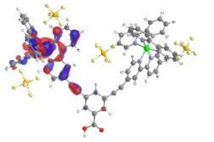	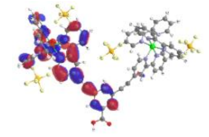
	-6.077	-2.843			
DKH2/DKH2 (ACN)	HOMO-2	LUMO	489	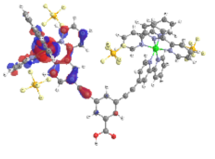	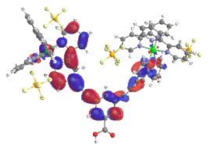
	-5.632	-2.256			
	HOMO-2	LUMO+1		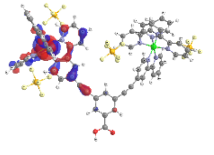	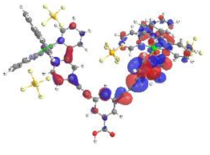
	-5.632	-2.445			

The inner MLCT peak, calculated for the B_2 molecule using DHK2/DHK2 method, is created by the strong HOMO-3 → LUMO transfer, the same as it is obtained for DFT/B3LYP method. Also, transition HOMO-2 → LUMO+3 has some contribution (see Fig. 7.10). The DKH2/DKH2 method splits the MLCT peak into two peaks at 491 nm and 478 nm. The solvent makes a single peak of the MLCT with the highest oscillator strength, from all of the calculated structures. However, the critical issue for B_2 calculations using DKH2/DKH2 method is the significant redshift noticed for MLCT transition in a vacuum as well as in ACN. In ACN the λ_{max} is located at 512 nm but the experimentally obtained peak is noticed at 465 nm.

Table 7.10. Molecular orbitals giving a contribution to the MLCT transfer of electrons calculated by the DKH2/DKH2 method for B_2 molecule with stabilizers $(PF_6^-)_4$ in vacuum and ACN

Method	HOMO-n (eV)	LUMO+n (eV)	λ_{max} (nm)	HOMO-n	LUMO+n
DKH2/DKH2	HOMO-3	LUMO	491	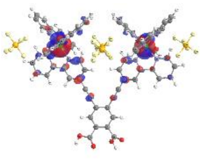	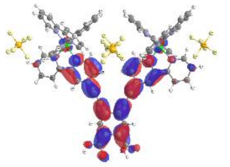
	-6.325	-3.413			
	HOMO-2	LUMO+3		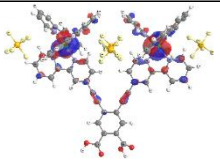	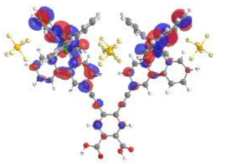
	-6.291	-2.857			
	HOMO-3	LUMO	478	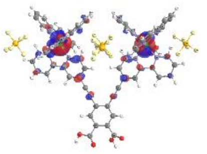	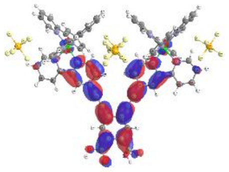
	-6.325	-3.413			
	HOMO-3	LUMO+2		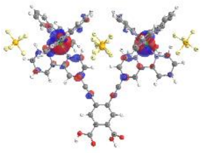	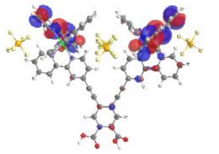
	-6.325	-2.857			
DKH2/DKH2 (ACN)	HOMO-3	LUMO	512	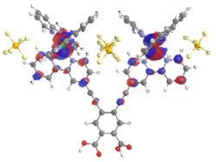	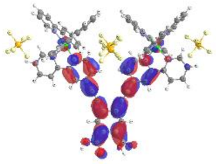
	-5.678	**-2.907**			

In the case of B_3, the DKH2/DKH2 method shows the same tendencies as DFT/B3LYP calculations. The strong inner MLCT transition is seen here (see Fig. 7.11). The solvent increases the charge separation, shifting it into the anchoring group. The charge accumulates on the phenyl located in the spacer acting as a charge gate.

Table 7.11. Molecular orbitals giving a contribution to the MLCT transfer of electrons calculated by the DKH2/DKH2 method for B_3 molecule with stabilizers $(PF_6^-)_4$ in vacuum and ACN

Method	HOMO-n (eV)	LUMO+n (eV)	λ_{max} (nm)	HOMO-n	LUMO+n
DKH2/DKH2	HOMO-3	LUMO+1	462	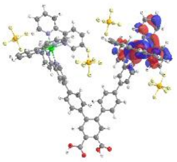	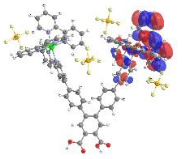
	-6.317	-3.001			
	HOMO-3	LUMO+5		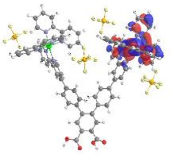	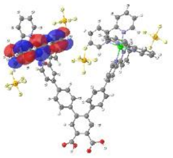
	-6.317	-2.615			
	HOMO-3	LUMO+5	435	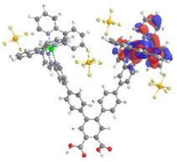	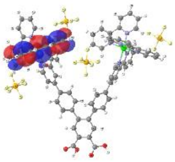
	-6.317	-2.615			
	HOMO-1	LUMO+3		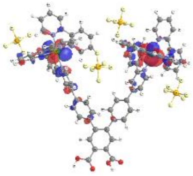	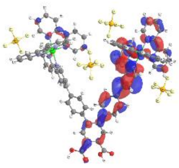
	-6.226	-2.817			
DKH2/DKH2 (ACN)	HOMO-4	LUMO+5	455	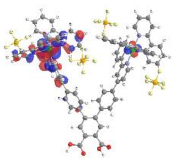	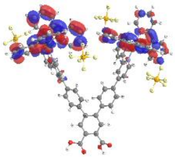
	-5.639	-2.096			
	HOMO-3	LUMO		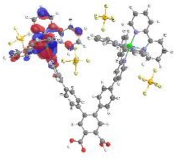	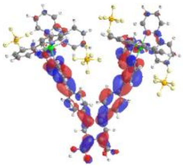
	-5.621	-2.378			
	HOMO-4	LUMO+3	448	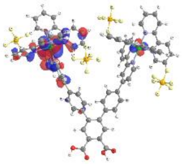	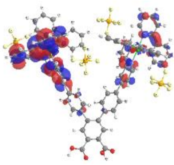
	-5.639	-2.152			
	HOMO-3	LUMO+5		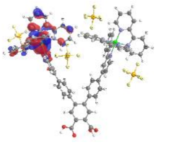	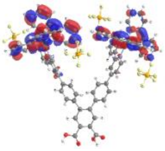
	-5.621	-2.096			

To calculate the electron properties of the B_X molecules anchored at the surface of the semiconductor more simple method of calculations than the DFT/B3LYP or DKH2/DKH2 ones is needed. As it was implemented for the RuLp molecule (see Chapter 7.1) also here the PM6[30] and PM7[31] semiempirical methods were tested. Calculations of electron properties of the B_1 molecule were performed for two geometries, optimized by the DFT/B3LYP-DKH2(jorge-TZP-DKH) (DKH2) and optimized by HF method with LANL2DZ basis set for Ru and 6-31G for remaining atoms (HF). The results obtained for the B_1 molecule are collected in Table 7.12. In this case, the CIS/PM6, TD/PM6, and CIS/ PM7 methods were tested. Analyzing these data one can see that TD/PM6 shows much better results than the other ones regardless of the type of optimization performed. The ILCT peak is well reproduced for both geometries of the B_1 molecule taking into account the TD/PM6 method. To prove this statement UV-vis absorption spectra for the B_1 molecule were calculated in vacuum and ACN using semiempirical tested methods.

Table 7.12. Main absorption peaks of MLCT and ILCT transitions calculated for B_1 molecule using semiempirical CIS/PM6, CIS/PM7, and TD/PM6 methods for molecular geometries calculated at DFT/B3LYP-DKH2(jorge-TZP-DKH) (DKH2) and HF method with LANL2DZ basis set for Ru and 6-31G for remaining atoms (HF) compared with experimental data

Method of geometry optimization		CIS/PM6 (nm)	CIS/PM7 (nm)	TD/PM6 (nm)	EXP (nm)
DKH2	MLCT	444,452	470	457,463	464
	ILCT	---	326	291	287
HF	MLCT	420	470	435,438	
	ILCT	280	325	287	

In Fig. 7.19 are presented UV-vis absorption spectra calculated by using TD/PM6, CIS/PM6, and CIS/PM7 methods for the B_1 molecule with geometry obtained by DKH2 (see Fig. 7.19a) and HF (see Fig. 7.19b) approach. Analyzing the obtained results, it can be concluded that the CIS/PM7 method gives the worst agreement between experimental and calculated spectra, regardless of the geometry of the B_1 molecule used. Due to the fuzzy nature of the electron distribution around heavy atoms, the PM7 method too significantly shifts the spectra toward long wavelengths. Absorption in this case starts from 700 nm which is not true in experimental systems. In addition, the CIS/PM7 method does not correctly reflect the position of the MLCT and ILCT peaks. Therefore, the PM7 method in the CIS implementation will not be used for further calculations. The CIS/PM6 method hardly shows the shape of the MLCT peak for both DKH2 and HF geometries of B_1. The best results are obtained by the TD/PM6 method used for structures optimized by the DKH2 method. In the charts, it is marked with the acronym HDKH2/TD/PM6(see Fig. 7.19a). These conclusions were made mainly based on the analysis of the position of the MLCT and ILCT peaks. Also, the intensity of oscillator strength for the discussed excitations is preserved. The DKH2/TD/PM6 method best reflects the MLCT peak, taking into account the value of the oscillator strength for excitations around 450 nm. Although the spectrum for HF/TD/PM6 is shifted to the long-wave side and the oscillator strength for the excitation at 550 nm is too significant.

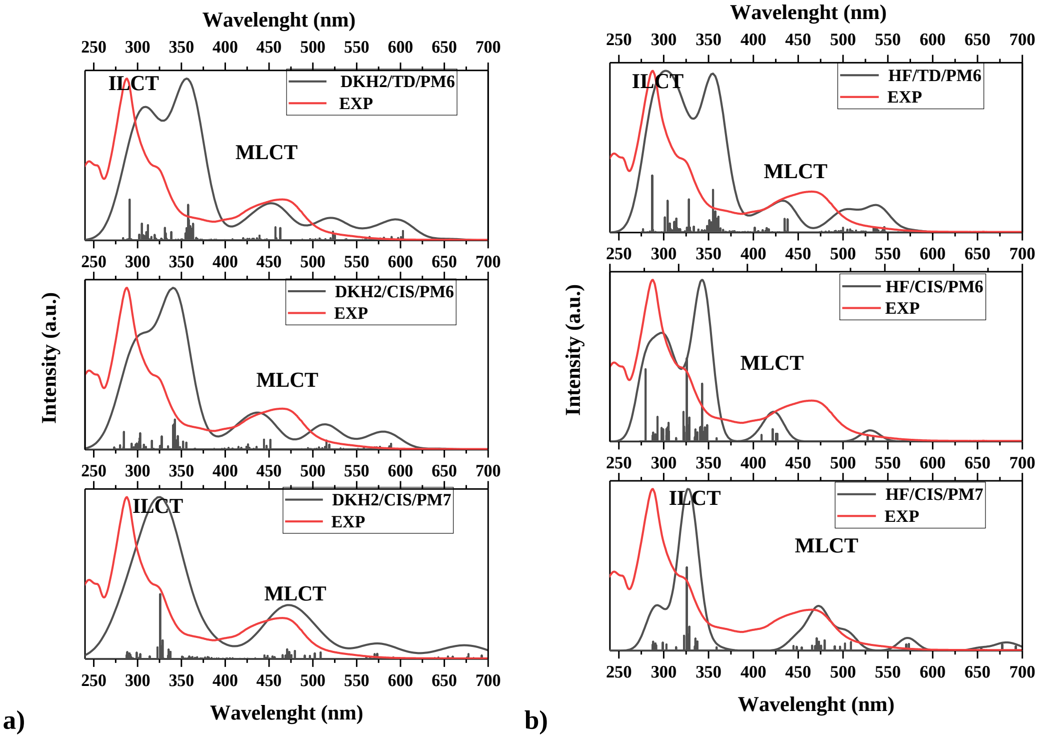

Figure 7.19. Normalized UV–vis absorption spectra calculated by semiempirical methods TD/PM6, CIS/PM6, and CIS/PM7 for the B_1 molecule stabilized by the $(PF_6^-)_2$ in vacuum (black) optimized by the DFT/B3LYP-DKH2(jorge-TZP-DKH) method (DKH2) (a) and optimized by HF method with LANL2DZ basis set for Ru and 6-31G for remaining atoms (HF) (b) compared with experimental data (red line)

Table 7.13 presents molecular orbitals giving a contribution to the electron excitation creating the MLCT peak located at 400 – 550 nm for the B_1 molecule. The CIS/PM7 method gives too-widespread orbitals representing the ground states in all considered cases. The typical $Ru(pby)_3^{+2}$-based complexes should possess a HOMO orbital located at the Ru atom. The first excitation is from Ru-located orbitals to the ligand. In the case of the B_1 molecule calculated by CIS/PM7 and optimized by DKH2 and HF methods, some metal-to-metal transitions are shown. This may be the reason why the CIS/PM7 method cannot be used to calculate the optical properties of ruthenium molecules. The CIS/PM6 method gives a quite good description of studied molecular orbitals but the doublet observed at 435 and 438 nm obtained by TD/PM6 correspond better to the experimental data.

Table 7.13. The molecular orbitals accessing the electron excitations corresponding to the MLCT peaks calculated by the TD/PM6, CIS/PM6, and CIS/PM7 for the B$_1$ molecule optimized by the DFT/B3LYP-DKH2(jorge-TZP-DKH) (DKH2) and HF method with LANL2DZ basis set for Ru and 6-31G for remaining atoms (HF)

Geometry	**HF**			**DKH2**		
Method	λ_{max}(nm) / (oscillator str.)	Ground state	Excited state	λ_{max}(nm) / (oscillator str.)	Ground state	Excited state
TD/PM6	435 (0.121)	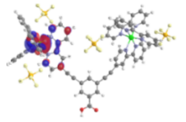	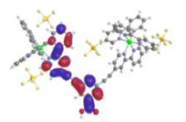	463 (0.164)	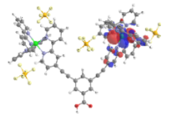	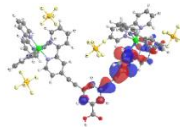
	438 (0.117)	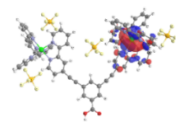	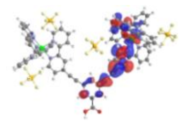	457 (0.156)	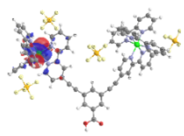	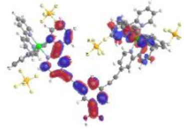
CIS/PM6	420 (0.124)	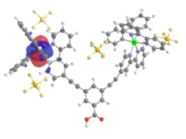	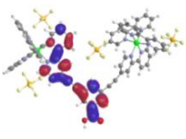	452 (0.150)	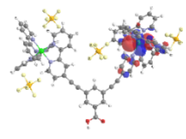	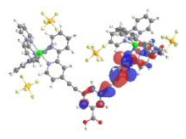
	425 (0.078)	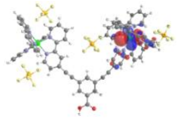	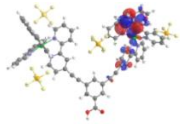	444 (0.152)	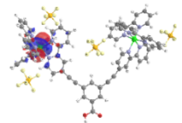	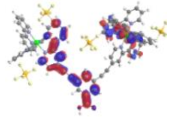
	427 (0.078)	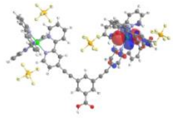	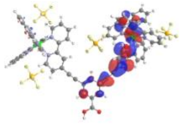		-	-
CIS/PM7	480 (0.173)	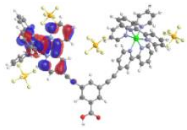	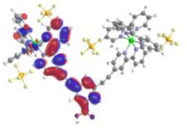	480 (0.173)	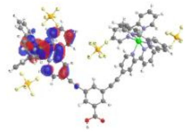	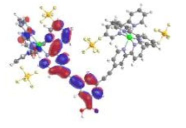
	473 (0.150)	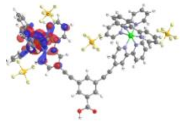	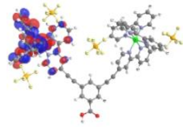	473 (0.150)	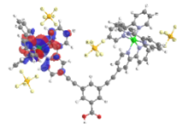	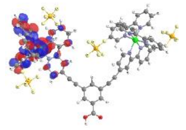
	471 (0.209)	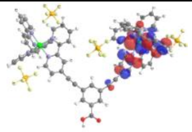	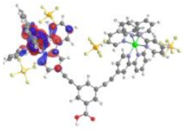	470 (0.209)	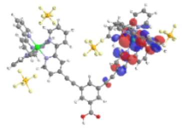	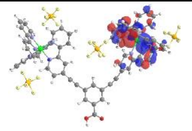

In Fig. 7.20 the UV-vis absorption spectra measured experimentally for the B_1 molecule and calculated by DKH2 and semiempirical methods for the structure optimized at DKH2 and HF method are presented. One can see that the best method to reproduce the UV-vis absorption spectra is DKH2/DKH2 method. Unfortunately, it is a very time-consuming approach to calculate the physical properties of hybrids in the future. The HF/TD/PM6 method shifts the absorption spectrum too much to the red side of the spectrum. In this case, the best results are given by the DKH2/TD/PM6 method.

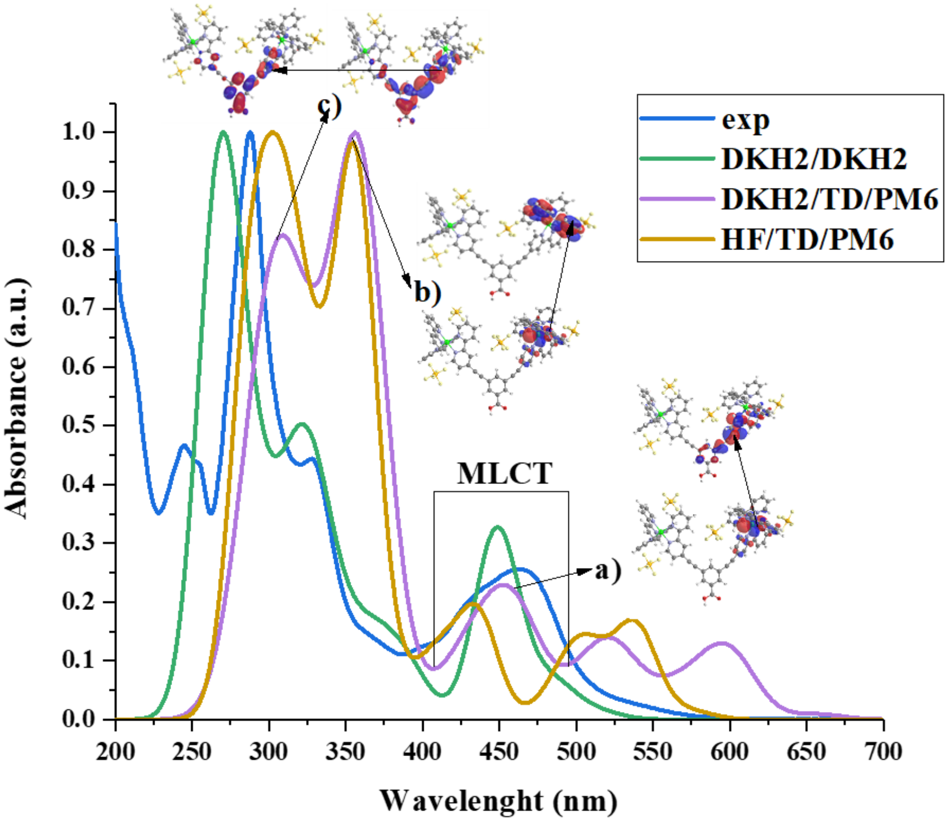

Figure 7.20. Normalized UV-vis absorption spectra calculated in vacuum by the DFT/B3LYP-DKH2(jorge-TZP-DKH) method for B_1 molecule optimized by DFT/B3LYP-DKH2(jorge-TZP-DKH) method (DKH2/DKH2), calculated by TD/PM6 method for the molecule optimized by DFT/B3LYP-DKH2(jorge-TZP-DKH) method (DKH2/TD/PM6), and calculated by TD/PM6 method for molecule optimized by HF method with LANL2DZ basis set for Ru and 6-31G for remaining atoms (HF/TD/PM6) compared to the experimental results. The molecular orbitals accessing the electron excitations corresponding to the MLCT and ILCT peaks calculated at HF/TD/PM6 level

In the case of B_2 the best data are given by the HF/TD/PM6 (see Fig.7.21) with not-so-diffused spectra into long wavelength as it is given by the DKH2/TD/PM6 method, and significant oscillator strength of excitations located in inherent places. The DKH2/TD/PM6 performed calculations show that the oscillator strength of transition near 600 nm is bigger than near 475 nm. This fact makes the DKH2/TD/PM6 simulation of the B_2 completely incorrect compared with the experiment.

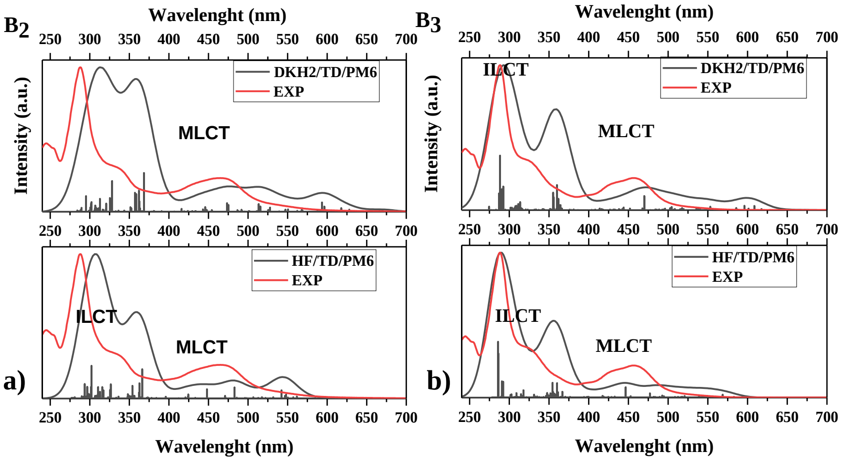

Figure.7.21. Normalized UV–Vis absorption spectra calculated by semi-empirical method TD/PM6, CIS/PM6, and CIS/PM7 for the B_2 molecule stabilized by the $(PF_6-)_2$ in vacuum (black) optimized by the DFT/B3LYP-DKH2(jorge-TZP-DKH) method (DKH2) (a) and optimized by HF method with LANL2DZ basis set for Ru and 6-31G for remaining atoms (HF) (b) compared with experimental data (red)

The MLCT peak of the B_3 molecule calculated by DKH2/TD/PM6 is comparable to B_3 HF/TD/PM6 data (Fig 7.21b), but the main issues are in detail. Experimental data give the most important peak at 470 nm, and in the case of HF/TD/PM6 and DKH2/TD/PM6, this peak is located at 456 nm and 447 nm, respectively. Also, the DKH2/TD/PM6 method gives a more diffused spectrum. For those reasons, the HF/TD/PM6 method will be used as the base model for future simulation of the B_3.

Molecular orbitals taking part of the ground and excited state assigned to the MLCT transfer calculated by HF/TD/PM6 method for the B_2 and B_3 are presented in Table 7.14. They are very similar to the ones calculated by DKH2/DKH2. It confirms the suggestion that the TD/PM6 method can be used in the future to calculate the electron and optical properties of hybrids based on the B_2 and B_3 molecules discussed in Chapter 8. In this case, the best molecular geometry will be the one optimized by the HF method contrary to the B1 dye where the molecule should be optimized at the DKH2 level.

One can conclude that in future calculations taking into consideration B_x-based hybrid materials the TD/PM6 method will be used to calculate their electron and optical properties. The B_1 molecule will be taken into account in geometry optimized at the DKH2 level. The B_2 and B_3 molecules will be considered with geometry optimized by the HF method.

Table 7.14. Electron properties of the B_2 and B_3 molecules calculated by the semiempirical method TD/PM6 for the structures stabilized by the $(PF_6^-)_2$ in a vacuum with geometry optimized by the HF method

B_2 HF/TD/PM6			**B_3 HF/TD/PM6**		
λ_{max}(nm) (oscillator strength)	Ground state	Excited state	λ_{max}(nm) (oscillator strength)	Ground state	Excited state
448 (0.129)	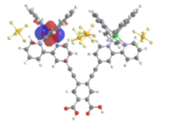	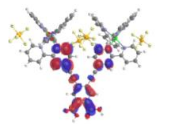	**447 (0.173)**	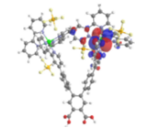	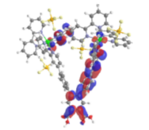
	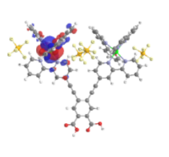	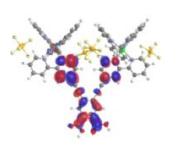		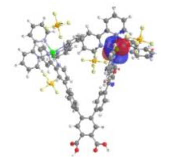	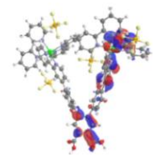
	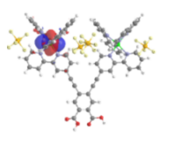	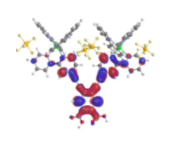		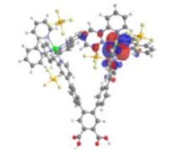	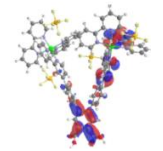

7.3. D102 and D149-based molecules with different anchoring groups.

To study the influence of the anchoring groups on the charge transfer occurring between the dyes and semiconducting oxide the indoline-based molecules were studied. In this case, two commercially available molecules were chosen, namely D102 and D149. These molecules were extended by two groups: catechol and phthalate moieties joined to the dye by the amide group (1) or directly (2) to the thiazol. Structures based on the D102 and D149 molecules are presented in Fig. 7.22 and Fig 7.23, respectively. The I_D denotes the indoline part of the D102 and D149 molecules attached to the catechol or phthalate moiety.

Calculations procedure for the metal-free selected indoline dyes based on D102 and D149 structures were performed similarly to the ones described for Ru-based dyes with few main differences.

1) In these structures are only light atoms and their geometry relaxations were carried with the 6-31G basis set for all atoms.

2) Optical properties of the selected indoline dyes were calculated in a vacuum and DMF using TDHF and TDDFT methods with B3LYP and LC-BLYP functionals. In this case, the 6-31++G** basis set was used.

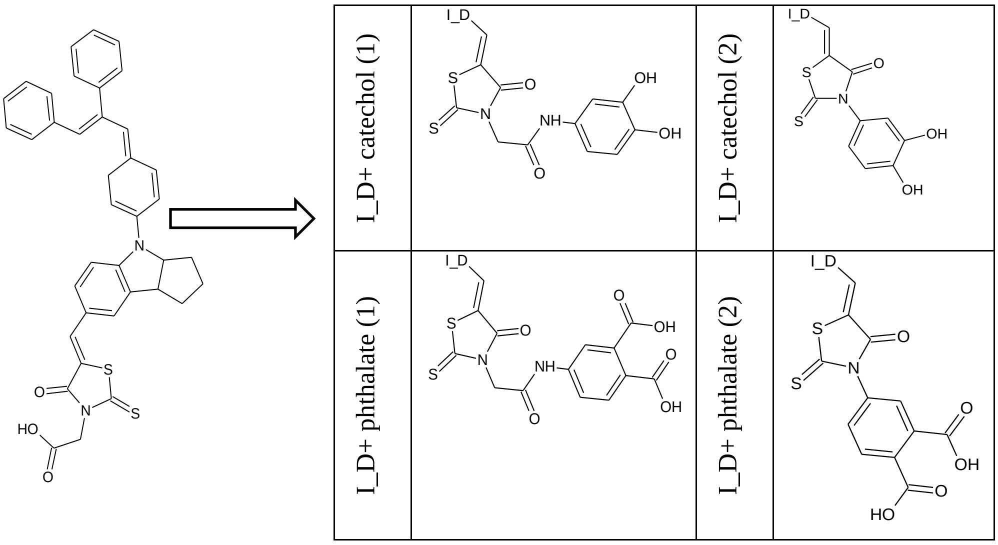
I_D+ catechol (1)
I_D+ catechol (2)
I_D+ phthalate (1)
I_D+ phthalate (2)
I_D

Figure 7.22. Schematic structures of the four new dyes, based on D102

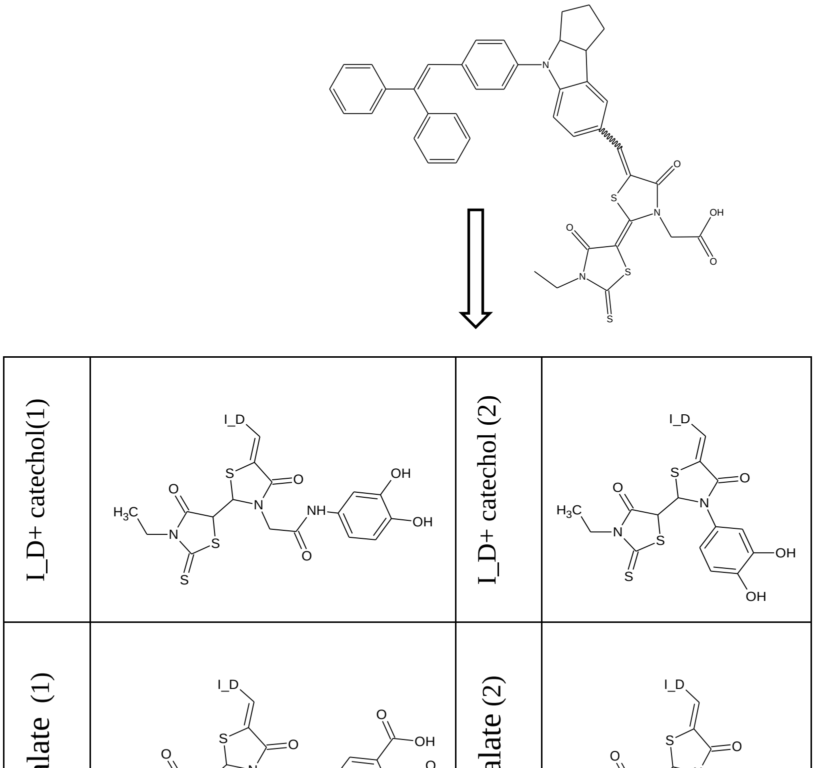
I_D+ catechol(1)
I_D+ catechol (2)
I_D+ phthalate (1)
I_D+ phthalate (2)
I_D

Figure 7.23. Schematic structures of the four new dyes, based on D149

The chosen methods of calculations were tested on the D102 and D149 molecules calculating their UV-vis absorption spectra in a vacuum. As was predicted for the Ru-based molecules discussed in Chapters 7.1 and 7.2 the DFT/B3LYP method gives better results than the DFT/LC-BLYP functional. The LC-BLYP functional shift the absorption spectra of the D102 and D149 molecules into the shorter wavelength of the spectrum than the DFT/B3LYP. The DFT/B3LYP method gives the first absorption peak calculated in vacuum at 447 nm and 489 nm for the D102 and D149 molecules, respectively. The first absorption peak measured for D102 and D149 in tert-butyl alcohol/acetylonitryl (1/1) solvent is located at 503 nm and 532 nm, respectively[43]. In consequence, all further calculations of the UV-vis spectra in vacuum and DMF were performed applying the DFT/B3LYP method.

In Fig. 7.24 the UV-vis absorption spectra calculated in vacuum and DMF solvent by DFT/B3LYP method for D102-based molecules are presented. One can see that the broad absorption band located between 300 nm and 400 nm for the D102 molecule has the same position for all of the investigated D102-based structures. The position of this band is not affected by the solvent. The first absorption peak corresponding to the HOMO→LUMO transition is very intensive for all molecules and is sensitive to the solvent. This peak is separated from other excitations and the solvent effect moves it more than 50 nm into the red side of the spectrum for all molecules.

In Table 7.15 electron parameters calculated for the D102 modified structures are presented. One can see that modification of the D102 molecule shifts its first absorption peak λ_{max} into a longer wavelength. It is seen for the molecules calculated in a vacuum as well as in DMF. The presence of the amide group increases the electric dipole moment of the D102 derivatives (D102+catechol (1) and D102+phthalate (1)). One can also notice that both anchored groups in case (1) and case (2) decrease the HOMO-LUMO energy difference ($\Delta E_{HOMO-LUMO}$). Concluding one can say that the newly designed molecules become less transparent (see Fig. 7.24) and more polar (except D102+catechol (2)). The DMF solvent increases the polarizability of all molecules and also decreases their $\Delta E_{HOMO-LUMO}$. The modification of the anchoring group changes the energy of the HOMO and LUMO simultaneously. The selected solvent slightly freezes the HOMO energy positions shifting the LUMO position into lover energy. These changes caused by the modification of the anchoring group in the D102 do not favor these molecules for photovoltaics.

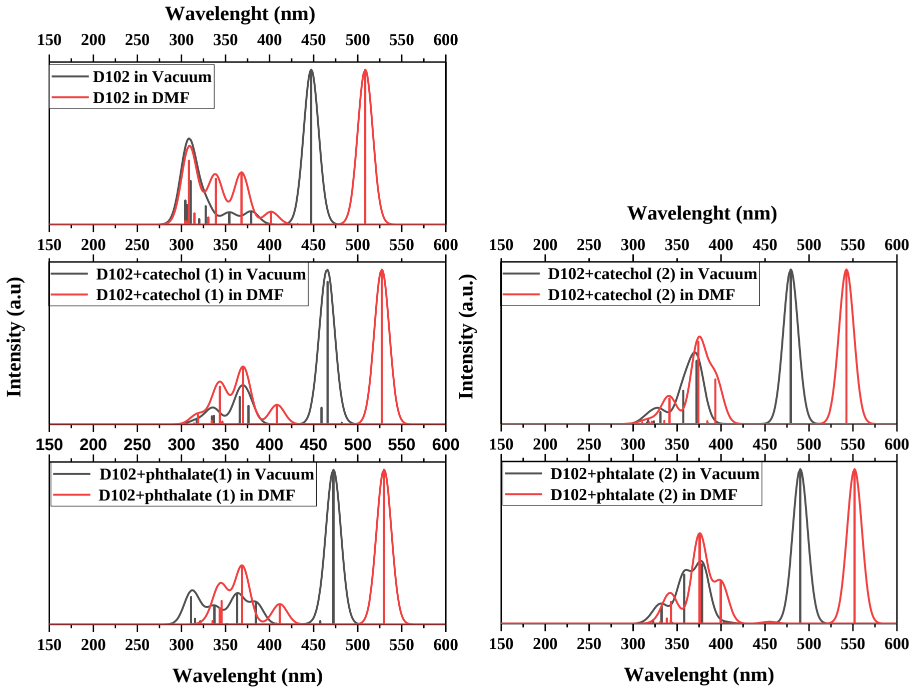

Figure 7.24. UV–vis absorption spectra calculated by TDDFT/B3LYP for D102-based molecules in vacuum (black) and in DMF (red)

Table 7.15. Electron parameters calculated by DFT/B3LYP method for D102-based molecules with different anchoring groups

Molecule	Environment	HOMO (eV)	LUMO (eV)	$\Delta E_{HOMO-LUMO}$ (eV)	Dipol moment (D)	λ_{max} (nm)
D102	in vacuum	-5.34	-2.34	3.00	8.71	447
	in DMF	**-5.27**	**-2.55**	**2.72**	**11.83**	**508**
D102+catechol (1)	in vacuum	-5.42	-2.54	2.88	10.72	464
	in DMF	**-5.25**	**-2.63**	**2.62**	**14.73**	**527**
D102+catechol (2)	in vacuum	-5.27	-2.42	2.85	8.09	479
	in DMF	**-5.32**	**-2.59**	**2.73**	**10.33**	**543**
D102+phthalate (1)	in vacuum	-5.55	-2.72	2.83	13.45	473
	in DMF	**-5.27**	**-2.66**	**2.61**	**16.99**	**530**
D102+phthalate (2)	in vacuum	-5.13	-2.54	2.59	11.31	490
	in DMF	**-5.16**	**-2.62**	**2.54**	**13.61**	**552**

In Table 7.16 the frontier orbitals of the D102-based molecules are presented. One can see that mostly separated HOMO from LUMO orbitals are observed for pristine D102 molecules. The change of the anchored group from -COOH into catechol or phthalate moves the LUMO into lower energy. It is seen for all molecules. The observed situation will not give benefits in DSSC application.

Table 7.16. Frontiers orbitals calculated by DFT/B3LYP method for D102-based molecule with different anchoring groups

	Environment	HOMO	LUMO
D102	Vacuum	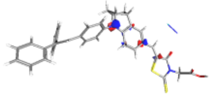	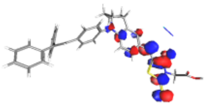
	DMF	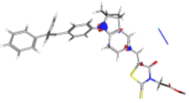	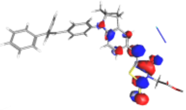
D102+catechol (1)	Vacuum	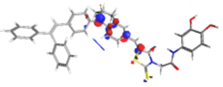	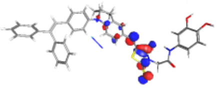
	DMF	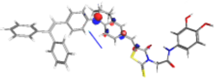	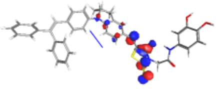
D102+phthalate (1)	Vacuum	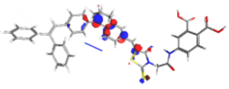	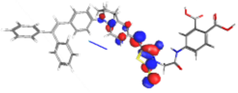
	DMF	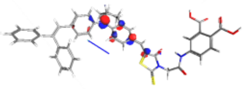	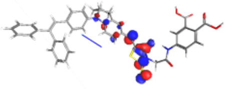
D102+catechol (2)	Vacuum	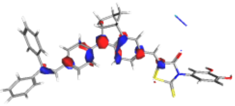	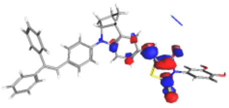
	DMF	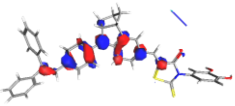	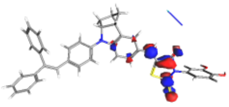
D102+phthalate (2)	Vacuum	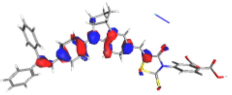	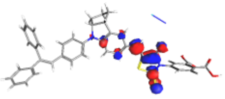
	DMF	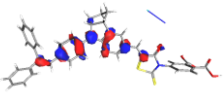	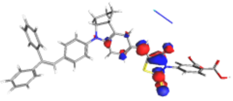

Calculations, as described above, were performed also for the D149-based structures. These structures are also augmented by catechol and phthalate groups with and without amide moiety. The D149 dye is more polar than the D102 molecule and also the electron dipole moments of the new derivative of the D149 (see Table 7.17) are much higher than the values predicted for the D102-based structures (see Table 7.15). The performed modifications increase the dipole moment of D149 except for the catechol (2) which decreases the dipole moment of the D149 dye as it was observed for the D102. The solvent effect increases the dipole moment for all molecules based on D149. The catechol (2) and phthalate (2) move the first absorption peak according to the hypsochromic shift. The spacer with amide group (D149+catechol (1) and D149+phthalate (1)) moves the spectra in the read direction. It is also valid for the DMF solvent.

Table 7.17. Electron parameters calculated by DFT/B3LYP method for D149-based molecules with different anchoring groups.

Molecule	Environment	HOMO (eV)	LUMO (eV)	$\Delta E_{HOMO-LUMO}$ (eV)	Dipol moment (D)	λ_{max} (nm)
D149	in vacuum	-5.32	-2.48	2.84	11.37	489
	in DMF	**-5.17**	**-2.59**	**2.58**	**14.90**	**549**
D149+catechol (1)	in vacuum	-5.37	-2.57	2.80	15.31	492
	in DMF	**-5.18**	**-2.60**	**2.58**	**20.59**	**549**
D149+catechol (2)	in vacuum	-5.21	-2.32	2.89	9.41	481
	in DMF	**-5.12**	**-2.49**	**2.63**	**13.09**	**539**
D149+ phthalate (1)	in vacuum	-5.44	-2.68	2.76	13.68	498
	in DMF	**-5.19**	**-2.62**	**2.57**	**17.38**	**552**
D149+ phthalate (2)	in vacuum	-5.31	-2.46	2.85	11.52	487
	in DMF	**-5.15**	**-2.55**	**2.60**	**15.45**	**546**

The frontier orbitals HOMO and LUMO of the D149 are located in the middle of the molecular structure (see Table 7.18). Also, the modification of the anchoring group does not change significantly the HOMO and LUMO distribution. It is confirmed by the shape of the UV-vis absorption spectra (see Fig. 7.25). For all derivatives of the D149, the obtained UV-vis absorption spectra are the same. It confirms that the anchoring groups do not participate in the first electron excitations. The obtained results for the D149 derivatives confirm that the anchoring groups will not change the optical properties of the newly created molecules. Also one can conclude that the anchoring groups do not have any contribution in LOMO orbitals favorably influencing the possible charge transfer from the dye to the semiconductor in DSSC devices. The chosen D102 and D149 derivatives are not good candidates to propose their modification by the catechol and phthalate groups to be used in photovoltaics.

Table 7.18. Frontier orbitals calculated by DFT/B3LYP method for D149-based molecules with different anchoring groups

	Environment	HOMO	LUMO
D149	Vacuum	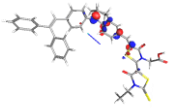	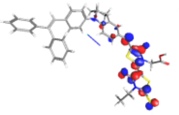
	DMF	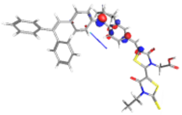	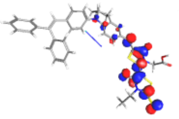
D149+catechol (1)	Vacuum	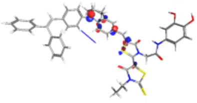	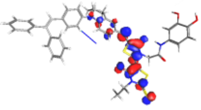
	DMF	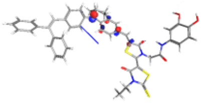	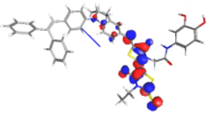
D149+ phthalate (1)	Vacuum	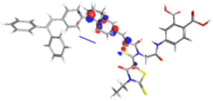	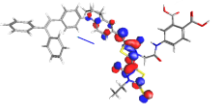
	DMF	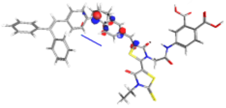	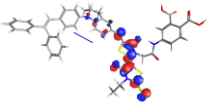
D149+catechol (2)	Vacuum	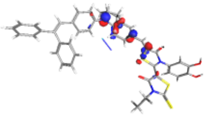	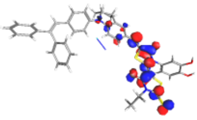
	DMF	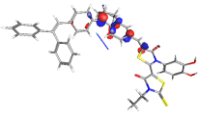	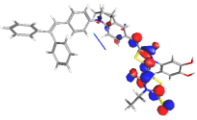
D149+ phthalate (2)	Vacuum	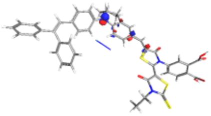	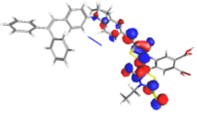
	DMF	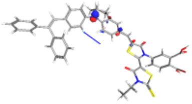	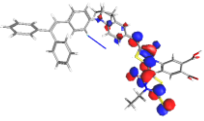

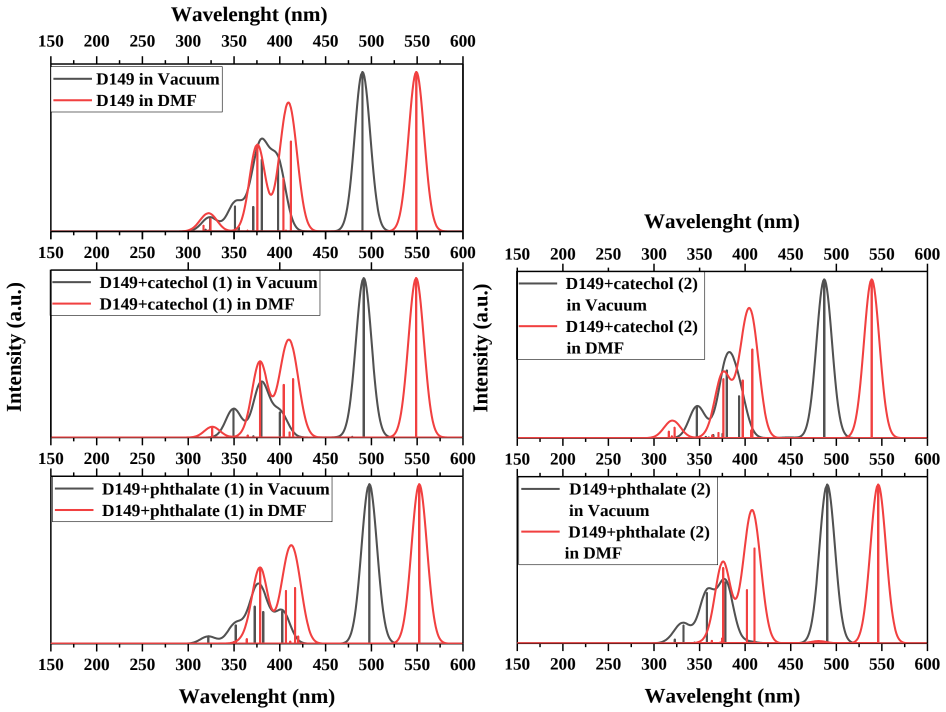

Figure 7.25. UV–vis absorption spectra calculated by TDDFT/B3LYP for D149-based molecules in vacuum (black) and in DMF (red)

7.4. Conclusions

In the presented Chapter the electron and optical properties of the selected Ru-based molecules as well as D102 and D149 derivatives were investigated computationally and the obtained results were compared with experimental data. These molecules were studied in the context to be used as dyes for the DSSC applications with titanium dioxide (TiO_2) structures as anodes. In this case, special attention was paid to their UV-vis absorption spectra and frontier orbitals distribution. The performed work also aimed at searching for the best computational method to calculate the electron and optical parameters of hybrid materials based on studied dyes and TiO_2.

As a consequence of performed calculations was shown that the $Ru(bpy)_3^{2+}$-based molecules should be modeled with PF_6^- structures as stabilizers. It concerns the geometry optimization procedure as well as the electron and optical properties calculations. The PF_6^- structures prevent distortion of the $Ru(bpy)_3^{2+}$ moiety. Modification of the $Ru(bpy)_3^{2+}$ structure by the spacer and anchoring group does not change the geometry of the Ru environment. Therefore two kinds of Ru-based molecules were investigated. One group with a single $Ru(bpy)_3^{2+}$ structure possessing –COOH anchoring group in meta-, orto- or para-position to the spacer, and the second group of dendrimeric molecules with two $Ru(bpy)_3^{2+}$ structures in each molecule with one (B_1) or two anchoring -COOH groups (B_2, B_3, B_4).

Was shown that alteration of the -COOH group connection from the meta- or ortho-isomer into para-position improves charge separation occurring between HOMO and LUMO orbitals of the studied dyes. In consequence, it allows for forming the intramolecular charge transfer (ICT) occurring in the para-series of dyes and can facilitate higher electron injection from the photoexcited dye into the conduction band of the TiO_2. The LUMO orbital of the RuLp molecules (para-position of -COOH) spreads along the molecule and is located at the spacer and anchor group. The position of the LUMO orbital at the -COOH group favors the charge transfer from the dye molecule into the semiconducting material. The calculations point out that the RuLp molecules should be potentially suitable for sensitizing semiconductors in DSSCs devices.

The modification of the $Ru(bpy)_3^{2+}$-based molecules from one Ru-moiety to a dendrimeric structure does not change their optical properties drastically. The MLCT-associated peak, located close to 450 nm, characteristic for $Ru(bpy)_3^{2+}$-based dyes stays frozen. The B_X molecules have the absorption peak shifted a little bit in the red side of the spectrum compared with RuLp, RuLm, and RuLo dyes. These peaks are associated with the HOMO-to-LUMO transition but their oscillator strengths are very low. The changes made in the spacer structure of the B_3 molecule increase the value of its molar absorption coefficient.

In the B_2 molecule, its LUMO orbital is strongly separated from the other excited states. It makes electron transition to the LUMO orbital more privileged than it is observed for energetically higher excitations. Transition noticed as HOMO-3 → LUMO observed for the B_2 molecule corresponds to the MLCT-associated peak and possesses the highest oscillator strength of all simulated structures. Solvent makes the separation of LUMO from other excited orbitals even more significant than it was observed for vacuum. The LUMO localized on the anchoring group makes the B_2 molecule a good candidate for DSSC application. In B_1, B_3, and B_4 molecules the MLCT transfer occurs at $Ru(bpy)_3{}^{2+}$ moiety. The solvent has a small impact on shifting excited states to the anchoring group and these transitions are characterized by small oscillator strength. The solvent effect in molecules B_3 and B_4 causes the higher contribution of spacer molecular orbitals to the first, energetically low-lying excitations. All made observations allow us to conclude that the molecules B_3 and B_4 are rather good candidates for photovoltaic applications, but their suspense should be worst than for the B_2 molecule.

Was proved that the best agreement between computational and experimental data was obtained by calculating the properties of $Ru(bpy)_3^{2+}$-based molecules at DKH2/DKH2 level. Unfortunately, the mentioned method is very time and memory-consuming and cannot be used for the big atom system. Therefore the semiempirical methods were tested. In conclusion, one can say that the TD/PM6 method can be used to calculate the optical properties of the RuLp molecules as well as B_X molecules adsorbed on the surface of TiO_2.

To check the influence of anchored groups on the electron and optical properties of dyes the commercial D102 and D149 molecules were augmented by catechol or phthalate moiety. The performed calculations show that the proposed modifications do not give significant changes in improving the properties of dyes in the desired direction.

Concluding, one can say that the RuLp, B_2, and B_3 molecules can be used to study their photovoltaic properties based on TiO_2 semiconductor.

7.5. Literature

[1] Desilvestro, J., Graetzel, M., Kavan, L., Moser, J., & Augustynski, J. "Highly efficient sensitization of titanium dioxide." *Journal of the American Chemical Society*, vol.107, no.10, pp.2988–2990, **(1985)**. doi:10.1021/ja00296a035

[2] Foresman, J. B., & Frisch, A., "Exploring Chemistry with Electronic Structure Methods, methods second edition." *U.S.A.: Gaussian, Inc.*, **(1993)**.

[3] M.J. Frisch, G.W. Trucks, H.B. Schlegel, G.E. Scuseria, M.A. Robb, J.R. Cheeseman, G. Scalmani, V. Barone, B. Mennucci, G.A. Petersson, H. Nakatsuji, M. Caricato, X. Li, H.P. Hratchian, A.F. Izmaylov, J. Bloino, G. Zheng, J.L. Sonnenberg, M. Hada, M. Ehara, K. Toyota, R. Fukuda, J. Hasegawa, M. Ishida, T. Nakajima, Y. Honda, O. Kitao, H. Nakai, T.

Vreven, J.A. Montgomery, J.E. Peralta Jr., F. Ogliaro, M. Bearpark, J.J. Heyd, E. Brothers, K.N. Kudin, V.N. Staroverov, R. Kobayashi, J. Normand, K. Raghavachari, A. Rendell, J.C. Burant, S.S. Iyengar, J. Tomasi, M. Cossi, N. Rega, J.M. Millam, M. Klene, J.E. Knox, J.B. Cross, V. Bakken, C. Adamo, J. Jaramillo, R. Gomperts, R.E. Stratmann, O. Yazyev, A.J. Austin, R. Cammi, C. Pomelli, J.W. Ochterski, R.L. Martin, K. Morokuma, V.G. Zakrzewski, G.A. Voth, P. Salvador, J.J. Dannenberg, S. Dapprich, A.D. Daniels, O¨. Farkas, J. B. Foresman, J.V. Ortiz, J. Cioslowski, D.J. Fox, *Gaussian 09, Gaussian, Inc., Wallingford CT*, **(2009)**.

[4] Douglas, M., & Kroll, N. M. "Quantum electrodynamical corrections to the fine structure of helium." *Annals of Physics*, vol.82, no.1, pp.89–155, **(1974)**. doi:10.1016/0003-4916(74)90333-9

[5] Hess, B. A. "Applicability of the no-pair equation with free-particle projection operators to atomic and molecular structure calculations." *Physical Review A*, vol.33, pp. 3742-3748, **(1986)**.

[6] Jansen, G., & Hess, B. A. "Revision of the Douglas-Kroll transformation." *Physical Review A*, vol.39, no.11, pp.6016–6017, **(1989)**. doi:10.1103/physreva.39.6016

[7] Jorge, F. E., Canal Neto, A., Camiletti, G. G., & Machado, S. F. "Contracted Gaussian basis sets for Douglas–Kroll–Hess calculations: Estimating scalar relativistic effects of some atomic and molecular properties." *The Journal of Chemical Physics*, vol.130, pp.064108, **(2009)**. doi:10.1063/1.3072360.

[8] Rillema D.P., Jones D.S., Woods C., & Levy H.A. "Comparison of the crystal structures of tris heterocyclic ligand complexes of ruthenium(II)." *Inorg. Chem.*, vol.31, pp.2935-2938, **(1992)**.

[9] Davidson E.R. "The iterative calculation of a few of the lowest eigenvalues and corresponding eigenvectors of large real-symmetric matrices." *Journal of Computational Physics*, vol.17, pp.87-94, **(1975)**.

[10] Ghosh, A., Mandoli, A., Kumar, D. K., Yadav, N. S., & Das, A. "DNA binding and cleavage properties of a newly synthesised Ru(II)-polypyridyl complex." *Dalton Transactions*, vol.42, pp.9312, **(2009)**. doi:10.1039/b906756f

[11] Zalas M., Gierczyk B., Bossi A., Mussini P. R., & W. Stampor., "The influence of anchoring group position in ruthenium dye molecule on performance of dye-sensitized solar cells." *Dyes and Pigments*, vol.150, pp.335–346, **(2018).** doi:10.1016/j.dyepig.2017.12.029

[12] Schmidt, M. W., Baldridge, K. K., Boatz, J. A., Elbert, S. T., & Montgomery, J. A. "General atomic and molecular electronic structure system." *Journal of Computational Chemistry,* vol.14,no.11, pp.1347–1363, **(1993)**. doi:10.1002/jcc.540141112

[13] Gordon, M. S., & Schmidt, M. W.. "Advances in electronic structure theory: GAMESS a decade later." *Theory and Applications of Computational Chemistry: the first forty years; Dykstra, C. E., Frenking, G., Kim, K. S., Scuseria, G. E.,* pp.1167–1189 **(2005)**. doi:10.1016/b978-044451719-7/50084-6.

[14] Roothaan, C. C. J. "New Developments in Molecular Orbital Theory." *Reviews of Modern Physics*, vol.23, no.2, pp.69–89, **(1951)**. doi:10.1103/revmodphys.23.69

[15] Jensen, F. "Locating transition structures by mode following: A comparison of six methods on the Ar8 Lennard-Jones potential. *" The Journal of Chemical Physics*, vol.102, no.17, pp.6706–6718, **(1995)**. doi:10.1063/1.469144

[16] Miertuš S, Scrocco E, & Tomasi J. "Electrostatic interaction of a solute with a continuum. A direct utilizaion of AB initio molecular potentials for the prevision of solvent effects." *Chemical Physics*, vol.55, no.1, pp.117–129, **(1981)**. doi:10.1016/0301-0104(81)85090-2

[17] Barone, V., & Cossi, M. "Quantum Calculation of Molecular Energies and Energy Gradients in Solution by a Conductor Solvent Model." *The Journal of Physical Chemistry A*, vol.102, no.11, pp.1995–2001, **(1998)**. doi:10.1021/jp9716997

[18] Cossi M, Rega N, Scalmani G, & Barone V. "Energies, structures, and electronic properties of molecules in solution with the C-PCM solvation model." *Journal of Computational Chemistry*, vol.24, no.6, pp.669–681. **(2003)**. doi:10.1002/jcc.10189

[19] Tomasi, J., Mennucci, B., & Cammi, R., "Quantum Mechanical Continuum Solvation Models." *Chemical Reviews*, vol.105, no.8, pp.2999–3094, **(2005)**. doi:10.1021/cr9904009

[20] Cossi M, Mennucci B, & Cammi R. "Analytical first derivatives of molecular surfaces with respect to nuclear coordinates." *Journal of Computational Chemistry* vol.17, no.1, pp.57–73, **(1996)**.

[21] Cui, X., Zhao, J., Karatay, A., Yaglioglu, H. G., & Küçüköz, B. "A Ru(bipyridine)$_3$[PF$_6$]$_2$ Complex with a Rhodamine Unit - Synthesis, Photophysical Properties, and Application in Acid-Controllable Triplet-Triplet Annihilation Upconversion." *European Journal of Inorganic Chemistry*, vol.2016, no.32, pp.5079–5088, **(2016)**. doi:10.1002/ejic.201600755

[22] Taratula, O., Rochford, J., Piotrowiak, P., Galoppini, E., & Meyer, G. J. "Pyrene-Terminated Phenylenethynylene Rigid Linkers Anchored to Metal Oxide Nanoparticles." *The Journal of Physical Chemistry B*, vol.110, no.32, pp.15734–15741, **(2006)**. doi:10.1021/jp0623847

[23] Juris, A., Balzani, V., Barigelletti, F., Campagna, S., & von Zelewsky, A., "Ru(II) polypyridine complexes: photophysics, photochemistry, eletrochemistry, and chemiluminescence." *Coordination Chemistry Reviews*, vol.84, pp.85−277, **(1988)**.

[24] Rühle, S., Greenshtein, M., Chen, S.-G., Merson, A., & Zaban, A. "Molecular Adjustment of the Electronic Properties of Nanoporous Electrodes in Dye-Sensitized Solar Cells." *The Journal of Physical Chemistry B*, vol.109, no.40, pp.18907–18913, **(2005)**. doi:10.1021/jp0514123.

[25] Korolevych, O., Zalas, M., Stampor, W., Kassiba, A. H., & Makowska-Janusik, M. "Impact of dyes isomerization effect on the charge transfer phenomenon occurring on the dye/nanosemiconductor interface." *Solar Energy Materials and Solar Cells*, vol.219, pp.110771, **(2021)**. doi:10.1016/j.solmat.2020.110771

[26] Bublitz G., & Boxer S. "Stark spectroscopy: Applications in Chemistry, Biology, and Materials Science." *Annual Review of Physical Chemistry*, vol.48, pp.213-242. **(1997)**

[27] Ohta N. "Electric field effects on photochemical dynamics in solid films." *Bulletin of the Chemical Society of Japan*, vol.75, pp.1637-1655, **(2002)**.

[28] Liptay W, "Dipole moments and polarizabilities of molecules in excited electronic states", *in Excited States, Lim E.C. Ed.; Academic Press: New York, USA*, vol. 1, pp.129-229, **(1974).**

[29] Pelczarski D, Korolevych O, Gierczyk B, Zalas M, Makowska-Janusik M, Stampor W. "Electronic States of Tris(bipyridine) Ruthenium(II) Complexes in Neat Solid Films Investigated by Electroabsorption Spectroscopy." *Materials (Basel).* vol.19, no.15, pp.2278, **(2022)**. doi:10.3390/ma15062278.

[30] Stewart J.J.P., "Optimization of parameters for semiempirical methods V: Modification of NDDO approximations and application to 70 elements", *Journal of Molecular Modeling*, vol.13, pp.1173–1213, **(2007)**. doi:10.1007/s00894-007-0233-43

[31] Stewart J.J.P., "Optimization of parameters for semiempirical methods VI: more modifications to the NDDO approximations and re-optimization of parameters." *Journal of molecular modeling*, vol.19 no.1, pp.1-32, **(2013)**. doi:10.1007/s00894-012-1667-x

[32] Runge, E., & Gross, E. K. U. "Density-Functional Theory for Time-Dependent Systems." *Physical Review Letters*, vol.52, no.12, pp.997–1000, **(1984)**. doi:10.1103/physrevlett.52.997

[33] Stewart J.J.P., "Optimization of parameters for semiempirical methods VI: more modifications to the NDDO approximations and re-optimization of parameters." *Journal of molecular modeling*, vol.19 no.1, pp.1-32, **(2013)**. doi:10.1007/s00894-012-1667-x

[34] Abrahamsson, M., Taratula, O., Persson, P., Galoppini, E., & Meyer, G. J. "Meta-substituted Ru^{II} rigid rods for sensitization of TiO_2." *Journal of Photochemistry and Photobiology A: Chemistry*, vol.206, no.2-3, pp.155-163. **(2009)**.

[35] Zalas, M., Gierczyk, B., Klein, M., Siuzdak, K., & Łuczak, T., "Synthesis of a novel dinuclear ruthenium polypyridine dye for dye-sensitized solar cells application." *Polyhedron*, vol.67, pp.381-387, **(2014)**. doi:10.1016/j.poly.2013.09.023

[36] Funaki, T., Yanagida, M., Onozawa-Komatsuzaki, N., Kawanishi, Y., & Sugihara, H., "Ruthenium (II) complexes with π expanded ligand having phenylene–ethynylene moiety as sensitizers for dye-sensitized solar cells." *Solar energy materials and solar cells*, vol.93, no.6-7, pp.729-732. **(2009)**.

[37] Hess B.A. "Applicability of the no-pair equation with free-particle projection operators to atomic and molecular structure calculations." *Physical Review A*, vol.33**,** pp.3742-3748, **(1986)**.

[38] Zalas M., Gierczyk B., Cegłowski M., & Schroeder G., "Synthesis of new dendritic antenna-like polypyridine ligands", *Chemical Papers*, vol.66 pp.733-740, **(2012)**. doi:10.2478/s11696-012-0196-5

[39] Veikko, U., Zhang, X., Peng, T., Cai, P., & Cheng, G., "The synthesis and characterization of dinuclear ruthenium sensitizers and their applications in photocatalytic hydrogen production." *Spectrochimica Acta Part A: Molecular and Biomolecular Spectroscopy*, vol.105, pp.539-544, **(2013)**.

[40] Polo, A. S., Itokazu, M. K., & Iha, N. Y. M. "Metal complex sensitizers in dye-sensitized solar cells." *Coordination Chemistry Reviews*, vol.248, no.13-14, pp.1343-1361, **(2004)**.

[41] Dongare, P., Myron, B. D., Wang, L., Thompson, D. W., & Meyer, T. J. " $[Ru(bpy)_3]^{2+*}$ revisited. Is it localized or delocalized? How does it decay?." *Coordination Chemistry Reviews*, vol.345, pp.86-107, **(2017)**. doi:10.1016/j.ccr.2017.03.009

[42] Miar, M., Shiroudi, A., Pourshamsian, K., Oliaey, A. R., & Hatamjafari, F. "Theoretical investigations on the HOMO–LUMO gap and global reactivity descriptor studies, natural bond orbital, and nucleus-independent chemical shifts analyses of 3-phenylbenzo [d] thiazole-2 (3 H)-imine and its para-substituted derivatives: Solvent and substituent effects." *Journal of Chemical Research*, vol.45, no.1-2, pp.147-158, **(2021)**. doi:10.1177/1747519820932091

[43] Wang, B., Li, N., Yang, L., Dall'Agnese, & Wang, X. F. "Organic dye/$Cs_2AgBiBr_6$ double perovskite heterojunction solar cells." *Journal of the American Chemical Society*, vol.143, no.36, pp.14877-14883, **(2021)**. doi:10.1021/jacs.1c07200

Chapter 8

STRUCTURAL AND ELECTRONIC PROPERTIES OF SELECTED DYES/TiO_2 HYBRIDS

Photoconversion efficiency of the TiO_2-based DSSCs depends, among others, on the sensitizers anchored to the semiconductor layers. As was presented in Chapter 7, one of the critical properties of the sensitizers is their anchoring groups making a stable connection between dyes and the TiO_2 nanostructure. In the present Chapter, the influence of the dyes on the efficiency of the DSSCs will be presented. In this case, the quantum chemical simulations on the structural, electron, and optical properties of the TiO_2-based hybrids were performed and discussed. As the dyes, the Ru-based molecules described in Chapter 7, were chosen. The modeled semiconductors were based on nanostructures presented in Chapter 6.

Modeling of the hybrid materials should be performed based on the simulation model defining the dye/semiconductor connection including its geometry relaxation. In addition, the optical properties prediction should be based on the approximation development necessary to calculate the electron properties of many-electron systems possessing metal ions. In this case, the developed model should have a few critical issues. The TiO_2 cluster must be structurally minimized in size keeping the electron nature of native semiconductors to prevent time-consuming calculations. The geometry of the $Ru(bpy)_3^{2+}$ based dyes must be protected during the structural relaxation of the hybrids. As it was mentioned in Chapter 7, the geometry of the Ru environment is very important in the case of their electron property calculations. The correctness of the developed calculation model was examined by comparing the obtained results with experimental data.

8.1. Structural and electron properties of B_X/TiO_2 hybrids

As was presented in Chapter 7.2 the molecules B_1, B_2, and B_3 (called B_X) can be used as the dyes in DSSC applications. There was proved that the quantum chemical calculations, applying the DKH2/DKH2 methodology, give very good results concerning the structural and electron properties of the studied molecules. Unfortunately, these calculations make simulations extremely long. In consequence, the DKH2/DKH2 method cannot be used to study computationally the hybrid structures due to their huge amount of electrons. In this case, the less demanding method, giving the data in good agreement with experimental results should be found.

Firstly, the studied hybrid systems were built based on the $(TiO_2)_{49}$ spherical clusters. The size of the cluster was proposed according to the simulations discussed in Chapter 6. Attaching the B_X molecules to the $(TiO_2)_{49}$ clusters makes the hybrids too important in size and electron number, that the quantum chemical calculations for these systems are impossible applying *ab initio* HF or DFT methods. In consequence, the PM6[1] and PM7[2] semi-empirical methods were examined. The main advantages of those methods are their efficiency in many-electron system investigations. However, the main disadvantage of semiempirical computations is the incorrect description of Ru and Ti electron configuration. These methods destroy the surface of the TiO_2 clusters during their structure relaxation procedure. Freezing the atoms on the surface of the cluster also does not give good results. Additionally, the obtained geometries do not possess realistic electron properties. In consequence, the other cluster model should be chosen.

Was decided to study hybrid structures based on (101) nanosheets of anatase[3]. The two clusters were chosen to be used in simulations: $(TiO_2)_{28}H_{15}$ and $(TiO_2)_{35}H_{15}$ with radius lengths 7 and 8 Å, respectively. The construction of these clusters was described in Chapter 6.3. Other there mentioned clusters such as $(TiO_2)_{42}H_{12}$ and $(TiO_2)_{51}H_{26}$ were not even tried to be used as components of hybrids due to their size and the difficulty of their quantum chemical calculations.

Unfortunately, also in this case, the geometry optimizations of the B_X/TiO_2 hybrids performed by semi-empirical methods do not give good results. The geometries of the $Ru(bpy)_3^{2+}$-based structures, relaxed semiempirically, were destroyed. Also freezing of the $Ru(bpy)_3^{2+}$ part of the dyes did not give appropriate results. These calculations were very complicated according to the SCF convergence and the obtained data were not satisfactory compared with experimental results.

As a result of many trials, was decided to implement the model of dye/TiO_2 based on the $(TiO_2)_{28}H_{15}$ semiconductor and the benzene attached to the semiconductor surface by the –COOH group. The chosen structure anchored at the surface of the TiO_2 represents the spacer and the anchoring group of the B_X dyes. The idea of the implemented model was to optimize the geometry of the constructed structure named model/$(TiO_2)_{28}H_{15}$ in search of the optimal interconnection between the semiconducting cluster and dye. After geometry relaxation, the B_X molecule was substituted instead of the benzene present in the model/$(TiO_2)_{28}H_{15}$ structure. The substitution was done by overlapping the benzene of the model/$(TiO_2)_{28}H_{15}$ system and the benzene of the B_X dye. The B_1 molecule taken into consideration possess the geometry optimized by DKH2 and the B_2 and B_3 molecules have geometry optimized by *ab initio*/HF formalism, as it was proposed in Chapter 7. The proposed methodology to model the geometry of the dye/semiconductor anchoring group is new and it was never used before by any of the research groups. There are known cases in the literature where the structure of the dye/semiconductor is not optimized taking them for quantum chemical calculations. There the hybrids are built by simple attachment of the dye to the surface of the semiconductor[4,5,6,7]. After preliminary research, it can be concluded that the implemented approach gives correct results.

Full atom optimization of the model/$(TiO_2)_{28}H_{15}$ was performed by the GAMESS program package[8,9]. The model/$(TiO_2)_{28}H_{15}$ structures were built in a vacuum using ACD/ChemSketch, an integrated software package from Advanced Chemistry Development, Inc. The lowest total energies of the model/$(TiO_2)_{28}H_{15}$ were searched with C1-defined symmetry in a vacuum using the HF formalism implemented in GAMESS. The calculations were made by applying 6-31G basis sets for all atoms. The minimum of the potential energy surface was calculated at a restricted Hartree-Fock (RHF) level[10]. Optimal geometries of the model/$(TiO_2)_{28}H_{15}$ were found by applying the quadratic approximation (QA) optimization algorithm based on the augmented Hessian technique[11]. The gradient convergence tolerance was equal to 10^{-5} Hartree/Bohr. At the end of the geometry optimization, the Hessian evaluation was performed to exclude structures giving the negative modes and ensure a thermodynamic equilibrium of the model/$(TiO_2)_{28}H_{15}$. In consequence, the three possible connections of the model/$(TiO_2)_{28}H_{15}$ were obtained (see Fig. 8.1). The obtained bond types are named as follows: Type 1, Type 2, and Type 3.

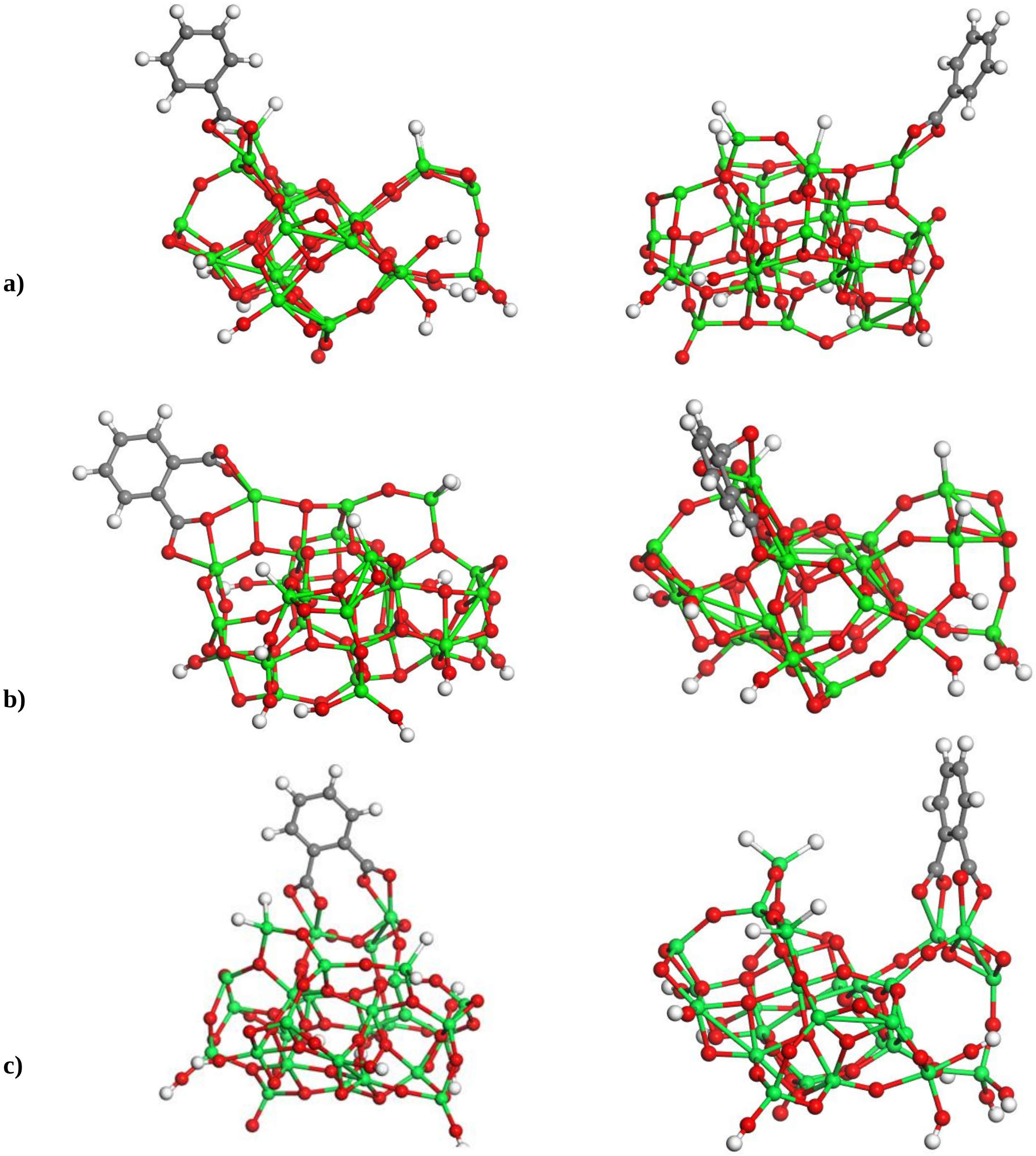

Figure 8.1. Structure of the $(TiO_2)_{28}H_{15}$ cluster with benzene attached to the semiconductor by -COOH anchoring groups in various configurations (in two different perspectives) a) single connection (Type 1) b) double connection with one privileged anchor of the -COOH (Type 2) and c) strong double connection (Type 3). (Ti—green, O—red, C—grey, and H—white color).

The bond of Type 1 is a single connection occurring between dye and $(TiO_2)_{28}H_{15}$ (Fig. 8.1a). The lengths of the created two O-Ti distances between the dye and semiconductor are equal to 2.170 and 2.149 Å. The molecule B_1 can be anchored to the TiO_2 cluster only in this way because the B_1 molecule possesses only one –COOH anchoring group. However, the B_2 and B_3 molecules can be also anchored on the surface of the TiO$_2$ in this way. The second –COOH anchoring group of the B$_2$ and B$_3$ dyes will be not active in this case. Additionally, the B$_2$ and B$_3$ molecules can be attached to the semiconductor by bonds of Type 2 and Type 3.

The connection of Type 2 (Fig. 8.1b) and Type 3 (Fig. 8.1c) possess two -COOH anchoring groups active in the deposition process of dye on the surface of the semiconductor. The Type 2 connection gives one oxygen incorporated into the TiO$_2$ anatase structure, making this arrangement privileged. The O-Ti bond in this case are symmetrical and their lengths are equal to 2.090 Å. The occurring second weaker dye/semiconductor connection is not symmetrical and its O-Ti bonds are equal to 2.240 and 2.290 Å. These distances are the longest ones from all bonds occurring between the dye and TiO$_2$ cluster. In connection with Type 3 both –COOH anchoring groups are strongly bounded to the TiO$_2$ cluster. The O-Ti bonds in this case are equal to 2.068 and 2.153 Å, as well as 2.147 and 2.117 Å. So close distance between dye and semiconductor can create an appropriate situation for charge transfer occurring between both structures.

In Table 8.1 the total energies of the simulated model/(TiO$_2$)$_{28}$H$_{15}$ structures are collected taking into account three predicted types of bonds. Analyzing the total energy per atom one can see that the model/(TiO$_2$)$_{28}$H$_{15}$ structure with bonds of Type 1 is the most stable one and in consequence the most probable. However, one can see that the structures with bonds of Type 2 and Type 3 possess energy insignificantly higher. It means that these two types of structures also can exist.

Table 8.1. Structural stability of the selected hybrid structures presented in Fig 8.1 possessing bonds mentioned as Type 1, Type 2, and Type 3.

	Type 1	Type 2	Type 3
Total energy (Hartree)	-28375.4	-28562.2	-28562.3
Number of atoms	111	113	113
Energy per atom (Hartree)	-255.63	-252.8	-252.8

The three obtained structures (see Fig. 8.1) were used to build the B$_X$/(TiO$_2$)$_{28}$H$_{15}$ structures. Then for each of them, their electron properties were calculated using TD/PM6 method[12]. In Chapter 7 was proved that it is the less demanding method that can reproduce the properties of B$_X$ dyes. Chapter 6 also shows that the TD/PM6 method can be used to predict the electron properties of the TiO$_2$ clusters.

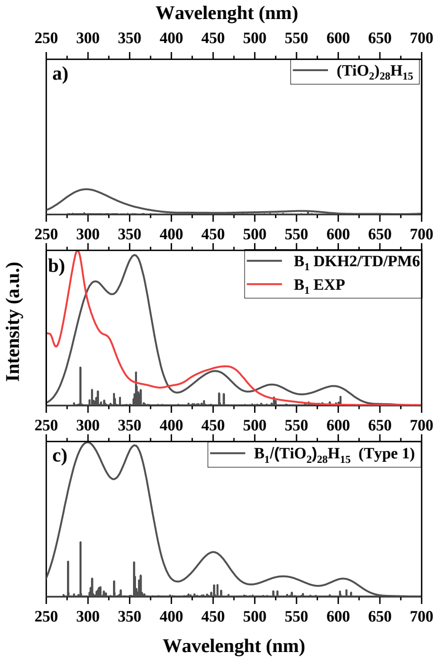

Figure 8.2. The UV-vis absorption spectra calculated by TD/PM6 method for a) $(TiO_2)_{28}H_{15}$ cluster, b) for B_1 dye in a vacuum, and c) for $B_1/(TiO_2)_{28}H_{15}$ hybrid possessing Type 1 connection

The UV-vis absorption spectra of hybrids based on B_X dyes and $(TiO_2)_{28}H_{15}$ were calculated in Gaussian 16 program package[13,14] applying TD/PM6 method. The SCF convergence criterion was equal to 10^{-12} Hartree. The calculations were performed at a restricted Hartree-Fock (RHF) level[10]. One can see that the $(TiO_2)_{28}H_{15}$ cluster does not absorb visible light (see Fig. 8.2a). The λ_{max} of the absorption is equal to 300 nm. It is in agreement with the experimental data referring to E_g = 3.84 eV obtained for (101) nanosheet of the TiO_2[3]. One can see that the oscillator strengths of observed excitations are not significant. The UV-vis absorption spectra were also calculated by TD/PM6 method for the B_1 molecule with geometry optimized by the DKH2 method. In this case, the 160 excited states were calculated. One can see that the DKH2/TD/PM6 method can reproduce the first MLCT peak observed for B_1 dye, also, the strong ILCT peak located near 291 nm is seen (see Fig. 8.2b). The small peaks occurring near 520 nm and 600 nm possessing small oscillator strength are the major error of the TD/PM6 method. However, they are insignificant and one can conclude that the proposed semiempirical method can be used to calculate the electron properties of the proposed hybrids.

The UV-vis spectrum calculated for the $B_1/(TiO_2)_{28}H_{15}$ hybrid is very similar to the spectrum of B_1 (see Fig. 8.2c). One can conclude that the low energy laying absorption peaks are created by the B_1 molecule. In this case, the TiO_2 cluster does not affect the UV-vis spectra of the constructed hybrid. The first MLCT broadband consists of two peaks at 455 nm (oscillator strength f=0.149) and 451 nm (oscillator strength f=0.148). These peaks correspond to the MLCT band observed for the B_1 molecule. They are associated with the presence of two $Ru(bpy)_3$ donor groups. The contributions of the molecular orbitals to the two mentioned transitions are presented in Fig. 8.3. Two electron transitions have a contribution to each transition. The ground state of both transitions associated with a wavelength of 455 nm is located at $Ru(bpy)_3$ and their excited states are located at the spacer of the dye (see Fig. 8.3a). The excited state of the second transition is more extended to the semiconducting cluster. The calculated charge transfer from the dye to the cluster associated with excitation at 455 nm shows a 2.9 % of electron transfer to the cluster. The peak at 451 nm is created by a similar transition coming from the second $Ru(bpy)_3$ (see Fig. 8.3b). In this case, charge transfer between dye and cluster is very low possessing a value of 0.4 %.

In Fig. 8.4 are presented UV-vis absorption spectra calculated by TD/PM6 for $B_2/(TiO_2)_{28}H_{15}$ and $B_3/(TiO_2)_{28}H_{15}$ possessing bond of Type 1 and their components. In this case, the B_2 and B_3 molecules optimized by the HF method were used. In Chapter 7 was proved that the TD/PM6 method better reproduces UV-vis absorption spectra for these geometries than for the geometries obtained by the DKH2 method. Analyzing the obtained spectra one can conclude that they have the same tendency as was observed in the case $B_1/(TiO_2)_{28}H_{15}$ hybrid (see Fig. 8.2). In the visible region of the spectrum, the main absorption peaks are created by dyes. The TiO_2 cluster affects the nature of peaks located in the region of the first MLCT. Contrary to the $B_1/(TiO_2)_{28}H_{15}$ hybrid, the $B_2/(TiO_{2,})_{28}H_{15}$ possessing connection of Type 1 exhibits a significant single transition in the MLCT region located at 454 nm (oscillator strength f=0.154). The $B_3/(TiO_2)_{28}$H15 connected by Type 1 posses transition at 462 nm (f=0.132) belonging to MLCT transfer and peak at 455 nm belonging to the inner MLCT.

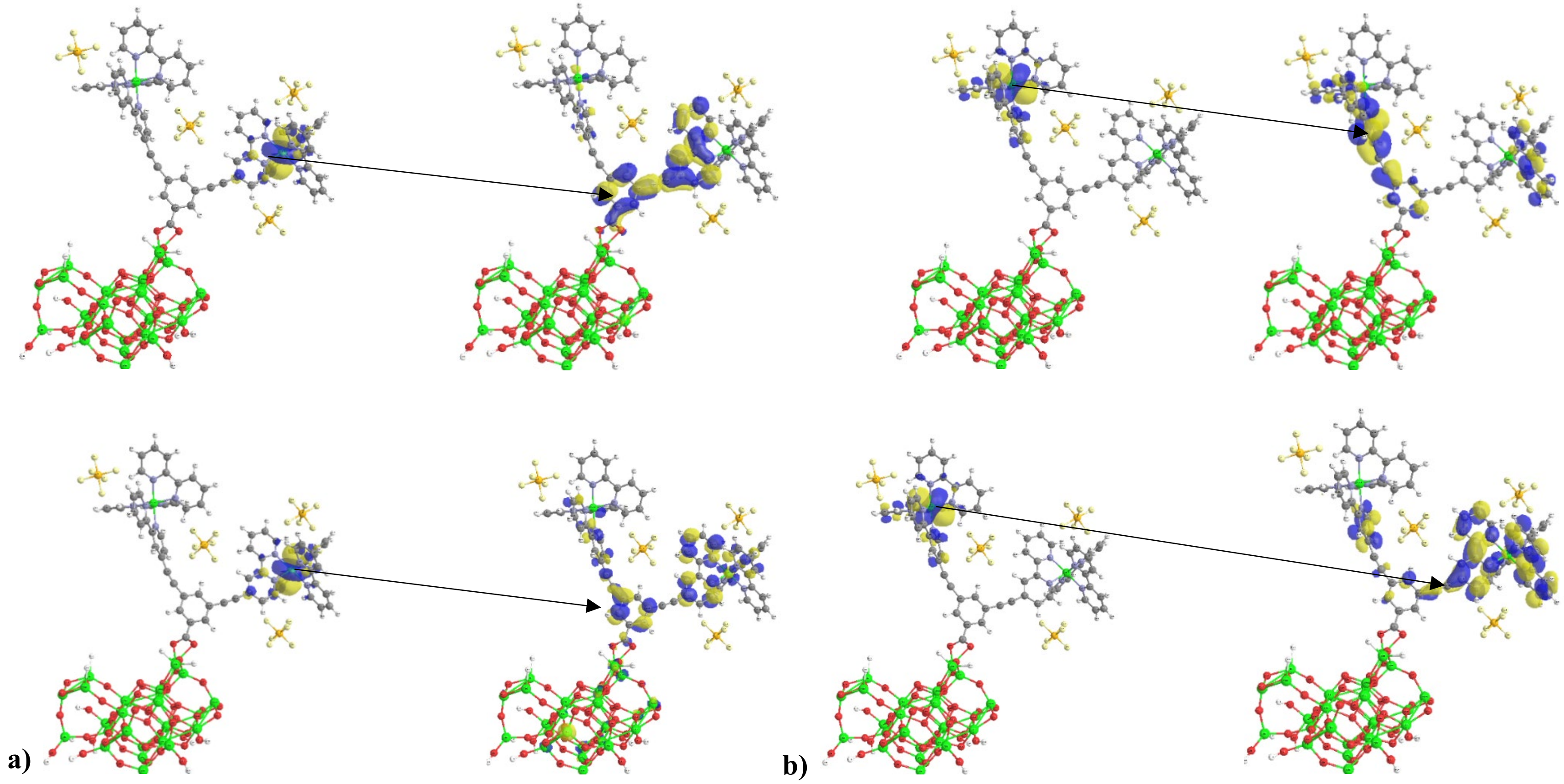

λ=455 nm (*f*=0.149)

λ=451 nm (*f*=0.148)

Figure 8.3. Molecular orbitals contributing to the ground and excited states of excitation at 455 nm and 451 nm calculated by using TD/PM6 method for the $B_1/(TiO_2)_{28}H_{15}$ structure possessing Type 1 bonds between dye and semiconducting nanostructure

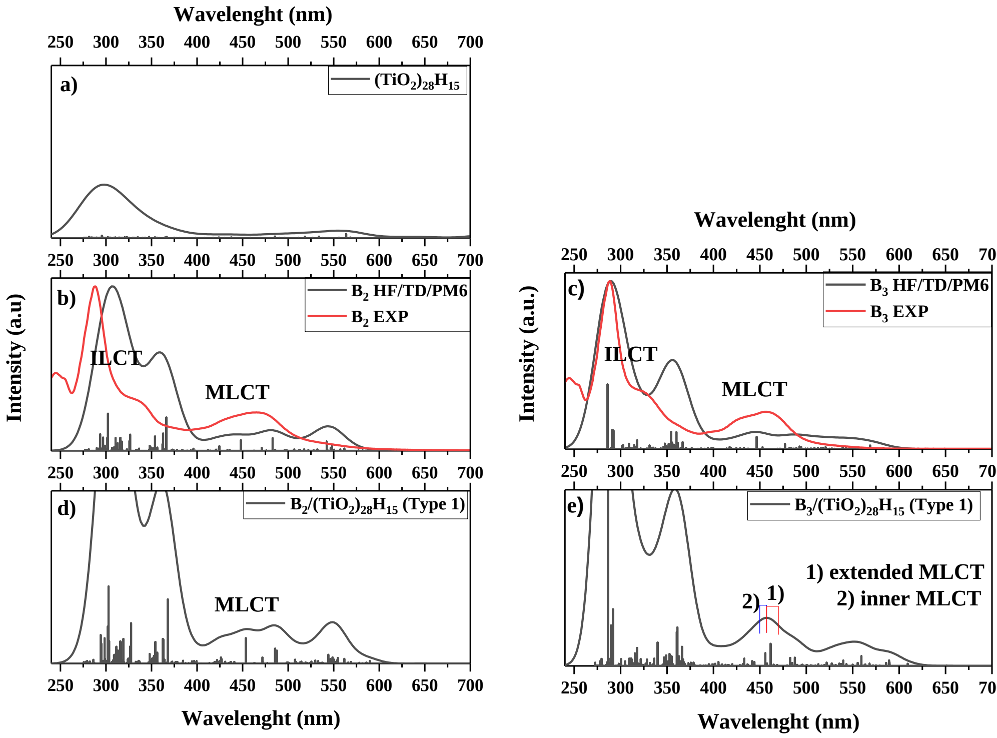

Figure 8.4. The UV-vis absorption spectra calculated by TD/PM6 method for a) $(TiO_2)_{28}H_{15}$ cluster, b) for B_2 dye in a vacuum, c) for B_3 dye in a vacuum, d) for $B_2/(TiO_2)_{28}H_{15}$ hybrid, and e) for $B_3/(TiO_2)_{28}H_{15}$ hybrid possessing bond of Type 1

Fig. 8.5 presents molecular orbitals contributing to the ground and excited states of excitation at 454 nm for $B_2/(TiO_2)_{28}H_{15}$ and at 462 nm for $B_3/(TiO_2)_{28}H_{15}$ calculated by using TD/PM6 method. Between the dye and TiO_2 cluster the Typ 1 bond is created. The excitation at 454 nm calculated for $B_2/(TiO_2)_{28}H_{15}$ is created by two transitions (see Fig. 8.5a). In both situations, electrons transfer from the Ru atom to the external ligands is observed. The major part of orbitals creating an excited state of transition at 454 nm is located on the dye near the anchoring group. In this case, the 2.63 % transfer of electrons from dye to TiO_2 cluster is noticed. The orbitals contributing to the ground and excited states of excitation at 462 nm for $B_3/(TiO_2)_{28}H_{15}$ are presented in Fig. 8.5b. Also here, in both contributing electron transitions, electrons go from the Ru atom to the external ligands. In this case, the stronger electron injection into the TiO_2 cluster equal to 13.70 % is observed. Based on data presented in Fig. 8.3 and 8.5 one may conclude that the best photoexcited charge transfer between B_X dyes and TiO_2 cluster bonded by connection of Typ 1 occurs for $B_3/(TiO_2)_{28}H_{15}$ hybrid (13.70 %). For the $B_1/(TiO_2)_{28}H_{15}$ and $B_2/(TiO_2)_{28}H_{15}$, these values are much lower possessing values of 2.91 % and 2.63 %, respectively.

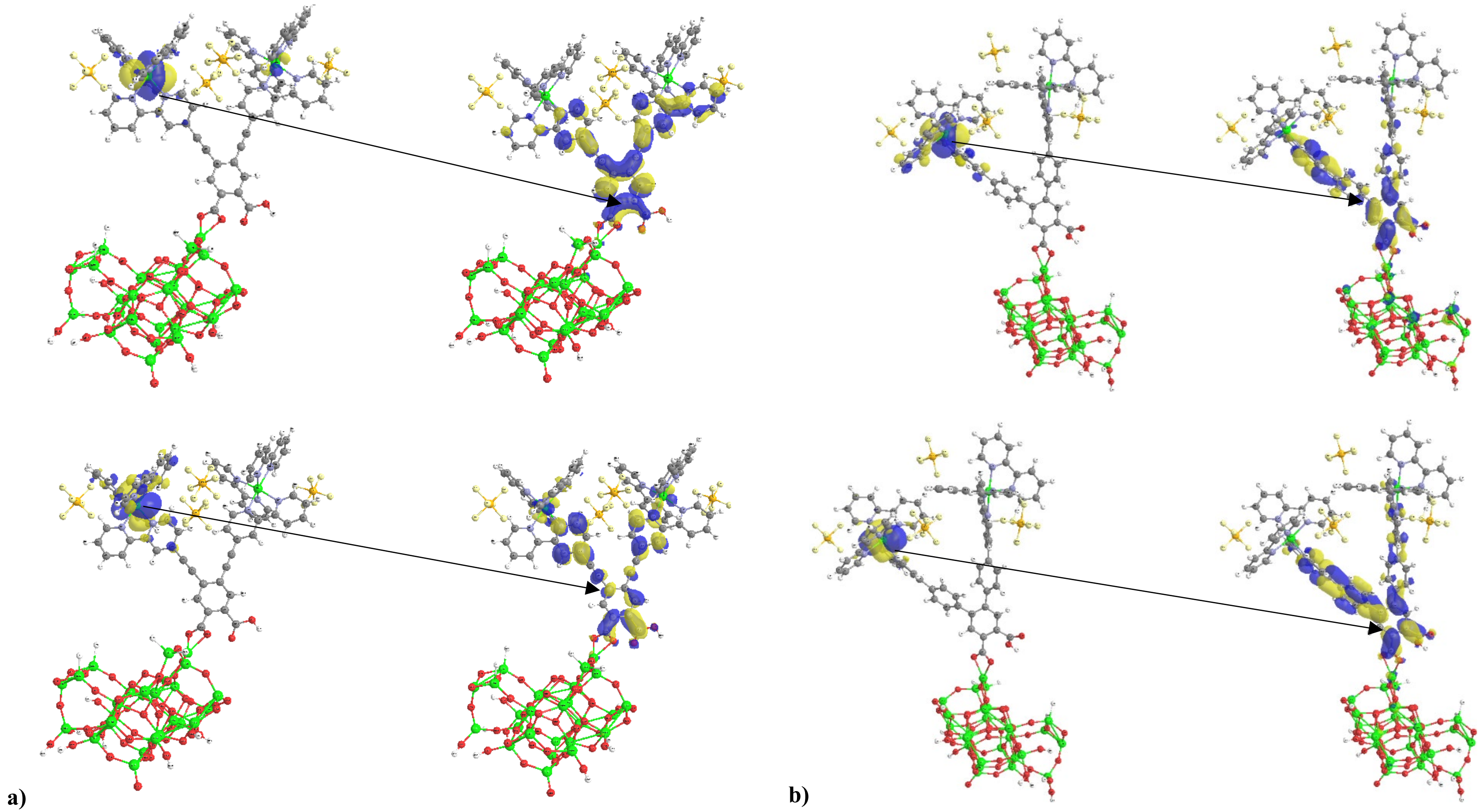

λ=454 nm (*f*=0.154) **λ=462 nm (*f*=0.132)**

Figure 8.5. Molecular orbitals contributing to the ground and excited states of excitation at 454 nm for $B_2/(TiO_2)_{28}H_{15}$ (a) and at 462 nm for $B_3/(TiO_2)_{28}H_{15}$ (b) calculated by using the TD/PM6 method. Between the dye and TiO$_2$ cluster the Type 1 bond is created

The UV-vis absorption spectra calculated for B_2 and B_3-based hybrids with the connection between dyes and semiconductor of Type 2 are very similar to those possessing the bonds of Type 1, discussed above. Fig. 8.6 presents molecular orbitals contributing to the ground and excited states of excitation at 456 nm for $B_2/(TiO_2)_{28}H_{15}$ and at 463 nm for $B_3/(TiO_2)_{28}H_{15}$ calculated by using the TD/PM6 method. Between the dye and TiO_2 cluster the Typ 2 bond is created. In both cases, the transfer of electrons from the Ru to the external ligand is observed. In the case of the $B_2/(TiO_2)_{28}H_{15}$ the privileged transfer through "meta" bounded B_2 to TiO_2 is observed (see Fig. 8.6a, bottom panel). The electron transfer occurring between B_2 and TiO_2 cluster is equal to 16.75 %. This effect is not seen for the $B_3/(TiO_2)_{28}H_{15}$ structure (see Fig. 8.6b). In this case, the photoexcited electrons are accumulated on phenyl spacer moiety allowing electron transfer from B_3 to TiO_2 cluster equal to 16.15 %. Analyzing these data one can conclude that the double anchoring group creating Type 2 bonds in $B_x/(TiO_2)_{28}H_{15}$ hybrids favor electron transfer from dye to semiconductor.

In Fig. 8.7 the molecular orbitals contributing to the ground and excited states of excitation at 468 nm for $B_2/(TiO_2)_{28}H_{15}$ and at 467 nm for $B_3/(TiO_2)_{28}H_{15}$ calculated by using the TD/PM6 method are presented. Between the dye and TiO_2 cluster the Typ 3 bonds are created. Previously this kind of bond was called "strong" which is to be understood that the two Ti-O bonds in both legs are short, with the same length, and they are symmetrical. The bonds of Type 3 show some advantages giving more closely localized dyes to semiconducting clusters than those observed for bonds of Type 1 and Type 2. The bond of Type 3 has a positive effect on charge transfer from B_2 to the cluster giving electron injection equal to 22.43% (see Fig. 8.7a) for the excitation at 468 nm (f=0.112). However, $B_3/(TiO_2)_{28}H_{15}$ shows a significant decrease in charge transfer to 6.01% for the peak at 467 nm (f=0.083). Two electron transfers contribute to mentioned excitation (see Fig. 8.7b). In both cases, the localization of photoexcited electrons is observed at the phenyl group of the spacer. It seems that the phenyl present in the spacer of the B_3 molecule works like a blocker of phototransferred electrons from dye to TiO_2.

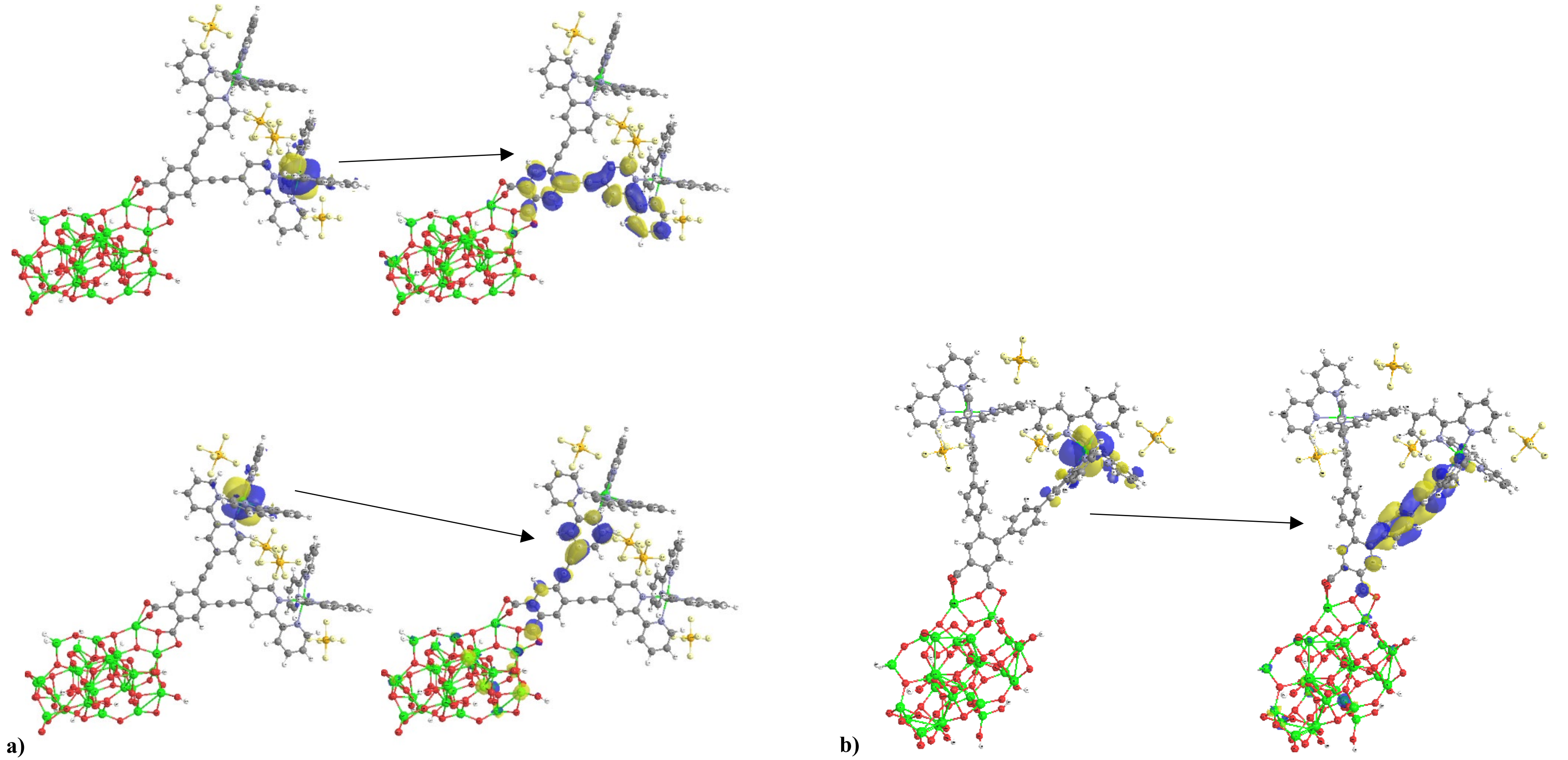

λ=456 nm (*f*= 0.155) **λ=463 nm (*f*=0.167)**

Figure 8.6. Molecular orbitals contributing to the ground and excited states of excitation at 456 nm for $B_2/(TiO_2)_{28}H_{15}$ (a) and at 463 nm for $B_3/(TiO_2)_{28}H_{15}$ (b) calculated by using the TD/PM6 method. Between the dye and TiO_2 cluster the Type 2 bond is created

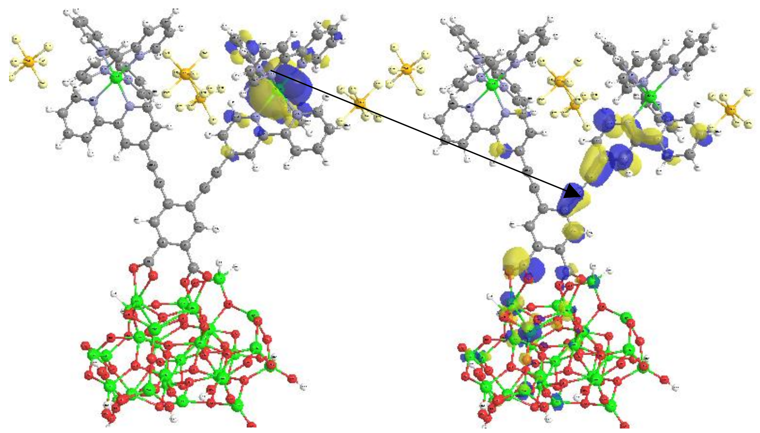

a) **λ=468 nm (*f*=0.112)**

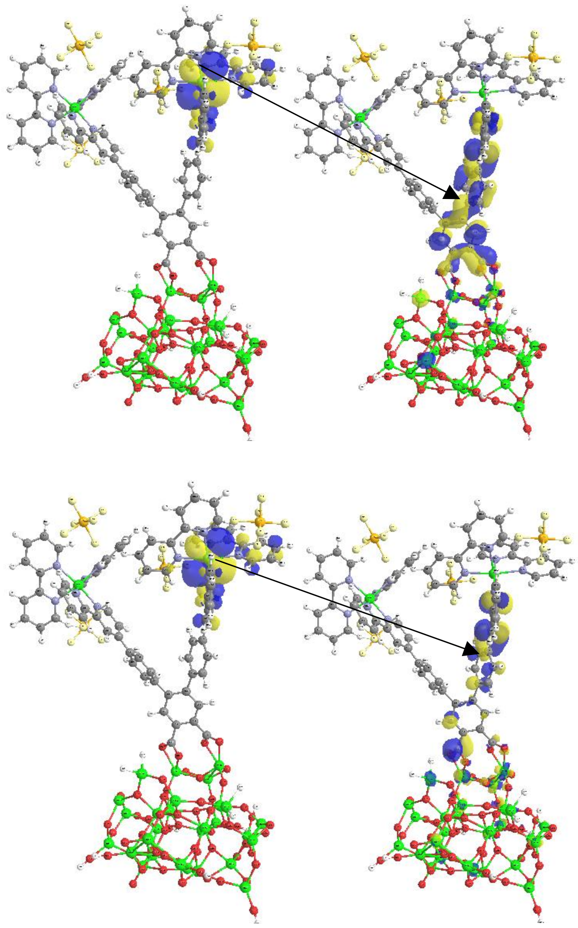

b) **λ=467 nm (f=0.083)**

Figure 8.7. Molecular orbitals contributing to the ground and excited states of excitation at 468 nm for $B_2/(TiO_2)_{28}H_{15}$ (a) and at 467 nm for $B_3/(TiO_2)_{28}H_{15}$ (b) calculated by using the TD/PM6 method. Between the dye and TiO_2 cluster the Typ 3 bond is created

Analyzing the data presented above, one can conclude that in the case of Type 1 bonds between B_X and TiO_2 cluster the most efficient charge transfer between dye and semiconductor occurs in the case of $B_3/(TiO_2)_{28}H_{15}$. The charge transfer in this case is equal to 13.70 %. For the B_2 and B_1-based hybrids, the discussed charge transfer is equal to 2.63 % and 2.90 % respectively. In the case of a double connection of Type 2 and Type 3 (two –COOH anchoring groups are active), the photoexcited charge transfer between dye and semiconductor is more efficient. In the case of Type 2 bond the occurring electron transfer has the same efficiency for the $B_2/(TiO_2)_{28}H_{15}$ and $B_3/(TiO_2)_{28}H_{15}$ little bit higher than 16 %. The strong connection (Type 3) between dye and TiO_2 increases the charge transfer from B_2 to the semiconductor and decreases electron transfer from B_3 giving values equal to 22.43 % and 6.01 %, respectively. The tendency of electron accumulation on phenyl rings located in the spacer creates a problem for charge injection in $B_3/(TiO_2)_{28}H_{15}$ system. The Type 3 bond creates a lot of inner MLCT peaks decreasing the oscillator strength of the main MLCT transfer (see Fig. 8.8). The spectra obtained for $B_2/(TiO_2)_{28}H_{15}$ and $B_3/(TiO_2)_{28}H_{15}$ possessing Type 1 and Type 2 bonds have the same shape. The bonds of Type 3 change the location of absorption peaks as is seen for $B_3/(TiO_2)_{28}H_{15}$ system. In this case, the splitting of the MLCT peaks is observed. The most significant electron transfer occurring for the $B_2/(TiO_2)_{28}H_{15}$ system possessing a Type 3 bond can be explained by the privileged charge transfer between dye and semiconductor by the para-position of the anchoring group relative to the bipyridine moiety. This situation will be more deeply discussed in Chapter 8.2. It allows us to conclude that the $B_2/(TiO_2)_{28}H_{15}$ structure with a Type 3 bond is a good candidate for PV applications. However, from Table 8.1 one can conclude that the Type 1 bond between studied components is mostly privileged. In consequence, the $B_3/(TiO_2)_{28}H_{15}$ system with Type 1 bond will be also appropriate to be used in the DSSC application.

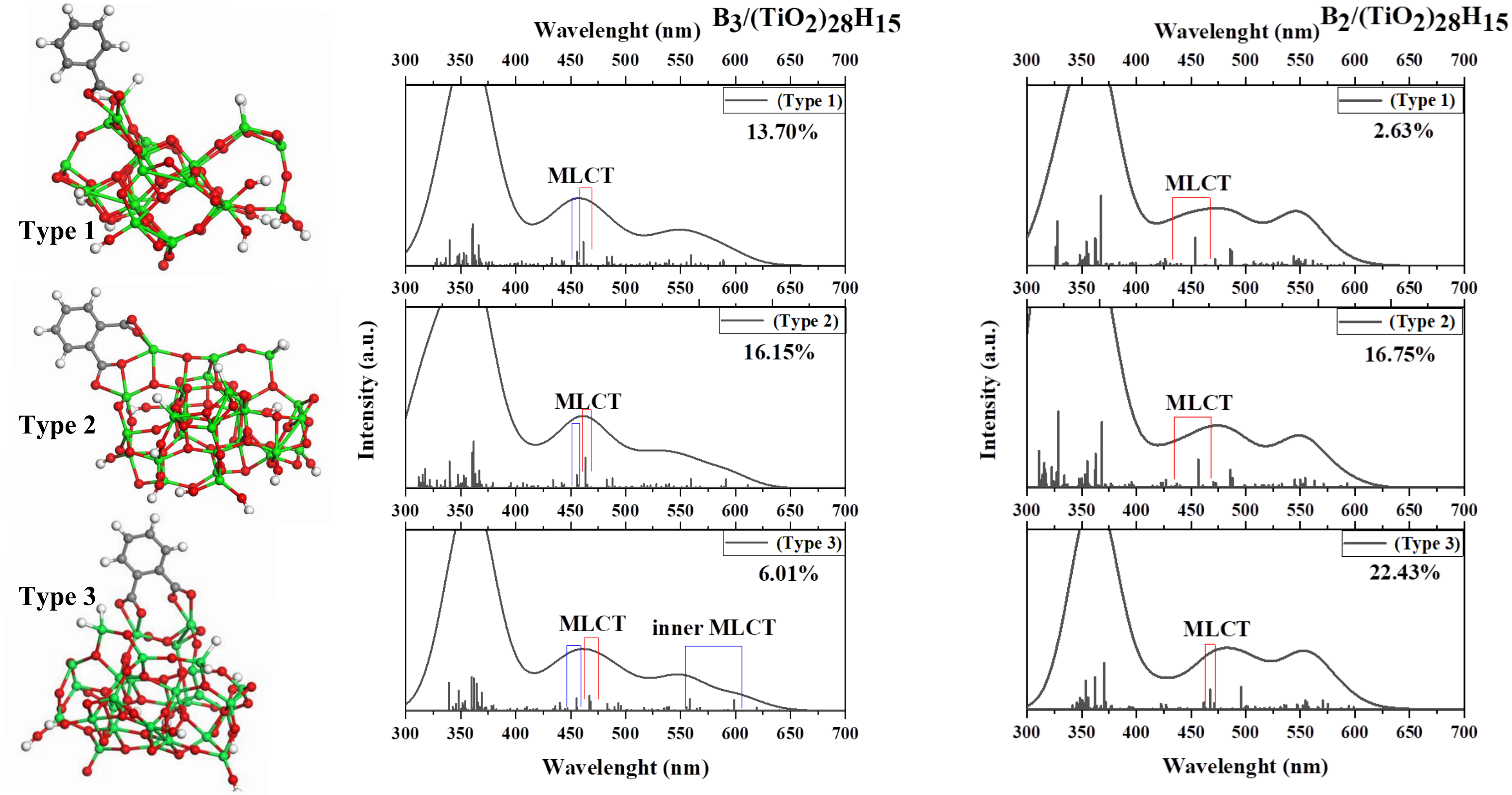

Figure 8.8. Collection of the UV-vis absorption spectra calculated for $B_2/(TiO_2)_{28}H_{13}$ and $B_3/(TiO_2)_{28}H_{15}$ possessing Type 1, Type 2, and Type 3 bonds. The main important excitations with MLCT nature and electron transfer occurring at mentioned photoexcitations are marked.

The measurements of photovoltaic properties of the B_X and TiO_2-based DSSC prototypers were performed at Adam Mickiewicz University in Poznań by the research group of Professor Zalas. The results are assembled in a paper titled "Anchoring ligands modifications of binuclear ruthenium sensitizers and their influence on an electron transport mechanism in dye-sensitized solar cells" authored by A. Bartkowiak, O. Korolevych, B. Gierczyk, D. Pelczarski, A. Bossi, M. Klein, Ł. Popenda, W. Stampor, M. Makowska-Janusik M., and Zalas. This work was sent to be published in Nature Communications. My contribution to this work was mainly the realization of the quantum chemical calculations described above.

Experiments show that the dye-loading increases significantly for B_2 and B_3 dyes possessing two -COOH anchoring groups when compared with B_1. It is probably caused by the more efficient protonation of the semiconductor surface. The photocurrent density also increases significantly with the addition of a second anchoring group into the dye molecule (B_2 and B_3). However, experimentally was proved that the photocurrent density increases with the substitution of ethynyl moieties into phenyl ones (in B_3 dye). At the same time, it is worth noting that the increase in photocurrent density of B_3-based cells, when compared with B_2, may also be associated with the increase of the molar extinction coefficient at MLCT band growth. The additional -COOH anchor also modifies the LUMO level of the dyes. The decrease in LUMO level disturbs the electron injection process and may negatively influence the photocurrent density. An additional anchor downshifts the LUMO level of B_2 dye compared to B_1. At the same time, the screening effect of phenyl linkers causes a significant increase in the LUMO level of B_3 dye, reaching the highest value in the B_X series. This considerable change in the LUMO level also improves the photocurrent density value of B_3-based DSSC. The experimentally obtained data are in agreement with the results presented in Chapter 7.

Taking into account the experimental and computationally obtained data one can conclude that probably Type 1 bond occurs between B_3 and TiO_2 giving the highest photocurrent density for $B_3/(TiO_2)_{28}H_{15}$ system.

8.2. Structural and electron properties of mono-ruthenium/TiO_2 hybrids

As it was described in Chapter 7 the interesting molecules for DSSC application are the RuLp, RuLm, and RuLo dyes. In this Chapter, the simulations of the electron and optical properties of the hybrids based on the mentioned dyes and TiO_2 cluster will be discussed. The obtained results will be compared with data coming from experiments performed by the research group of Professor Zalas from UAM University in Poznan. Performed research aimed to investigate the influence of the anchoring group on the electron and optical properties of hybrid material for photovoltaic applications.

According to the fact that the RuLp, RuLo, and RuLm molecules are not as important in size as the molecules B_X, their electron properties can be calculated directly for the entire structure without any approximations. In this case, was decided to take into consideration the TiO_2 cluster in configuration $(TiO_2)_{49}$. The studied cluster was created from a pristine TiO_2 anatase structure by its size limitation without any structural reconstruction. The structural optimization was performed only for the surface atoms. The core atoms were frozen to keep anatase geometry. The evaluated cluster was significantly bigger than the one discussed in Chapter 8.1 why this kind of freeze operation was possible. Calculations were performed at the restricted Hartree-Fock (RHF) level using the PM6 method. The SCF converge criterion was chosen as 10^{-8} Hartree. The gradient convergence tolerance was equal to 10^{-6} Hartree/Bohr using quadratic approximation (QA) updating the hessian matrix.

The initial geometries of hybrid systems were built with RuLp, RuLm, and RuLo molecules anchored to the $(TiO_2)_{49}$ cluster. The dyes were anchored to the cluster by a bond created between the -COOH anchoring group and the Ti atom, removing the H atom. The geometries of constructed hybrid structures were optimized by parameterized PM6 method with SCF converge criterion equal to 10^{-8} Hartree. The gradient convergence tolerance was equal to 10^{-6} Hartree/Bohr. The structural minimization procedure was limited to a dye molecule bound to the Ti atom and its neighbor atoms. In this case, the major part of the cluster was kept frozen. The PM6 method was also used to evaluate the electron and optical properties of the hybrid structures with optimized geometries. The adsorption energy of the RuLp, RuLm, and RuLo molecules at the surface of TiO_2 was calculated to be equal to 201 kcal/mol, 180 kcal/mol, and 175 kcal/mol, respectively. The highest value of adsorption energy was obtained for the RuLp molecules and it shows the stability of the hybrid system. The lowest adsorption energy of RuLo at the surface of the TiO_2 has experimental confirmation. Experimentally was proved that only a small amount of initially adsorbed RuLo molecules remain on the surface after washing of samples. The main part of RuLo molecules could be simply washed off from TiO_2 with acetonitrile. One can conclude that in the case of RuLo at TiO_2 surface the physisorption prevails under chemisorption.

The frontier orbitals of the constructed RuLp/$(TiO_2)_{49}$, RuLm/$(TiO_2)_{49}$, and RuLo/$(TiO_2)_{49}$ hybrids were calculated by the PM6 method in vacuum (see Fig. 8.9). One can see that for all investigated hybrids the LOMO orbitals are located at the semiconducting cluster. It means that photoexcited electron transfer is privileged for photovoltaics. It is a better situation than was noticed for the B_x-based hybrids described previously. According to the performed calculation, the LUMO orbitals of RuLm/TiO_2 and RuLo/TiO_2 are localized at the opposite side of semiconductor clusters concerning anchored molecules. Only in the RuLp/$(TiO_2)_{49}$ hybrid, the LUMO is located at the surface of TiO_2 nanoparticles near the anchoring group of the dye. This arrangement of the LUMO orbital contributes to increasing the ability of the charge flow between the dye and the nanostructure. The tilted orientation of ortho-derivatives brings the central ruthenium metal close to the TiO_2 surface which facilitates the charges recombination. It has been reported that ruthenium dyes with a small angle between the main axis of the sensitizing molecule and the TiO_2 surface exhibit faster charge recombination reducing the overall photoconversion efficiency[15,16]. In general, all of the para-carboxyphenyl derivatives outperform their meta-carboxyphenyl counterparts in achieving higher photoconversion efficiency and better DSSCs performance.

Analyzing the charge transfer process occurring at the dye/semiconductor surface one can propose the scenario presented in Fig. 8.10. Upon irradiation, dyes absorb light and create an electron/hole par – exciton (1) (see Fig. 810a). The LUMO energy level of dye is higher than the conductional band of TiO_2 and this creates the possibility of exciton diffusion to the interface. The exciton is formed at the dye/semiconductor interface (2). In the second stage, the electron must be injected into the TiO_2 before electron-hole recombination (3) (see Fig. 8.10b).

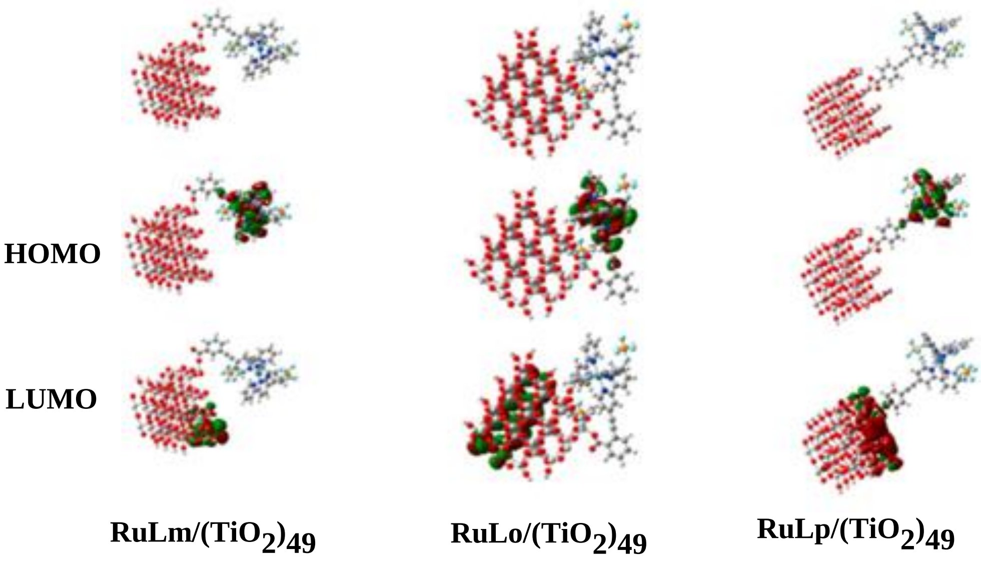
HOMO
LUMO
RuLm/(TiO2)49
RuLo/(TiO2)49
RuLp/(TiO2)49

Figure 8.9. Location of frontiers orbitals calculated by parametrized PM6 semiempirical method for RuLp/$(TiO_2)_{49}$, RuLm/$(TiO_2)_{49}$, and RuLo/$(TiO_2)_{49}$ hybrids

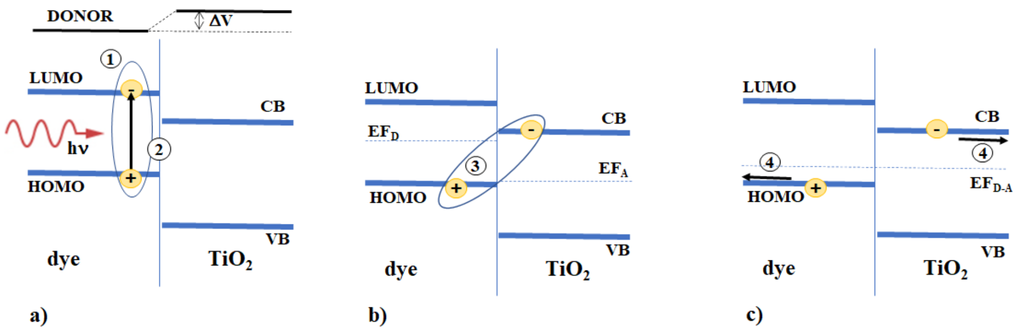
DONOR
ΔV
①
LUMO
CB
hv
②
HOMO
VB
dye
TiO2
a)
LUMO
EFD
CB
③
EFA
HOMO
VB
dye
TiO2
b)
LUMO
CB
④
④
HOMO
EFD-A
VB
dye
TiO2
c)

Figure 8.10. Charge generation in dye/TiO_2 interface in DSSC[20]

Therefore, the exciton binding energy must be small. The exciton Coulomb attractive energy was evaluated for investigated RuLp/TiO_2, RuLm/TiO_2, and RuLo/TiO_2 hybrids to be equal to 2.36 eV, 2.86 eV, and 2.61 eV, respectively. One can see that the easiest exciton dissociation can be achieved in RuLp/TiO_2 hybrid system. Step (3) consists of a transient bounded state formed by the electron transfer from the dye to the CB of TiO_2 while the hole remains in the dye. In this state, also called charge-transfer (CT) exciton[17,18], the free charges (free electron in CB of the TiO_2 and free hole in the dye) interact via Coulomb interaction. In this case, the binding energy of an exciton may be so large to prevent its dissociation at room temperature without a supply of energy. However, vibrational energy may ensure the dissociation of CT excitons leading the free electrons and holes to flow in opposite directions due to the difference in the work functions of both: dye and TiO$_2$ nanostructures constituents (4) (Fig. 8.10c).

Experimentally was shown that the RuLp and RuLm dyes adsorbed on the TiO$_2$ anode exhibit better photovoltaic properties than the RuLo [20]. Therefore, the electron properties of the RuLp and RuLm dyes anchored at the surface of the TiO$_2$ cluster by the bond of Type 1 implemented in Chapter 8.1 for B$_X$ molecules were studied. To build the RuLp/(TiO$_2$)$_{28}$H$_{15}$ and RuLp/(TiO$_2$)$_{28}$H$_{15}$ hybrids the RuLp and RuLm structures optimized by the HF method were used. The TiO$_2$ cluster was taken the same as it was described in Chapter 8.1.

Full atom optimization of the hybrids was performed by the GAMESS program package, applying C1 symmetry for the system. Minimum energy searching was performed in a vacuum using the HF formalism applying 6-31G basis sets for all atoms. The minimum of the potential energy surface was calculated at a restricted Hartree-Fock (RHF) level[19]. Optimal geometries of the hybrids were found by applying the quadratic approximation (QA) optimization algorithm based on the augmented Hessian technique. The gradient convergence tolerance was equal to 10^{-5} Hartree/Bohr. At the end of the geometry optimization, the Hessian evaluation was performed to exclude structures giving negative modes.

The electron and optical properties of the hybrids were calculated by TD/PM6 method using the Gaussian package. The obtained RuLp/(TiO$_2$)$_{28}$H$_{15}$ and RuLp/(TiO$_2$)$_{28}$H$_{15}$ hybrids exhibit a broad peak associated with the MLCT transfer of electrons characteristic for ruthenium complexes (see Fig. 8.11b and Fig. 8.11c). The mentioned peaks are noticed at more-less 450 nm for both systems. In this area, the TiO$_2$ cluster does not absorb the light at all (see Fig. 8.11a). It means that the dyes are responsible for the absorption of visible light, as was observed for B$_x$-based hybrids. Additionally, one can say that the semiconductor does not affect the optical properties of ruthenium-based dyes significantly.

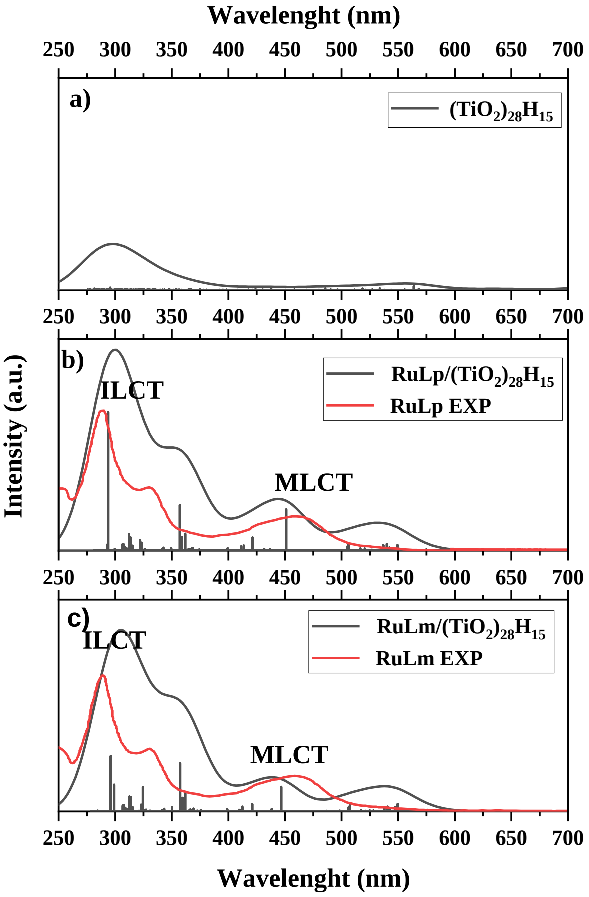

Figure 8.11. The UV-vis absorption spectra calculated by TD/PM6 method a) for the $(TiO_2)_{28}H_{15}$ cluster, b) for the RuLp/$(TiO_2)_{28}H_{15}$ hybrid, and c) for RuLm/$(TiO_2)_{28}H_{15}$ hybrid. The bond of Type 1 between dye and TiO_2 is created

The peaks located at 451 nm for RuLp/$(TiO_2)_{28}H_{15}$ and at 447 nm for RuLm/$(TiO_2)_{28}H_{15}$ were chosen for the more deep analysis. Was found that two electron transfers contribute to each excitation (see Fig. 8.12). In the case of RuLp/$(TiO_2)_{28}H_{15}$ hybrid, the electron transfer from the dye to TiO_2 occurring during the discussed photoexcitation is equal to 13.24 % (see (Fig. 8.12a). The calculated photoinduced electron transfer is very similar to the one calculated for the B_3/$(TiO_2)_{28}H_{15}$ hybrid possessing bond of Type 1. Meanwhile, the RuLm/$(TiO_2)_{28}H_{15}$ hybrid gives a charge transfer near 2.90 %. Concluding one can say that the photoinduced charge transfer occurring in the RuLp/$(TiO_2)_{28}H_{15}$ hybrid will enhance the photovoltaic processes compared with RuLm/$(TiO_2)_{28}H_{15}$ hybrid. It was also seen experimentally, that the RuLp molecule is more favorable for photovoltaic applications compared with RuLo and RuLp dyes[21]. One can conclude that the para-position of the anchoring group in ruthenium complexes favors the photoinduced charge transfer from the dye to semiconducting TiO_2.

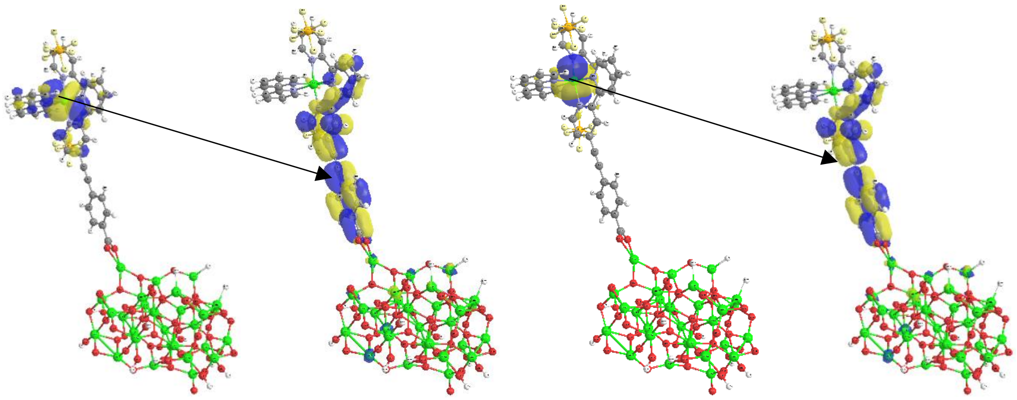

a)

451 nm (*f*=0.291)

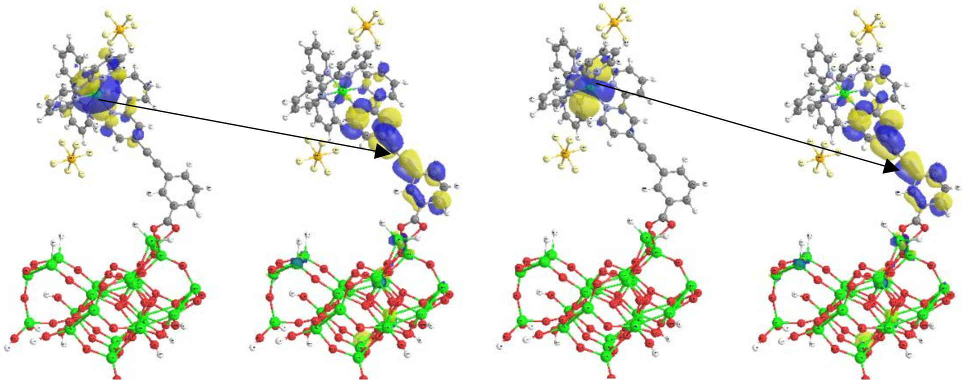

b)

447 nm (*f*=0.174)

Figure 8.12. Molecular orbitals contributing to the ground and excited states of excitation at 451 nm for RuLp/(TiO$_2$)$_{28}$H$_{15}$ (a) and at 447 nm for RuLm/(TiO$_2$)$_{28}$H$_{15}$ (b) calculated by using the TD/PM6 method. Between the dye and TiO$_2$ cluster the Typ 1 bond is created

The results presented in Chapter 8.2 are partially reported in the paper titled "Impact of dyes isomerization effect on the charge transfer phenomenon occurring on the dye/nanosemiconductor interface." and published in *Solar Energy Materials and Solar Cells*[20]. This work is authored by O. Korolevych, M. Zalas, W. Stampor, A. Kassiba, and M. Makowska-Janusik. The experimental part of this work was performed at Adam Mickiewicz University, Poznań. My contribution to this work was the realization of all quantum chemical calculations.

8.3. Conclusions

In the presented Chapter the structural and optical properties of the selected dye/TiO$_2$ hybrids were investigated computationally and the obtained results were compared with experimental data. Studies were focused on B_x, RuLm, and RuLo molecules attached to the $(TiO_2)_{28}H_{15}$ clusters in the context of their use in DSSC applications. In this case, particular attention has been paid to specifying the connection type between dye and TiO_2. In consequence, the UV-vis absorption spectra, location of frontier orbitals, and charge transfer occurring between dyes and TiO_2 were investigated.

Searching for the best approach allowing to compute the electron and optical parameters of hybrid materials based on studied dyes and TiO_2 the method to construct a dye/TiO_2 hybrid structure was developed. The developed approach of modeling the structure of hybrids consists of the structural evaluation of the cluster with the anchor functional group of the dye, and then the substitution of the entire dye with the anchor-separator group. Such a modeling approach allows the maintenance of the correct geometry of the ruthenium-based dyes, which has a significant impact on the electron properties of the entire system. The proposed approximation has not been used in works known to me so far. As a consequence, it gave good computational results for hybrid structures, taking into consideration their electron and optical properties.

Three possible types of connections between dyes and semiconducting nanostructures were found. The single connection, through the –COOH anchor, that can occur between RuLp, RuLm, and B_x molecules is named Type 1, and the double connection where one –COOH group is more active and the other is less active is named Type 2, and connection of Type 3, where both -COOH groups are strongly active in the bond creation was found. The two last types of bonds can be found for the B_2 and B_3 dyes anchored on the surface of TiO_2. The bond of Type 1 creates the most stable B_x-based hybrid structures, compared with Type 2 and Type 3.

Calculations of the electron and optical properties of the hybrid materials were carried out. The mechanism of charge transfer between dye and semiconductor in the process of photoexcitation was explained. Simulations clearly show the preference of para-position of -COOH group to the donor part as it is noticed for RuLp connected by the bond of Type 1 as well as for B_2 and B_3 dyes connected to the semiconductor by the bond of Type 2.

In the case of the bond of Type 1, the best properties were achieved for B_3. The charge transfer occurring in this case between B_3 and TiO_2 in the act of photoexcitation is equal to 13.70 %. A similar value of the electron transfer was obtained for the RuLp/$(TiO_2)_{28}H_{15}$ hybrid. In the case of the $B_2/(TiO_2)_{28}H_{15}$ with a bond of Type 3 the observed charge transfer is equal to 22.43 %, but the probability of occurrence of the bond of Type 2 is less than the bond of Type 1.

Experiment measurements performed at Adam Mickiewicz University in Poznan by the research group of Professor Zalas show that the RuLp and B_3 dyes are the best for the DSSC applications. Based on performed computer simulation one can suggest that the bond of Type 1 gives the most stable hybrid systems. Comparing the computationally obtained data and the results of computer simulations one can conclude that investigated B_x molecules are anchored on the surface of the TiO_2 nanostructure by bond of Type 1. Both hybrids, the RuLp/$(TiO_2)_{28}H_{15}$ and $B_3/(TiO_2)_{28}H_{15}$, can be used in photovoltaic applications. However, better efficiency of light-to-electron energy conversion is observed for the RuLp-based structures. The obtained computational results are close to the experimental data. Additionally, based on the performed calculations the mechanism of the charge transfer from the dyes to the TiO_2 was explained. The conclusion is that for the ruthenium-based dyes, a two-stage charge transfer mechanism is observed.

8.4 Literature

[1] Stewart J.J.P., "Optimization of parameters for semiempirical methods V: Modification of NDDO approximations and application to 70 elements", *Journal of Molecular Modeling*, vol.13, pp.1173–1213, **(2007)**. doi:10.1007/s00894-007-0233-43

[2] Stewart J.J.P., "Optimization of parameters for semiempirical methods VI: more modifications to the NDDO approximations and re-optimization of parameters." *Journal of molecular modeling*, vol.19 no.1, pp.1-32, **(2013)**. doi:10.1007/s00894-012-1667-x

[3] Sakai, N., Ebina, Y., Takada, K., & Sasaki, T., "Electronic band structure of titania semiconductor nanosheets revealed by electrochemical and photoelectrochemical studies." *Journal of the American Chemical Society,* vol.126, no.18, pp.5851-5858, **(2004)**.

[4] De Angelis, F., Vitillaro, G., Kavan, L., Nazeeruddin, M. K., & Grätzel, M. ″Modeling ruthenium-dye-sensitized TiO2 surfaces exposing the (001) or

(101) faces: a first-principles investigation." *The Journal of Physical Chemistry C*, vol.116, no.34, pp.18124-18131, **(2012).**

[5] Li, J., Kondov, I., Wang, H., & Thoss, M. "Theoretical study of photoinduced electron-transfer processes in the dye− semiconductor system alizarin−TiO_2." *The Journal of Physical Chemistry C*, vol.114, no.43, pp.18481-18493, **(2010)**.

[6] Oprea, C. I., & Gîrțu, M. A "Structure and electronic properties of TiO_2 nanoclusters and dye–nanocluster systems appropriate to model hybrid photovoltaic or photocatalytic applications." *Nanomaterials* vol.9, no.3 pp.357**, (2019)**.

[7] Li, J., Nilsing, M., Kondov, I., Wang, H., Persson, P., & Thoss, M. "Dynamical simulation of Photoinduced electron transfer Reactions in Dye− Semiconductor systems with different Anchor groups. " *The Journal of Physical Chemistry C*, vol.112, no.32, pp.12326-12333 **(2008)**.

[8] Schmidt, M. W., Baldridge, K. K., Boatz, J. A., Elbert, S. T., & Montgomery, J. A. "General atomic and molecular electronic structure system." *Journal of Computational Chemistry,* vol.14,no.11, pp.1347–1363, **(1993)**. doi:10.1002/jcc.540141112

[9] Gordon, M. S., & Schmidt, M. W.. "Advances in electronic structure theory: GAMESS a decade later." *Theory and Applications of Computational Chemistry: the first forty years; Dykstra, C. E., Frenking, G., Kim, K. S., Scuseria, G. E.,* pp.1167–1189 **(2005)**. doi:10.1016/b978-044451719-7/50084-6.

[10] Roothaan, C. C. J. "New Developments in Molecular Orbital Theory." *Reviews of Modern Physics,* vol.23, no.2, pp.69–89, **(1951)**. doi:10.1103/revmodphys.23.69

[11] Jensen, F. "Locating transition structures by mode following: A comparison of six methods on the Ar8 Lennard-Jones potential." *The Journal of Chemical Physics*, vol.102, no.17, pp.6706–6718, **(1995)**. doi:10.1063/1.469144

[12] Runge, E., & Gross, E. K. U. "Density-Functional Theory for Time-Dependent Systems." *Physical Review Letters*, vol.52, no.12, pp.997–1000, **(1984)**. doi:10.1103/physrevlett.52.997

[13] Foresman, J. B., & Frisch, A., "Exploring Chemistry with Electronic Structure Methods, methods second edition." *U.S.A.: Gaussian, Inc.*, **(1993)**.

[14] M.J. Frisch, G.W. Trucks, H.B. Schlegel, G.E. Scuseria, M.A. Robb, J.R. Cheeseman, G. Scalmani, V. Barone, B. Mennucci, G.A. Petersson, H. Nakatsuji, M. Caricato, X. Li, H.P. Hratchian, A.F. Izmaylov, J. Bloino, G. Zheng, J.L. Sonnenberg, M. Hada, M. Ehara, K. Toyota, R. Fukuda, J. Hasegawa, M. Ishida, T. Nakajima, Y. Honda, O. Kitao, H. Nakai, T. Vreven, J.A. Montgomery, J.E. Peralta Jr., F. Ogliaro, M. Bearpark, J.J. Heyd, E. Brothers, K.N. Kudin, V.N. Staroverov, R. Kobayashi, J. Normand, K. Raghavachari, A. Rendell, J.C. Burant, S.S. Iyengar, J. Tomasi, M. Cossi, N. Rega, J.M. Millam, M. Klene, J.E. Knox, J.B. Cross, V. Bakken, C. Adamo, J. Jaramillo, R. Gomperts, R.E. Stratmann, O. Yazyev, A.J. Austin, R. Cammi, C. Pomelli, J.W. Ochterski, R.L. Martin, K. Morokuma, V.G. Zakrzewski, G.A. Voth, P. Salvador, J.J. Dannenberg, S. Dapprich, A.D. Daniels, O¨. Farkas, J. B. Foresman, J.V. Ortiz, J. Cioslowski, D.J. Fox*, Gaussian 09, Gaussian, Inc., Wallingford CT,* **(2009)**.

[15] M. Pastore, F. & De Angelis, "Computational modelling of TiO$_2$ surfaces sensitized by organic dyes with different anchoring groups: adsorption modes, electronic structure and implication for electron injection/recombination", *Physical Chemistry Chemical Physics*, vol.14, pp.920–928, **(2012)**.

[16] Clifford, J. N., Palomares, E., Nazeeruddin, M. K., Grätzel, M., & Durrant, J. R. "Molecular control of recombination dynamics in dye-sensitized nanocrystalline TiO2 films: Free energy vs distance dependence. " *Journal of the American Chemical Society*, vol.126, no.16, pp.5225-5233, **(2004)**.

[17] Narayan, M. R., & Singh, J. "Roles of binding energy and diffusion length of singlet and triplet excitons in organic heterojunction solar cells." *physica status solidi (c)* vol.9, pp.2386–2389, **(2012)**.

[18] Narayan, M. R., & Singh, J. "Study of the mechanism and rate of exciton dissociation at the donor-acceptor interface in bulk-heterojunction organic solar cells." *Journal of Applied Physics*, vol.114 pp.73510–73517, **(2013)**.

[19] Roothaan, C. C. J. "New Developments in Molecular Orbital Theory." *Reviews of Modern Physics*, vol.23, no.2, pp.69–89, **(1951)**. doi:10.1103/revmodphys.23.69

[20] Korolevych, O., Zalas, M., Stampor, W., Kassiba, A. H., & Makowska-Janusik, M. "Impact of dyes isomerization effect on the charge transfer phenomenon occurring on the dye/nanosemiconductor interface." *Solar Energy Materials and Solar Cells*, vol.219, pp.110771. **(2021)**. doi:10.1016/j.solmat.2020.110771

[21] Zalas, M., Gierczyk, B., Bossi, A., Mussini, P. R., Klein, M., Pankiewicz, R., Makowska-Janusik, M., Popenda, L., Stampor, W., The influence of anchoring group position in ruthenium dye molecule on performance of dye-sensitized solar cells, *Dyes and Pigments* vol. 150, pp.335 **(2018)**. doi.org/10.1016/j.dyepig.2017.12.029

Chapter 9

CONCLUSIONS AND PERSPECTIVES

Alternative to fossil fuels and nuclear energy are currently intensively developed technologies using so-called renewable energy sources such as biomass, geothermal energy, wind or tidal power, and solar energy. Particularly attractive from the point of view of sustainable development and ecology seems to be the perspective of using sunlight. Among many intensively developed photovoltaic technologies in particular dye-sensitized solar cells (DSSC) present important scientific interests.

The scientific goal of the presented thesis was to explain the mechanism of charge transfer occurring between dyes and semiconductors in selected hybrid materials used in DSSC applications. The work is part of the global trend of research on the use of alternative energy sources and has resulted in the development of new hybrid materials and their components. The work was based on computer simulations of the structural, electron, and optical properties of hybrid dye/semiconductor materials. It aimed to determine the effect of doping and defecting of the TiO_2 semiconductor on the light-to-current efficiency conversion. Also, the impact of the modification of dyes, especially ruthenium-based complexes, on the photovoltaic properties of dye/TiO_2 hybrids was studied computationally and the results were tested by experimental investigations.

As a result of the performed quantum-chemical calculations of the structural and electron properties of stoichiometric and non-stoichiometric TiO_2 crystals, it was shown that using the DFT calculation method with appropriate Hubbard corrections, it is possible to map the physicochemical properties of oxide semiconductor materials, which so far was unattainable in many literature reports. Using selected numerical parameters, the electron properties of TiO_2 crystals in the anatase phase, doped with X=Zr, Ni, Mn, Cu, or N ions and containing oxygen vacancies, were characterized. The role of vacancies in TiO_2:X materials as the main stimulator of the appearance of donor and acceptor levels in the TiO_2 band gap was determined.

As a result of experimental studies and quantum-chemical calculations, it was shown that doping TiO_2 with Zr ions stabilizes its structure in the form of anatase and generates oxygen vacancies, which positively affects the photoconversion properties. It has been proven that the modification of TiO_2 with X^{2+} ions creates additional electron states in the band gap region. It has been shown that the creation of additional energy levels near the conduction band (donor levels) has a positive effect on the driving force of electron injection from the sensitizer into the semiconductor material. Analyzing the shape and location of the donor levels, it was shown that the increase in their dispersion supports the charge transport in the conduction band (TiO_2:Ni). The flattened structure of the donor level (TiO_2:Cu) supports unwanted recombination processes by reducing the lifetime of the injected electron. It was also shown that the creation of additional energy (acceptor) levels close to the edge of the valence band does not affect the charge transfer process in DSSC systems (TiO_2:Mn). The results of the conducted research indicate that both the type of admixture and its percentage content have a significant impact on the charge transfer in DSSC cells.

Electron properties of two groups of organic dyes were investigated: those with one trisbipyridine group per molecule (RuLp, RuLo, RuLm) and dendrimer molecules containing two trisbipyridine groups (B_1, B_2, B_3, B_4). The dyes differed in the position and number of anchor groups (-COOH) and in the construction of the separator between the trisbipyridine and the anchor. It was shown that the intramolecular electron transfer and injection capabilities of TiO_2 depend on the position of the anchor group. Cells sensitized with ortho-substituted dye (RuLo), possessing steric hindrance coupled causing specific intramolecular interactions, suppress the dye adsorption capacity, compromising DSSC performance. Dyes with an anchor in the meta (RuLm) and para (RuLp) positions adsorb on the TiO_2 surface in a similar amount, but the efficiency of para-sensitized DSSC is higher. Additionally, the role of stabilizers was explained by performing quantum-chemical calculations of electron and optical properties of mono and biruthenium organic dyes.

A method for the construction of organic dye/nanostructured semiconductor hybrid materials based on computer simulations was developed. The proposed approach is based on simulations of the model/TiO_2 system and then by substitution of dye molecule in the position of anchor group. Was shown that the implemented methodology of hybrid system modeling gives good results in calculating the optical properties of hybrids. The proposed approach is reasonable in the case of structurally complicated dyes. The small dyes can be taken into consideration during the geometry optimization procedure without any restrictions.

Three possible types of connections between dyes and semiconducting nanostructures were found. The bond of Type 1 creates the most stable B_x-based hybrid structures, compared with Type 2 and Type 3. Calculations of the electron and optical properties of the hybrid materials were carried out. The mechanism of charge transfer between dye and semiconductor in the process of photoexcitation was explained. Simulations clearly show the preference of para-position of -COOH group to the donor part as it is noticed for RuLp connected by the bond of Type 1 as well as for B_2 and B_3 dyes connected to the semiconductor by the bond of Type 2. In the case of the bond of Type 1, the best properties were achieved for B_3. The charge transfer occurring in this case between B_3 and TiO_2 is equal to 13.70 %. A similar value of the electron transfer was obtained for the RuLp/$(TiO_2)_{28}H_{15}$ hybrid. In the case of the B_2/$(TiO_2)_{28}H_{15}$ with a bond of Type 3 the observed charge transfer is equal to 22.43 %, but the probability of occurrence of the bond of Type 2 is less than the bond of Type 1. Both hybrids, the RuLp/$(TiO_2)_{28}H_{15}$ and B_3/$(TiO_2)_{28}H_{15}$, can be used in photovoltaic applications. However, better efficiency of light-to-electron energy conversion is observed for the RuLp-based structures. The conclusion is that for the ruthenium-based dyes, a two-stage charge transfer mechanism is observed.

The completed research complements the state of knowledge regarding charge transfer processes in dye cells. It was found that when planning structural modifications of nanomaterials, one should primarily take into account its adjustment to the energy levels of the dye. Experimental studies supplemented with quantum-chemical calculations helped in the interpretation of the obtained results and showed that the proposed holistic approach should become a standard in research on the design of photomaterials. The presented results are important for the search for new sensitizers and may be a starting point for further research beyond the field of photovoltaics.

OŚWIADCZENIE

Ja, niżej podpisany/a ....
Imię i Nazwisko

doktorant* / doktorantka* Wydziału ....
Uniwersytetu Humanistyczno-Przyrodniczego im. Jana Długosza w Częstochowie oświadczam, że przedkładaną pracę doktorską pt.

....

....

....

napisałem/am samodzielnie. Oznacza to, że przy pisaniu pracy, poza niezbędnymi konsultacjami, nie korzystałem/am z pomocy innych osób, a w szczególności nie zlecałem/am opracowania rozprawy lub jej części innym osobom, ani nie odpisywałem/am tej rozprawy lub jej części od innych osób.

Oświadczam również, że drukowana wersja pracy jest identyczna z załączoną wersją elektroniczną.

Jednocześnie przyjmuję do wiadomości, że gdyby powyższe oświadczenie okazało się nieprawdziwe, decyzja o wydaniu mi dyplomu zostanie cofnięta.

Ponieważ niniejsza praca jest moją własnością intelektualną, chronioną prawem autorskim, w związku z zamysłem wydania jej drukiem wyrażam zgodę* / nie wyrażam zgody* na udostępnianie mojej rozprawy doktorskiej do celów naukowych i badawczych w internecie.

Częstochowa, dnia ....
podpis

* - niepotrzebne skreślić